ATOMIC-SCALE SPECTROSCOPY AND CONTROL OF LAYERED MATERIALS WITH TERAHERTZ FIELDS

By

Stefanie Adams

A DISSERTATION

Submitted to
Michigan State University
in partial fulfillment of the requirements
for the degree of

Physics—Doctor of Philosophy

2026

ABSTRACT

The development of faster and more efficient next-generation technologies relies on controlling materials at ever smaller length and time scales. As the design of electronic components approaches atomic thicknesses, the choice of material becomes increasingly critical, since electronic and optical properties at reduced dimensionality can fundamentally differ from those of the bulk. Symmetry breaking at interfaces and atomic-scale disorder, such as defects in the crystal lattice, can influence macroscopic material behavior and give rise to emergent collective phenomena. Many of these processes, including lattice vibrations or phase transitions, occur on sub-picosecond time scales. Harnessing material properties at their fundamental limits requires an experimental tool capable of probing and controlling matter with combined atomic spatial resolution and ultrafast temporal resolution.

Scanning tunneling microscopy is a well-established technique to study the local density of electronic states of a material with atomic resolution, yet it is typically limited to steady-state measurements. In contrast, pump-probe spectroscopy resolves ultrafast collective dynamics by using short laser pulses to excite and probe a material. However, its spatial resolution is largely limited by the optical focal spot size. Terahertz laser pulses are of particular interest because the period of a single terahertz-cycle oscillation corresponds to sub-picosecond time scales, where they can access low-energy excitations. A central techniques in terahertz science is time-domain spectroscopy, in which the temporal evolution of the electric field waveform is measured to extract the complex dielectric response of a sample (how the material absorbs and delays electromagnetic radiation). The spatial resolution of this approach has previously been limited to tens to hundreds of nanometers, leaving the atomic scale inaccessible.

Terahertz scanning tunneling microscopy bridges the gap between ultrafast spectroscopy and atomic-resolution microscopy by using single-cycle terahertz pulses coupled to a scanning tunneling microscope tip. This thesis introduces atomic-scale terahertz time-domain spectroscopy as a generally applicable technique within the terahertz scanning tunneling microscopy framework. Careful optimization of the measurement parameters combined with a self-consistent data-driven analysis approach enables retrieval of the complex dielectric response of atomic-scale features relative to their immediate environment. This method provides access to study how local disorder, such as interfaces and atomic defects, influences longer-range collective material properties.

As terahertz electric fields are strongly enhanced at the tip apex, they can not only probe, but also actively modify the properties of materials exhibiting resonances in the terahertz frequency range. This is demonstrated on a layered material where the terahertz electric field drives a topological phase transition of a single atomic layer by coupling to an interlayer shear mode that changes the lattice symmetry. The transition is visualized with picometer-scale spatial resolution by capturing the structural displacement and electronic contrast between the ground state and metastable excited

state phase as a differential signal.

The work presented here advances terahertz scanning tunneling microscopy as an ultrafast, atomically-resolved technique by establishing a generally applicable method for atomic-scale measurements of the complex dielectric response and demonstrating terahertz-driven local manipulation and readout of electronic properties. These results offer a framework for future investigations of collective excitations and their interplay with local disorder and, more broadly, expand the experimental toolkit for probing and controlling materials at their intrinsic spatiotemporal scales.

To my grandmother and my godmother, in loving memory.

"Many high barriers exist in this world: barriers between nations, races, and creeds. Unfortunately, some barriers are thick and strong. But I hope, with determination, we will find a way to tunnel through these barriers easily and freely, to bring the world together ..."
– Leo Esaki (Nobel Laureate in Physics, 1973)

ACKNOWLEDGMENTS

My Ph.D. journey would not have been possible without all the incredible people who supported me along the way.

First and foremost, I would like to thank my advisor Prof. Tyler Cocker. Working under his guidance has helped me grow into the role of a researcher and has inspired me to continue to pursue a career in research. I am thankful to Tyler for giving me the opportunity to work in his group on cutting-edge research and for allowing me to present our results and engage with the research community at national and international conferences. His enthusiasm for science is contagious, and I truly appreciate having had an involved advisor who is always curious about the progress of our projects.

Another very important mentor for me during my time at Michigan State University was Dr. Vedran Jelic, with whom I spent countless hours taking measurements in the lab. I would like to thank Vedran for sharing all his knowledge and enthusiasm about research with me.

The last five years would not have been half as joyful, and none of this research would have been possible without my labmates in Tyler's research group. I am especially grateful to Mohamed (Mo) Hassan for always supporting me, not only as a coworker in the lab but also as a good friend. I would also like to thank my office mates Kaedon Cleland-Host and Austin Hayes (in addition to Mo Hassan) for creating a great atmosphere in the office and for the many fruitful discussions about research and beyond. Even though we had little overlap, I would also like to acknowledge Eve Ammerman for her groundwork for many of the data analysis methods that I have built on and for instructing me how to use them before her graduation. I would also like to acknowledge Sheng Lee, Jacob Conley, and Connor Kramp for their dedication to our group's research and being wonderful coworkers.

Next, I would like to express my gratitude to the members of my Ph.D. committee, Prof. Huey-Wen Lin, Prof. Carlo Piermarocchi, Prof. Stuart Tessmer, Prof. Weiwei Xie and Prof. Pengpeng Zhang for their guidance and valuable input over the course of my doctoral studies.

Most of the work presented in this thesis would not have been possible without collaborations with other research groups. Here, I would like to acknowledge Prof. Pengpeng Zhang and her group, specifically Yasmin Ozbek and Maya Bostock, for custom sample growth and for helping establish an ultra-high-vacuum pathway between our labs. Further, I am deeply grateful to Prof. Jose Mendoza-Cortes and his group for their theory support. I especially valued the regular meetings with his students Daniel Maldonado-Lopez, Ismail A. Buliyaminu, and Axel Melchor Gaona who not only performed calculations but also taught me so much about how density functional theory works. A special thank you goes to Prof. Woei-Wu (Larry) Pai for his expertise in sample preparation and growth. Also, I would like to thank the technical and administrative staff in the Physics and Astronomy Department of Michigan State University, especially Reza Loloee, Baokang

Bi, and Kim Crosslan. I would like to acknowledge the sponsors and funding agencies that made the research presented here possible. This includes sponsorship through the Office of Naval Research, the Army Research Office, the Air Force Office of Scientific Research, the Department of Energy, the Fulbright Association, the Cowen Family Endowment, the Alfred J. and Ruth Zeits Endowment and the College of Natural Science at Michigan State University.

I would also like to thank my undergraduate mentors and teachers at the University of Stuttgart, especially Prof. Sebastian Loth and his research group, who advised me during my undergraduate studies and research and supported me in applying for graduate school abroad in the middle of a pandemic.

For me, graduate school meant moving across continents and starting in a completely new environment. Little did I know when I started this journey that I would meet so many wonderful people who would become close friends and make Michigan truly a new home for me. I am especially thankful for the sense of community that I felt with other physics Ph.D. students at Michigan State University and for my graduate-school friends. Whenever research or classes were tough, I had fun things to look forward to that helped me recharge. I will cherish the memories I made during weekend trips around Michigan and beyond. I am grateful to everyone I met through various athletic activities like soccer, basketball, kickball, or running, that not only kept me physically fit but also helped me cope with the pressures of graduate school. A special thanks to my condensed matter friends with offices on the same floor, who were always up for good conversations during coffee and lunch breaks. I am equally thankful for having been able to keep in touch with my close friends in Germany and their continuous encouragement over the past few years.

A very special thank you goes to the Schulze family, who turned from "neighbors down the street" to "family away from home". Whether during camping trips or casual front-yard hangouts, our time together means a great deal to me and always brings me happiness.

Of course, I would also like to thank the people who have known me the longest and shaped me into the person I am today. I feel very grateful to my parents and my sister for their love and support and for always believing in me. Even though we have seen each other only a few times over the past few years, we have made those times count and maintained a close connection. I also think with deep gratitude of my late grandmother and my late godmother whose love and support continues to stay with me.

Finally, I would like to thank my fiancé Johannes for always being there for me with love, patience, and kindness and for supporting me through my sometimes pretty chaotic graduate student life. I do not know how I would have made it through these past years without you. Being in it together has made everything feel like a big adventure.

PREFACE

This dissertation presents the results of multiple projects carried out during my time as a Ph.D. student in Prof. Tyler Cocker's research group from 2021 to 2026. The work, performed with a terahertz scanning tunneling microscope, is aimed at probing and controlling the atomic-scale properties of transition metal dichalcogenide materials with atomic scale resolution while advancing the experimental technique and its data analysis. The content of the main chapters is based on two peer-reviewed publications, one manuscript under review and one manuscript in preparation. The relation between publications and chapters as well as my original contributions are listed in the following.

Chapter 3 - Control and validation of terahertz near-fields for atomic-scale time-domain spectroscopy: The majority of this chapter is adapted from the submitted manuscript S. Adams, V. Jelic, M. Hassan, K. Cleland-Host, E. Ammerman and T. L. Cocker *Control and Validation of Terahertz Near-Fields for Atomic-Scale Time-Domain Spectroscopy* (under review, 2026). I performed the data acquisition, data analysis and preparation of the manuscript. This chapter also includes content published in V. Jelic, S. Adams, M. Hassan, K. Cleland-Host, E. Ammerman and T. L. Cocker *Atomic-scale terahertz time-domain spectroscopy* (Nature Photonics, 2024). My primary contribution was the development of the data analysis methodology and measurement simulation to validate the novel experimental technique. This approach informed the choice of measurement parameters and control experiments the majority of which I participated in. The code related to these projects is available on GitHub (github.com/NanoTHzCoding/THz_STS_Algorithm).

Chapter 4 - Atomic-scale phonon spectroscopy of 2D heterostructures: I performed the data acquisition and data analysis for this work. This project is a collaboration with the groups of P. Zhang (Michigan State University) for sample growth and J. L. Mendoza-Cortes for theory (Michigan State University). A manuscript is in preparation. This chapter further includes preliminary data of samples provided by W.-W. Pai (National Taiwan University), who also contributed to the *in situ* sample preparation at Michigan State University.

Chapter 5 - Terahertz field control of surface topology probed with subatomic resolution: This chapter is adapted from V. Jelic*, S. Adams*, D. Maldonado-Lopez*, I. A. Buliyaminu, M. Hassan, J. L. Mendoza-Cortes, and T. L. Cocker *Terahertz field control of surface topology probed with subatomic resolution* (Nature Photonics, 2025). I contributed to the data acquisition, data analysis and preparation of the manuscript with V. Jelic as well as coordinated the theory collaboration with the group of J. L. Mendoza-Cortes (Michigan State University).

TABLE OF CONTENTS

LIST OF FIGURES

LIST OF ABBREVIATIONS

1D	One-dimensional
2D	Two-dimensional
3D	Three-dimensional
AC	Autocorrelation
ADC	Analog-to-digital converter
AFM	Atomic force microscopy
ARPES	Angle-resolved photoemission spectroscopy
BS	Beam splitter
CDW	Charge density wave
CEP	Carrier envelope phase
DAC	Digital-to-analog converter
DFT	Density functional theory
DG	Diffraction grating
DOS	Density of states
DSP	Digital signal processing
EOS	Electro-optic sampling
FFT	Fast Fourier transform
FM	Flip mirror
HOPG	Highly oriented pyrolytic graphite
HV	High voltage
IGP	Ion getter pump
IR	Infrared
LDOS	Local density of states
LL	Load lock

MBE Molecular beam epitaxy

MSE Mean squared error

NIR Near-infrared

OPA Optical parametric amplifier

PDOS Phonon density of states

PES Photoemission sampling

PI Proportional–integral

RGA Residual gas analyzer

RP Roughing pump

RT Room temperature

s-SNOM Scattering-type scanning near-field optical microscopy

SNOM Scanning near-field optical microscopy

SOC Spin-orbit coupling

STEM Scanning transmission electron microscopy

STM Scanning tunneling microscopy

STS Scanning tunneling spectroscopy

THz-AC Terahertz autocorrelation

THz-CC Terahertz cross-correlation

THz-STM Terahertz scanning tunneling microscopy

THz-STS Terahertz scanning tunneling spectroscopy

THz-TDS Terahertz time-domain spectroscopy

TMD Transition metal dichalcogenide

TP Turbo pump

TSP Titanium sublimation pump

UHV Ultra high vacuum

UV Ultraviolet

WGP Wire grid polarizer

WKB Wentzel-Kramers-Brillouin

WP Weyl point

CHAPTER 1

INTRODUCTION

Across many areas of physics, research is not only driven by the curiosity to explore fundamental phenomena but also by the need for technological progress.

In the 1965, Gordon Moore predicted that the number of transistors in an integrated circuit doubles every two years [1]. This is known as *Moore's law* and has proven accurate for at least five decades. It is highly debated whether the rule still applies today and, if so, when it will eventually cease to be valid [2]. Over the past 60 years, the exponential trend has been upheld primarily by making silicon-based transistors smaller [3]. However, there is a fundamental limit to such dimensional scaling. A transistor's performance deteriorates significantly when the silicon thickness is reduced to the few nanometer scale. This is due to increased carrier scattering that results in heating, short channel effects (poor gate control) and overall increased device-to-device variability due to quantum confinement [4]. While the slowing of dimensional scaling has been partially counteracted by improvements to the device architecture, e.g., improved gate design, it is clear that a more fundamental breakthrough is inevitable to continue expanding the transistor density in integrated circuits [2]. This is where demand for technological advancement converges with fundamental scientific research – specifically the field of two-dimensional (2D) materials.

2D materials have a layered 'quasi 2D' structure. The atoms within a layer are linked with strong covalent bonds whereas the layers are held together by weak van-der-Waals forces [5]. This makes it easy to exfoliate or fabricate 2D materials down to few or even single atomic layer thicknesses [6]. The most prominent example is single-layer graphene [7]. In recognition of this discovery, Andre Geim and Konstantin Novoselov were awarded the Nobel prize in physics in 2010 *"for groundbreaking experiments regarding the two-dimensional material graphene"* [8]. Today, the term *2D materials* encompasses numerous subclasses with unique properties and opportunities for technological applications far beyond transistors [9]. The work presented in this dissertation focuses on transition metal dichalcogenides (TMDs), one of the most prominent subclasses, and on materials with TMD-like structures and properties.[1]

TMDs have stoichiometry MX_2. Each atomic layer is made of a transition metal atom (M) sandwiched between two chalcogen atoms (X) [10] as shown in the center of Fig. 1.1. The diversity of chemical compositions, for instance the number of d-orbital electrons of the transition metal atom, leads to a variety of atomic lattice structures and electronic properties, and can promote the emergence of quantum phases [11]. This makes TMDs an ideal platform to explore new fundamental phenomena, in addition to their relevance for technology.

[1] Chapter 4 discusses experiments with $SnSe_2$. Although Sn is a main-group metal, rather than a transition metal, the properties of $SnSe_2$ are closely related to TMDs. For simplicity, it will be discussed alongside TMDs.

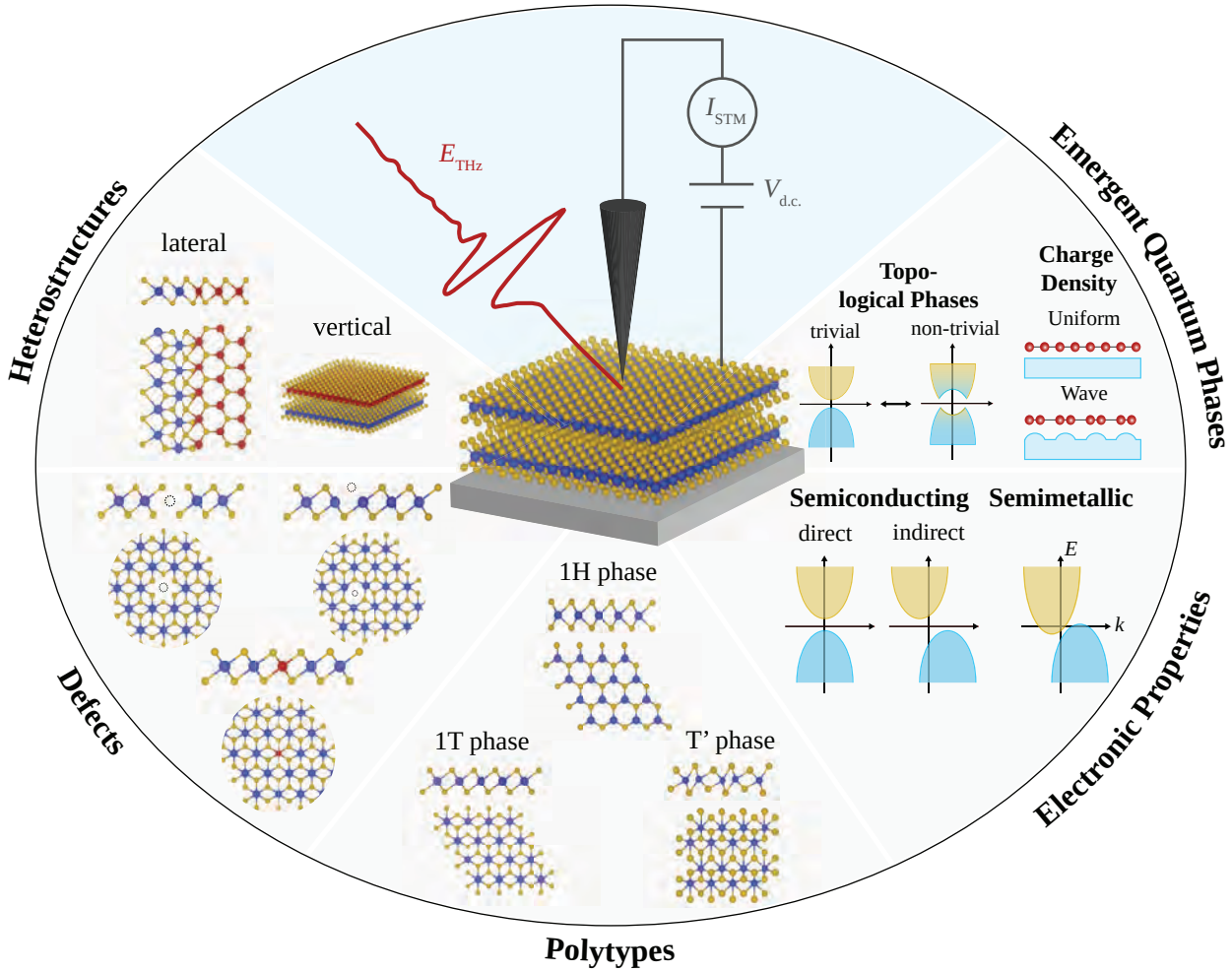

Figure 1.1 THz-STM of TMD materials. Overview of TMDs and their properties probed and controlled using a terahertz scanning tunneling microscope.

Monolayer TMDs primarily exist in three structural phases, also referred to as polytypes (Fig. 1.1, bottom). The thermodynamically stable structural phase is determined by the specific combination of transition metal (typically from group IV, V, VI, VII, IX or X) and chalcogen (Se, S or Te) atoms; however, other polytypes often exist as metastable states [12]. In the 1H phase, the transition metal atom is in trigonal-prismatic coordination, and the chalcogen atoms are vertically aligned in the out-of-plane direction, corresponding to an ABA arrangement of the three atomic planes within a monolayer. In contrast, the 1T phase exhibits octahedral coordination and an ABC arrangement of the chalcogen–metal–chalcogen planes in each layer. In some materials, if energetically favorable, this structure distorts into the 1T' phase via zig-zag dimerization of the transition metal atoms [13].

The polytype of a material determines the nature of its electronic band structure and controls the degeneracy as well as the energy splitting of the transition metal d-orbitals. The filling of these

orbitals gives rise to either semiconducting (when partially filled) or metallic (when completely filled) behavior [11]. The electronic band structure is further influenced by the thickness of the sample. For multi-layer and bulk systems, three-dimensional structural phases can be defined via the stacking order of the different monolayer polytypes, resulting in an even larger variety of properties. For example, MoS_2 changes its symmetry with the number of stacked layers. This has been demonstrated using second-harmonic generation, which showed a strong signal for an odd number of layers (including a monolayer), indicating broken inversion symmetry, but the signal is strongly suppressed or absent for an even number of layers, implying that inversion symmetry is present [14]. Some semiconducting TMDs exhibit an indirect to direct band gap transition in the monolayer limit (Fig. 1.1, bottom right). This results from of an increase of the indirect band gap width due to enhanced out-of-plane quantum confinement with fewer layers [15, 16]. The band gap in monolayer TMDs is typically on the order of 1-2 eV, leading to high optical absorption in the near-infrared (NIR) and visible regime due to the direct transitions between valence and conduction bands [17].

The 2D character of TMDs, combined with their crystal symmetry, promotes rich phase diagrams with emergent quantum phases such as charge density waves (CDWs) and topological non-trivial phases. At low temperatures, some metallic TMDs host CDW states where the electronic charge density becomes spatially modulated and is accompanied by a periodic lattice distortion (Fig. 1.1, top right). The underlying cause is enhanced electron-phonon interaction because the electrostatic potential generated by lattice vibrations (phonons) is less screened with reduced dimensionality of the material [18]. Topologically non-trivial phases exist predominantly in TMDs containing heavier elements (e.g., M=W or Ta, X=Te), because their large nuclear charge produces stronger internal electric fields and therefore enhanced spin–orbit coupling (SOC). Strong SOC reshapes the electronic band structure by lifting degeneracies. Combined with specific lattice symmetries, such as broken inversion symmetry, this can lead to band inversions that constitute a topologically non-trivial phase [19] (Fig. 1.1, top right). Depending on the material, transitions between two trivial phases as well as between trivial and topological phases can, for example, be induced via pressure, strain and temperature, and in some cases using ultrafast laser pulses, as discussed in Chapter 5.

Light-induced phase transitions are just one aspect of the enormous potential that TMDs (and 2D materials in general) offer to study light-matter interaction phenomena. Coupling of external electro-magnetic fields to TMDs is enhanced due to reduced dielectric screening. Depending on the frequency of the electric field, a variety of properties can be studied [18]. A major research direction in this context is the absorption and emission of NIR and visible radiation to develop next-generation optoelectronic devices (e.g., photo detectors and light emitting diodes) [20]. The pronounced optical resonances in many semiconducting TMDs originate from excitons (bound

electron-hole pairs) with a large binding energy, on the order of hundreds of meV, due to enhanced Coulomb interaction [21]. While NIR and visible electric fields can probe interband excitonic transitions, many of the relevant low-energy modes and excitations in TMDs lie in the sub-meV to few-tens of meV range and are therefore naturally accessible with terahertz frequencies [22]. Measuring the complex dielectric response (frequency-dependent permittivity and conductivity) via terahertz spectroscopy can provide insights about the following material properties: charge carrier dynamics, transitions between excitonic states, phonon dynamics, collective excitations such as phonon polaritons (photon-phonon quasiparticle) and also phenomena related to emergent quantum phases, such as CDW formation/melting and terahertz-induced phase transition pathways [23–25]. A significant advantage of probing a material with short terahertz pulses, compared to continuous wave measurements, is the ability to access ultrafast phenomena by combining two pulses into a pump-probe experiment, where the temporal evolution of the system after excitation is recorded on the femto- to picosecond time scale [25]. Because of the Abbe diffraction limit (minimum resolved distance ~ wavelength/2) [26], free space focusing of terahertz pulses is limited to the 0.1–1 mm scale. Free-space terahertz experiments are therefore far-field measurements that average over a macroscopic area of the sample.

An additional key aspect about TMDs not addressed so far is the role of atomic defects (vacancies, substitutional atoms, adatoms, etc.; see Fig. 1.1, top left) and other impurities, such as domain boundaries and step edges. Because of the weak screening vertical to the layers, intrinsic defects in TMDs are more exposed and typically more abundant compared to bulk three-dimensional materials [18]. Individual heterogeneities in the atomic lattice modify the electronic structure, vibrational spectrum, and energy-dissipation pathways locally. If present with a certain density, they can strongly influence the macroscopic properties of a material. One example is MoS_2 where S vacancies act as donors and and sources of short-range disorder, leading to low mobility and n-type doping of the overall material [27]. Defects in TMDs can also play an important role in pinning phases and seeding phase transitions by acting as nucleation sites and breaking local symmetries [18].

To probe the local properties of defects and relate them to the material's macroscopic behavior, it is essential to employ an experimental technique whose spatial resolution is on the characteristic length scale of the features, namely the sub-nanometer or atomic-scale regime. The most prominent methods are scanning transmission electron microscopy (STEM) and scanning tunneling microscopy (STM). STEM provides direct atomic-resolution imaging of the lattice and enables chemical identification of atomic sites. It has proven valuable for identifying defects and interfaces in TMDs [28, 29]. However, STEM does not provide information about the electronic or optical behavior on and around the defects and the samples are susceptible to electron beam-induced defects. In contrast, STM combines atomic spatial resolution with access to the local density of electronic

states (LDOS), making it a well suited technique to characterize the electronic environment and defect-induced signatures, such as in-gap states or band bending [30–34].

To attain a comprehensive picture of the role of defects and the local behavior of phase transitions in TMDs, the atomic-scale information on the electronic structure obtained by STM must be complemented by two key capabilities provided by terahertz techniques: (1) ultrafast time resolution to probe dynamical processes and (2) access to the complex dielectric response.

In terahertz scanning tunneling microscopy (THz-STM) terahertz pulses are coupled to an STM tip (Fig. 1.1, top center) and achieve simultaneous atomic-scale spatial resolution and ultrafast temporal resolution to successfully address the required capability (1) [35, 36]. THz-STM is possible because terahertz fields coupled to an STM tip act as ultrashort voltage pulses between tip and sample (see Chapter 2 for details) and allow for pump-probe-style measurements with ultrafast resolution [37]. THz-STM has already proven useful on multiple TMD samples, for example in studies of CDW materials [38, 39] and investigations of atomic-scale defects and their impact on the surrounding local environment [40–43].

Prior to the work presented in Chapter 3 of this thesis, scattering-type scanning near-field optical microscopy (s-SNOM) offered the highest spatial resolution among techniques capable of probing the complex optical response of a sample, and addressing requirement (2). In s-SNOM, far-field terahertz pulses are coupled to nanoscale tips, which creates a near-field interaction and pushes the spatial resolution far below the diffraction limit, typically to about 10-100 nm [25, 37]. The electric field scattered from the tip contains the sample's local near-field response and can be compared to a reference signal to extract information about the complex optical properties [44, 45]. However, the resolution of s-SNOM is ultimately limited by the radius of the tip apex. To extend probing of the local near-field properties to the atomic-scale, the temporal shape of the terahertz field must be measured directly via the tunnel current to leverage the sub-nanometer spatial resolution inherent to the tunneling process. The development of this technique is presented in Chapter 3. It is applied to TMD defects and interfaces in the work described in Chapter 4 as well as to a localized terahertz induced phase transition material, presented in Chapter 5.

To summarize, the work presented in this dissertation is motivated both by fundamental scientific curiosity and by technological demand to probe and control the properties of two-dimensional quantum materials at the atomic scale. From a fundamental science perspective, TMDs constitute a versatile playground with rich phase diagrams and low-energy excitation modes that are sensitive to atomic-scale features. From an applied perspective, the development of high-performance devices, such as nanoelectronics and nanophotonics, relies on tuning material properties on the atomic scale through parameters such as thickness (number of layers), dopants and defects, strain, and stacking of vertical and lateral heterostructures [12, 46].

These goals are addressed by advancing and applying the technique of THz-STM to several

TMD material systems. The state of the art of THz-STM has now reached the point where static and dynamic properties of the local electronic environment and complex dielectric response can be probed simultaneously with atomic-scale spatial resolution. This is a much needed advancement, specifically in the context of low dimensional materials.

The remainder of this dissertation is organized in the following chapters.

- *Chapter 2 – Terahertz scanning tunneling microscopy* introduces the experimental technique by first showcasing the history and state of the art of the field and then describing the experimental setup at Michigan State University used to perform the measurements for this dissertation.

- *Chapter 3 – Control and validation of terahertz near-fields for atomic-scale terahertz time-domain spectroscopy* describes the development of a novel technique to capture the temporal evolution of terahertz near-field pulse shapes at atomically precise locations. This is the basis for atomic-scale THz-TDS, where information about the local dielectric environment can be retrieved. This is demonstrated on a GaAs defect. The focus of this chapter lies on the measurement parameter selection, data analysis and the validation procedure.

- *Chapter 4 – Atomic-scale phonon spectroscopy of 2D heterostructures* reports results on a heterostructure sample ($SnSe_2$ and WSe_2) with lateral and vertical interfaces as well atomic-scale defects. It showcases the influence of such features on the dielectric environment, specifically the attenuation of an out-of-plane acoustic phonon mode, by probing the near-field via atomic-scale THz-TDS measurements. This chapter also includes an outlook and some preliminary data towards probing and controlling collective order in TMDs with ultrafast time resolution.

- *Chapter 5 – Terahertz field control of surface topology probed with subatomic resolution* presents how terahertz pulses can not only probe, but also control a topological phase transition to a metastable state in WTe_2. The switching between the phases is confined to the top atomic layer of the sample and can be read out as a differential signal, which provides unprecedented spatial resolution of the electronic differences between the ground state and excited state phase. Because most of the bulk sample remains in the ground state, the locally induced metastable region effectively forms a light-induced heterostructure between the two phases.

- *Chapter 6 – Conclusions and outlook* summarizes the results of this dissertation and provides and outlook.

BIBLIOGRAPHY

[1] Moore, G. Cramming More Components Onto Integrated Circuits. *Proceedings of the IEEE* **86**, 82–85 (1998).

[2] Kim, K. S. *et al.* The future of two-dimensional semiconductors beyond Moore's law. *Nature Nanotechnology* **19**, 895–906 (2024).

[3] Hu, C. Future CMOS scaling and reliability. *Proceedings of the IEEE* **81**, 682–689 (1993).

[4] Pop, E., Sinha, S. & Goodson, K. Heat Generation and Transport in Nanometer-Scale Transistors. *Proceedings of the IEEE* **94**, 1587–1601 (2006).

[5] Novoselov, K. S., Mishchenko, A., Carvalho, A. & Castro Neto, A. H. 2D materials and van der Waals heterostructures. *Science* **353**, aac9439 (2016).

[6] Novoselov, K. S. *et al.* Two-dimensional atomic crystals. *Proceedings of the National Academy of Sciences* **102**, 10451–10453 (2005).

[7] Novoselov, K. S. *et al.* Electric Field Effect in Atomically Thin Carbon Films. *Science* **306**, 666–669 (2004).

[8] The Nobel Prize in Physics 2010. Available at `https://www.nobelprize.org/prizes/physics/2010/summary/`.

[9] Liu, A. *et al.* The Roadmap of 2D Materials and Devices Toward Chips. *Nano-Micro Letters* **16**, 119 (2024).

[10] Wilson, J. & Yoffe, A. The transition metal dichalcogenides discussion and interpretation of the observed optical, electrical and structural properties. *Advances in Physics* **18**, 193–335 (1969).

[11] Voiry, D., Mohite, A. & Chhowalla, M. Phase engineering of transition metal dichalcogenides. *Chemical Society Reviews* **44**, 2702–2712 (2015).

[12] Manzeli, S., Ovchinnikov, D., Pasquier, D., Yazyev, O. V. & Kis, A. 2D transition metal dichalcogenides. *Nature Reviews Materials* **2**, 17033 (2017).

[13] Choi, W. *et al.* Recent development of two-dimensional transition metal dichalcogenides and their applications. *Materials Today* **20**, 116–130 (2017).

[14] Li, Y. *et al.* Probing Symmetry Properties of Few-Layer MoS_2 and h-BN by Optical Second-Harmonic Generation. *Nano Letters* **13**, 3329–3333 (2013).

[15] Mak, K. F., Lee, C., Hone, J., Shan, J. & Heinz, T. F. Atomically Thin MoS_2: A New

Direct-Gap Semiconductor. *Physical Review Letters* **105**, 136805 (2010).

[16] Splendiani, A. *et al.* Emerging Photoluminescence in Monolayer MoS_2. *Nano Letters* **10**, 1271–1275 (2010).

[17] Mak, K. F. & Shan, J. Photonics and optoelectronics of 2D semiconductor transition metal dichalcogenides. *Nature Photonics* **10**, 216–226 (2016).

[18] Li, W., Qian, X. & Li, J. Phase transitions in 2D materials. *Nature Reviews Materials* **6**, 829–846 (2021).

[19] Yang, H., Kim, S. W., Chhowalla, M. & Lee, Y. H. Structural and quantum-state phase transitions in van der Waals layered materials. *Nature Physics* **13**, 931–937 (2017).

[20] Bhimanapati, G. R. *et al.* Recent Advances in Two-Dimensional Materials beyond Graphene. *ACS Nano* **9**, 11509–11539 (2015).

[21] Wang, G. *et al.* Colloquium: Excitons in atomically thin transition metal dichalcogenides. *Reviews of Modern Physics* **90**, 021001 (2018).

[22] Han, P., Wang, X. & Zhang, Y. Time-Resolved Terahertz Spectroscopy Studies on 2D Van der Waals Materials. *Advanced Optical Materials* **8**, 1900533 (2020).

[23] Ulbricht, R., Hendry, E., Shan, J., Heinz, T. F. & Bonn, M. Carrier dynamics in semiconductors studied with time-resolved terahertz spectroscopy. *Reviews of Modern Physics* **83**, 543–586 (2011).

[24] Jepsen, P., Cooke, D. & Koch, M. Terahertz spectroscopy and imaging – Modern techniques and applications. *Laser & Photonics Reviews* **5**, 124–166 (2011).

[25] de Abajo, F. J. G. *et al.* Roadmap for Photonics with 2D Materials. *ACS Photonics* **12**, 3961–4095 (2025).

[26] Born, M. & Wolf, E. *Principles of Optics: Electromagnetic Theory of Propagation, Interference and Diffraction of Light* (Cambridge University Press, Cambridge, 1999), 7 edn. Available at https://www.cambridge.org/core/books/principles-of-optics/D12868B8AE26B83D6D3C2193E94FFC32.

[27] Qiu, H. *et al.* Hopping transport through defect-induced localized states in molybdenum disulphide. *Nature Communications* **4**, 2642 (2013).

[28] Luo, R. *et al.* Probing Functional Structures, Defects, and Interfaces of 2D Transition Metal Dichalcogenides by Electron Microscopy. *Advanced Functional Materials* **34**, 2307625 (2024).

[29] Han, X. *et al.* Atomically engineering metal vacancies in monolayer transition metal dichalcogenides. *Nature Synthesis* **3**, 586–594 (2024).

[30] Zhussupbekov, K. *et al.* Imaging and identification of point defects in $PtTe_2$. *npj 2D Materials and Applications* **5**, 14 (2021).

[31] Addou, R., Colombo, L. & Wallace, R. M. Surface Defects on Natural MoS_2. *ACS Applied Materials & Interfaces* **7**, 11921–11929 (2015).

[32] Barja, S. *et al.* Identifying substitutional oxygen as a prolific point defect in monolayer transition metal dichalcogenides. *Nature Communications* **10**, 3382 (2019).

[33] Schuler, B. *et al.* How Substitutional Point Defects in Two-Dimensional WS_2 Induce Charge Localization, Spin–Orbit Splitting, and Strain. *ACS Nano* **13**, 10520–10534 (2019).

[34] Schuler, B. *et al.* Large Spin-Orbit Splitting of Deep In-Gap Defect States of Engineered Sulfur Vacancies in Monolayer WS_2. *Physical Review Letters* **123**, 076801 (2019).

[35] Cocker, T. L. *et al.* An ultrafast terahertz scanning tunnelling microscope. *Nature Photonics* **7**, 620–625 (2013).

[36] Jelic, V. *et al.* Ultrafast terahertz control of extreme tunnel currents through single atoms on a silicon surface. *Nature Physics* **13**, 591–598 (2017).

[37] Cocker, T. L., Jelic, V., Hillenbrand, R. & Hegmann, F. A. Nanoscale terahertz scanning probe microscopy. *Nature Photonics* **15**, 558–569 (2021).

[38] Sheng, S. *et al.* Terahertz spectroscopy of collective charge density wave dynamics at the atomic scale. *Nature Physics* **20**, 1603–1608 (2024).

[39] López, L. E. P. *et al.* Atomic-scale ultrafast dynamics of local charge order in a THz-induced metastable state of 1T-TaS_2 (2025). Available at `http://arxiv.org/abs/2505.20541`. Issue: arXiv:2505.20541 arXiv:2505.20541 [cond-mat].

[40] Bobzien, L. *et al.* Ultrafast state-selective tunneling in two-dimensional semiconductors with a phase- and amplitude-controlled THz-scanning tunneling microscope. *APL Materials* **12**, 051110 (2024).

[41] Roelcke, C. *et al.* Ultrafast atomic-scale scanning tunnelling spectroscopy of a single vacancy in a monolayer crystal. *Nature Photonics* **18**, 595–602 (2024).

[42] Allerbeck, J. *et al.* Ultrafast Coulomb blockade in an atomic-scale quantum dot. *Nature Communications* **16**, 10806 (2025).

[43] Rai, V. N. *et al.* Influence of atomic-scale defects on coherent phonon excitations by THz near

fields in an STM. *Science Advances* **11**, eadz6549 (2025).

[44] Ribbeck, H.-G. v. *et al.* Spectroscopic THz near-field microscope. *Optics Express* **16**, 3430–3438 (2008).

[45] Koch, M., Mittleman, D. M., Ornik, J. & Castro-Camus, E. Terahertz time-domain spectroscopy. *Nature Reviews Methods Primers* **3**, 48 (2023).

[46] Hu, Z. *et al.* Two-dimensional transition metal dichalcogenides: interface and defect engineering. *Chemical Society Reviews* **47**, 3100–3128 (2018).

CHAPTER 2

TERAHERTZ SCANNING TUNNELING MICROSCOPY

Building on the motivation laid out in the introduction, this chapter presents THz-STM as an experimental technique that combines atomic-scale spatial with ultrafast time resolution, making it well suited for studying open scientific questions and technological challenges in 2D materials.

This chapter begins by placing THz-STM in context, linking it with preceding developments in both scanning tunneling microscopy and ultrafast terahertz science. It then introduces the relevant theoretical background, including the working principles of STM and light-matter interaction in a tip-sample junction. Next, the history and current state of the art of THz-STM are reviewed, from the first realization of a THz-STM setup under ambient conditions in 2013 to the most recent experiments performed under ultra-high vacuum (UHV) and at cryogenic temperatures to study a broad range of material systems. The final subsection is particularly relevant for the remainder of this thesis, as it describes the experimental setup at Michigan State University as well as the different types of measurement procedures.

2.1 Combining ultrafast time scales with atomic length scales

THz-STM can be viewed as the convergence of developments from two previously separate fields: (1) the addition of spatial resolution to ultrafast spectroscopy techniques, ultimately reaching the atomic-scale (sub-nanometer) regime to study ultrafast phenomena of individual surface features, and (2) the addition of time resolution to scanning probe techniques, ultimately reaching the ultrafast (picoseconds or shorter) regime to study surface phenomena on their intrinsic time scales (Fig. 2.1).

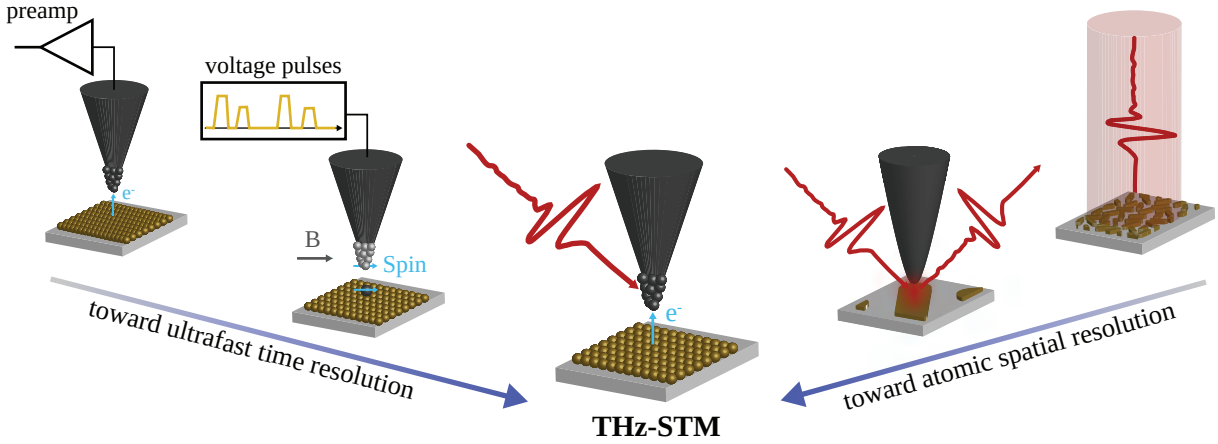

Figure 2.1 Combined ultrafast and atomic-scale resolution. Evolution of STM and ultrafast terahertz techniques toward THz-STM, combining atomic spatial and ultrafast temporal resolution.

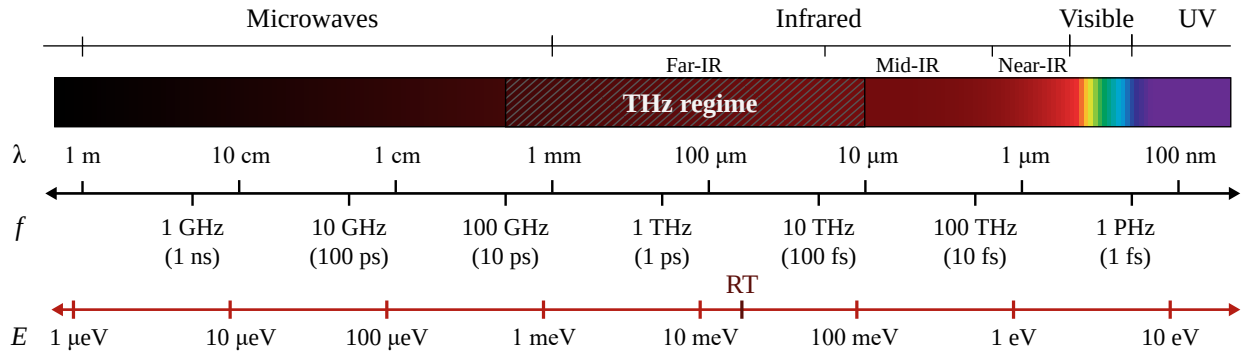

Figure 2.2 The electromagnetic spectrum. The electromagnetic spectrum, showing the position of the terahertz regime in terms of wavelength λ, frequency f and energy E, (RT = Room temperature, IR = infrared, UV = ultraviolet).

2.1.1 Extending ultrafast pulses to atomic length scales

The characteristic frequency range of the electromagnetic wave in an experiment determines the type of phenomena that it can access. Figure 2.2 illustrates the electromagnetic spectrum, where the terahertz regime (~0.1–30 THz) lies at the intersection between microwaves, traditionally treated as electronic signals, and the infrared to visible regime, commonly referred to as optical light [1]. At frequencies in the microwave range, excitations such as electron spin resonance and molecular rotations can be addressed. The terahertz regime provides direct access to low-energy lattice and electronic excitations, including phonon dynamics and electron-hole pair excitations, interlayer shear and breathing modes and carrier scattering dynamics. At higher energies above ~1 eV (near-IR/visible), the response is dominated by electronic-structure-related processes such as carrier recombination dynamics and interband electronic excitation [2–4].

In this context, units of time, frequency, wavelength and energy are directly connected through the relations $f = 1/T$ (frequency = 1 / oscillation period), $\lambda = c/f$ (wavelength = speed of light / frequency) and $E = hf$ (energy = Planck's constant × frequency). "Ultrafast" science typically entails experiments that aim to measure non-equilibrium dynamics on time scales of picoseconds or less [5, 6].

Here, the focus is specifically on the use of ultrafast terahertz pulses and on the development of their spatial resolution toward the goal of studying low-energy excitations in 2D materials on the atomic scale. Importantly, resolving ultrafast dynamics in a pump–probe experiment requires a field transient that is sufficiently short. The pulse duration therefore sets the temporal resolution. In contrast, the pulse center frequency (and bandwidth) determines the spectral content and thus the energy scale of the excitations that can be accessed. Since mode-locked ultrafast pulsed lasers became readily available [7], single-cycle, sub-picosecond broadband terahertz pulses can be reliably generated using, for example, optical rectification in nonlinear crystals or photoconductive antennas (see Chapter 2.5 for details) [1].

As mentioned previously, free-space focusing of light pulses is generally limited to focal spot diameters of about half their wavelength, due to the diffraction limit. For terahertz radiation, this means that the spot size, or illuminated area on a sample, is at a minimum 0.01–3 mm [5] (Fig. 2.1, far right). Such a far-field experiment will still infer electronic transport properties from length scales below this limit, such as local depolarization fields or carrier confinement [8]. However, the response is averaged over the entire focal spot [9]. In 2D materials, key properties often hinge on (sub)nanoscale inhomogeneities such as grain boundaries, structural domains, local strain, layer-number variations, and point defects, all of which can strongly modify carrier scattering and ultrafast transport. This spatial heterogeneity can manifest only indirectly in macroscopic measurements, for example through spectral broadening, and the underlying mechanisms often remain obscured [9].

This limitation has driven the development of terahertz near-field experiments, which bypass the diffraction limit by locally confining the electromagnetic field and enabling nanoscale mapping of material properties. These techniques, referred to as scanning near-field optical microscopy (SNOM), exploit the fact that evanescent fields can locally interact with a sample when they are localized around sub-wavelength structures [5, 10]. Scattering-type SNOM (s-SNOM) is a tip-based SNOM approach that employs a scanning probe geometry similar to STM, as depicted in Fig. 2.1 (center right). In terahertz s-SNOM, pulses are focused onto a sharp metallic tip, where they are confined to a nanofocus defined by the tip apex radius of curvature due to the lightning rod and antenna effects [11–13]. The scattered electric field, which is encoded with the near-field response of the local region on the sample, is detected with a far-field method such as electro-optic sampling (EOS) [14]. Recent studies on TMDs have demonstrated that s-SNOM can map heterogeneous material properties with nanometer-scale spatial resolution [15]. While the spatial resolution of terahertz s-SNOM can be improved through optimized tip designs [16, 17], the signal-to-noise ratio typically decreases for sharper tip apex radii, which currently limits the spatial resolution to the tens-of-nanometers range [15, 18].

True atomic resolution requires a tunneling interaction, whose exponential dependence on tip–sample separation enables sensitivity to individual atoms (see Chapter 2.2). Ultrafast temporal and atomic spatial resolution finally come together in the tunneling-based technique of THz-STM. Before introducing THz-STM in detail, the following subsection returns to the STM perspective and traces the evolution toward ultrafast STM by summarizing its key developments. It is noted here that, recently, a technique named near-field optical tunneling emission has pushed toward atomic spatial resolution in a terahertz s-SNOM system by using sub-nanometer tip-tapping amplitudes at very close tip heights combined with free-space EOS detection [19]. The high spatial resolution is attributed to lightwave-driven emission from the tunneling current between tip and sample.

2.1.2 Extending STM to ultrafast time scales

From the perspective of scanning probe techniques, the complementary challenge has been to push the temporal resolution to the ultrafast scale. The key starting point of atomic-scale scanning probe techniques was the invention of the scanning tunneling microscope in 1981 [20, 21]. This technique was so groundbreaking that only five years later Gerd Binnig and Heinrich Rohrer were awarded the Nobel Prize in Physics *"for their design of the scanning tunneling microscope"* [22].

Traditionally, STM is a quasi-static technique in which signals are measured by averaging over long time scales to acquire data with high spatial resolution and high tunnel current sensitivity. The tunneling process in the tip-sample junction occurs quasi-instantaneously on the time scale of electronics. However, the temporal resolution of the measurement is limited by the experimental readout. The time resolution in conventional STM is governed by the measurement electronics, specifically the transimpedance amplifier (often referred to as "preamp"). The tunnel current, typically on the order of pico- to nanoamperes, is converted into a measurable voltage by this part of the circuit, which acts as a current-to-voltage converter. The preamp output voltage is proportional to the tunnel current, with the proportionality constant set by the transimpedance gain (a large resistor in the circuit). However, a large gain (high sensitivity) comes at the expense of bandwidth (response speed). The resistor in combination with the circuit capacitance (e.g., cable capacitance, tip/sample capacitance and stray capacitance in the resistor), acts as a low-pass filter that limits the current readout bandwidth [23]. For typical STM operation preamps with a bandwidth of ~1–10 kHz are used. Therefore, the accessible time resolution is limited to the microsecond regime, which is orders of magnitude slower than phenomena related to charge carrier or vibrational dynamics, which typically occur on pico- to femtosecond time scales [24].

All-electronic pump–probe STM extends conventional STM by applying fast voltage pulses as a time-dependent bias to the junction. Combined with external magnetic fields and spin-polarized tips, this approach enables nanosecond time resolution and the measurement of single-atom spin relaxation times [25–27]. While this represents a major advance over quasi-static STM and has evolved into its own subfield within the STM community, the temporal resolution of all-electronic STM is fundamentally limited by the electronic pulse generation and the bandwidth of the tip-sample junction. To approach the time scales of ultrafast phenomena, excitation frequencies must be increased from the gigahertz regime (nanosecond time scales), where signals can still be delivered to the junction using radio-frequency electronics and impedance-controlled wiring, into the terahertz regime (picosecond to sub-picosecond time scales), which marks a crossover into the optical domain.

Since the invention of STM, numerous approaches have been developed to integrate short optical pulses in order to access ultrafast time resolution. Early attempts to combine ultrafast lasers with STM demonstrated that optical excitation arising from surface photovoltages could be detected

through changes in the tunneling current [28]. This motivated a range of concepts combining STM with optical pulses in the following years, including photoconductively gated STM [29, 30], tunnel-distance modulation STM [31], and junction-mixing STM [32, 33].

In photoconductively gated STM, one optical pulse is used to activate a photoswitch and thereby close the tunneling circuit in the STM electronics while a second pulse excites the sample [29]. However, the measured signal was later shown to be largely capacitive in origin [34], which fundamentally limits the spatial resolution and complicates its interpretation as true ultrafast tunneling. In tunnel-distance modulation STM, an optical pulse induces heating to temporarily change the gap width (distance between tip and sample) of the junction [31]. However, even when using high frequency piezoelectric crystals, the mechanical motion and therefore the gap width modulation are limited to the tens-of-nanoseconds regime. In junction-mixing STM, two optical pulses generate picosecond electrical transients on a transmission-line sample, which are detected at the tunnel junction via the intrinsic nonlinearity of the STM current-voltage characteristic [32, 33]. Because it requires specialized transmission-line geometries, this method is not broadly applicable to arbitrary samples.

Naively, one could expect that coupling ultrafast optical pulses directly to the STM tip in order to excite the tunnel junction would provide the most direct and versatile solution toward ultrafast STM. However, intense infrared and visible laser pulses typically introduce strong thermal loads at the junction, in particular through tip heating and expansion. These effects can substantially alter measured tunneling signals, especially when the pulses are modulated for lock-in detection, making it impossible to distinguish ultrafast dynamics from thermal artifacts [35]. To mitigate this, specialized techniques such as shaken-pulse-pair STM [36] and two-color shaken-pulse schemes [37] were developed. More recently, increasingly complex experimental implementations have revived this direction with the goal of pushing STM toward attosecond-scale temporal resolution [38–40]. At present, however, these methods have yet to be applied to complex material systems. Taken together, these efforts established the foundation of time-resolved STM, while also revealing the fundamental difficulty of implementing light-coupled STM in a robust and widely applicable way. This obstacle was later overcome with THz-STM, as discussed in detail in the following subsections.

2.2 Theoretical description of scanning tunneling microscopy and spectroscopy

This section provides an overview of the fundamental theoretical principles underlying STM. It is based on the textbooks by Chen [23], Wiesendanger [41], and Voigtländer [42].

To describe the physical mechanism that makes atomically resolved scanning tunneling microscopy (STM) and energetically resolved scanning tunneling spectroscopy (STS) possible, the STM tunnel junction (Fig. 2.3(a)) can be modeled by using the following parameters:

- d: The vacuum distance between the last atom of the tip apex and the first atom of the sample

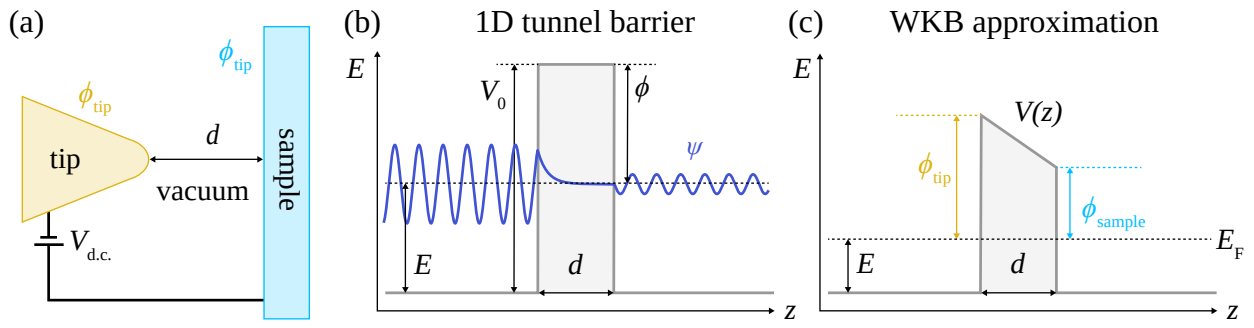

Figure 2.3 Overview of different STM tunnel barrier approximations. (a) Schematic of the STM tunnel junction. (b) 1D tunnel barrier with a square potential (bottom) and wavefunction decaying inside the barrier (top). (c) WKB approximation of a trapezoidal barrier.

surface, also referred to as the tip height.

- ϕ_{tip} and ϕ_{sample}: The work functions of the tip and sample material, respectively. The work function is the minimum energy required to remove an electron from a solid into vacuum.
- $V_{\text{d.c.}}$: The bias voltage applied between the tip and the sample through the external STM circuit, referenced such that the sample side is positive.

In the following, increasingly complex models are introduced to provide a realistic description of the tip-sample-junction using these parameters.

2.2.1 The one-dimensional tunnel barrier – atomic resolution from exponential distance dependence

In quantum mechanics, unlike classical mechanics, particles can penetrate into a potential barrier. A standard one-dimensional (1D) problem is that of an electron with energy E tunneling through a square potential barrier $V(z)$ of height V_0 and width d (Fig. 2.3(b)). This resembles a very simplified picture of the tip-vacuum (barrier)-sample tunnel junction in STM, but is sufficient to explain why the technique can achieve atomic resolution.

The problem is addressed by solving the time-independent Schrödinger equation (because the potential is static) with a plane wave *Ansatz* for the wave function of the electron (see, for example Ref. [42] for a step-by-step solution). This yields solutions for the regions to the left and right of the barrier in the form of an oscillating wave for a free electron (Fig. 2.3(b), top). The solution relevant for STM is the one inside the barrier. For $E - V_0 < 0$, i.e., if the electron energy is smaller than the potential barrier, the solution is given by:

$$\psi = \exp\left(-\sqrt{\frac{2m}{\hbar^2}(V_0 - E)} \cdot z\right) \tag{2.1}$$

This solution implies that a particle can enter and even pass through a classically forbidden barrier, which is called "tunneling". By considering the left and right traveling solutions, as well

as boundary conditions the probability of finding an electron at the end of the potential barrier (transmission factor T) can be calculated, which ultimately corresponds to the particle flux, i.e. electric current, through the potential barrier. The transmission factor T and the barrier width d have an exponential relationship, described by

$$T \propto \exp\left(-2d\sqrt{\frac{2m}{\hbar^2}(V_0 - E)}\right) \tag{2.2}$$

(E and V_0 additionally enter through a prefactor, which is omitted from the discussion here.)

For STM this implies that the tunneling current (1) decreases exponentially with the barrier width and (2) decreases exponentially with the square root of the difference between the barrier height and the electron energy. Even though the model presented here is very simplified, result (1) clearly shows the origin of the extreme sensitivity of STM to variations in barrier width, such as atomic features on a surface. A change of the barrier width of only 1 Å leads to a change in the current by approximately one order of magnitude. The first current-distance curves were reported by Binnig *et al.* in 1982 [20]. Result (2) implies that the effective barrier height plays an important role. In a metal, the difference between the vacuum energy and the energy of the highest occupied state (Fermi energy) is called the work function, ϕ. For most metals, ϕ is on the order of ~4–5 eV. Often, the tip and sample in STM are made of different materials, which is taken into account in the next, more refined, approximation model.

2.2.2 WKB approximation – including the work functions ϕ_{tip} and ϕ_{sample}

To accurately represent different work functions for the tip and the sample, the barrier height needs to be adjusted on each side individually, which results in a trapezoidal barrier shape (Fig. 2.3(c)). To solve this type of spatially varying potential barrier, an approximation must be applied, because the Schrödinger equation cannot be solved analytically. A common approach is the classical Wentzel-Kramers-Brillouin (WKB) approximation, which leads to the transmission factor

$$T \propto \exp\left(-\frac{2\sqrt{2m}}{\hbar}\int_0^d \sqrt{\phi_{\text{tip}} - z/d(\phi_{\text{tip}} - \phi_{\text{sample}})}\,\mathrm{d}z\right) \tag{2.3}$$

with an integral, which can be solved analytically.

2.2.3 From barrier models to STM current: Bardeen tunneling formalism and approximations

Another consequence of looking at materials in a quantum mechanical way is that their electronic structure is described by a discrete number of states N in a specific energy range, referred to as the density of states (DOS), $\rho(E)$. For a system with n discrete states it can be written as

$$\rho(E) = \sum_n \rho(E - E_n) \quad . \tag{2.4}$$

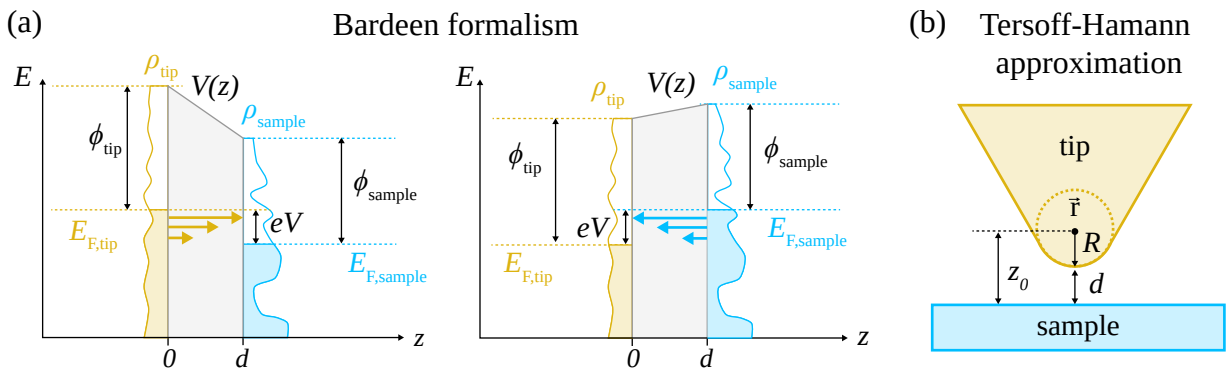

Figure 2.4 Bardeen formalism and Tersoff Hamann approximation. (a), (b) Schematic of the tunnel junction in the Bardeen formalism with electrons tunneling from tip to sample (a) and sample to tip (b). (c) Schematic of the tip and sample in the Tersoff Hamann approximation.

This can be extended to the spatial distribution of the DOS, namely the local density of states (LDOS) by weighting it with $|\psi_n(\vec{r})|^2$, the probability of an electron being at position $\vec{r}$

$$\text{LDOS} = \rho(E, \vec{r}) = \sum_n |\psi_n(\vec{r})|^2 \rho(E - E_n) \quad . \tag{2.5}$$

To correctly model the tunneling process in an STM junction, the tip DOS and the sample LDOS have to be taken into account. Bardeen developed a model (originally for tunneling through an oxide barrier between two electrodes, since this work predates STM), in which two systems are considered separately in the first step: the tip-barrier system, and the sample-barrier system [43]. For each system the electronic states are calculated using the time-independent Schrödinger equation. The derivations for the 1D and three-dimensional (3D) case are described in Ref. [23]. The solutions in both cases are wave functions with different energy eigenvalues that decay into the barrier. These results can then be used within time-dependent perturbation theory to calculate the transition (or scattering) rate of electrons from the initial tip states to the final sample states. The transition rate w from any initial state i to any final state f is calculated as

$$w_{\text{tip}\to\text{sample}} = \sum_{\text{i,f}} \frac{2\pi}{\hbar} |M_{\text{fi}}|^2 \delta(E_{\text{sample,f}} - E_{\text{tip,i}}) \tag{2.6}$$

using a variant of Fermi's golden rule, where $M_{\text{f,i}}$ is the transition matrix element calculated from the tip and sample wave function overlap. The Dirac delta function enforces energy conservation, requiring the energy of the final state to match that of the initial state. The resulting current is given by $I = 2e \cdot w_{\text{tip}\to\text{sample}}$, where e is the electron charge and the factor of two accounts for spin degeneracy.

To apply the Bardeen formalism to the STM junction, two approximations are commonly made: (1) the energy-dependent approximation, which emphasizes the energy dependence of the DOS

of the tip and sample, and (2) the Tersoff-Hamann approximation [44, 45], which focuses on the spatial dependence of the surface wave functions.

In the energy-dependent approximation, the tip and sample wave functions are replaced by treating the tunneling barrier as a 1D model with rectangular shape. This allows for introducing the DOS of tip and sample into the equation for the transition rate by replacing the double sum over initial and final states with an energy integral over the DOS and the tunneling current can be written as

$$I = 2ew_{\text{tip}\to\text{sample}} = \frac{4\pi e}{\hbar}\int_{E_{\text{F,sample}}}^{E_{\text{F,tip}}} \rho_{\text{tip}}(\epsilon)\rho_{\text{sample}}(\epsilon)|M(\epsilon)|^2 \mathrm{d}\epsilon \quad . \tag{2.7}$$

In the 1D case, the matrix element $|M(\epsilon)|^2$ corresponds to the transmission factor in Equation 2.2. At this point, the externally applied bias voltage $V_{\text{d.c.}}$ can be introduced into the system, which sets the relative energy between the Fermi energies of the tip $E_{\text{F,tip}}$ and sample E_{sample}. Defining $E_{\text{F,sample}} = 0$ and $E_{\text{F,tip}} = eV$ simplifies Equation 2.7 to

$$I = \frac{4\pi e}{\hbar}\int_{0}^{eV} \rho_{\text{tip}}(\epsilon - eV)\rho_{\text{sample}}(\epsilon)T(\epsilon, V, d)\mathrm{d}\epsilon \quad . \tag{2.8}$$

This expression shows that the tunneling current is proportional to the density of occupied states in the tip and the density of unoccupied states in the sample, integrated over the energy range in which occupied tip states overlap with empty sample states for $V > 0$. Figure 2.4(a) illustrates both tunneling directions for a positive and negative bias voltage. The transmission factor $T(\epsilon, V, d)$ determines the tunneling strength and decreases exponentially for lower energies. For small tunneling voltages $eV << \phi$, T can be approximated as energy independent. In this case, the tunneling current is proportional to the combined density of states of tip and sample. For the commonly assumed constant tip DOS, one obtains

$$I \propto \int_{0}^{eV} \rho_{\text{sample}}(\epsilon)\mathrm{d}\epsilon \tag{2.9}$$

which forms the basis of STS, where the tunneling current is recorded as a function of voltage to probe the sample LDOS.

To explain the high spatial resolution of STM, Tersoff and Hamann proposed a different approximation to the Bardeen formalism [44, 45]. In contrast to the energy-dependent approximation, the wave functions in the matrix element are retained but the energy dependence is neglected and the matrix element is evaluated in the limit of small voltages close to the Fermi level. To do so, the sample wave function $\psi_{n,\text{sample}}(\vec{r})$ is approximated by a plane wave Fourier expansion, with the surface structure given by the Fourier components. Further, the STM tip is approximated as a point source at position $\vec{r}_{\text{tip}}$ (Fig. 2.4(b)). For small voltages, the tunneling current reduces to

$$I \propto \sum_{n} |\psi_{n,\text{sample}}(\vec{r}_{\text{tip}})|^2 \delta(E_{\text{F}} - E_{n,\text{sample}}) \tag{2.10}$$

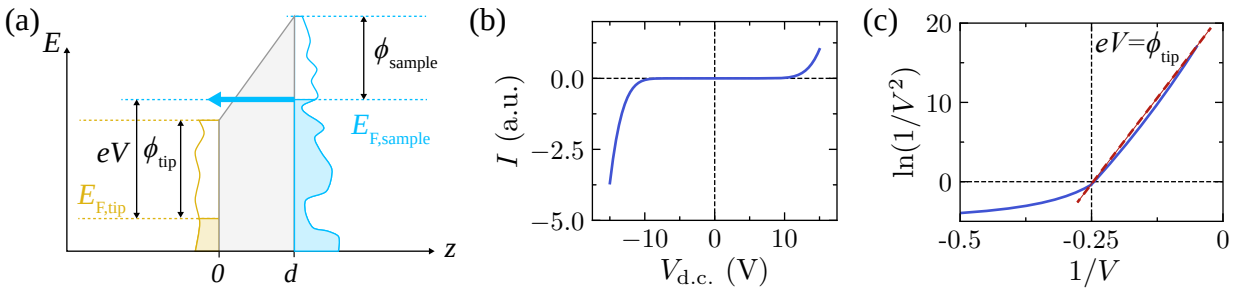

Figure 2.5 Tunneling versus field emission regime. (a) Schematic of tunneling through the vacuum barrier in the field emission regime. (b) Simmons current-voltage characteristic. (c) Fowler-Nordheim linearization of (b) with the field emission regime indicated by the linear fit (red line).

which is equivalent to the expression for the sample LDOS (see Equation 2.5) evaluated at the tip position. This result implies that the tip probes the surface wave functions directly at its position. Tersoff and Hamann further demonstrated that this approximation remains valid regardless of the tip size, provided it can be approximated with a spherical wave function with $\vec{r}_{\text{tip}}$ denoting the center of the tip curvature. The STM therefore measures the LDOS of the surface at the Fermi level at the distance z_0 between the center of tip curvature and the surface.

2.2.4 Tunneling versus field emission regime

So far, the focus was on the regime where $eV < \phi$. The Simmons model explicitly distinguishes three bias regimes [46].

- In the low-bias regime ($eV \simeq 0$) the tunneling current is approximately ohmic with a linear relationship between I and V.
- In the intermediate regime ($eV < \phi$) the relationship becomes non-linear because, due to the bias voltage, the barrier becomes increasingly trapezoidal and the transmission becomes energy-dependent.
- In the high-voltage regime ($eV > \phi$), the barrier becomes triangular and the current exhibits Fowler-Nordheim-type field emission behavior (Fig 2.5(a)).

To distinguish the regimes experimentally, one can apply the Fowler-Nordheim linearization $\ln(1/V^2) \propto -1/V$ [47]. This is demonstrated by plotting the positive bias side of the current-voltage characteristic (generated using the Simmons model with $\phi_{\text{tip}} = 4\,\text{eV}$, $\phi_{\text{sample}} = 5\,\text{eV}$) in Fig. 2.5(b) on the linearization scale in Fig. 2.5(c). The linear slope, and therefore the field emission regime, begins at approximately $0.25\,\text{V}^{-1}$, which corresponds to a tip work function of 4 eV (matching the model parameter), thereby confirming the crossover between the tunneling and field emission regimes near the point where the applied voltage equals the work function.

In the field emission regime, compared to the tunneling regime, the distance sensitivity is decreased due to the less localized emission process associated with the high electric field in the junction. This results in reduced spatial resolution when operating in this regime.

2.3 Light-matter interaction in a tip-sample-junction

This section addresses the light-matter interaction of radiation with the STM junction, which forms the basis for ultrafast lightwave-driven STM. The discussion draws mainly on the review papers by Müller [48], Lloyd-Hughes *et al.* [5] and Cocker *et al.* [9]. Building on the previous discussion of tunneling, light-induced tunneling mechanisms are introduced, as well as the generation of lightwave-driven tunneling currents. Furthermore, the coupling mechanism of radiation to a sharp STM tip is briefly laid out. The main questions addressed in this section are why and how pulses in the terahertz spectral range, as opposed to pulses with other frequencies, are particularly well suited to perform lightwave-driven ultrafast STM, i.e. for generating an ultrashort tunneling current that can serve as a probe pulse, a pump pulse, or both.

2.3.1 Field-driven versus photon-driven tunneling

Tunneling between an STM tip and sample is, in principle, only limited by the speed of the tunneling process of an electron through a barrier, as introduced in the previous section. This process occurs on the time scale of atto- to femtoseconds [49–51]. Section 2.1.2 already introduced the idea of using short laser pulses in an STM to overcome the "slow" electronics. Here, a closer look is taken at light-induced tunneling mechanisms arising from direct illumination of the STM junction. The interaction of an electromagnetic field pulse (with a specific frequency and intensity) with a tunnel junction can be understood in two limiting physical pictures: photon-driven versus field-driven tunneling.

In the photon-driven case (Fig. 2.6(a)), electrons absorb one or multiple photons from the light field, which increases their effective energy relative to the static tunnel barrier and thereby opens

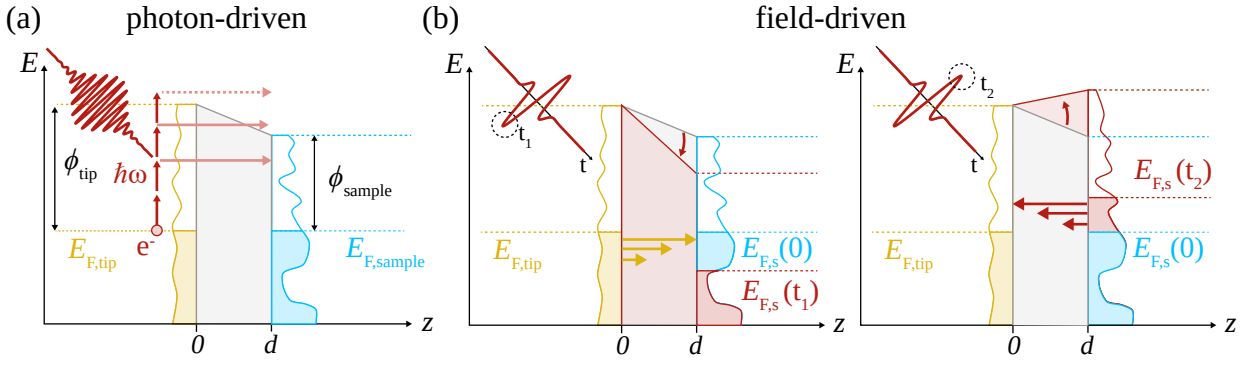

Figure 2.6 Photon-driven versus field-driven regime. (a) Schematic of the multi-photon tunneling and field emission regime. (b) Field-driven (lightwave-driven tunneling) regime with electrons tunneling to the sample (left) and to the tip (right) during different parts of the pulse.

additional inelastic (non-adiabatic) tunneling or field-emission pathways that are not accessible to unexcited electrons. By contrast, in the field-driven regime, the light pulse acts as an ultrafast, time-dependent voltage across the tip-vacuum-sample junction (Fig. 2.6(b)). The tunneling process remains elastic (adiabatic) and can be described within Bardeen's formalism and related static STM theories (see Chapter 2.2). The effective bias becomes $V(t)$ and directly follows the instantaneous electric field. At different times during the pulse, the relative Fermi level between tip and sample can allow tunneling in either direction depending on the polarity and intensity of the field. As a result, the tunneling barrier and the energy window are modulated on the time scale of the electric field, producing ultrafast tunneling currents, thereby enabling ultrafast STM operation [9].

Depending on the frequency and intensity of the light, the light-matter interaction is either dominated by the electric field of the pulse or by the photon nature of the radiation. There are several theoretical models to distinguish between the two regimes. First, the Keldysh criterion for adiabatic tunneling is considered [52]. This theory was originally developed to explain tunnel ionization (photoemission) from an atom or solid with work function ϕ into vacuum in the presence of strong electromagnetic fields.

Keldysh introduced the adiabaticity parameter

$$\gamma = \sqrt{\frac{\phi}{2U_p}} \tag{2.11}$$

to distinguish between photoemission in the field-driven (adiabatic) or photon-driven (non-adiabatic) regime [48, 52–54]. Here, U_p is the ponderomotive energy, i.e., the time-averaged kinetic energy of a free electron in an electromagnetic field. It can be easily derived as follows. If an electron with charge e interacts with an electric field $E(t) = E\cos(\omega t)$, where E is the field strength and $\omega = 2\pi f$ is the angular frequency, it experiences a force $F(t) = -e \cdot E(t)$. From this force, the acceleration of the electron follows as $a(t) = F(t)/m$, leading to an oscillatory trajectory

$$x(t) = \frac{a(t)}{\omega^2} = \frac{eE}{m_e\omega^2}\cos(\omega t) \tag{2.12}$$

The time-averaged kinetic ponderomotive energy is then defined by

$$U_p = \frac{1}{2}m_e\omega^2\langle x^2\rangle = \frac{e^2E^2}{4m_e\omega^2} \tag{2.13}$$

showing that the frequency and field strength of the laser light determine the Keldysh parameter as $\gamma \propto \omega/E$.

For high frequencies and weak fields, $\gamma >> 1$, and multiphoton emission dominates the process. The current across the junction due to n-photon absorption is expected to follow the power-law dependence $I_n \propto (E^2)^n$ [55, 56]. It is important to note that the presence of hot carrier populations

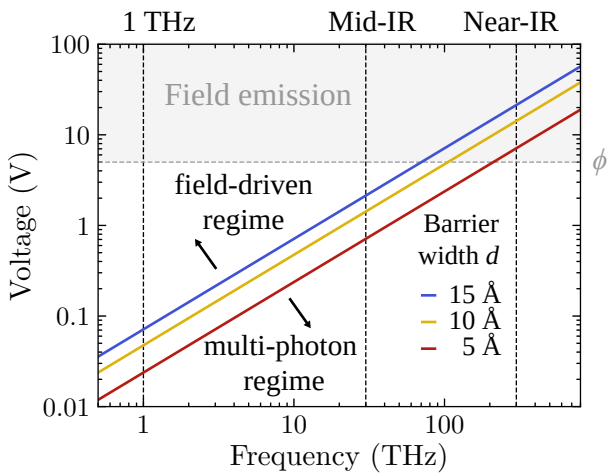

Figure 2.7 Keldysh parameter regimes. Tunneling regimes according to the Keldysh parameter ($\gamma = 1$) for different field strengths, frequencies and tunnel barrier widths (reproduced from [5]).

in the tip or sample is neglected in this description and all electrons are assumed to be in the ground state.

For low frequencies and high fields, $\gamma << 1$, and the ponderomotive energy of the electrons becomes comparable to their binding energy, i.e., the electric field distorts the potential barrier sufficiently for electrons to tunnel adiabatically through it. Since the electric field acts effectively as a bias voltage, the dependence of the tunneling current on the electric field strength, follows the trends described for the tunneling regime (linear for small fields, non-linear for intermediate fields) and field emission regime (Fowler-Nordheim scaling) described in Chapter 2.2. Importantly, unlike in the photon-driven regime, the current is independent of the frequency (photon energy).

For ultrafast STM, operation in the field-driven regime below field emission is desired in order to achieve both atomic spatial resolution and energy resolution, i.e., to remain within the validity of Bardeen's tunneling formalism and its relation to the sample LDOS. Figure 2.7 shows the tunneling regimes for different laser pulse frequencies across realistic STM tip-sample vacuum gaps. The onset of field emission occurs above a typical work function of 5 eV. For high frequency pulses in the near-IR range, the crossover between field-driven and photon-driven (γ=1) occurs above the field emission threshold. At lower frequencies, particularly in the terahertz range, the field-driven tunneling regime spans a broad range of bias voltages across the junction ($V = E \cdot d$). Terahertz pulses coupled to an STM junction are therefore especially well suited for lightwave-driven tunneling experiment.

An alternative distinction between the multi-photon and field-driven regimes, introduced by Keldysh, compares the tunneling time to the period of the laser oscillation. For low frequency light, the tunnel barrier can be considered static during the tunneling process (tunneling time « oscillation period). For higher frequency pulses, however, the barrier evolves during the tunneling process

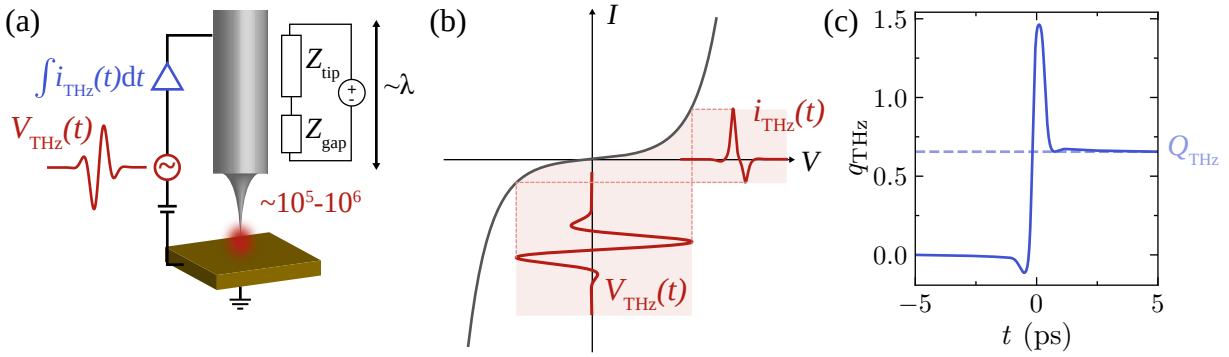

Figure 2.8 Lightwave-driven tunneling in a THz-STM junction. (a) The tip acts as an optical antenna (reproduced from [48]). The terahertz fields are enhanced by $\sim 10^5 - 10^6$ at the tip apex. (b) and (c) illustrate the generation of ultrafast terahertz-induced currents.

(tunneling time » oscillation period) and the adiabatic approximation no longer applies [48, 52]. The tunneling time is also a key concept in the Büttiker-Landauer theory of tunneling through a potential barrier [57]. In this framework, electrons tunnel through a barrier of fixed width but periodically modulated height due to the applied light field. The Büttiker–Landauer tunneling time provides the characteristic time scale that determines whether tunneling follows the instantaneous barrier adiabatically or becomes frequency-dependent. However, this is an ongoing debate and Zheltikov [58] argues that the important time scale for photoionization is the time needed for an electron to acquire a ponderomotive energy equal to the ionization potential instead of its tunneling time though the barrier.

The concepts introduced in this section highlight that terahertz excitation is a particularly promising regime for lightwave-driven tunneling. As a result, it has become the most widely used frequency range, to the extent that "THz-STM" is often used synonymously with "ultrafast STM".

2.3.2 Field-enhancement and generation of lightwave-driven ultrafast tunneling currents

The reason why terahertz pulses, which in free-space have a diffraction limit on the order of over 100 μm, can couple efficiently to an STM junction is that the tip acts as an optical antenna. In the context of near-field optics, an optical antenna converts free-space radiation into localized near-fields of sub-wavelength dimensions [59]. At terahertz to mid-IR frequencies, the tip can be treated as a long-wire antenna that enhances the electric field via the lightning rod effect [60]. The mesoscopic tip shape and possibly, the angle of incidence play an important role for the coupling efficiency.

The light-coupled junction can be considered as an RF circuit (Fig. 2.8(a)). The tip acts as an inductor with impedance $|Z_{tip}| = \omega L_{tip}$ and the vacuum gap acts as a capacitor with impedance $|Z_{gap}| = 1/(\omega C_{gap})$. Together, the junction can be modeled as an LC circuit with resonance frequency $f = 1/(2\pi\sqrt{LC})$. Because of the small size of the gap compared to the tip, which

extends over the millimeter scale, the response is dominated by the tip. Assuming an inductance of a few nanohenries for the tip (long wire inductor) and stray capacitance on the order of tens of femtofarads yields an antenna resonance frequency in the 10-100 GHZ range, below the terahertz frequency band [48]. The tip in a THz-STM therefore acts as a non-resonant, broadband antenna with low-pass filtering behavior and decreasing field enhancement for higher frequencies [11, 61]. The large size mismatch between the terahertz wavelength and tip apex and gap size results in field enhancements on the order of $10^5 - 10^6$ due to the lightning rod effect [62, 63]. As a result, far-field terahertz fields of a few hundred V/cm can generate local fields in the junction on the order of several V/nm. Compared to light coupling in the near-IR or visible frequency range (eV), the small photon energy of terahertz radiation and the high reflectivity of most metals lead to minimal terahertz-induced heating in the STM junction, thereby avoiding thermal-expansion-related artifacts [62].

In addition to frequency-dependent enhancement and filtering, the tip geometry can also affect the phase of the terahertz pulse and even introduce distortions due to reflections when the terahertz pulses travels along the tip. Furthermore, the local optical response of the sample region to which the field is confined also influences the effective field in the junction. For quantitative data analysis and for extracting material-specific terahertz properties of the sample, it is therefore crucial to know the waveform shape inside the STM junction. Chapter 3 introduces a technique designed to overcome this challenge.

As indicated in Fig. 2.8(a) and discussed above, on most samples the terahertz pulses can be treated as a time-dependent voltage source in series with the static bias $V_{\mathrm{d.c.}}$ in the STM circuit. The total voltage between tip and sample at time t is $V_{\mathrm{total}} = V_{\mathrm{d.c.}} + V_{\mathrm{THz}}$, where $V_{\mathrm{d.c.}}$ sets the static operating point of the junction, as illustrated in Fig. 2.4, and V_{THz} adds a time-dependent modulation, as shown in Fig. 2.6.

Figure 2.8(b) illustrates how a single terahertz pulse, in the absence of an additional bias voltage, samples the current-voltage (I-V) characteristic of a junction to generate an ultrafast current pulse. Negative portions of the pulse generate negative current, while positive portions generate positive current. Due to the finite bandwidth of the preamplifier, the measured current corresponds to the time integral of the ultrafast current pulse. The running integral shown in Fig. 2.8(c) demonstrates that a non-linearity in the $I - V$ curve is required to generate a non-zero net current, as the electric field of a light pulses integrates to zero otherwise. Applying a static bias voltage shifts the pulse along the voltage axis of the $I-V$ curve and thereby introduces a static offset to the current response.

The generation of terahertz-induced ultrafast currents on the sub-picosecond time scale at atomic-scale locations on the sample constitutes the basis of ultrafast STM, as it enables time-resolved measurements with temporal resolution set by the duration of the current pulse. These measurements are typically based on the principle of pump-probe spectroscopy, in which one pulse (terahertz or optical) acts as a pump to excite the sample, while a second terahertz pulse, delayed

in time, probes the system response. Repeating the measurement for increasing pump-probe delays maps out the temporal evolution of the sample excitation. The next section provides a historical walkthrough from the first demonstration of ultrafast THz-STM to the investigation of cutting-edge phenomena using highly developed THz-STM systems.

2.4 History and state-of-the-art of terahertz scanning tunneling microscopy

The previous sections in this chapter introduced the theoretical as well as experimental background that motivated the realization of an ultrafast terahertz-coupled STM system. This was first accomplished by Cocker *et al.* [62] in 2013.

Figure 2.9 shows the number of publications employing the THz-STM technique over time since 2013. The development of THz-STM and its experimental advances have been reviewed in multiple review and perspective articles focused on ultrafast nanoscopy techniques [4, 9, 24, 48, 64–70] and have also been included in several broader technology roadmaps [5, 71–73]. In the following, the key technological developments are first introduced chronologically. From 2016 onward, the number of THz-STM systems worldwide increased, and more groups began producing results. These findings are presented below, organized into several subtopics.

2.4.1 Foundational milestones of THz-STM

THz-STM was first demonstrated under ambient conditions in air by Cocker *et al.* in 2013 [62]. The study demonstrated ultrafast charging dynamics of a single InAs nanodot excited by an 800 nm pump pulse with nanometer-scale spatial resolution (limited by operation in air) and projected that THz-STM operated in vacuum would permit measuring sub-picosecond dynamics of single atoms

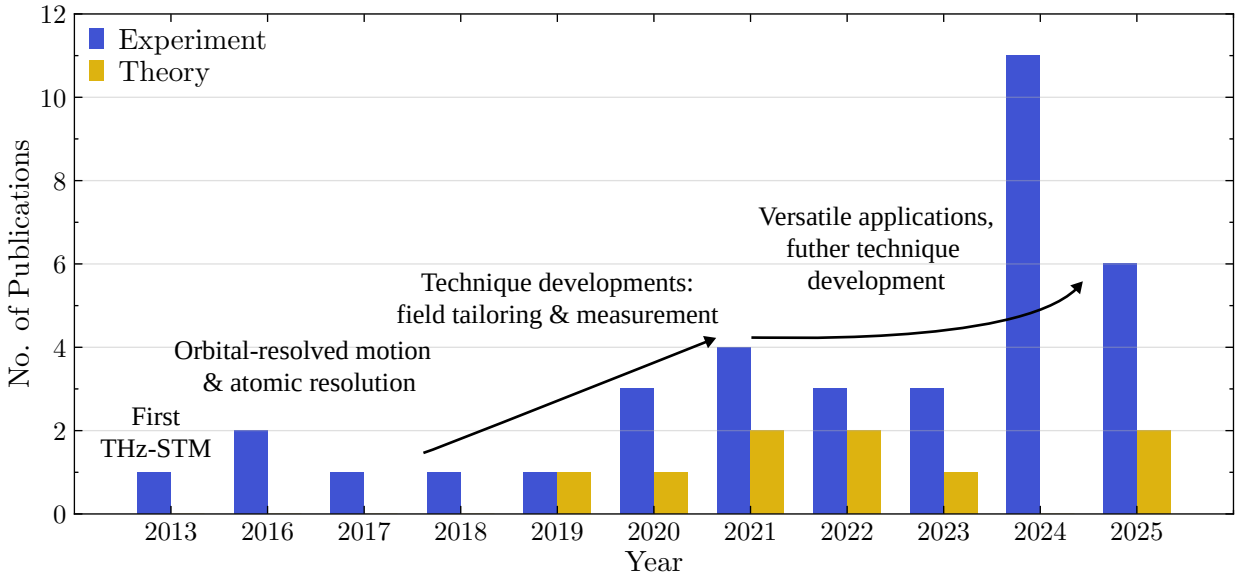

Figure 2.9 THz-STM publications over the years. Evolution of experimental and theoretical THz-STM publications since its first demonstration.

and molecules. The latter was successfully demonstrated a few years later in a cryogenic UHV system on a single pentacene molecule [74]. In this work, the terahertz pulses were tuned such that only the peak of the electric field opened a tunneling channel through a single molecular state (state-selective tunneling). This enabled the authors to record an ultrafast coherent molecular vibration directly in the time domain with spatial resolution of the molecular orbital structure (< 1 Å). In 2017, single atoms in a Si(111) surface were resolved using THz-STM by Jelic *et al.* [75]. This study further demonstrated that tunnel currents generated by terahertz frequency pulses can be orders of magnitude higher than in conventional STM because a conducting surface state with a plasma frequency below the terahertz range is unable to efficiently screen the electric field from the bulk. Taken together, these three studies not only established that THz-STM is capable of probing single molecules and atoms with ultrafast resolution, but also laid the foundation for a new surface-science technique that has gained substantial traction over the following decade.

2.4.2 Tailoring the terahertz waveform

As described earlier in Fig. 2.8, the signal measured in THz-STM is the current integrated over the temporal shape of the terahertz electric field pulse, also referred to as the terahertz waveform. THz-STM measurement typically use single-cycle pulses which integrate to zero, $\int E_{\mathrm{THz}}(t)\mathrm{d}t = 0$. Without interaction with a nonlinearity ($I(V) = \alpha V$), the pulse terahertz-induced voltage $V_{\mathrm{THz}} \propto E_{\mathrm{THz}}$ will result in zero net current, $\int I(V_{\mathrm{THz}}(t))\mathrm{d}t = \alpha \int V_{\mathrm{THz}}(t)\mathrm{d}t = 0$. However, the field amplitude and carrier envelope phase (CEP) can be adjusted to influence the sampling range of the $I-V$ curve and therefore the terahertz-induced current (further described in Chapter 3).

This was first demonstrated with the initial realization of THz-STM and remains an active area of development.The first approaches [62, 74, 75, 75] showed the tunneling current can be recorded as a function of the peak field strength for both field polarities (CEP=0, maximized to positive strength; and CEP = π, maximized to negative field strength). High spatial resolution was added to such measurements by Ammerman *et al.* [76] establishing terahertz scanning tunneling spectroscopy (THz-STS).

Yoshioka *et al.* [77] employed a continuous CEP shifter, which allowed them to model the difference between near- and far-field CEP based on a tip-circuit model, similar to the one introduced in Section 2.3.2. Continuous CEP phase shifting based on frustrated total internal reflection in polymer prisms [78], as well as a Gouy-phase-shift-based technique in which two pulses of opposite polarity are overlapped with a small time delay [79], provide additional cost-effective methods. The latter will be discussed in more detail later, as it was developed during the project introduced in Chapter 3.

Finally, Sheng *et al.* [80] systematically investigated the influence of the micrometer- to millimeter-scale electromagnetic environment of the tunnel junction on the terahertz waveform

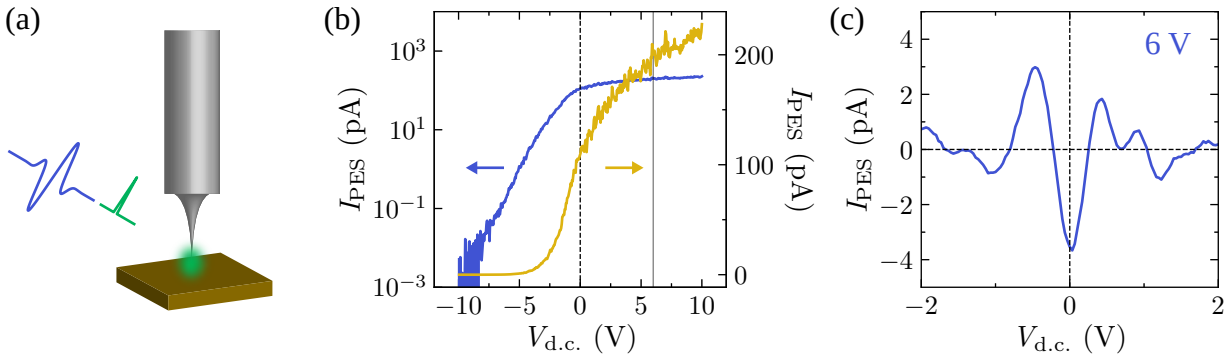

Figure 2.10 *In situ* waveform measurement via photoemission sampling. (a) Schematic of the setup. (b) Current-voltage characteristic of the PES junction. (c) Near-field waveform captured with PES.

shape. They identified spectral distortions and reflections arising from terahertz surface plasmon propagation along the tip wire and from cavity modes at the tip apex. They further showed that the near-field waveform can be flattened by optimizing the tip shape and tip-holder geometry.

2.4.3 Measuring the waveform *in situ*

The terahertz waveform in the far field can easily be measured with conventional methods such as EOS, but ultimately it is the near-field waveform that samples the $I - V$ curve of the junction and produces the THz-STM signal. Therefore, several efforts have focused on developing methods that measure the near-field as close as possible to typical THz-STM tunneling conditions.

The first technique addressing this challenge is photoemission sampling (PES) [61, 81, 82]. In PES, an optical pulse incident on the STM tip excites electrons via single- or multiphoton absorption.The experimental concept is schematically shown in Fig. 2.10(a). The resulting photocurrent, shown here for a 515 nm optical pulse, can be recorded as a function of the applied bias voltage. When plotted on a logarithmic scale, the multiphoton photoemission regime (linear region of the blue curve at negative bias voltages) and the photo-assisted tunneling regime (linear part of the yellow curve at positive bias voltages) can be clearly distinguished (Fig. 2.10(a)). The terahertz pulses modulate the local potential energy landscape and thereby modulate the photoemission current when they overlap in time with the optical pulse. Scanning the relative delay between the optical and the terahertz pulses reveals the temporal profile of the terahertz waveform at the tip apex (Fig. 2.10(c)).

Although this technique can reliably reproduce the terahertz near-field waveform across a range of incident optical pulse energies, it requires tightly focused pulses to generate sufficient photo-assisted tunneling currents. During PES, the tip is typically retracted from the sample surface by several nanometers, thereby leaving the tunneling-condition environment. Another difficulty is that, when operating at megahertz-scale repetition rates, the optical pulses deposit a significant

thermal load onto the tunnel junction. The optical pulses can also modify the atomic-scale structure of the tip apex or photoexcite the sample, which further complicates the waveform readout.

Another method for measuring the terahertz near-field waveform in a THz-STM junction utilizes a single-molecule switch to read out the local field [83]. Although this technique is local and non-destructive, it cannot be used at arbitrary tip positions or sample surfaces.

Chapter 3 introduces a technique that overcomes the challenges of PES and the molecular switch and can be employed on arbitrary samples and at atomic-scale positions to perform atomic-scale terahertz time-domain spectroscopy (THz-TDS) [79, 84]. Owing to its straightforward integration into existing THz-STM systems, this method has been rapidly adopted by multiple research groups [80, 85–87].

2.4.4 Studies of materials

In recent years, particularly in 2024 (see Fig. 2.9), THz-STM has expanded rapidly and has transitioned from a mainly technique-focused field to one increasingly addressing material-specific questions.

Metallic samples provide a testbed for establishing the capabilities of THz-STM, for example through benchmark studies on Cu(111) [88] or by using THz-STM as a "nanosonar" to measure the thickness of Au films on mica via the launch of coherent acoustic phonon waves [89].

The observation of ultrafast dynamics in a pentacene molecule [74] motivated further THz-STM studies of molecular system as well as extended graphene-based structures. Seven-atom-wide armchair graphene nanoribbons revealed detailed electron density distributions that strongly depend on the tip height. This was enabled by the ultra-low tip-sample distances accessible in THz-STM [76]. This study also demonstrated THz-STS with sub-nanometer spatial contrast on the graphene nanoribbons. THz-STM was later extended to zig-zag graphene nanoribbons by Li *et al.* [90]. In a different experiment, C_{60} molecular multilayers were shown to exhibit ultrafast free electrons dynamics following optical excitation [91]. Combined THz-STM and STM luminescence studies on single molecules, in which light emitted from the junction is collected in addition to the tunneling current, demonstrated ultrafast control of exciton formation and revealed the state-selective tunneling process [92].

A major focus for publications in 2024 and 2025 (and of the work presented in this thesis) is the study of 2D materials with THz-STM. Investigations of defects have demonstrated state-selective tunneling into defect states [86], ultrafast tunneling spectroscopy of a breathing mode, where readout is facilitated by an atomic defect [93], ultrafast Coulomb blockade dynamics associated with a single-atom vacancy [87] and the influence of such defects on the local phononic environment [94]. Beyond defect-related phenomena, charge density waves dynamics in TMDS have also been investigated using THz-STM [95, 96].

2.4.5 Additional measurement modes, technical developments and theoretical studies

The studies mentioned above mostly focus on lightwave-driven tunneling, but there are additional measurement modes enabled by THz-STM setups that can be used to study material systems.

One such approach is action spectroscopy. Peller *et al.* [97] demonstrated that single-cycle terahertz pulses can exert sub-cycle Coulomb forces on a single molecule in an STM junction, coherently driving ultrafast switching between metastable molecular configurations. From these switching probabilities, information about the molecular potential-energy landscape can be inferred. Effectively such an approach probes the noise response of a system to an excitation rather than the excitation itself.

In terahertz rectification spectroscopy, a very weak terahertz field is used to modulate the STM bias and the rectified current is interpreted in terms of the second derivative of the $I-V$ characteristic. This technique has been applied to measure quantum beating of a hydrogen H_2 molecule in an STM junction arising from the coherent superposition of two low-energy states [98–100].

Another application of THz-STM is the simultaneous excitation and probing of phase transitions into metastable states using terahertz pulses via differential imaging [101]. This approach is the focus of Chapter 5.

Aside from diverse measurement techniques, technological development of THz-STM systems remains an active area of research. Ongoing advances include on one hand diversification of the optical setups, such as through variable repetition rate lasers [63] and ultrabroadband terahertz pulse generation for THz-STM using spintronic terahertz emitters [61], and on the other hand developments of light-coupled STM systems with advanced cryostat design [102, 103], variable temperature control [104, 105] and magnetic field capabilities [106].

Theoretical work addressing different aspects of THz-STM is also an ongoing. These efforts include general theoretical descriptions of THz-STM [67, 107, 108], as well as studies focused on molecular systems and graphene-based materials [109–113] An algorithm developed to disentangle the terahertz waveform shape from the rectified current signal in THz-STS [114] is described and further developed in Chapter 3.

2.5 Experimental setup

This section introduces the THz-STM setup used for the experiments described in the remainder of this thesis. Figure 2.11 provides an overview of the full experiment, including the optical setup on the left (gray background) and the STM system on the right (yellow background). In the following, both parts are described in detail, first separately and then coupled together, demonstrating how they combine into a THz-STM system.

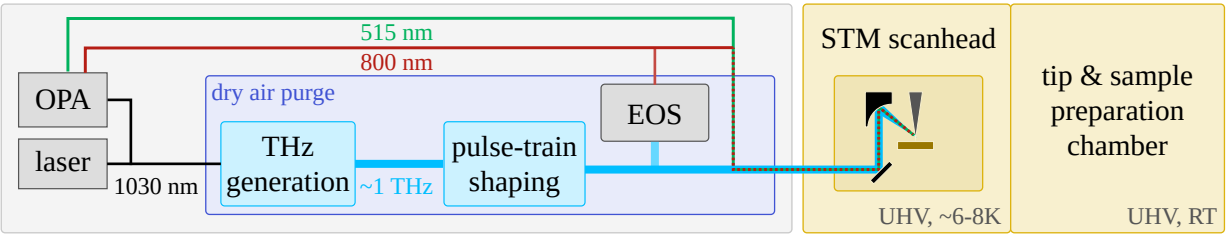

Figure 2.11 Schematic overview of the full THz-STM experimental setup. Left (gray box): optical setup with terahertz beamline (bottom) and pump beamlines (top). OPA = optical parametric amplifier, EOS = electro-optic sampling. Right (yellow): STM UHV chamber divided into an STM chamber with scanhead at liquid helium temperatures and a preparation chamber.

2.5.1 Optical setup

All beamlines in the optical setup in Fig. 2.11 are fed by a single commercial ytterbium-doped potassium gadolinium tungstate (Yb:KGW) ultrafast laser (Light Conversion CARBIDE). It operates with a repetition rate of $f_{\text{rep}} = 1\,\text{MHz}$, a center wavelength of $\lambda = 1030\,nm$ (near-IR) and a pulse duration of $\tau = 230$ fs at full width at half maximum. The average power output of the laser is $P_{\text{avg}} = 40\,\text{W}$. The energy per pulse is $E = P_{\text{avg}}/f_{\text{rep}} = 40\,\mu\text{J}$.

The laser output is split equally into the terahertz beamline and pump beamline. The 20 W of the pump beamline are input into the optical parametric amplifier (OPA), which, in a very simplified description, acts as a frequency converter and can convert the 1030 nm input into a desired output frequency. The pump beamline serves only a supporting role in the measurements presented in this thesis and is therefore not discussed in further detail. The OPA output of 800 nm is used as a gate for EOS and both 515 nm and 800 nm can be used for PES.

For stability and reproducibility, the entire optical setup sits on optical tables with air-controlled legs for vibration damping and the room is both humidity- and temperature-controlled. In addition, the optical components are enclosed by boxes or shielded by curtains as a safety measure, and also to prevent air currents on the table and the accumulation of dust. The discussion now focuses on the terahertz beamline. It is enclosed in an airtight box purged with dry air because terahertz radiation strongly interacts with water molecules in the air, which leads to attenuation as well as oscillations in the terahertz electric field. Figure 2.12 shows the optical setup of the terahertz beamline between the laser and the STM. First, the pulses pass through a delay stage. This can be used to lengthen or shorten the terahertz beam path relative to the pump beam path, which sets the time delay between terahertz and pump pulses when they are recombined in later parts of the setup. The following subsections discuss the individual beam path sections in more detail (highlighted with different background colors in Fig. 2.12).

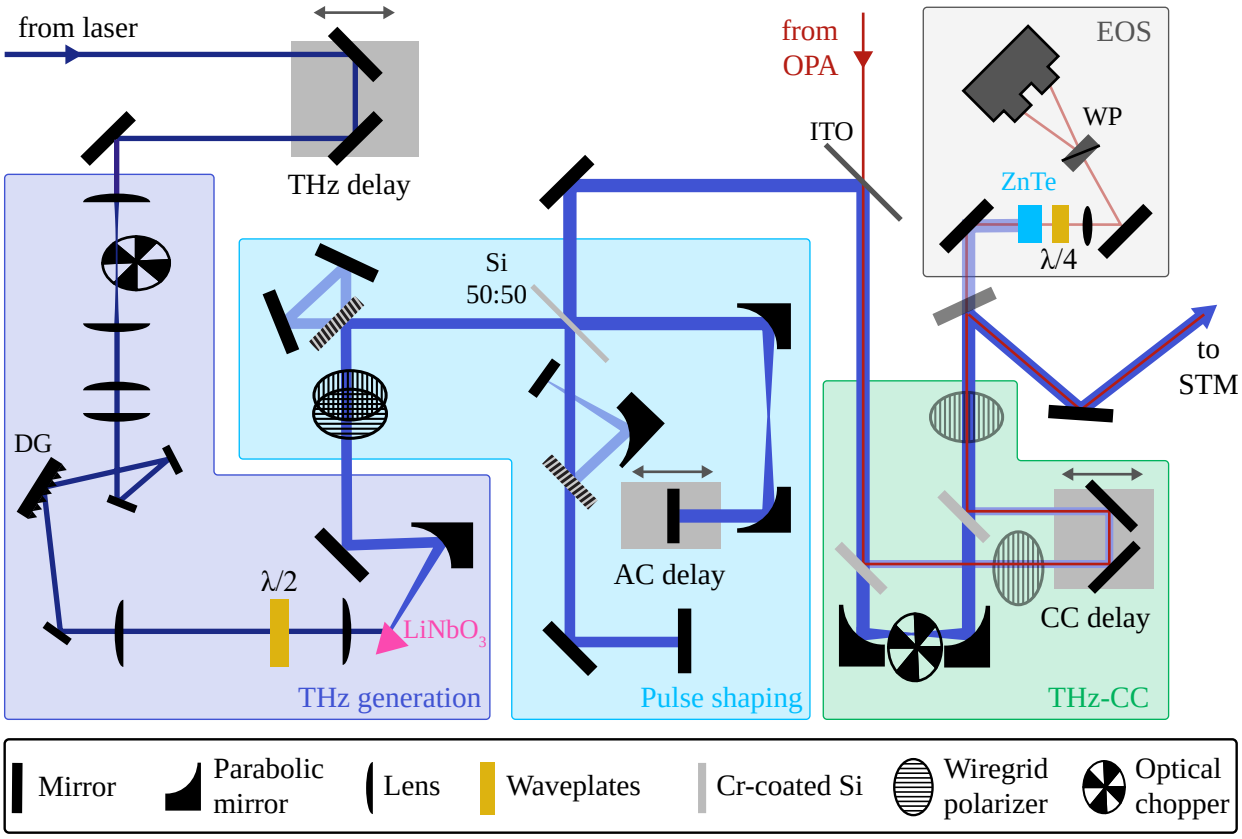

Figure 2.12 THz-STM optical setup. Detailed schematic of the optical setup in the dry air purge box divided into several sections. DG = diffraction grating, ITO = Indium tin oxide, WP = Wollaston prism.

2.5.1.1 Terahertz generation

The purple box on the left of Fig. 2.12 illustrates the terahertz generation setup. Single-cycle phase-stable terahertz pulses are generated from the 1030 nm pulses input pulses via tilted-pulse-front optical rectification in a lithium niobate ($LiNbO_3$) crystal [115].

Optical rectification is a second-order nonlinear optical process in which an intense electromagnetic field induces a nonlinear polarization in a material, resulting in the emission of radiation at much lower frequencies than the driving field. When femtosecond 1030 nm laser pulses are incident on a lithium niobate crystal, the strong optical field drives the electrons far from equilibrium, giving rise to a polarization proportional to the square of the electric field, $P(t) \propto |E(t)|^2$. For ultrashort pulses, the rapidly varying pulse envelope leads to a time-dependent polarization that contains frequency components in the terahertz range, which are radiated from the crystal. Optical rectification can only occur in non-centrosymmetric materials, as the efficiency and direction of the generated terahertz field are governed by the crystal's second-order nonlinear susceptibility and its orientation relative to the incident optical field [1]. Lithium niobate is particularly well suited for this process due to its large second-order nonlinearity, enabling efficient terahertz generation when

appropriately oriented [115, 116].

In dispersive media, like lithium niobate, the group velocity of the near-IR input pulse is significantly faster than the phase velocity of the generated terahertz radiation. This limits the coherent buildup of terahertz field and the radiation is emitted at an angle determined by the velocity mismatch. To counteract this effect, a tilt of the near-IR pulse front can be used to reduce the effective velocity of the optical excitation along the propagation direction, allowing it to match the terahertz phase velocity. This tilted pulse-front geometry enables phase matching between the nonlinear polarization and the terahertz field, leading to efficient and directional terahertz generation [117].

The optical components in Fig. 2.12 between the THz delay stage and the $LiNbO_3$ crystal implement the tilted pulse front using a diffraction grating (DG) and a 4f imaging system [74, 118]. First, the beam is shaped and expanded by a pair of cylindrical lenses, giving rise to a vertical elliptical beam shape, and a pair of spherical lenses. The beam expansion reduces the power density to avoid damage to the 300 lines/mm diffraction grating. The optical chopper between the first pair of lenses further reduces the average power by blocking the beam half of the time and is important for the lock-in detection of the THz-STM tunneling current, as described later. After the grating, the spectral components of the beam diverge and propagate toward the lithium niobate crystal, passing through the 4f setup defined by two spherical lenses. The first lens collimates and focuses the diverging spectral components. The $\lambda/2$ waveplate between the lenses rotates the polarization to vertically align with the lithium niobate electro-optic axis. The second lens collects the spectral components into a common focus onto the crystal. Further details of the terahertz generation in this setup are described in Chapter 3 of the thesis by Ammerman [119].

2.5.1.2 Terahertz pulse shaping

After generation, the terahertz beam is collimated by a parabolic mirror and enters the pulse shaping section (blue box in Fig. 2.12). This part of the setup is designed to allow a high degree of flexibility in shaping individual terahertz pulses and in assembling two pulses into a pulse sequence with variable delay using a Michelson interferometer. In the following, two mechanisms for single-pulse tailoring and two mechanisms for pulse-sequence shaping are described.

The first mechanism is electric-field attenuation via a pair of wiregrid polarizers (WGP) shown in Fig. 2.13(a). The wires in a WGP are conductive and absorb the component of the terahertz electric field parallel to their axis. The WGP encountered first by the terahertz field, WGP_1, is on a rotation stage, whereas the second, WGP_2, is stationary with the wires oriented horizontally, such that only vertically polarized fields are transmitted. By rotating WGP_1, the field can be attenuated from full transmission when parallel ($\theta = 0°$) to near-zero transmission when they are cross-polarized ($\theta = 90°$). The absolute electric field amplitude is attenuated according to

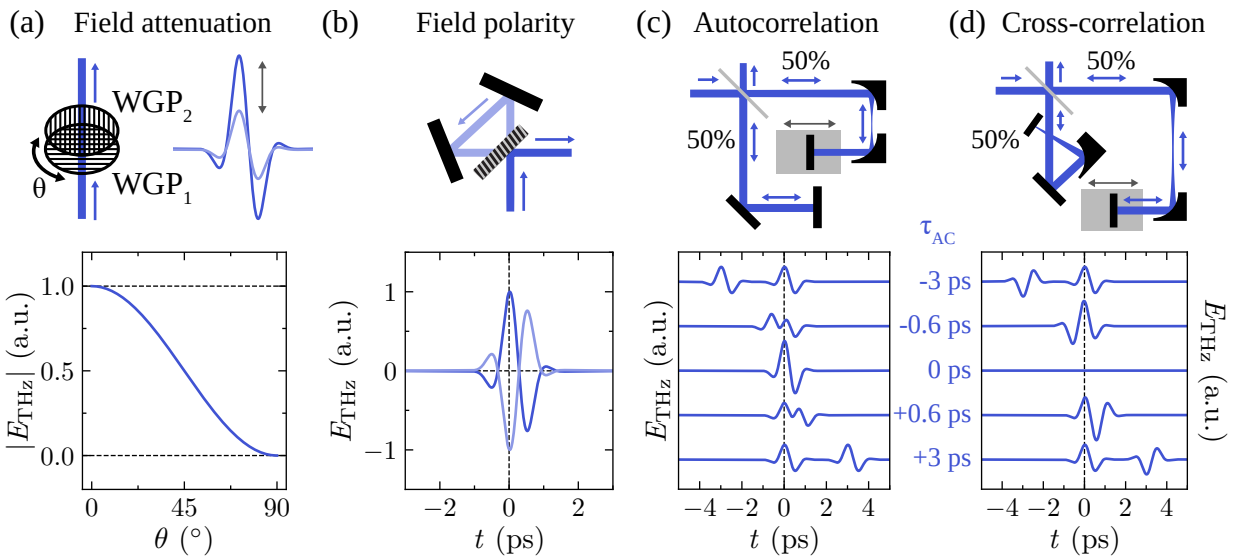

Figure 2.13 Pulse tailoring in the optical setup. (a) Field attenuation via wire grid polarizers. Field transmission as a function of polarizer angle (bottom). (b) Inversion of the field polarity by reflecting off an additional mirror. (c) Autocorrelation measurement by scanning the delay between two identical pulses. (d) Cross-correlation measurement by scanning the delay between two pulses with opposite polarity.

$|E_{\mathrm{THz}}| \propto \cos^2\theta$.

The second mechanism controls the polarity, i.e., sign of the peak electric field (2.13(a)). The mirror, sketched in the setup with a striped pattern, is mounted on a flip stage, allowing automated insertion into or removal from the beamline. When removed, the terahertz pulses reflect off two mirrors instead of one. This provides field-polarity control, considering that each reflection inverts the polarity.

By combining field attenuation and field polarity, THz-STS measurements can be performed, where the terahertz-induced tunneling current is measured as a function of field strength for both polarities.

Next, the terahertz pulses are split evenly into two pulses at a silicon wafer acting as a beam splitter (Si 50:50 in Fig. 2.12). The reflected portion enters the stationary arm of the Michelson interferometer, and the transmitted pulses enter an adjustable arm, whose length is controlled via a delay stage ("AC delay"). There are two configurations for the stationary arm: (1) autocorrelation (AC) and (2) cross-correlation. The configuration can be switched by adjusting the striped-pattern mirror on the flip stage in Fig. 2.12, in the same way as for the polarity control.

With the mirror removed, two identical copies of the terahertz pulse traverse the Michelson interferometer and are recombined at the exit, with a delay set by the delay stage in the adjustable arm (Fig. 2.13(c), top). The bottom of Fig. 2.13(c) shows the pulse sequence at different delay times. A continuous sweep of the delay is referred to as a THz-AC measurement.

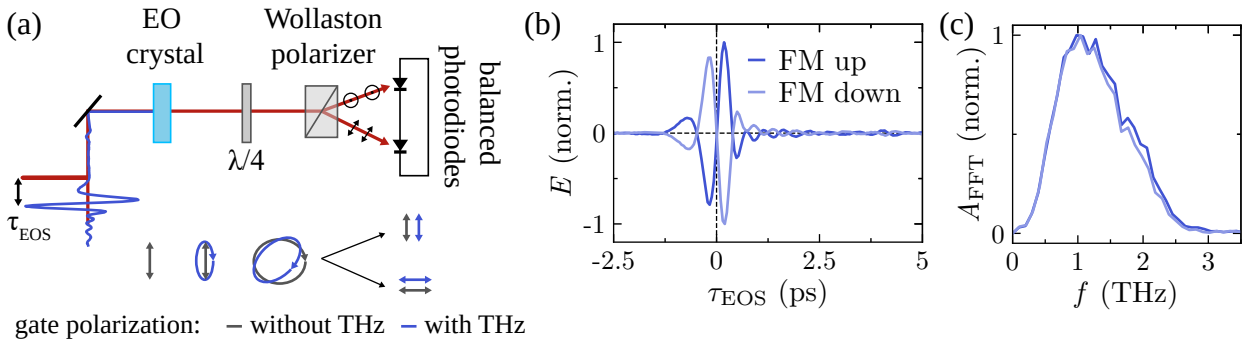

Figure 2.14 Electro-optic sampling of terahertz pulses in free space. (a) Schematic of an EOS setup. (b) Terahertz waveforms of both polarities measured with EOS. (c) Fourier transform amplitude spectra of the waveforms in (b).

If the mirror on the flip stage is inserted in the stationary arm, the terahertz pulses are reflected to a parabolic mirror that focuses the beam onto another mirror. This inverts the polarity of these terahertz pulses compared to the pulses from the adjustable arm (Fig. 2.13(c), top). At zero delay time, the pulses from the two arms cancel. If a small delay is introduced, the two pulses can be used to construct new pulse shapes and effectively control the CEP (Fig. 2.13(c), bottom). For THz-STM, it is advantageous to use cosine-like pulses, where the ratio between the maximum positive and negative field amplitudes is maximized.

The terahertz cross-correlation (THz-CC) setup (green box in Fig. 2.12) is an extension of the pulse shaping section. It was developed and built for the project in Chapter 3 and is described in detail there.

2.5.1.3 Free space terahertz field detection

To measure the terahertz pulses in free space, before they enter the STM, a mirror can be removed from the beamline after the THz-CC section to allow the beam to enter into the electro-optical sampling (EOS) setup in the top right of Fig. 2.12. For EOS, optical pulses (here, a 800 nm near-IR pulses compressed by the OPA to 30-40 fs), are used as a gate. They enter the terahertz beamline through an indium tin oxide (ITO) window that reflects terahertz radiation but transmits near-IR light. The WGPs in the THz-CC setup (sketched semi-transparently in Fig. 2.12) are typically removed for EOS to avoid thermal fluctuations from chopping the optical pulses and to prevent distortion or attenuation effects due to the WGP. The "THz delay" stage can be used to control the delay between the gate and terahertz pulses.

Figure 2.14 shows the EOS components at the top and the polarization of the gate beam at the bottom. When the terahertz electric field and the gate pulse temporally overlap in the ZnTe crystal, the instantaneous terahertz field induces a transient birefringence in the crystal. This affects the near-IR polarization, meaning that light polarized along different directions experiences different refractive indices and leads to a slightly elliptical polarization of the gate pulse, where

the ellipticity is proportional to the terahertz field amplitude. After the crystal, a quarter-wave plate ($\lambda/4$) converts this polarization change into an intensity imbalance between two orthogonal polarization components. These components are then spatially separated by a Wollaston prism and detected using a pair of balanced photodiodes, which measure the intensity difference between the polarization signals. This detection scheme enables sensitive, phase-resolved measurement of the terahertz electric field as a function of the delay between the gate pulse and the terahertz transient [1, 120, 121].

This approach can, for example, be used to verify that the terahertz pulses of positive versus negative field polarity from the mechanism in Fig. 2.13(a) have the same temporal electric field and spectrum. The good agreement between the two polarities is shown in Fig. 2.14(a) for the time domain (signal from EOS) and Fig. 2.14(c) for the spectral amplitude in the frequency domain (after Fourier transform).

2.5.2 STM setup

The STM system and its operation are described in three parts: (1) General overview of the STM system, (2) STM electronics including feedback loop and lock-in detection, and (3) STM tip preparation and calibration.

2.5.2.1 STM system overview

The STM is a custom-designed, commercial system from CreaTec Fischer & Co. GmbH, which typically operates in UHV (base pressure of 5×10^{-11} mBar) at near liquid-helium temperatures. Figure 2.15(a) provides a schematic overview and Fig. 2.15(b) shows a photograph of the STM system. The frame sits on air-damped legs to minimize external vibrations. The system is divided into two UHV chambers (yellow-shaded region) connected by a valve. On the left is the STM chamber, housing the scanhead, and on the right is the preparation chamber.

The light gray components represent the pumping system. A series of different pumps is used to reach the base pressure. Starting from ambient pressure, a roughing pump (RP) is employed first, followed by a turbo pump (TP). Together, they can reach pressures of about 10^{-8} mBar. To further decrease the pressure, both chambers are equipped with ion getter pumps (IGP) with an integrated titanium sublimation pump (TSP), which can evacuate the system from 10^{-5} mBar to $\sim 10^{-10}$ mBar. To reach such low pressures, the system has to be baked out for multiple days after it has been exposed to air, in order to outgas atoms and molecules (especially water) adsorbed on the chamber walls. To avoid having to bake the entire system every time a sample or STM tip is loaded, the STM is equipped with a load lock chamber (LL, red-shaded), which is connected to the preparation chamber via a UHV valve that typically remains closed. The LL can be opened to load samples and tips from air into the system without exposing other units of the STM to the high pressures. It can be baked as an isolated small unit overnight to restore good vacuum using the TP

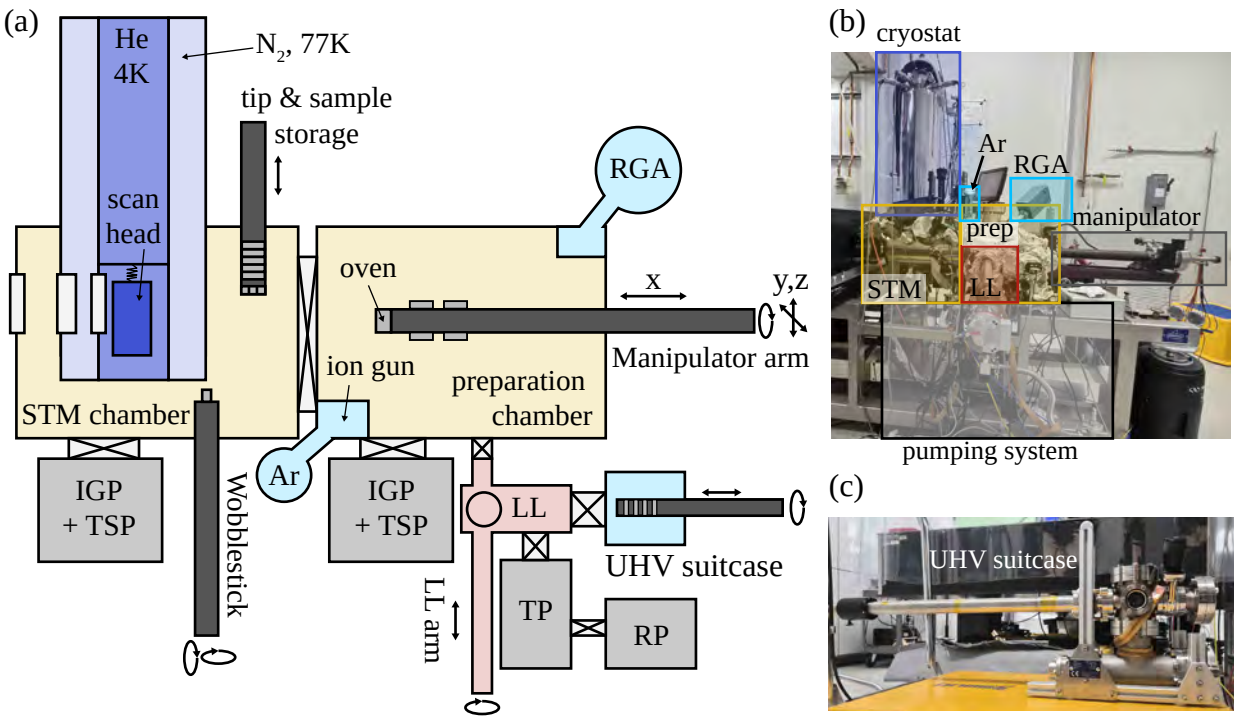

Figure 2.15 Overview of the STM setup. (a) Schematic of the STM chambers, pumps and manipulation system (IGP = ion getter pump, TSP = titanium sublimation pump, TP = turbo molecular pump, RP = roughing pump, RGA = residual gas analyzer, LL = load lock). (b) Photo of the STM system. (c) Photo of UHV portable suitcase.

and RP pump. Samples can also be transferred from another UHV system using a UHV suitcase (Fig. 2.15(c)) that can be attached to the LL. This method was, for example, used to transfer the samples studied in Chapter 4.

Once the vacuum in the load lock is restored after sample or tip loading and baking, the LL arm can be used to transfer them onto the manipulator arm in the preparation chamber. The manipulator arm can be rotated and moved in all three directions to position samples and tips for various preparation operations. The arm has several slots to store samples, one of which can be used to apply heat, for example, to anneal a sample. The preparation chamber is equipped with a residual gas analyzer (RGA), which measures the partial pressures of different gas species in the chamber by ionizing the residual gas and separating the ions according to their mass-to-charge ratio, and with an ion gun that can be used for argon sputtering, as explained later.

After the samples and tips have been prepared, they can be transferred into the STM chamber by opening the valve separating the chambers and extending the manipulator arm. The STM chamber is the cleanest unit and is therefore closed off from the rest of the system except during transfers. A wobblestick can be used to grab the sample or tip from the manipulator arm and either store it in the storage system or transfer it directly into the scanhead. The scanhead, which houses the

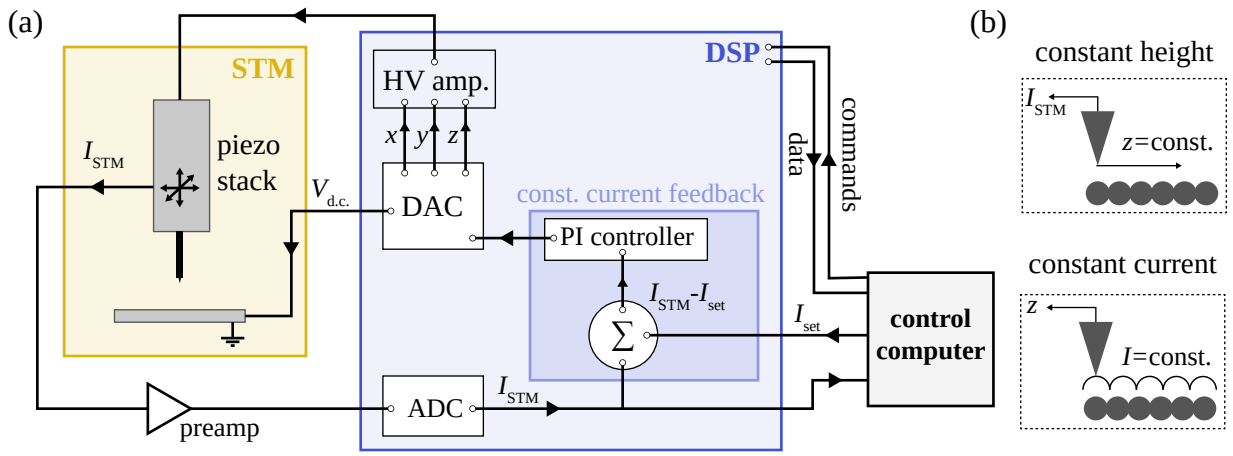

Figure 2.16 Basic STM electronics. (a) Schematic overview over the interfaces between STM and control computer. (HV = High voltage, DAC = Digital-to-analog converter, ADC = analog-to-digital converter, DSP = Digital signal processing controller, PI = proportional-integral). (b) Constant height and constant current scanning modes.

tip and sample and is suspended by springs to ensure maximum vibration isolation, resides in a liquid-helium temperature environment. This is achieved by enclosing the scanhead within an inner helium shield at 4 K and an outer nitrogen shield at 77 K. To allow optical and terahertz access to the tip-sample junction, the shields are equipped with closable windows on the left and back (not pictured in the schematic). The presence of these windows, especially if opened, increases the operation temperature to approximately 8-10 K depending on the specific configuration.

2.5.2.2 STM electronics

This subsection focuses on understanding the electronic control and data acquisition of a generic STM system. Further details can be found, for example, in the textbooks by Voigtländer [42] and Chen [23].

Numerous electrical wires run down the cryostat into the STM scanhead to connect it with the main external control unit, namely the digital signal processing controller (DSP), which provides an interface between the STM hardware and the control computer. The control computer runs an operating system that allows users to interact with the STM via a command line or a graphical user interface. The interactions between the STM scanhead, DSP unit and control computer are schematically shown in Fig. 2.16(a).

The tunneling current I_{STM} first passes through a preamplifier (FEMTO Low-noise, DLCPA-200, 1 kHz bandwidth), which amplifies the small tunneling current into a measurable voltage (as described in Chapter 2.1.2) and is then fed into the DSP. There, the analog voltage signal is converted into a digital signal (ADC: analog-to-digital converter), transferred to the control computer and made available for further processing.

The control computer sends commands and measurement configurations to the DSP. This

includes setting basic parameters, such as moving the tip in x and y to a specific location on the sample and applying a sample bias $V_{\mathrm{d.c.}}$, as well as more complex routines, such as sweeping a range of bias voltages to acquire the current-voltage characteristic of the junction or scanning the tip over a defined 2D area of the sample to record a surface image. Two common imaging modes are constant height and constant current imaging (Fig. 2.16(b)). In constant height mode, the tip height is fixed by the control computer and the tip is raster-scanned across the sample surface while the tunneling current is recorded. For large or uneven scan areas, or in the presence of thermal drift, constant height imaging risks tip-sample contact, potentially altering the tip apex and leading to inconsistent data sets. A safer mode of operation is constant current imaging, in which a feedback loop implemented in the DSP is engaged. The control computer sets a target tunneling current I_{set} and configures the proportional–integral (PI) feedback controller. The feedback loop continuously compares the measured tunneling current I_{STM} with I_{set} and calculates the required adjustment of the tip height. The resulting variation of the tip height during the constant current scan constitutes the topography image.

The DSP converts the digital control signals generated by the feedback loop and commands sent from the control computer into analog voltages using a digital-to-analog converter (DAC). To move the tip laterally and vertically with sub-nanometer precision, high voltages (HV) are applied to piezo stacks. Piezoelectric materials expand and contract reproducibly on very small length scales in response to applied electric fields, effectively behaving as actuators, which enable precise control of the tip position. In addition to the fine control scanning piezos, the scanhead has a second stack for coarse movement (tens of nanometers to millimeters) across the sample and to retract the tip away from the sample.

Electronic setups for STM systems usually include lock-in amplifiers, either as part of the DSP or as an additional external device (Fig. 2.17(a)). The goal for lock-in detection is to extract a small signal at a known reference frequency from a large noise background, as illustrated in Fig. 2.17(b). The lock-in amplifier either generates the modulation signal $V_0 \cos(\omega t)$ internally or receives it as an external reference and combines it with the noisy measured input signal $V_{\mathrm{meas}} \cos(\omega t + \phi)$. For a lock-in with X and Y outputs, the input signal is multiplied directly by the reference signal to obtain X and by the reference phase-shifted by 90° to obtain the Y-component. Mathematically, this corresponds to the product of two harmonic functions at the same frequency

$$V_{\mathrm{meas}} \cos(\omega t + \phi) \times V_0 \cos(\omega t) = \frac{1}{2} V_{\mathrm{meas}} V_0 (1 + \cos(2\omega t + \phi)) \tag{2.14}$$

After multiplication, a low pass filter acts as a time-averaging element and removes the oscillating term $2\omega t$, extracting the DC component $(1/2)V_{\mathrm{meas}}V_0 \cos\phi$. This output is therefore proportional to the signal amplitude V_{meas} and sensitive to the phase difference between the input and reference signals.

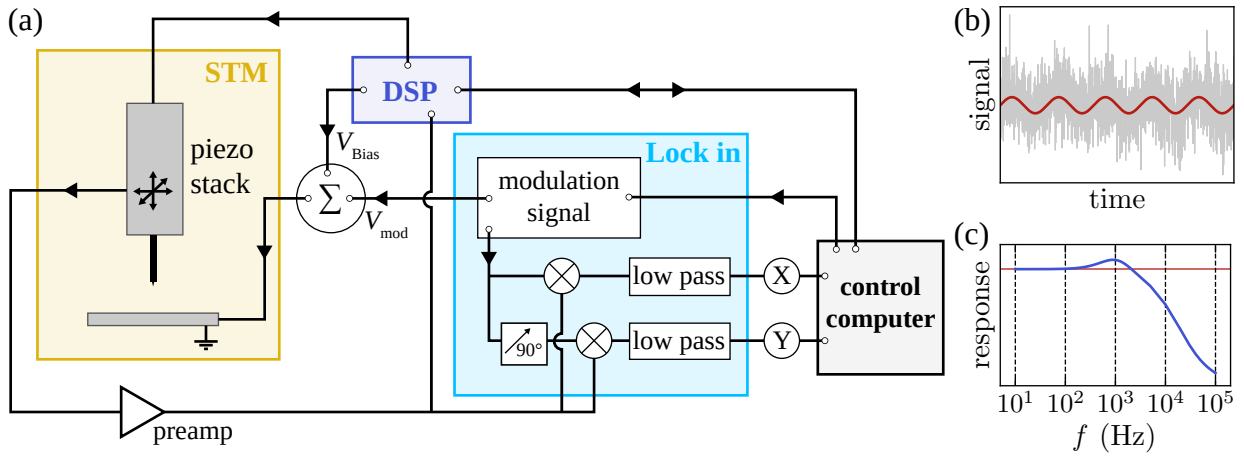

Figure 2.17 Lock-in detection within an STM setup. (a) Schematic of the electronic configuration of the lock-in amplifier. (b) Typical lock-in input signal (gray), where a small signal (red) at frequency ω is embedded in a large noise background. (c) Frequency-dependent response (mv/100 mV) of the FEMTO preamplifier The red horizontal line indicates a measured response of 1 mV/100 mV.

A finite signal in the Y channel indicates a phase mismatch between the measured signal and the reference. This can arise from frequency-dependent phase shifts introduced by the preamplifier, filters, cables or the STM junction itself. Such an omnipresent static phase shift can be compensated by adjusting the reference phase such that the X output represents the in-phase measurement channel, while the Y output is shifted by an additional 90°.

A Y-signal can also originate from intrinsically delayed physical responses of the system. In an ideal purely in-phase measurement, the reference phase is adjusted such that the signal appears entirely in the X channel and the Y channel vanishes. A nonzero Y component therefore serves as a diagnostic tool for time-delayed processes in the measurement, as demonstrated in the form of a phase transition to a metastable state in Chapter 5.

The bandwidth of the preamplifier determines the accessible range of reference frequencies. Figure 2.17(c) shows the frequency-dependent response (i.e., the output voltage relative to a known input voltage) of the FEMTO preamplifier used here, exhibiting the expected roll-off at approximately 1 kHz. Signal modulation frequencies must therefore remain below this value.

Lock-in detection is required for STS measurements in conventional STM, where a small voltage modulation V_{mod} is added on top of the bias voltage $V_{\mathrm{d.c.}}$ to extract $\mathrm{d}I/\mathrm{d}V \propto$ LDOS (see Chapter 2.2.3), as well as for THz-STM measurements, where the chopping frequency of the terahertz pulse train serves as the reference signal.

2.5.2.3 Tip preparation and calibration

Atomically resolved imaging with STM requires atomically sharp tips. Additionally, for THz-STM, the macro- and mesoscopic-scale shape is important for reproducible terahertz coupling. In

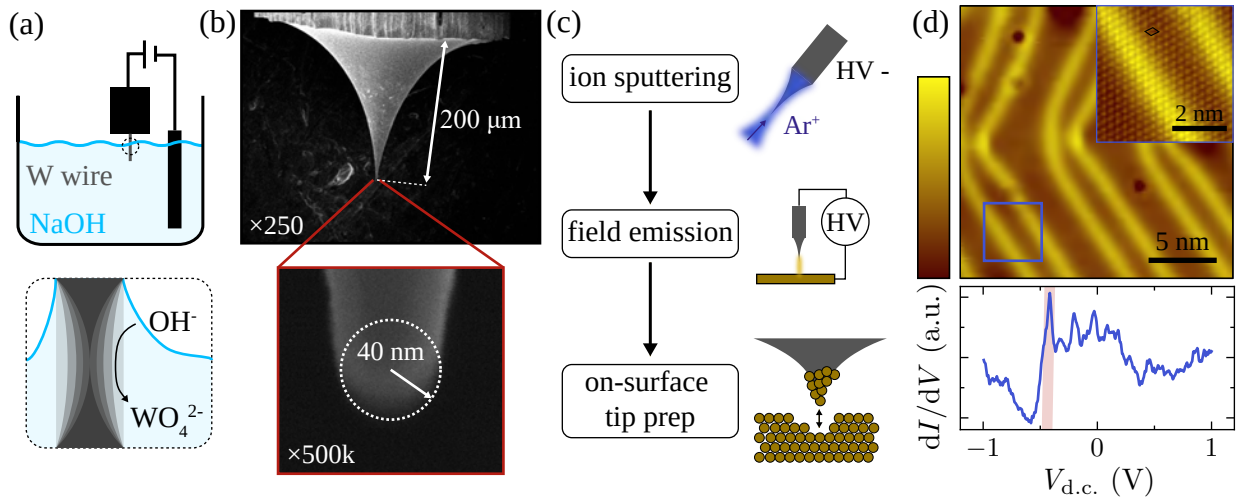

Figure 2.18 Tip preparation techniques. (a) Electro-chemical etching of W wire in a NaOH solution. (b) Scanning electron microscopy image of W tips after etching. (c) *In situ* tip preparation techniques. (d) Calibration measurements on Au(111) to test tip condition. Top: topography image with Herringbone reconstruction and inset of atomically resolved surface. The height range of the colormap scale bar is 35 pm. Bottom: dI/dV measurement, showing the characteristic Au(111) surface state (red-shading).

the projects described in this thesis, tungsten (W) tips are used, which are electrochemically etched from long tungsten wire in a NaOH solution [122–124]. The tip-etching setup is schematically shown in Fig. 2.18(a). The wire is partially submerged in the electrolyte solution and a positive voltage is applied to the W wire with respect to an electrode in the solution. During the etching process, preferential dissolution occurs near the liquid-air interface, where the tungsten surface oxidizes and forms WO_4^{2-}. Over time, the wire diameter decreases at this location until the lower part detaches. This method reliably produces sharp tips with with radius of curvature below 50 nm (shown in the scanning electron microscope images in Fig. 2.18(b)).

After etching, the tip is mounted in a tip holder, compatible with the STM transfer system, and loaded into the preparation chamber via the load lock. As a result of the etching process and exposure to air, the tungsten surface is covered by an oxide layer. This oxide can be removed by sputtering the tip with ionized argon gas [125, 126]. The Ar^+ ions are generated by an ion gun and accelerated toward the tip by applying a high voltage (Fig. 2.18(c), top). Removing the oxide ensures a conductive tip that can be inserted into the scanhead and approached to a sample. Field-directed sputtering also further sharpens the tip.

To bring the tip into tunneling range of the sample, it is carefully approached toward the surface using a sequence of coarse and fine steps until a current is detected. After successful approach, the tip typically requires further *in situ* preparation to achieve atomic resolution. Two *in situ* tip shaping procedures are shown schematically in Fig. 2.18(c). One of the more aggressive methods

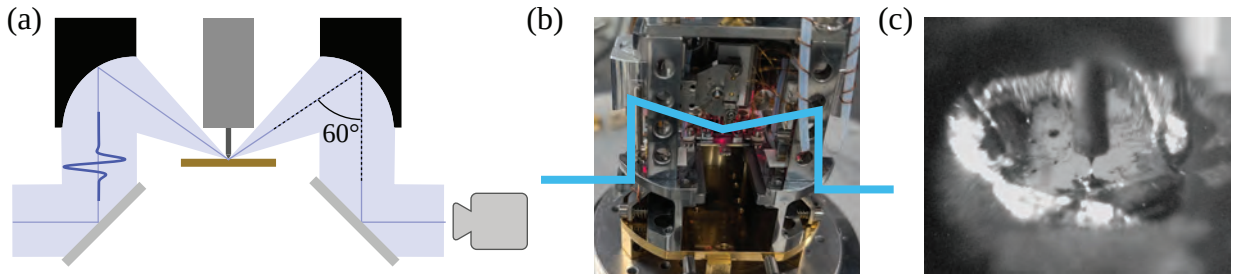

Figure 2.19 Coupling terahertz pulses to the STM scanhead. (a) Schematic of the optical setup at the STM scanhead. (b) Photograph of the scanhead. (c) Image of the tip-sample junction taken with a camera from the back of the scanhead as shown in (a).

is high-voltage field emission, in which the tip is retracted by approximately 50 nm from the surface and biased at a voltages of up to 100 V. The resulting currents in the junction can reach hundreds of nanoamperes up to microamperes, leading to a restructuring of the tip apex. Finally, fine optimization can be achieved by gently indenting the tip into a metallic surface to pick up metallic atoms, which constitute the final atoms at the apex and ultimately determine the atomic resolution and DOS of the tip.

These final tip preparation steps are performed on single crystal Au(111), which is cleaned by several cycles of argon sputtering and annealing up to 900 K. The tip condition can be evaluated by imaging the surface and recording STS spectra. Figure 2.18(d) shows the characteristic herringbone surface reconstruction [127] in a larger-scale scan (recorded in constant-current mode at $V_{\mathrm{d.c.}} = 1\,\mathrm{V}$ and $I = 100\,\mathrm{pA}$). The upper-right inset shows a smaller area with atomic resolution, demonstrating a sharp and stable tip apex (recorded in constant-current mode at $V_{\mathrm{d.c.}} = 5\,\mathrm{mV}$ and $I = 5\,\mathrm{nA}$). At the bottom, a $\mathrm{d}I/\mathrm{d}V$ spectrum is shown, with the characteristic surface state of Au(111) appearing as a step at around -0.5 V [128]. For the $\mathrm{d}I/\mathrm{d}V$ measurement, the feedback loop was disengaged at $V_{\mathrm{d.c.}} = 1\,\mathrm{V}$ and $I = 500\,\mathrm{pA}$, and the tip was approached toward the surface by 0.5 Å before starting the voltage sweep.

2.5.3 THz-STM setup

Once tip and sample are operational for conventional STM, typically during the final on-sample tip preparation steps, the terahertz fields can be coupled into the junction. The THz-STM coupling setup, electronics and further tip calibration are described in the following.

2.5.3.1 Terahertz pulse coupling to the STM scanhead

To couple the vertically polarized terahertz pulses into the STM system toward the scanhead, the radiation passes through three c-cut sapphire windows: one to enter the STM chamber, a second at the nitrogen shield and a final window at the helium shield. The STM scanhead is specifically equipped with an optical assembly to focus the terahertz pulses onto the tip-sample

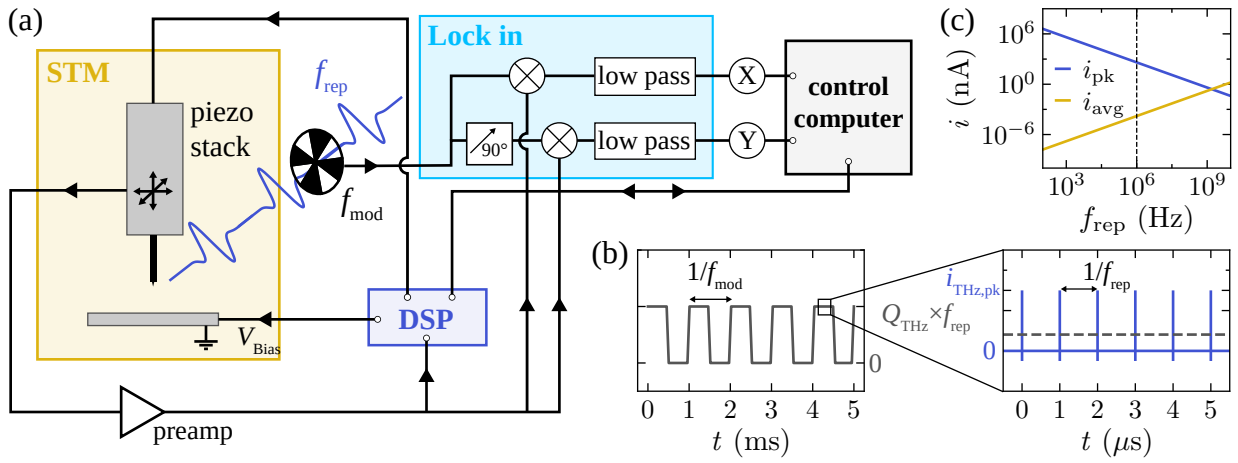

Figure 2.20 THz-STM signal acquisition. (a) Schematic overview of the THz-STM electronic setup with lock-in detection. (b) Time scales of the laser repetition rate and optical chopper frequency. (c) Duty cycles considerations for THz-STM.

junction (schematic shown in Fig. 2.19(a) and photograph of the scanhead in Fig. 2.19(b)). The pulses enter the scanhead horizontally from the left and are reflected upward by a aluminum plane mirror onto a 60° off-axis aluminum parabolic mirror, which focuses the terahertz beam down into the junction. The mirrors are highly reflective over a broad spectral range, enabling the coupling of radiation from the near-UV to the terahertz regime into the STM. Because the mirrors cannot be realigned without breaking vacuum, care must be taken to ensure that all samples are mounted at the same height so that the junction lies within the focal plane. The beam diameter at the focus is approximately 1 mm. Since the focusing parabolic mirror is directly attached to the upper part of the scanhead that moves together with the tip via coarse motion control, the focal spot follows the tip position to the desired location on the sample surface. As shown in Fig. 2.19(a), the optical layout is symmetric, allowing optical access from both sides of the scanhead. A camera with high magnification can be positioned opposite the incoming terahertz beam to image the junction (Fig. 2.19(c)). This is useful for approaching uneven samples and for aligning optical pulses to the STM tip which are visible with the camera (in contrast to the terahertz radiation).

2.5.3.2 THz-STM electronics

The terahertz-induced tunneling current is recorded using lock-in detection. Chapter 2.5.2.2 already introduced the operating principles of a lock-in amplifier. For THz-STM measurements, an external lock-in amplifier is used that interfaces with the DSP and the control computer (Fig. 2.20(a)). The modulation frequency f_{mod}, given by the rotation frequency of the chopper blade modulating the terahertz beam in the terahertz generation section of the optical setup (see Fig. 2.12), serves as the reference signal. The tunneling current provides the input signal to the lock-in. The chopper frequency must lie within the bandwidth of the FEMTO preamplifier (1 kHz) and is set to 744 Hz

for most experiments presented in this thesis.

Figure 2.20(b) (left) shows the terahertz-induced tunneling current on the time scale of the chopper modulation. For half of each modulation period the beam is blocked, resulting in no terahertz-induced current, while during the unblocked half a finite terahertz-induced signal is present. The laser operates at a repetition rate of $f_{\mathrm{rep}} = 1\,\mathrm{MHz}$. When the beam is unblocked, the measured signal consists of the rectified charge Q_{THz} generated by many successive pulses that probe the $I - V$ characteristic of the junction (Fig. 2.20(b), right). The instantaneous current $i(t)$ per pulse is time-integrated by the preamplifier. The signal detected by the lock-in amplifier is therefore proportional to $Q_{\mathrm{THz}} \times f_{\mathrm{rep}}$.

There are multiple things that determine the sensitivity of the electronic setup to the current generated by a single terahertz pulse. Assuming that on average one electron tunnels per single terahertz pulse, this corresponds to a rectified charge of pulse of $Q_{\mathrm{THz}} = 1e/\mathrm{pulse} \approx 1.6 \times 10^{-19} C/\mathrm{pulse}$. Multiplication by the laser repetition rate of 1 MHz yields an average current of $i_{\mathrm{avg}} = 160\,\mathrm{fA}$ going to the preamp. The average current as a function of repetition rate is shown in yellow in Fig. 2.20(c). After amplification the input signal to the lock-in amplifier is $V_{\mathrm{amp}} = 160\,\mu\mathrm{V}$ since the preamp has a transimpedance gain of $G = 10^9\,\mathrm{V/A}$.

To estimate the peak current i_{pk} during an individual pulse, the duty cycle of the terahertz pulse train $D = \tau_{\mathrm{THz}} \times f_{\mathrm{rep}}$ must be considered. For terahertz voltage transients on the order of 100 to 500 fs and a repetition rate of 1 MHz, the duty cycle lies in the range $10^{-6} - 10^{-7}$. Assuming a pulse duration of 400 fs and a unipolar current pulse proportional to a rectified charge of one electron per pulse (a precise calculation requires knowledge of the $I - V$ curve and terahertz waveform shape), the peak current is estimated as

$$i_{\mathrm{pk}} = \frac{i_{\mathrm{avg}}}{\tau_{\mathrm{THz}} \times f_{\mathrm{rep}}} = \frac{160\,\mathrm{fA}}{400\,\mathrm{fs} \times 10^6\,\mathrm{Hz}} = 400\,\mathrm{nA}. \tag{2.15}$$

Figure 2.20(c) shows the corresponding average and peak currents for different laser repetition rates for a rectified charge of one electron per pulse. To ensure a sufficient signal-to-noise ratio for lock-in detection, while simultaneously avoiding peak currents large enough to perturb or modify the tunnel junction, the repetition rate plays a critical role. In addition, THz-STM is often performed at reduced tip-sample separations to compensate for the small duty cycle. This is a operating mode that has proven to be a key strength of the technique, enabling access to surface features that are inaccessible at conventional STM tip heights [76].

2.5.3.3 THz-STM tip calibration

Before employing the THz-STM technique to complex samples such as 2D materials, the tip must be further prepared and calibrated on a well-defined metallic reference sample, such as Au(111). In addition to conventional STM measurements in Fig. 2.18(c), THz-STM imaging

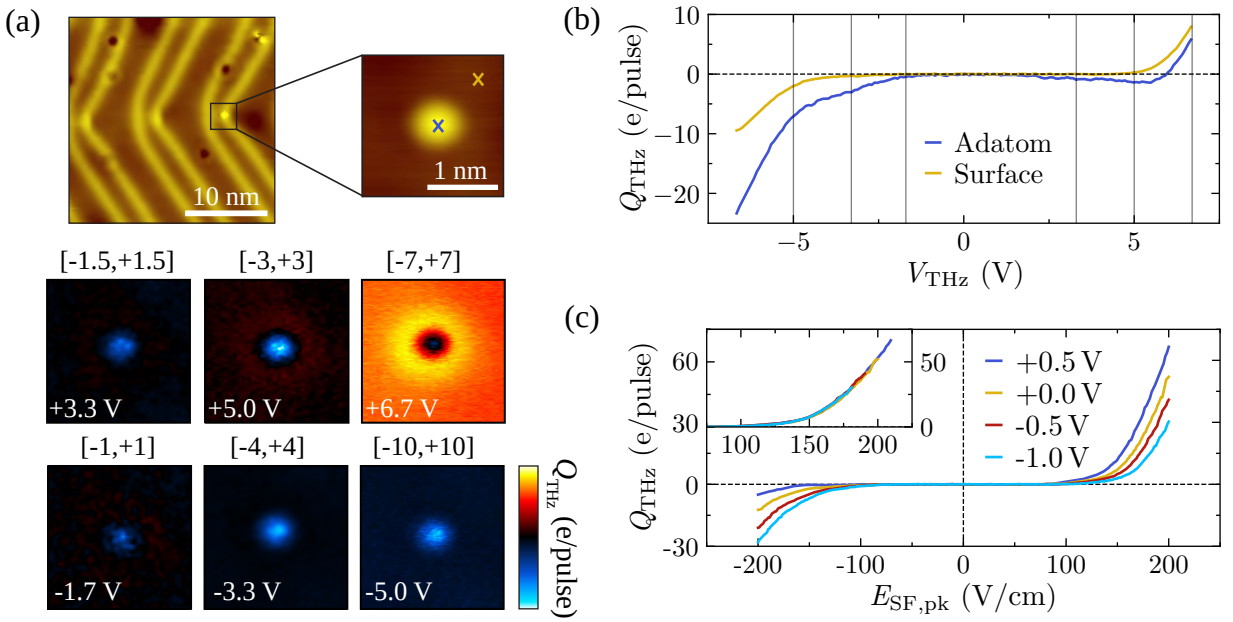

Figure 2.21 Tip preparation and calibration for THz-STM on Au(111). (a) Imaging of a gold adatom at different field strengths. (b) THz-STS of the adatom versus the surface. (c) Calibrating the terahertz-induced voltage via THz-STS at different bias voltages.

is performed (Fig. 2.21(a)). To obtain contrast in THz-STM on Au(111), a single gold adatom, commonly found at the corners of the herringbone reconstruction, is selected. The adatom is imaged at various terahertz voltages with both field polarities. A circular adatom shape and a strong rectified charge signal arising from the onset of field emission indicate a suitable tip condition for THz-STM operation. Depending on the field strength, the relative contrast between the surface and adatom varies. The evolution of the rectified charge as a function of field strength is resolved in THz-STS measurements performed directly on the adatom and at a position only 1 nm away in Fig. 2.21(b). The dominant contrast arises from the more pronounced negative response of the adatom relative to the surface, explaining the opposite-sign contrast observed in the THz-STM image at +5.0 V.

A key question for THz-STM is how the terahertz-induced voltage in the junction compares to the voltage applied by the STM electronics, as this determines which part of the $I - V$ curve, and hence the LDOS, is probed. For samples like Au(111), which act as a near-perfect metal at terahertz frequencies, the terahertz voltage in the junction is equivalent to an oscillating d.c. bias. This allows determination of a conversion factor between the terahertz field strength and bias voltage, α, by performing THz-STS at different static bias voltages (with the feedback loop disengaged), using terahertz-induced field emission to generate a signal (Fig. 2.21(c)). By shifting the measured curves along the voltage axis by $\alpha \times V_{\mathrm{d.c.}}$ until they overlap (Fig. 2.21(c) inset), a conversion factor of $\alpha = E_{\mathrm{SF,pk}}/V_{\mathrm{SF,pk}} = 19\,(\mathrm{Vcm}^{-1}/\mathrm{V})$ is obtained. Calibration measurements on different Au(111) samples using multiple tips typically yield values between $15\,(\mathrm{Vcm}^{-1})/\mathrm{V}$

and 20 $(\mathrm{Vcm}^{-1})/\mathrm{V}$. Notably, α is sample-dependent and generally only practical to determine on metallic samples, where the static bias voltage does not modify the local band bending (unlike in semiconductors).

With the THz-STM experimental setup calibrated and characterized, the following chapters focus on its application and further development.

BIBLIOGRAPHY

[1] Lee, Y.-S. *Principles of Terahertz Science and Technology* (Springer US, Boston, MA, 2009). Available at https://link.springer.com/10.1007/978-0-387-09540-0.

[2] Dressel, M. & Grüner, G. *Electrodynamics of Solids: Optical Properties of Electrons in Matter* (Cambridge University Press, Cambridge, 2002). Available at https://www.cambridge.org/core/books/electrodynamics-of-solids/DFDDF1640793690DAFD338BFDD1A18BF.

[3] Jepsen, P., Cooke, D. & Koch, M. Terahertz spectroscopy and imaging – Modern techniques and applications. *Laser & Photonics Reviews* **5**, 124–166 (2011).

[4] Tian, Y., Yang, F., Guo, C. & Jiang, Y. Recent advances in ultrafast time-resolved scanning tunneling microscopy. *Surface Review and Letters* **25**, 1841003 (2018).

[5] Lloyd-Hughes, J. *et al.* The 2021 ultrafast spectroscopic probes of condensed matter roadmap. *Journal of Physics: Condensed Matter* **33**, 353001 (2021).

[6] Maiuri, M., Garavelli, M. & Cerullo, G. Ultrafast Spectroscopy: State of the Art and Open Challenges. *Journal of the American Chemical Society* **142**, 3–15 (2020).

[7] Kafka, J., Watts, M. & Pieterse, J.-W. Picosecond and femtosecond pulse generation in a regeneratively mode-locked Ti:sapphire laser. *IEEE Journal of Quantum Electronics* **28**, 2151–2162 (1992).

[8] Cocker, T. L. *et al.* Microscopic origin of the Drude-Smith model. *Physical Review B* **96**, 205439 (2017).

[9] Cocker, T. L., Jelic, V., Hillenbrand, R. & Hegmann, F. A. Nanoscale terahertz scanning probe microscopy. *Nature Photonics* **15**, 558–569 (2021).

[10] Hillenbrand, R., Abate, Y., Liu, M., Chen, X. & Basov, D. N. Visible-to-THz near-field nanoscopy. *Nature Reviews Materials* **10**, 285–310 (2025).

[11] Wang, K., Mittleman, D. M., van der Valk, N. C. J. & Planken, P. C. M. Antenna effects in terahertz apertureless near-field optical microscopy. *Applied Physics Letters* **85**, 2715–2717 (2004).

[12] Huber, A. J., Keilmann, F., Wittborn, J., Aizpurua, J. & Hillenbrand, R. Terahertz Near-Field Nanoscopy of Mobile Carriers in Single Semiconductor Nanodevices. *Nano Letters* **8**, 3766–3770 (2008).

[13] Mastel, S. *et al.* Terahertz Nanofocusing with Cantilevered Terahertz-Resonant Antenna Tips. *Nano Letters* **17**, 6526–6533 (2017).

[14] Keilmann, F. & Hillenbrand, R. Near-field microscopy by elastic light scattering from a tip. *Philosophical Transactions of the Royal Society A: Mathematical, Physical and Engineering Sciences* **362**, 787–805 (2004).

[15] Plankl, M. *et al.* Subcycle contact-free nanoscopy of ultrafast interlayer transport in atomically thin heterostructures. *Nature Photonics* **15**, 594–600 (2021).

[16] Maissen, C., Chen, S., Nikulina, E., Govyadinov, A. & Hillenbrand, R. Probes for Ultrasensitive THz Nanoscopy. *ACS Photonics* **6**, 1279–1288 (2019).

[17] Siday, T., Hale, L. L., Hermans, R. I. & Mitrofanov, O. Resonance-Enhanced Terahertz Nanoscopy Probes. *ACS Photonics* **7**, 596–601 (2020).

[18] Zhang, S. *et al.* Nano-spectroscopy of excitons in atomically thin transition metal dichalcogenides. *Nature Communications* **13**, 542 (2022).

[19] Siday, T. *et al.* All-optical subcycle microscopy on atomic length scales. *Nature* **629**, 329–334 (2024).

[20] Binnig, G., Rohrer, H., Gerber, C. & Weibel, E. Surface Studies by Scanning Tunneling Microscopy. *Physical Review Letters* **49**, 57–61 (1982).

[21] Binnig, G., Rohrer, H., Gerber, C. & Weibel, E. Tunneling through a controllable vacuum gap. *Applied Physics Letters* **40**, 178–180 (1982).

[22] Binnig, G. & Rohrer, H. Scanning tunneling microscopy—from birth to adolescence. *Reviews of Modern Physics* **59**, 615–625 (1987).

[23] Chen, C. J. *Introduction to Scanning Tunneling Microscopy Third Edition*. Monographs on the Physics and Chemistry of Materials (Oxford University Press, Oxford, New York, 2021), third edition, new to this edition:, third edition, new to this edition: edn.

[24] Liang, K., Bi, L., Zhu, Q., Zhou, H. & Li, S. Ultrafast Dynamics Revealed with Time-Resolved Scanning Tunneling Microscopy: A Review. *ACS Applied Optical Materials* **1**, 924–938 (2023).

[25] Loth, S., Etzkorn, M., Lutz, C. P., Eigler, D. M. & Heinrich, A. J. Measurement of Fast Electron Spin Relaxation Times with Atomic Resolution. *Science* **329**, 1628–1630 (2010).

[26] Baumann, S. *et al.* Electron paramagnetic resonance of individual atoms on a surface. *Science* **350**, 417–420 (2015).

[27] Veldman, L. M. *et al.* Free coherent evolution of a coupled atomic spin system initialized by electron scattering. *Science* **372**, 964–968 (2021).

[28] Hamers, R. J. & Cahill, D. G. Ultrafast time resolution in scanned probe microscopies. *Applied Physics Letters* **57**, 2031–2033 (1990).

[29] Weiss, S., Ogletree, D. F., Botkin, D., Salmeron, M. & Chemla, D. S. Ultrafast scanning probe microscopy. *Applied Physics Letters* **63**, 2567–2569 (1993).

[30] Donati, G. P., Rodriguez, G. & Taylor, A. J. Ultrafast, dynamical imaging of surfaces by use of a scanning tunneling microscope with a photoexcited, low-temperature-grown GaAs tip. *JOSA B* **17**, 1077–1083 (2000).

[31] Nunes, G. & Freeman, M. R. Picosecond Resolution in Scanning Tunneling Microscopy. *Science* **262**, 1029–1032 (1993).

[32] Steeves, G. M., Elezzabi, A. Y. & Freeman, M. R. Advances in picosecond scanning tunneling microscopy via junction mixing. *Applied Physics Letters* **70**, 1909–1911 (1997).

[33] Steeves, G. M., Elezzabi, A. Y. & Freeman, M. R. Nanometer-scale imaging with an ultrafast scanning tunneling microscope. *Applied Physics Letters* **72**, 504–506 (1998).

[34] Groeneveld, R. H. M. & van Kempen, H. The capacitive origin of the picosecond electrical transients detected by a photoconductively gated scanning tunneling microscope. *Applied Physics Letters* **69**, 2294–2296 (1996).

[35] Shigekawa, H. *et al.* Nanoscale dynamics probed by laser-combined scanning tunneling microscopy. *Thin Solid Films* **516**, 2348–2357 (2008).

[36] Yoshida, S., Terada, Y., Oshima, R., Takeuchi, O. & Shigekawa, H. Nanoscale probing of transient carrier dynamics modulated in a GaAs–PIN junction by laser-combined scanning tunneling microscopy. *Nanoscale* **4**, 757 (2012).

[37] Dolocan, A., Acharya, D. P., Zahl, P., Sutter, P. & Camillone, N. I. Two-Color Ultrafast Photoexcited Scanning Tunneling Microscopy. *The Journal of Physical Chemistry C* **115**, 10033–10043 (2011).

[38] Garg, M. & Kern, K. Attosecond coherent manipulation of electrons in tunneling microscopy. *Science* **367**, 411–415 (2020).

[39] Maier, S. *et al.* Attosecond charge transfer in atomic-resolution scanning tunnelling microscopy (2025). Available at http://arxiv.org/abs/2507.10206. ArXiv:2507.10206 [physics].

[40] Rossetti, A. *et al.* Modulation of sub-optical cycle photocurrents in an ultrafast near-infrared scanning tunnelling microscope (2025). Available at http://arxiv.org/abs/2507.16357. ArXiv:2507.16357 [physics].

[41] Wiesendanger, R. *Scanning Probe Microscopy and Spectroscopy* (Cambridge University Press, 1994).

[42] Voigtländer, B. *Scanning Probe Microscopy: Atomic Force Microscopy and Scanning Tunneling Microscopy*. NanoScience and Technology (Springer, Berlin, Heidelberg, 2015). Available at https://link.springer.com/10.1007/978-3-662-45240-0.

[43] Bardeen, J. Tunnelling from a Many-Particle Point of View. *Physical Review Letters* **6**, 57–59 (1961).

[44] Tersoff, J. & Hamann, D. R. Theory and Application for the Scanning Tunneling Microscope. *Physical Review Letters* **50**, 1998–2001 (1983).

[45] Tersoff, J. & Hamann, D. R. Theory of the scanning tunneling microscope. *Physical Review B* **31**, 805–813 (1985).

[46] Simmons, J. G. Generalized Formula for the Electric Tunnel Effect between Similar Electrodes Separated by a Thin Insulating Film. *Journal of Applied Physics* **34**, 1793–1803 (1963).

[47] Fowler, R. H. & Nordheim, L. Electron emission in intense electric fields. *Proceedings of the Royal Society of London. Series A, Containing Papers of a Mathematical and Physical Character* **119**, 173–181 (1928).

[48] Müller, M. Imaging surfaces at the space–time limit: New perspectives of time-resolved scanning tunneling microscopy for ultrafast surface science. *Progress in Surface Science* **99**, 100727 (2024).

[49] Landsman, A. S. & Keller, U. Attosecond science and the tunnelling time problem. *Physics Reports* **547**, 1–24 (2015).

[50] Février, P. & Gabelli, J. Tunneling time probed by quantum shot noise. *Nature Communications* **9**, 4940 (2018).

[51] Shafir, D. *et al.* Resolving the time when an electron exits a tunnelling barrier. *Nature* **485**, 343–346 (2012).

[52] Keldysh, L. V. Ionization in the field of a strong electromagnetic wave. *Soviet Physics JETP* **20**, 56–63 (1965).

[53] Hommelhoff, P., Sortais, Y., Aghajani-Talesh, A. & Kasevich, M. A. Field Emission Tip as a Nanometer Source of Free Electron Femtosecond Pulses. *Physical Review Letters* **96**, 077401 (2006).

[54] Dombi, P. *et al.* Strong-field nano-optics. *Reviews of Modern Physics* **92**, 025003 (2020).

[55] Ropers, C., Solli, D. R., Schulz, C. P., Lienau, C. & Elsaesser, T. Localized Multiphoton Emission of Femtosecond Electron Pulses from Metal Nanotips. *Physical Review Letters* **98**, 043907 (2007).

[56] Barwick, B. *et al.* Laser-induced ultrafast electron emission from a field emission tip. *New Journal of Physics* **9**, 142 (2007).

[57] Büttiker, M. & Landauer, R. Traversal Time for Tunneling. *Physical Review Letters* **49**, 1739–1742 (1982).

[58] Zheltikov, A. M. Keldysh parameter, photoionization adiabaticity, and the tunneling time. *Physical Review A* **94**, 043412 (2016).

[59] Bharadwaj, P., Deutsch, B. & Novotny, L. Optical Antennas. *Advances in Optics and Photonics, Vol. 1, Issue 3, pp. 438-483* (2009).

[60] Walther, M., Chambers, G. S., Liu, Z., Freeman, M. R. & Hegmann, F. A. Emission and detection of terahertz pulses from a metal-tip antenna. *JOSA B* **22**, 2357–2365 (2005).

[61] Müller, M., Martín Sabanés, N., Kampfrath, T. & Wolf, M. Phase-Resolved Detection of Ultrabroadband THz Pulses inside a Scanning Tunneling Microscope Junction. *ACS Photonics* **7**, 2046–2055 (2020).

[62] Cocker, T. L. *et al.* An ultrafast terahertz scanning tunnelling microscope. *Nature Photonics* **7**, 620–625 (2013).

[63] Abdo, M. *et al.* Variable Repetition Rate THz Source for Ultrafast Scanning Tunneling Microscopy. *ACS Photonics* **8**, 702–708 (2021).

[64] Gutzler, R., Garg, M., Ast, C. R., Kuhnke, K. & Kern, K. Light–matter interaction at atomic scales. *Nature Reviews Physics* **3**, 441–453 (2021).

[65] Tachizaki, T., Hayashi, K., Kanemitsu, Y. & Hirori, H. On the progress of ultrafast time-resolved THz scanning tunneling microscopy. *APL Materials* **9**, 060903 (2021).

[66] Zhang, Y., Du, S. & Hirakawa, K. Deep-nanometer-scale terahertz spectroscopy using a transistor geometry with metal nanogap electrodes. *Light: Advanced Manufacturing* **2**, 460–472 (2021).

[67] Banerjee, S. & Zhang, P. Scaling of Time-Dependent Tunneling Current in Terahertz Scanning Tunneling Microscopes. *Physical Review Applied* **18**, 024011 (2022).

[68] Bi, L. *et al.* Recent progress in probing atomic and molecular quantum coherence with scanning tunneling microscopy. *Progress in Surface Science* **98**, 100696 (2023).

[69] Katayama, I., Kimura, K., Imada, H., Kim, Y. & Takeda, J. Investigation of ultrafast excited-state dynamics at the nanoscale with terahertz field-induced electron tunneling and photon emission. *Journal of Applied Physics* **133**, 110903 (2023).

[70] Zhao, Z. *et al.* Applications of ultrafast nano-spectroscopy and nano-imaging with tip-based microscopy. *eLight* **5**, 1 (2025).

[71] Leitenstorfer, A. *et al.* The 2023 terahertz science and technology roadmap. *Journal of Physics D: Applied Physics* **56**, 223001 (2023).

[72] Borsch, M., Meierhofer, M., Huber, R. & Kira, M. Lightwave electronics in condensed matter. *Nature Reviews Materials* **8**, 668–687 (2023).

[73] Phark, S.-h. *et al.* Roadmap on Atomically-Engineered Quantum Platforms. *Nano Futures* (2025).

[74] Cocker, T. L., Peller, D., Yu, P., Repp, J. & Huber, R. Tracking the ultrafast motion of a single molecule by femtosecond orbital imaging. *Nature* **539**, 263–267 (2016).

[75] Jelic, V. *et al.* Ultrafast terahertz control of extreme tunnel currents through single atoms on a silicon surface. *Nature Physics* **13**, 591–598 (2017).

[76] Ammerman, S. E. *et al.* Lightwave-driven scanning tunnelling spectroscopy of atomically precise graphene nanoribbons. *Nature Communications* **12**, 6794 (2021).

[77] Yoshioka, K. *et al.* Tailoring Single-Cycle Near Field in a Tunnel Junction with Carrier-Envelope Phase-Controlled Terahertz Electric Fields. *Nano Letters* **18**, 5198–5204 (2018).

[78] Allerbeck, J. *et al.* Efficient and Continuous Carrier-Envelope Phase Control for Terahertz Lightwave-Driven Scanning Probe Microscopy. *ACS Photonics* **10**, 3888–3895 (2023).

[79] Jelic, V. *et al.* Atomic-scale terahertz time-domain spectroscopy. *Nature Photonics* **18**, 898–904 (2024).

[80] Sheng, S. *et al.* Control of Surface Plasmon Propagation and Terahertz Near-Field Waveforms in a Scanning Tunneling Microscope. *Nano Letters* **24**, 15291–15299 (2024).

[81] Yoshida, S. *et al.* Subcycle Transient Scanning Tunneling Spectroscopy with Visualization of Enhanced Terahertz Near Field. *ACS Photonics* **6**, 1356–1364 (2019).

[82] Martín Sabanés, N. *et al.* Femtosecond Thermal and Nonthermal Hot Electron Tunneling Inside a Photoexcited Tunnel Junction. *ACS Nano* **16**, 14479–14489 (2022).

[83] Peller, D. *et al.* Quantitative sampling of atomic-scale electromagnetic waveforms. *Nature Photonics* **15**, 143–147 (2021).

[84] Jelic, V. *et al.* A General Approach to THz Near-Field Waveform Sampling in a Lightwave-Driven Scanning Tunneling Microscope Junction. In *2023 48th International Conference on Infrared, Millimeter, and Terahertz Waves (IRMMW-THz)*, 1–2 (2023). Available at https://ieeexplore.ieee.org/abstract/document/10299095.

[85] Li, H. *et al.* Real-Space Sampling of Terahertz Waveforms Under Scanning Tunneling Microscope. *ACS Photonics* **11**, 1428–1437 (2024).

[86] Bobzien, L. *et al.* Ultrafast state-selective tunneling in two-dimensional semiconductors with a phase- and amplitude-controlled THz-scanning tunneling microscope. *APL Materials* **12**, 051110 (2024).

[87] Allerbeck, J. *et al.* Ultrafast Coulomb blockade in an atomic-scale quantum dot. *Nature Communications* **16**, 10806 (2025).

[88] Luo, Y. *et al.* Nanoscale terahertz STM imaging of a metal surface. *Physical Review B* **102**, 205417 (2020).

[89] Sheng, S. *et al.* Launching Coherent Acoustic Phonon Wave Packets with Local Femtosecond Coulomb Forces. *Physical Review Letters* **129**, 043001 (2022).

[90] Li, H. *et al.* Unveiling nanoscale THz-STM imaging techniques on graphene nanoribbons with zigzag edge topology. *Optics Express* **32**, 32062–32078 (2024).

[91] Yoshida, S. *et al.* Terahertz Scanning Tunneling Microscopy for Visualizing Ultrafast Electron Motion in Nanoscale Potential Variations. *ACS Photonics* **8**, 315–323 (2021).

[92] Kimura, K. *et al.* Ultrafast on-demand exciton formation in a single-molecule junction by tailored terahertz pulses. *Science* **387**, 1077–1082 (2025).

[93] Roelcke, C. *et al.* Ultrafast atomic-scale scanning tunnelling spectroscopy of a single vacancy in a monolayer crystal. *Nature Photonics* **18**, 595–602 (2024).

[94] Rai, V. N. *et al.* Influence of atomic-scale defects on coherent phonon excitations by THz near fields in an STM. *Science Advances* **11**, eadz6549 (2025).

[95] Sheng, S. *et al.* Terahertz spectroscopy of collective charge density wave dynamics at the atomic scale. *Nature Physics* **20**, 1603–1608 (2024).

[96] López, L. E. P. *et al.* Atomic-scale ultrafast dynamics of local charge order in a THz-induced metastable state of 1T-TaS_2 (2025). Available at http://arxiv.org/abs/2505.20541. Issue: arXiv:2505.20541 arXiv:2505.20541 [cond-mat].

[97] Peller, D. *et al.* Sub-cycle atomic-scale forces coherently control a single-molecule switch. *Nature* **585**, 58–62 (2020).

[98] Wang, L., Xia, Y. & Ho, W. Atomic-scale quantum sensing based on the ultrafast coherence of an H_2 molecule in an STM cavity. *Science* **376**, 401–405 (2022).

[99] Wang, L., Bai, D., Xia, Y. & Ho, W. Electrical Manipulation of Quantum Coherence in a Two-Level Molecular System. *Physical Review Letters* **130**, 096201 (2023).

[100] Xia, Y., Wang, L. & Ho, W. Mechanisms Underlying a Quantum Superposition Microscope Based on THz-Driven Coherent Oscillations in a Two-Level Molecular Sensor. *Physical Review Letters* **132**, 076903 (2024).

[101] Jelic, V. *et al.* Terahertz field control of surface topology probed with subatomic resolution. *Nature Photonics* **19**, 1048–1055 (2025).

[102] Xiang, K. *et al.* A Cryostat Applicable to Long-Wavelength Light-Driven Scanning Probe Microscopy. *Micromachines* **14**, 378 (2023).

[103] Zhang, H. *et al.* The development of a low-temperature terahertz scanning tunneling microscope based on a cryogen-free scheme. *Review of Scientific Instruments* **95**, 093703 (2024).

[104] Azazoglu, H., Kapitza, P., Mittendorff, M., Möller, R. & Gruber, M. Variable-temperature lightwave-driven scanning tunneling microscope with a compact, turn-key terahertz source. *Review of Scientific Instruments* **95**, 023703 (2024).

[105] Azazoglu, H., Möller, R. & Gruber, M. Thermal expansion in photo-assisted tunneling: Visible light *versus* free-space terahertz pulses. *Surface Science* **743**, 122465 (2024).

[106] Tachizaki, T., Kanemitsu, Y. & Hirori, H. Time resolution of terahertz scanning tunneling microscopy measurements inside a superconducting magnet using a hollow waveguide. *Review of Scientific Instruments* **96**, 043004 (2025).

[107] Ma, B. & Krüger, M. Robust strong-field theory model for ultrafast electron transport through metal-insulator-metal tunneling nanojunctions (2025). Available at http://arxiv.org/abs/2503.14531. Issue: arXiv:2503.14531 arXiv:2503.14531 [cond-mat].

[108] Ma, B., Babaze, A., Krüger, M., Aizpurua, J. & Borisov, A. G. Ultrafast optically induced tunneling in narrow metallic gaps from the time dependent density functional perspective (2025). Available at http://arxiv.org/abs/2509.14802. ArXiv:2509.14802 [physics].

[109] Kwok, Y., Chen, G. & Mukamel, S. STM Imaging of Electron Migration in Real Space and Time: A Simulation Study. *Nano Letters* **19**, 7006–7012 (2019).

[110] Shi, T., Cirac, J. I. & Demler, E. Ultrafast molecular dynamics in terahertz-STM experiments: Theoretical analysis using the Anderson-Holstein model. *Physical Review Research* **2**, 033379 (2020).

[111] Wang, R., Bi, F., Lu, W., Zheng, X. & Yam, C. Tracking Electron Dynamics of Single Molecules in Scanning Tunneling Microscopy Junctions with Laser Pulses. *The Journal of Physical Chemistry Letters* **12**, 6398–6404 (2021).

[112] Frankerl, M. & Donarini, A. Spin-orbit interaction induces charge beatings in a lightwave-STM – single molecule junction. *Physical Review B* **103**, 085420 (2021).

[113] Svaneborg, J. K., Lorentzen, A. B., Gao, F., Jauho, A.-P. & Brandbyge, M. Manipulation of magnetization and spin transport in hydrogenated graphene with THz pulses. *Frontiers in Physics* **11**, 1237383 (2023).

[114] Ammerman, S. E., Wei, Y., Everett, N., Jelic, V. & Cocker, T. L. Algorithm for subcycle terahertz scanning tunneling spectroscopy. *Physical Review B* **105**, 115427 (2022).

[115] Hirori, H., Doi, A., Blanchard, F. & Tanaka, K. Single-cycle terahertz pulses with amplitudes exceeding 1 MV/cm generated by optical rectification in $LiNbO_3$. *Applied Physics Letters* **98**, 091106 (2011).

[116] Kampfrath, T., Tanaka, K. & Nelson, K. A. Resonant and nonresonant control over matter and light by intense terahertz transients. *Nature Photonics* **7**, 680–690 (2013).

[117] Hebling, J., Stepanov, A., Almási, G., Bartal, B. & Kuhl, J. Tunable THz pulse generation by optical rectification of ultrashort laser pulses with tilted pulse fronts. *Applied Physics B* **78**, 593–599 (2004).

[118] Hoffmann, M. C., Yeh, K.-L., Hebling, J. & Nelson, K. A. Efficient terahertz generation by optical rectification at 1035 nm. *Optics Express* **15**, 11706–11713 (2007).

[119] Ammerman, S. E. *Ultrafast terahertz Microscopy of atomically precise graphene nanoribbons*. Ph.D. thesis, MIchigan State University (2023).

[120] Wu, Q. & Zhang, X. Free-space electro-optic sampling of terahertz beams. *Applied Physics Letters* **67**, 3523–3525 (1995).

[121] Jepsen, P. U. *et al.* Detection of THz pulses by phase retardation in lithium tantalate. *Physical Review E* **53**, R3052–R3054 (1996).

[122] Bryant, P. J., Kim, H. S., Zheng, Y. C. & Yang, R. Technique for shaping scanning tunneling microscope tips. *Review of Scientific Instruments* **58**, 1115 (1987).

[123] Oliva, A. I., Romero G., A., Peña, J. L., Anguiano, E. & Aguilar, M. Electrochemical preparation of tungsten tips for a scanning tunneling microscope. *Review of Scientific Instruments* **67**, 1917–1921 (1996).

[124] Ju, B.-F., Chen, Y.-L. & Ge, Y. The art of electrochemical etching for preparing tungsten

probes with controllable tip profile and characteristic parameters. *Review of Scientific Instruments* **82**, 013707 (2011).

[125] Albrektsen, O., Salemink, H. W. M., Mo/rch, K. A. & Thölen, A. R. Reliable tip preparation for high-resolution scanning tunneling microscopy. *Journal of Vacuum Science & Technology B: Microelectronics and Nanometer Structures Processing, Measurement, and Phenomena* **12**, 3187–3190 (1994).

[126] Schmucker, S. W. *et al.* Field-directed sputter sharpening for tailored probe materials and atomic-scale lithography. *Nature Communications* **3**, 935 (2012).

[127] Li, P. & Ding, F. Origin of the herringbone reconstruction of Au(111) surface at the atomic scale. *Science Advances* **8**, eabq2900 (2022).

[128] Chen, W., Madhavan, V., Jamneala, T. & Crommie, M. F. Scanning Tunneling Microscopy Observation of an Electronic Superlattice at the Surface of Clean Gold. *Physical Review Letters* **80**, 1469–1472 (1998).

CHAPTER 3

CONTROL AND VALIDATION OF TERAHERTZ NEAR-FIELDS FOR ATOMIC-SCALE TIME-DOMAIN SPECTROSCOPY

Lightwave-driven THz-STM enables the exploration of ultrafast dynamics across a wide range of materials with Ångström-scale spatial resolution (10^{-10} m). It uses a strong-field, single-cycle terahertz pulse to drive an ultrafast current across a tunnel junction, thereby probing the LDOS. In contrast, the technique of terahertz s-SNOM measures the electric field of terahertz pulses in the time domain by collecting the photons scattered by the tip apex. Such measurements enable terahertz time-domain spectroscopy (THz-TDS), which provides access to the local, complex optical properties such as the dielectric function, but are limited to the few tens to hundreds of nanometers scale. The terahertz field confined to even smaller scales in a THz-STM junction may also be spectrally modified by the local electromagnetic response of the sample, yet a method to capture this effect was lacking until recently.

This chapter first introduces relevant background on related THz-TDS and THz-STM measurements and emphasizes the importance of establishing a technique that can sample the terahertz near-field in tunnel conditions. Following that, the experimental setup is introduced, which includes the cross-correlation scheme (THz-CC). Next, the optimization of atomic-scale THz-TDS parameters is demonstrated using data-driven quantitative and qualitative validation techniques to ensure accurate sampling of the terahertz electric near-field. The quantitative validation procedure incorporates a deconvolution algorithm for THz-STS [1] and is demonstrated by contrasting an accurately sampled waveform with one that contains artifacts, illustrating that careful parameter selection is essential to avoid such distortions. Building on this, the successfully validated waveform is used to simulate the artifacts that appear in a distorted THz-CC measurement. The discussion then turns to using static bias voltages and free-space waveform tailoring as additional parameters to ensure accurate sampling of the terahertz near-field waveform. Taken together, the combination of experiments on Au(111) and data-driven simulations establishes a comprehensive understanding of the relevant parameter space of the THz-CC technique and verifies the conditions necessary for generating an isolated, unipolar terahertz-induced current pulse for accurate waveform sampling. With this validated framework in place, atomic-scale THz-TDS is demonstrated by combining reference waveform measurements on Au(111) with the study of a single gallium arsenide (GaAs) surface defect, which exhibits a strongly localized terahertz resonance.

The results presented in this chapter are primarily based on a submitted manuscript (Adams *et al.*) and additionally draw from Jelic, Adams *et al.* [2]. Together, these studies introduce a generally applicable and self-consistent approach for terahertz near-field waveform acquisition in a tunnel junction. This enables the first demonstration of near-field microscopy on the atomic scale and introduces a fundamentally new experimental capability to the THz-STM toolbox.

3.1 Terahertz time-domain spectroscopy (THz-TDS)

To demonstrate why atomic-scale THz-TDS is such an important measurement, far-field THz-TDS with conventional measurement procedures is considered first. Terahertz pulses produced by optical rectification of ultrafast near-IR pulses or by photoconductive switching are intrinsically phase stable, meaning that the oscillating electric field waveform of the pulse is consistent shot-to-shot, unlike the near-infrared output of a typical ultrafast laser. As a result, it is possible to measure the electric field of a terahertz pulse, $E(t)$, which provides more information than the simple intensity of the pulse. In the context of THz-TDS, access to the spectral amplitude and phase of the electric field allows one to calculate the complex dielectric function and related optical functions, such as the complex conductivity and complex index of refraction [3].

These are fundamental material properties describing the interaction of electromagnetic radiation with matter. In Maxwell's equations in the presence of matter, the material response enters through the electric displacement $\vec{D} = \epsilon(\omega)\vec{E}$, where $\epsilon(\omega)$ is the complex dielectric function. This quantity describes how charges polarize in response to an applied field at frequency ω. It may be directly converted into the complex refractive index, $\tilde{n}(\omega) = n(\omega) + i\alpha(\omega)$, which is composed of frequency-dependent real and imaginary parts with the absorption coefficient, $\alpha(\omega)$ [4]. The complex dielectric function directly relates the propagation of electromagnetic waves in a medium (phase velocity, attenuation, reflection and transmission) to intrinsic material properties such as carrier motion, phonon resonances, and other collective excitations. In general, the study of optical constants in the terahertz regime provides direct access to low-energy excitations involving charge, lattice, and spin degrees of freedom.

In a typical free-space THz-TDS experimental setup, a near-IR pulse train is split into two paths, where one of the paths contains a delay stage. In the first path, terahertz pulses are generated, for example using optical rectification, as described in Chapter 2.5. The terahertz pulses then propagate through or are reflected from a sample. The electric field of the pulses is then measured with, for example, electro-optic sampling (EOS) or photoconductive sampling. Within these measurement schemes, the near-IR pulses from the second beam path are scanned across the terahertz pulse in time using the delay stage to map out the temporal shape of the terahertz waveform. Typically, the electric field waveform acquired after transmission through the sample is compared to a reference waveform recorded with the sample removed from the beam path to extract spectroscopic information about the sample. This comparison is usually performed in the frequency domain by a Fourier transform of the time-domain waveform traces, $\mathcal{F}[E(t)] = E(\omega)$.

The electric fields of the sample and the reference can be described in terms of the starting electric field after generation, $E_0(\omega)$, and a transfer function for propagation to the detector, $H(\omega)$. The sample and reference electric fields can be expressed as

$$E_{\text{ref}}(\omega) = E_0(\omega)H_{\text{ref}}(\omega); \quad E_{\text{sample}}(\omega) = E_0(\omega)H_{\text{sample}}(\omega). \tag{3.1}$$

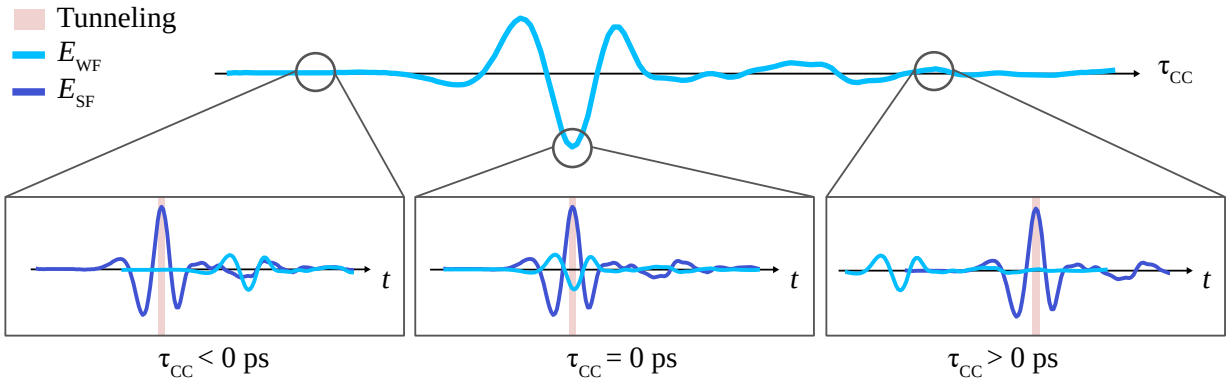

Figure 3.1 Time ordering of strong-field and weak-field pulses in a THz-CC measurement. Top: THz-CC waveform measurement (read out through ΔQ_{THz}) as a function of the delay between weak- and strong-field pulses, τ_{CC}. Bottom: Corresponding terahertz electric fields in the junction. The strong-field pulse (dark blue curve) sets the tunneling window (pink shading) at its main peak, thereby sampling the weak-field pulse (light blue curve). The weak-field pulse is scaled up relative to the strong-field pulse for visibility. For negative delay times, the strong-field pulse arrives before the weak-field pulse (left); at $\tau_{\mathrm{CC}} = 0$ ps, the main peaks of the pulses overlap (center); and for positive τ_{CC} delays, the strong-field pulse follows after the weak-field pulse (right).

By taking the ratio between them, $E_0(\omega)$ can be eliminated from the equation. The referenced sample transfer function can be written as a complex number with amplitude A and phase ϕ as

$$H_{\mathrm{sample/ref}}(\omega) = \frac{H_{\mathrm{sample}}(\omega)}{H_{\mathrm{ref}}(\omega)} = \frac{A_{\mathrm{sample}}(\omega)\exp(i\phi_{\mathrm{sample}}(\omega))}{A_{\mathrm{ref}}(\omega)\exp(i\phi_{\mathrm{ref}}(\omega))} \tag{3.2}$$

$$= \frac{A_{\mathrm{sample}}(\omega)}{A_{\mathrm{ref}}(\omega)} e^{i(\phi_{\mathrm{sample}}(\omega)-\phi_{\mathrm{ref}}(\omega))} = |H_{\mathrm{sample/ref}}(\omega)|e^{i\Delta\phi(\omega)}. \tag{3.3}$$

In free-space measurements, there are several models that can be used to extract the complex dielectric function depending on the experimental configuration [5]. The relation between the transfer function and the index of refraction, $n(\omega)$, and absorption coefficient, $\alpha(\omega)$ can be derived directly from the Fresnel coefficients and is, in the simple case of single-pass transmission through a sample with thickness d, for example, given by

$$H_{\mathrm{sample/ref}}(\omega) = |H_{\mathrm{sample/ref}}(\omega)|e^{i\Delta\phi(\omega)} = \frac{4n}{(n+1)^2} e^{\frac{-\alpha d}{2}} e^{i\frac{(n-1)d}{c}\omega} \quad , \tag{3.4}$$

which can be solved for the optical constant as

$$n(\omega) = 1 + \frac{c\Delta\phi}{d\omega}; \quad \alpha(\omega) = -\frac{2}{d}\ln\left(\frac{(n+1)^2}{4n}|H_{\mathrm{sample/ref}}(\omega)|\right) \quad , \tag{3.5}$$

where c is the speed of light in vacuum [6].

Generally, the spatial resolution of THz-TDS is limited by the focal spot size of the terahertz pulses ($\approx$ 1 nm). In the remainder of this chapter, terahertz cross-correlation (THz-CC) measurements are presented as a reliable and self-consistent approach for terahertz near-field waveform

acquisition directly within an atomic tunnel junction to enable THz-TDS with atomic-scale resolution, i.e., on length scales seven orders of magnitude smaller than far-field THz-TDS. This approach is generally applicable to electrically conductive surfaces. In the THz-CC geometry, in comparison to far-field waveform detection like EOS, the near-infrared sampling pulse is replaced by a sub-cycle, terahertz-induced tunneling event. The terahertz electric near-field is captured in the time domain via the tunnel current through a cross-correlation of a weak-field and a strong-field terahertz pulse with identical temporal profile (Fig. 3.1). Only the strong-field pulse can drive tunneling on its own. The complementary weak-field pulse is attenuated by two orders of magnitude in field strength relative to the strong-field pulse. A key aspect of sampling the terahertz near-field waveform via the tunneling current is that the strong-field pulse is tuned such that it induces a tunnel current only at its peak field (pink tunneling window in Fig. 3.1). This produces an ultrashort, unipolar current pulse that acts as the sampling/gate pulse. Scanning the delay time, τ_{CC}, of the weak-field pulse modulates the measured current at the peak of the strong-field pulse, and the resulting changes in the tunnel current directly reconstruct the local terahertz near-field waveform. Correctly capturing the near-field waveform requires (a) that the strong-field pulse generates a sub-cycle, unipolar current pulse, (b) that the weak-field pulse modulates the current generated by the strong-field pulse in a linear region of the $I - V$ curve, and (c) that the weak-field pulse does not induce a tunnel current on its own when not overlapped with the strong-field pulse.

The electromagnetic response of the atomically defined location on the sample is imprinted on both the strong- and weak-field waveforms. This implies that the spatial resolution of THz-TDS (comparing the electric field in a specific location to a reference) via THz-CC is only limited by the inherent resolution of the THz-STM system. Notably, since this measurement maps out the weak-field waveform using the peak of the strong-field pulse, the weak-field pulse always arrives before any excitation that might be induced by the strong-field pulse and therefore remains unaffected. Since the THz-CC waveform detection mechanism fundamentally differs from conventional THz-TDS approaches based on the free-space collection of transmitted, reflected, or scattered light, the parameter space and data analysis for this new method deviate from such measurements.

3.2 THz-CC measurements in the context of THz-STM and THz-TDS

One of the primary motivations for THz-STM experiments is to study ultrafast nonequilibrium sample dynamics on the atomic scale. A pump–probe scheme is typically employed, where an ultrafast optical [7–10] or terahertz pulse [11–20] acts as a pump and a subsequent time-delayed terahertz pulse acts as the probe. The field of the terahertz probe pulse coherently controls tunneling across the junction, enabling atomic-scale electronic readout [2, 10, 11, 14–18, 20–25] of the ultrafast sample dynamics as a function of pump-probe delay. Each strong-field terahertz voltage pulse produces an ultrafast current pulse that carries information about the junction's $I(V)$

characteristic, which in turn is related to the sample's LDOS through dI/dV ($\propto$ LDOS) [26, 27]. As discussed earlier, due to the limitations of experimental electronics, only the rectified component, Q_{THz}, of the terahertz-induced current pulse is measured. Nevertheless, THz-STS may be performed to extract the differential conductance probed by the terahertz field by recording the rectified charge as a function of peak field strength, $Q_{\mathrm{THz}}(E_{\mathrm{SF,pk}})$, and then either modeling the response [14, 21, 28] or applying an appropriate deconvolution algorithm [2, 29], as will be explained in more detail in this chapter. For all these approaches to THz-STM analysis, knowledge of the precise temporal profile of the terahertz near-field in the junction is critical. However, measuring it has been a significant challenge, since it is defined by the input field, the tip-coupling transfer function [30–33], and the local dielectric response of the sample [34].

In this chapter, atomic-scale THz-TDS is introduced as a new measurement modality for THz-STM, enabling direct time-domain sampling of the terahertz electric near-field amplitude and phase within the tunnel junction [2, 35]. Access to the full terahertz waveform *in situ* not only supports the analysis of THz-STS and pump–probe THz-STM measurements, but also provides a route to extract the local complex dielectric response of the sample in the immediate vicinity of individual atoms or defects. Before presenting the THz-CC measurement and data analysis in detail, it is useful to clarify the distinction between THz-CC and THz-STM pump-probe experiments is established. In contrast to static $I(V)$ measurements obtained using the bias voltage between tip and sample, the terahertz-driven currents in the STM junction are on ultrafast time scales comparable to those of many dynamic processes in condensed matter systems. This temporal correspondence forms the basis for pump–probe THz-STM measurements. Such time-resolved experiments, which involve scanning two pulses with respect to one another, can be divided into two categories according to the frequency of the pump pulse.

(i) Optical-pump / terahertz-probe experiments. Since the energy is much larger for visible or near-infrared photons than for terahertz photons, an optical pump pulse can excite the system into a nonequilibrium state through direct electronic transitions. In a pump-probe THz-STM experiment, a time-delayed terahertz probe can read out the subsequent dynamics via pump-induced changes to the terahertz-driven tunnel current. A broad challenge in such pump-probe measurements is that near temporal overlap the pump-induced dynamics and the terahertz electric field convolve, producing a mixed signal that complicates interpretation [29].

In contrast to the convolution that occurs when sample dynamics are on the same time scale as the terahertz oscillation cycle, photoemission sampling (PES) leverages optical excitation and decay of tip electrons on sub-terahertz-cycle time scales to measure the terahertz waveform when the tip is retracted from the sample [8, 23, 24, 28, 30, 32, 33, 36]. In PES, an intense optical pulse illuminates a tip under high bias conditions, leading to photo-assisted field emission (see Chapter 2.4.3). The terahertz field, meanwhile, adds to the static bias, allowing the terahertz waveform to be mapped

through the modulated photoemission current versus pulse delay [37, 38] provided that the optical excitation and decay is significantly shorter than half an oscillation cycle of the terahertz pulse. PES has provided insight into the nature of terahertz coupling to metal tips [30, 36], and has even been used as a reference for THz-STS [28]. However, PES is not well suited to *in situ* measurements of the waveform in tunneling conditions or atomic-scale THz-TDS because: (a) retracting the tip from the sample removes the sample's local dielectric response from the most relevant region of the tip's near-field; (b) the optical pump pulse can directly excite the sample; (c) the optical fluence needed for PES far exceeds the fluence range of interest for most samples; and (d) the optical power needed for PES exceeds the thermal load under which atomic resolution is stable. *In situ* THz-CC measurements of the waveform in the tunnel junction therefore provide a valuable complement to optical-pump / terahertz-probe experiments of ultrafast sample dynamics that is not available by other means.

(ii) Terahertz-pump / terahertz-probe experiments. Measurements of this type most commonly use terahertz pulses with identical temporal profile. When the amplitudes of the two pulses are equal (or nearly equal), the measurement is often called an autocorrelation (THz-AC) [7, 11, 13, 16–21, 28, 39–43]. The peak field strength may be tuned to produce tunneling only when the pulses constructively interfere to estimate the current pulse width [7, 11, 14, 21, 28, 39–41, 43, 44], or each pulse may be tuned to produce tunneling on its own for a pump-probe experiment [11, 13, 14, 16–20]. In the pump-probe configuration, near temporal overlap, the measured signal in a THz-AC experiment (Q_{THz} as a function of pulse delay) contains contributions from both coherent interference of the terahertz fields and, potentially, a dynamic material response impulsively launched by the leading terahertz pulse. Such an excitation may be triggered by tunneling and result in, for example, modulation of the junction gap width [11, 13, 14] or a Coulomb blockade [15]. Meanwhile, each terahertz pulse also interacts with the linear polarizability of the junction, and the electric near-field may feature complex trailing oscillations as a result if the sample hosts dipole-active terahertz resonances in the tip's near-field [2, 16–18, 20, 25]. Traditionally, in ultrafast science, the latter response would be considered linear near-field interference rather than nonequilibrium sample dynamics. Great care must be taken to disentangle these two contributions. This is made more challenging by the nonlinear rectification process, which depends sensitively on the local differential conductance ($\mathrm{d}I/\mathrm{d}V$). Specifically, a given terahertz pulse may drive a temporally structured, bipolar current pulse if multiple maxima and/or minima beyond the main peak induce tunneling, and this will generate a similarly complex autocorrelation trace [28]. Previously, sample dynamics have been discriminated from such effects by focusing on the region away from temporal overlap [11, 13, 14, 16–20] and, for example, independently tuning the strengths of the two pulses [14]. The comprehensive view of a tunnel junction revealed by combining THz-CC with THz-STS introduces a new possibility for data analysis that is unambiguous and generalizable. Since

the self-consistent validation procedure for THz-CC waveforms yields the differential conductance, multi-pulse experiments can be trivially simulated for any field strength based on the terahertz waveform measured *in situ*, thereby identifying all features unrelated to sample dynamics.

In addition to probing nonequilibrium sample dynamics, THz-AC measurements have also been used for atomic-scale spectroscopy [16–18, 20]. This type of spectroscopy corresponds to homodyne sampling, where the Fourier transform of the THz-AC interferrogram yields the amplitude but not phase of the local field, in analogy with Fourier transform infrared spectroscopy. In contrast, THz-TDS is a heterodyne measurement based on direct linear detection of the terahertz field. When the temporal evolution of the electric field is recorded, both the amplitude and phase can be retrieved, which provides direct access to the sample's complex dielectric response at terahertz frequencies. The complex dielectric function reveals which resonant terahertz excitations exist in the system. In far-field THz-TDS, selection rules apply, and the measurement is typically only sensitive to infrared-active modes at the Brillouin zone center. However, the strongly confined electric fields in a picocavity [45, 46], such as an STM junction, can relax symmetry constraints in ways that are still being understood for THz-TDS. Terahertz s-SNOM [34, 47, 48] and the introduction of near-field optical tunneling emission microscopy [49] promise complementary views of terahertz resonances at extreme length scales.

In the THz-CC approach to atomic-scale THz-TDS introduced in this chapter, the terahertz near-field is sampled directly within a THz-STM junction under tunneling conditions, providing sensitivity to minute variations in the local dielectric environment at terahertz frequencies [2, 25, 35], for example near atomic-scale features such as lattice defects and domain boundaries.

3.3 Experimental setup and parameter space

3.3.1 Setup and calibration measurements

To begin, the experimental setup is introduced and the key parameters required to perform an accurate THz-CC waveform measurement for atomic-scale THz-TDS are highlighted. After generation via tilted-pulse-front optical rectification, the terahertz pulse enters the optical setup shown in the simplified schematic in Fig. 3.2. The setup includes parts of the "pulse train shaping" unit and the "THz-CC" unit of the full optical setup in Fig. 2.12. The first relevant waveform shaping element is the flip mirror that inverts the polarity of the electric field. After that it passes through a first pair of WGPs that can be used to attenuate the full beam. Notably, Fig. 3.2 depicts a cosine-like pulse with an optimized peak-to-trough ratio. In THz-STM, and especially for THz-CC, it is advantageous to have a cosine-like waveform in order to induce a unipolar current pulse. There are several methods that can be used to control the pulse's carrier envelope phase (CEP) such as Gouy-phase-shift-based waveform shaping (see Fig. 2.13(d)), metamaterials [51], broadband silicon waveplates [52] or total internal reflection in a polymer prism [32]. Later in this chapter, the

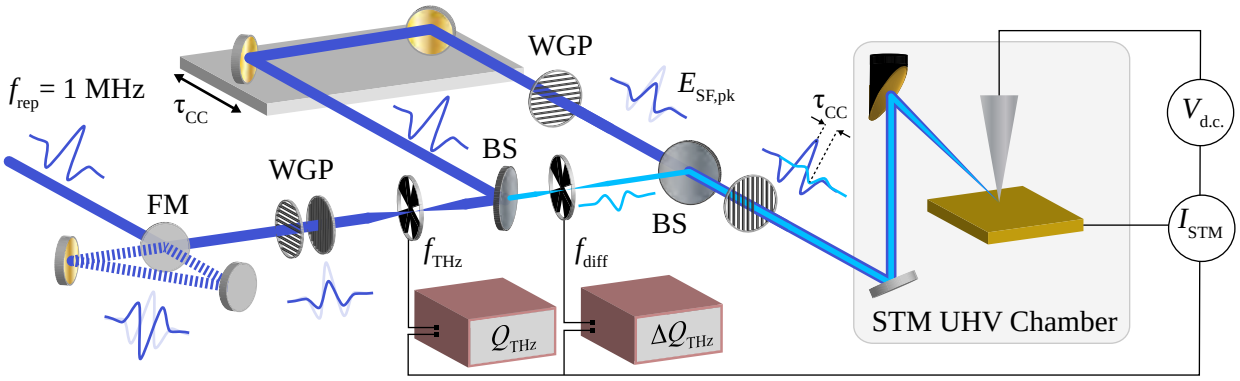

Figure 3.2 Schematic of the THz-CC setup used for near-field waveform acquisition. The optical setup includes waveform tailoring using a flip mirror (FM) to invert the field polarity and WGPs for attenuation. A chromium-coated silicon beam splitter (BS) splits the pulse train into strong-field (dark blue) and weak-field (light blue) pulses [50], with a delay stage in the strong-field beamline to adjust the cross-correlation delay, τ_{CC}. Two lock-in amplifiers (red boxes) demodulate I_{STM} at chopper frequencies of f_{THz} and f_{CC}, yielding Q_{THz} and ΔQ_{THz}, respectively.

effect of free-space pulse shaping via the setup in Fig. 2.13(d) is demonstrated. However, coupling the free-space shaped terahertz pulses into the tip can significantly change the CEP depending on the tip geometry [22, 52] and the incident pulse's spectrum [30]. Repeated measurements on different samples and with multiple tips showed, that simply maximizing the terahertz-pulse-induced tunnel current during pulse alignment reliably ensures a cosine-like waveform in the junction without requiring additional CEP modifications. Hence, the schematic pulses drawn along the beamline represent the waveform shape expected in the tunnel junction for a sample with a broadband spectral response like Au(111).

After the pulse shaping section, a chromium-coated silicon beam splitter splits each pulse into a strong-field pulse and a weak-field pulse (field ratio: 85%:15%). The weak-field pulses pass through a focus, where they are modulated by an optical chopper. This is used as a reference to detect the tunnel current changes, ΔQ_{THz}, caused by the weak-field pulse with a second lock-in amplifier, in addition to the one detecting the full terahertz beam, Q_{THz} (depicted with the chopper wheel before the beamsplitter in Fig. 3.2 for simplicity, instead of its actual location before the terahertz generation, see Fig. 2.12). The focus in the weak-field path leads to opposite polarities for the weak-field and strong-field pulses. The strong-field-pulse beampath contains a delay stage and a pair of WGPs to control its field strength (whereas the strength of the weak-field pulse is unaffected). The two pulses are then recombined on a second chromium-coated silicon beam splitter, resulting in an overall weak-to-strong field ratio of $\approx 3\%$. The pulse train is then coupled into the scanhead and focused onto the STM tip with a parabolic mirror.

In addition to modifying the spectral phase of the pulse, the tip also enhances the electric field by 5–6 orders of magnitude [34]. On a sample like Au(111), the conversion factor between the

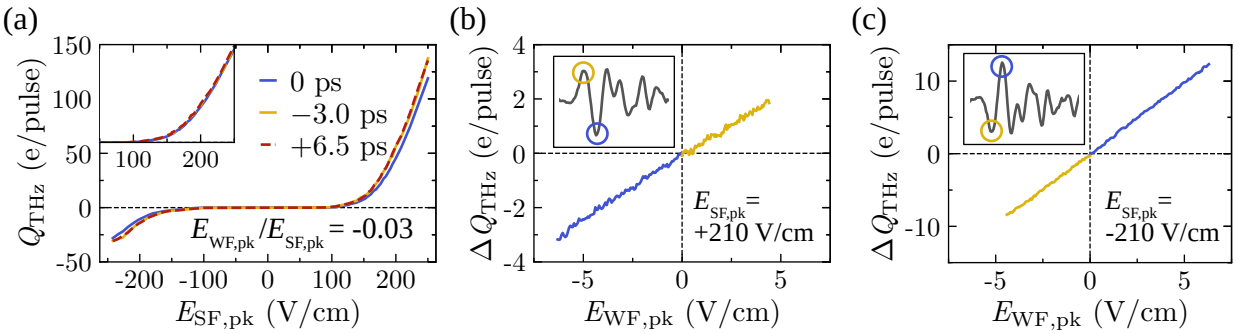

Figure 3.3 Weak-field pulse calibration. (a) THz-STS measurements to determine the relative weak- and strong-field amplitudes. The blue curve was acquired at temporal overlap between the two pulses. The red (yellow) curve was measured with the weak-field arriving before (after) the strong-field pulse, without time overlap. As shown in the inset, multiplying the field strength axis of the traces at negative and positive time-delay by 1.03 aligns all of the curves, implying $E_{\mathrm{WF,pk}}/E_{\mathrm{SF,pk}} = -0.03$. Measurement parameters: $I_{\mathrm{d.c.}} = 100\,\mathrm{pA}$, $V_{\mathrm{d.c.}} = 100\,\mathrm{mV}$ (these traces correspond to horizontal line cuts from the 2D map in Fig. 3.5(b)). (b) and (c) Linear trend of the modulated strong-field current when scaling sufficiently small weak-field pulse amplitudes. $\Delta Q_{\mathrm{WF,pk}}$ curves acquired at $\tau_{\mathrm{CC}} = 0$ fs (blue line) and $\tau_{\mathrm{CC}} = -530$ fs (yellow line) for a positive-dominant (b) and a negative-dominant (c) strong-field pulse polarity. The insets show the corresponding terahertz waveforms measured with THz-CC. The blue and yellow circles indicate the temporal locations of the corresponding measurements. The measurements were performed at constant height with $V_{\mathrm{d.c.}} = 0$ V and the tip-sample separation set by $V_0 = 10$ mV, $I_0 = 300$ pA.

terahertz-induced voltage in the junction and the voltage applied by the STM can be extracted using the method described in Chapter 2.5.3.3. This calibration was determined as $\alpha = 19\,(\mathrm{V/cm})/\mathrm{V}$ for a majority of the following measurements (see Fig. 2.21(c)), but since it is generally not required for accurate waveform reconstruction or validation, all measurements are presented in units of field strength (V/cm).

Conversely, to analyze and simulate the THz-CC measurements, it is important to quantify the ratio between the weak-field and strong-field pulse amplitudes in the junction. Since the weak-field pulse is not sufficient to drive a current on its own, the ratio is determined by comparing a THz-STS curve taken with only the strong-field pulse present ($|\tau_{\mathrm{CC}}| \gg 0$) to a THz-STS curve recorded when the strong-field and weak-field pulses are temporally overlapped ($\tau_{\mathrm{CC}} = 0\,\mathrm{ps}$). At temporal overlap, the peak of the weak-field pulse slightly reduces the strong-field-driven current because the polarity of the weak-field pulse is opposite to that of the strong-field pulse (Fig. 3.3(a)). By scaling the electric field axis until the curves overlap, a ratio of $E_{\mathrm{WF,pk}}/E_{\mathrm{SF,pk}} = -0.03$ is extracted for the maximum applied $E_{\mathrm{SF,pk}}$ in the experiments (which scales for different strong-field strengths because $E_{\mathrm{WF,pk}}$ is kept constant during THz-STS). Whether the weak-field pulse is sufficiently small compared to the strong-field pulse can be evaluated by modulating the strong-field pulse and placing the WGP in the weak-field beam. Figures 3.3(b) and (c) show that for small changes in $E_{\mathrm{WF,pk}}$, the

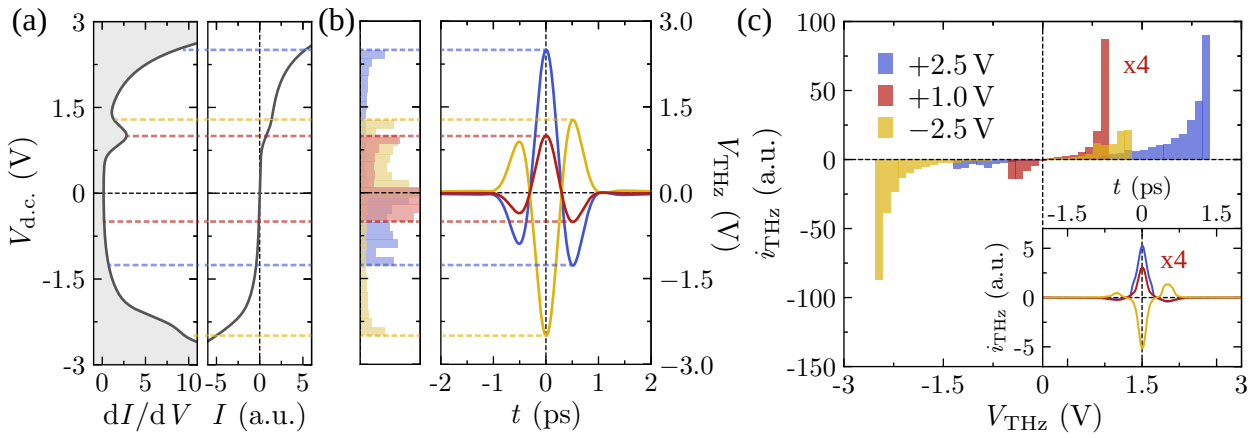

Figure 3.4 Principle of THz-induced current generation in a THz-STM junction. (a) Schematic representation of a generic (simulated) sample LDOS as a function of voltage in the STM tip location (left) and corresponding current versus voltage characteristic (right). (b) Example terahertz voltage pulses (right) at three different strengths (blue: $V_{\mathrm{SF,pk}}$ = +2.5 V, yellow: $V_{\mathrm{SF,pk}}$ = −2.5 V, red: $V_{\mathrm{SF,pk}}$ = +1.0 V). The distribution of the pulse across the voltage axis indicates the most sampled voltage ranges for each respective pulse (left). (c) Current induced by each of the terahertz pulses in (b) when applied to the $I-V$ curve in (a) as a function of voltage (main panel) and as a function of time (inset). The current in (c) is multiplied by 4 for $V_{\mathrm{d.c.}}$ = +1 V for clarity.

modulated strong-field unipolar current pulse depends linearly on the weak-field amplitude. This confirms that the weak-field voltage transient may be measured by scanning τ_{CC} and recording the change in the rectified charge ΔQ_{THz}, at the modulation frequency of the weak-field pulse train.

3.3.2 Terahertz-induced current in an STM junction

As noted in the introduction of this chapter, generating a sub-cycle unipolar current pulse with the strong-field pulse is essential for accurate waveform sampling with THz-CC. This subsection demonstrates how the key THz-CC measurement parameters (pulse polarity and field strengths) influence the THz-induced current sampling mechanism. The effects of the static bias voltage and free-space pulse shaping will be addressed in a later section.

Figure 3.4(a) shows an artificial dI/dV curve (left) and its corresponding $I-V$ curve (right). The main features in the dI/dV curve are band onsets at ±1.5 V and an in-gap state near 1 V. This $I-V$ curve is used to illustrate how cosine-like terahertz pulses of different amplitudes and/or polarities drive current in a THz-STM junction. Three example terahertz pulses are shown in Fig. 3.4(b) (right), with their voltage sampling densities displayed as histograms on the left (i.e., how much time the waveform spends at each voltage). The dashed lines in Fig. 3.4(a) indicate the voltage ranges of the dI/dV curve sampled by each pulse.

In contrast to conventional STM, where the current is measured at a fixed static voltage at each point of an $I-V$ measurement, a given terahertz pulse drives current across a range of positive and negative voltages (Fig. 3.4(c)) and does so dynamically over the waveform's temporal evolution

(Fig. 3.4(c) inset). The measured signal in THz-STM is the time-integrated current,

$$Q_{\mathrm{THz}} = \int_{-\infty}^{+\infty} I(V_{\mathrm{THz}}(t))dt, \tag{3.6}$$

because the instantaneous current is too fast to be measured directly. For the three waveforms shown in Fig. 3.4(a),(b): (i) The blue waveform primarily samples the positive band onset and therefore yields a mostly unipolar current response. (ii) The yellow waveform, with its opposite polarity, samples the negative band onset, but its positive segments also interact with the in-gap state, producing a significant positive current as well. (iii) When the pulse amplitude is reduced so that only the in-gap state is sampled (red waveform), a sharply peaked unipolar current pulse is produced, and the rectified charge originates largely from a narrow voltage region at the peak of the pulse.

These scenarios serve as examples of how the field strength and polarity must be tuned to obtain a sub-cycle, unipolar current pulse. For accurate waveform sampling via THz-CC, it is essential that the strong-field pulse generates such a sub-cycle, unipolar current pulse. Figure 3.1 illustrates the sampling process: the main peak of the strong-field pulse sets the tunneling window; the instantaneous weak-field within this window for a given τ_{CC} is captured via ΔQ_{THz}. It is noted that, unlike in THz-AC measurements, impulsive sample excitations launched by the strong-field pulse do not affect the measurement because tunneling readout occurs exclusively at the peak of the strong-field pulse, whereas the weak-field pulse cannot launch such excitations or read them out on its own. In a real experiment, the detailed interaction of the strong-field pulse with the LDOS must be carefully considered to satisfy the conditions for accurate sampling of the weak-field waveform for atomic-scale THz-TDS. The artifacts arising in the measurement when these conditions are not met will be discussed in the following sections.

3.3.3 Field-dependent waveform measurements

The discussion now moves from the simulated THz-STM junction in Fig. 3.4 to real experimental data recorded on Au(111). To build intuition, the influence of the terahertz field amplitude and polarity on the measured signal is first discussed qualitatively, before a quantitative procedure for setting these parameters to record accurate THz-TDS waveforms is introduced in the following section.

Fig. 3.5(a) shows the differential terahertz signal, ΔQ_{THz} as a function of τ_{CC} and $E_{\mathrm{SF,pk}}$ for both field polarities. The waveform shape clearly changes with $E_{\mathrm{SF,pk}}$ for negative field polarity ($E_{\mathrm{SF,pk}} < 0$). This behavior indicates that the strong-field pulse does not induce a sub-cycle unipolar current pulse over the full range of terahertz field strengths; instead, a situation similar to the yellow pulse in Fig. 3.4 occurs for some $E_{\mathrm{SF,pk}}$ values. This asymmetry between positive and negative polarities is further reflected in the THz-STS curve in Fig. 3.5(b), where the rectified charge is larger, and emerges for lower fields, for $E_{\mathrm{SF,pk}} > 0$ than for $E_{\mathrm{SF,pk}} < 0$. In this case, Q_{THz}

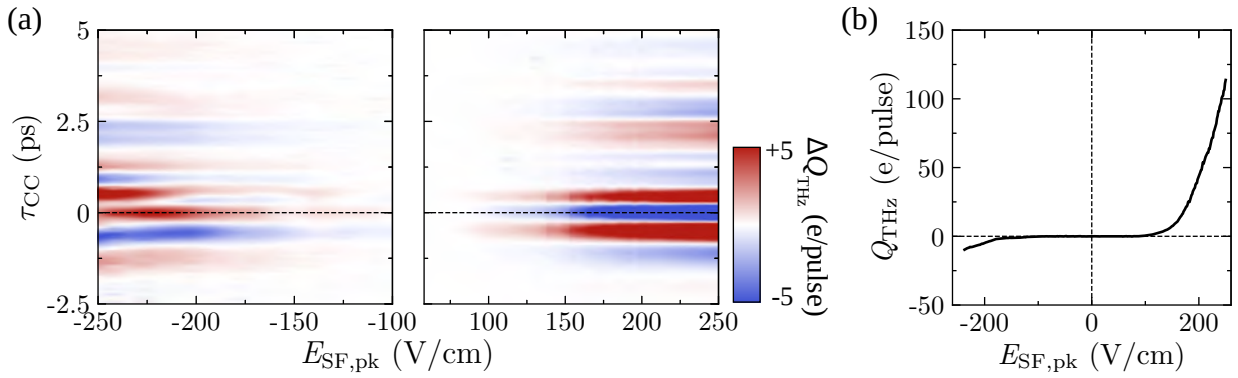

Figure 3.5 Measurements for atomic-scale THz-TDS. (a) Cross correlation waveform measurements as a function of field strength for both pulse polarities ($I_{d.c.}$ = 100 pA, $V_{d.c.}$ = 100 mV). (b) THz-STS curve recorded at $I_{d.c.}$ = 100 pA, $V_{d.c.}$ = 100 mV.

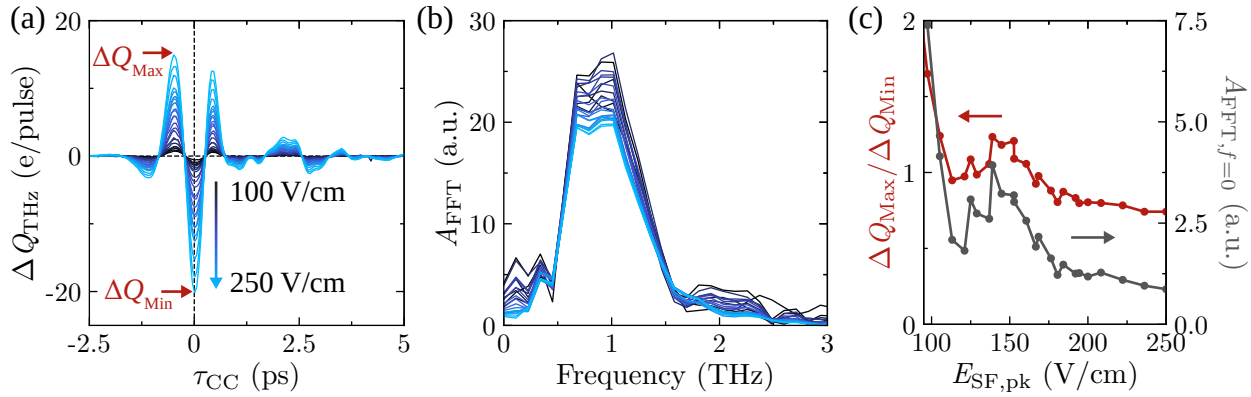

Figure 3.6 Qualitative analysis of THz-CC measurements. (a) Evolution of waveforms at positive polarity (vertical line cuts through Fig. 3.5(a)). (b) Amplitude of the fast Fourier transform of the waveforms in (a) (after normalization to their highest absolute value) using a Hamming window. (c) Red curve: ratio between the negative and positive peaks (red arrows in (a)) of the waveforms as a function of field strength. Grey curve: amplitude at f = 0 THz of the spectra in (b) as a function of field strength.

at both positive and negative polarity is produced by terahertz-driven field emission (from the tip for $E_{SF,pk} > 0$ and from the sample for $E_{SF,pk} < 0$), but the bias threshold is lower in the positive field direction because of the tip's small radius of curvature. Asymmetric THz-STM signals of this type are typical, since they can stem from different work functions for the tip and sample, asymmetric conduction and valence band onsets relative to the tip's Fermi level, local electronic states, or a variety of other experimental details. The result is a preferred polarity for accurate waveform detection. For some samples, a way to circumvent the constraint of a preferred terahertz polarity is to apply a static bias voltage, as will be discussed later.

Even for the THz-CC measurements performed at positive field strengths (Fig. 3.6(a)), which appear relatively uniform in the time-domain, differences become evident when comparing their

spectral amplitudes, especially at low frequencies (Fig. 3.6(b)). At high field strengths (light blue, $E_{\mathrm{SF,pk}} > 190$ V/cm), though, the shape of the waveform and spectral amplitude converge. This trend can be quantified by plotting the ratio between the minimum and maximum peaks (red curve in Fig. 3.6(c)) or the d.c. component of the FFT amplitude (grey curve in Fig. 3.6(c)). For an accurately measured electric field waveform, the field trace should integrate to zero, implying that the corresponding fast Fourier transform (FFT) amplitude should contain no d.c. component. Both curves in Fig. 3.6(c) approach a constant value above 190 V/cm, providing a qualitative verification that increasing the field strength further does not alter the measured waveform shape. This is consistent with the weak-field modulation acting in a linear response regime. However, to ensure the measured waveform is accurate, the strong-field-induced current pulse should also be confirmed to be sub-cycle and unipolar, as shown in the following sections.

3.4 Quantitative self-consistent near-field waveform validation

Whereas the change in the positive-to-negative peak ratio and the magnitude of the Fourier transform amplitude provide a qualitative indicator of waveform fidelity, a more rigorous and quantitative approach for waveform validation is now introduced.

Figure 3.7(a) outlines the validation procedure, where a single experimentally measured waveform together with a THz-STS measurement serve as inputs. Reference [29] shows how these inputs can be used in an algorithm to extract the underlying current-voltage characteristic of the sample. The first step in the algorithm involves fitting the measured THz-STS curve with a polynomial. To reliably apply this procedure to experimental data, a method has been developed to determine the appropriate level of complexity for the polynomial fit that prevents both over- and underfitting Next, using the extracted $I(V)$ curve, the THz-CC measurement can be simulated using the input waveform. This yields a simulated cross-correlation waveform, $\Delta Q_{\mathrm{sim}}(\tau_{\mathrm{CC}})$, as well as the time

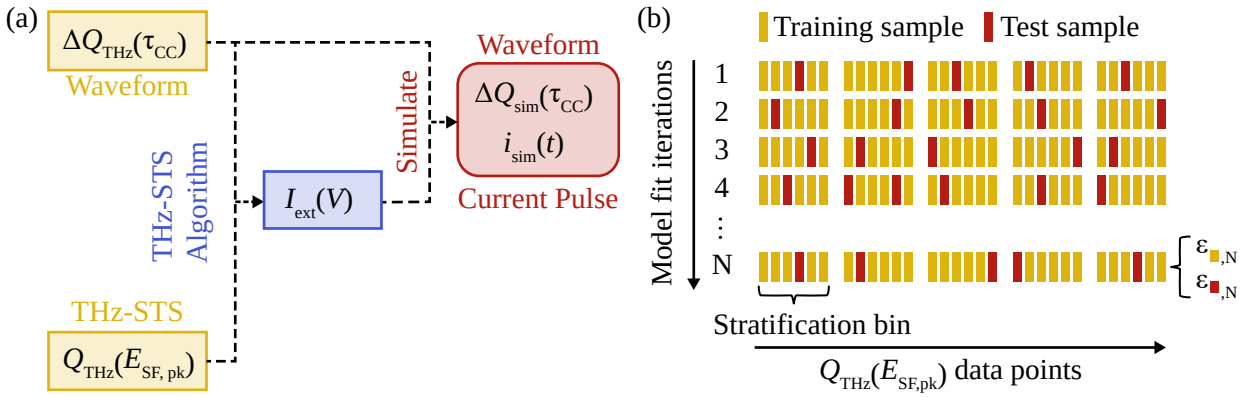

Figure 3.7 Quantitative self-consistent near-field waveform validation procedure. (a) Flow chart showing the self-consistent approach to waveform validation. (b) Schematic showing the principle of stratified shuffle-split cross validation sampling to prevent over- or underfitting, in which multiple copies of the dataset are randomly split into test and training data fractions.

evolution of the current in the STM junction, $i_{\mathrm{sim}}(t)$. Comparing the simulated and measured waveforms (together with an analysis of the simulated current pulse) enables us to assess whether the input waveform was accurately sampled, i.e., whether the pulse tailoring parameters were set correctly for a particular junction. This procedure can be repeated for the waveforms acquired at various field strengths in Fig. 3.5(a) to find the optimal field strength and polarity combination for reliable waveform measurements.

Notably, the THz-STM deconvolution algorithm originally established within Ammerman *et al*. [29] – which was refined within Jelic *et al*. [2], and is further advanced in the form presented here – relies on precise knowledge of the terahertz voltage waveform.

3.4.1 Determining model complexity for *I-V* extraction via shuffle-split cross validation

Each point of the THz-STS curve (see Fig. 3.5(b)) corresponds to the rectified charge, Q_{THz}, generated by a single terahertz voltage pulse with peak voltage $V_{\mathrm{SF,pk}}$. This quantity is related to the $I-V$ curve via Equation 3.6. Reference [29] introduces an algorithm that enables the extraction of $I(V)$ and $\mathrm{d}I/\mathrm{d}V$ directly from $Q_{\mathrm{THz}}(V_{\mathrm{SF,pk}})$ (or $I(E_{\mathrm{SF,pk}})$ and $\mathrm{d}I/\mathrm{d}E_{\mathrm{SF,pk}}$ directly from $Q_{\mathrm{THz}}(E_{\mathrm{SF,pk}})$) given the terahertz voltage waveform. Since $\mathrm{d}I/\mathrm{d}V$ is approximately proportional to the LDOS, this approach provides direct access to important sample properties. In the following, an updated version of this algorithm is used to extract the $I(V)$ characteristic and subsequently simulate both the time-dependent tunnel current in the junction and the THz-CC waveform measurement.

Following reference [29], the waveform is expressed as $V_{\mathrm{THz}} = V_{\mathrm{SF,pk}} V_0(t)$, where $V_0(t)$ is the normalized temporal waveform shape and $V_{\mathrm{SF,pk}}$ is its linear scaling factor. Alternatively, the waveform input for the algorithm can be in units of incident field strength, $E_{\mathrm{SF,pk}}$, if a voltage calibration has not been performed. To evaluate the integral in Equation 3.6, the $I(V)$ curve is approximated with a polynomial of order P, $I(V) = \sum_{p=1}^{P} A_p V^p$, where A_p is the coefficient for each polynomial order.

Substituting the polynomial approximation and the waveform expression into Equation 3.6 yields

$$Q_{\mathrm{THz}}(V_{pk}) = \int_{-\infty}^{+\infty} \sum_{p=1}^{P} A_p (V_{\mathrm{SF,pk}} V_0(t))^p \mathrm{d}t \tag{3.7}$$

$$= \sum_{p=1}^{P} A_p V_{\mathrm{SF,pk}}^p \int_{-\infty}^{+\infty} V_0(t)^p \mathrm{d}t \tag{3.8}$$

$$\equiv \sum_{p=1}^{P} A_p V_{\mathrm{SF,pk}}^p B_p \tag{3.9}$$

$$\equiv \sum_{p=1}^{P} C_p V_{\mathrm{SF,pk}}^p \tag{3.10}$$

where the integral expression, $B_p = \int_{-\infty}^{+\infty} V_0(t)^p \mathrm{d}t$, is determined solely by the normalized waveform shape. Therefore, if the waveform shape is known, the coefficients B_p can easily be calculated. This forms the basis of the waveform validation procedure in which a correctly measured waveform will yield an accurate extraction of $I(V)$, whereas a distorted waveform will not. Finally, the A_p coefficients are obtained by fitting Equation 3.10 to the experimental $Q_{\mathrm{THz}}(E_{\mathrm{SF,pk}})$ or $Q_{\mathrm{THz}}(V_{\mathrm{SF,pk}} = \alpha E_{\mathrm{SF,pk}})$ and then calculating $A_p = C_p/B_p$. It is important to note that the linear term of the $I(V)$ curve cannot be determined because $B_1 = \int_{-\infty}^{+\infty} V_0(t)dt = 0$; therefore, the lowest accessible polynomial order is $p = 2$.

The challenge in fitting the model to experimental data is that the mean squared error (MSE) ϵ between the model and the data generally decreases with increasing model complexity (in this case with increasing polynomial order P). A dataset with N points is best fit with a model with N parameters. However, such a model overfits the data and does not necessarily capture the underlying physical behavior of the system. Hence, it is important to have a metric that determines the polynomial complexity that neither under- nor overfits the STM junction response encoded in the THz-STS measurement.

To address this, a two-step fitting and validation procedure is employed. In step 1, a subset of the data (the training set) is used to determine the fit parameters. Then, in step 2, an independent test set is used to calculate the MSE, ϵ_{Test}, between the data points and the model obtained from the training set. There are multiple ways to split the data into training and test sets. Here, stratified shuffle-split cross validation sampling [53] is used, which is illustrated schematically in Fig. 3.7(b). The THz-STS data are ordered, which means that the x-axis (terahertz field or voltage) is continuously increasing. For stratified shuffle-splitting, the data are divided into a fixed number of stratification bins. Within each bin, the data are randomly split into training and test samples with a given ratio (e.g., 80% training, 20% test). This procedure ensures there are no large gaps along the x-axis of the training set. This is repeated to generate N independent shuffle-split sets to be used for training and testing the polynomial model. Each model fit iteration gives an MSE for the training set ($\epsilon_{\mathrm{Train}}$) and test set ($\epsilon_{\mathrm{Test}}$). Following this, the mean MSE over all iterations can be calculated as well as its standard deviation.

This procedure is applied to the THz-STS measurement shown in Fig. 3.5(b). The MSE for the training and test datasets, as well as the standard deviation of the test-set MSE is plotted as a function of the highest polynomial order in Fig. 3.8(a). As expected, the mean MSE of the training data decreases monotonically with increasing model complexity. In contrast, the mean MSE of the test data initially decreases for low polynomial orders (underfit), reaches a minimum at $P = 24$, and then increases again for higher orders. This increase reflects overfitting, where the model begins to capture noise and outliers in the training data that deviate from the test data, leading to a negative impact on the test MSE and its standard deviation. The polynomial order $P = 24$ represents the

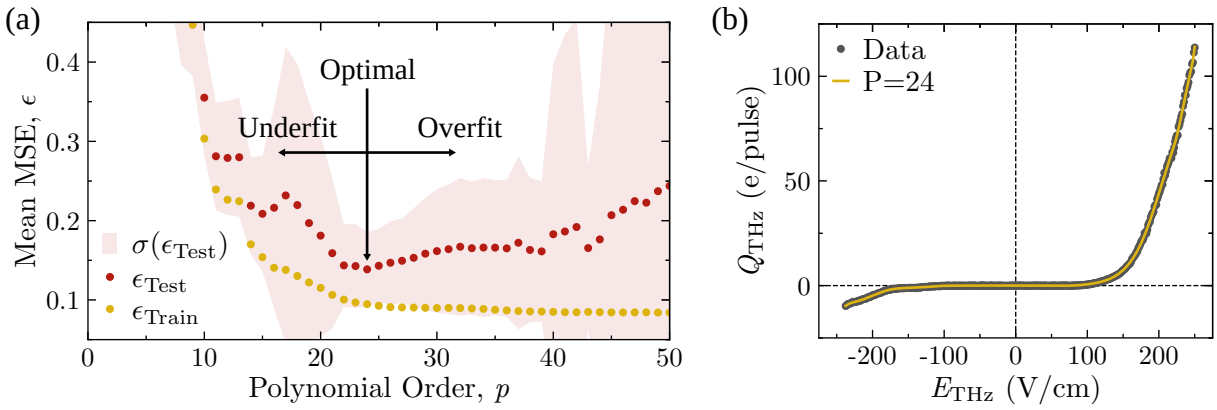

Figure 3.8 Waveform validation using shuffle-split cross validation. (a) Mean squared error (MSE, ϵ) of the training and test sets (averaged over 100 shuffle splits, 20:80 test versus training data ratio, 12 stratification bins for 392 data points) for the polynomial fit of the THz-STS curve in Fig. 3.5(b), plotted as a function of polynomial order (model complexity). The light red shaded region indicates the standard deviation of the MSE for the test data, $\sigma(\epsilon_{\text{Test}})$. The minimum mean MSE for the test data (the optimal fit complexity) is $P = 24$, coinciding with a low $\sigma(\epsilon_{\text{Test}})$. (b) THz-STS curve from Fig. 3.5(b) with the optimal complexity fit model of highest polynomial order $P = 24$.

optimal complexity, where the fitted model best captures the underlying behavior of the dataset without overfitting. The polynomial coefficients are averaged over all iterations (fitted data shown in Fig. 3.8(b)) to move forward with the waveform validation process.

3.4.2 Simulating terahertz-induced current and THz-CC waveform measurement

Following the procedure described in the previous section, an experimental THz-CC waveform can be combined with the coefficients obtained from the polynomial fit to the THz-STS curve to extract the corresponding I–V and $\mathrm{d}I/\mathrm{d}V$ curves. Yet, only an accurate waveform will yield accurate results. Section 3.3.3 provides some intuition regarding which terahertz-pulse field strength and polarity may induce a sub-cycle unipolar current pulse to faithfully sample the weak-field terahertz voltage waveform in the junction (see Fig. 3.6). Nonetheless, the procedure for extracting the $I-V$ and $\mathrm{d}I/\mathrm{d}V$ curves described in the previous section can be tested using the THz-CC measurements acquired under a range of parameters in Fig. 3.5(a).

Figure 3.9(a) shows the extracted $I-V$ and $\mathrm{d}I/\mathrm{d}V$ curves for a measurement at $E_{\text{SF,pk}} = +194.5\,\text{V/cm}$, while Fig. 3.10(a) shows the corresponding result for $E_{\text{SF,pk}} = -210.5\,\text{V/cm}$. The THz-CC waveforms used as inputs are shown in blue in Fig. 3.9(b) and Fig. 3.10(b). Although the same THz-STS polynomial fit is used in both cases, the extracted $I-V$ and $\mathrm{d}I/\mathrm{d}V$ curves differ significantly due to differences in the THz-CC waveforms.

A self-consistent waveform validation procedure, as employed in Refs. [2, 25], is detailed here. The concept is as follows: (i) An accurate THz-CC waveform used as input for the THz-STS

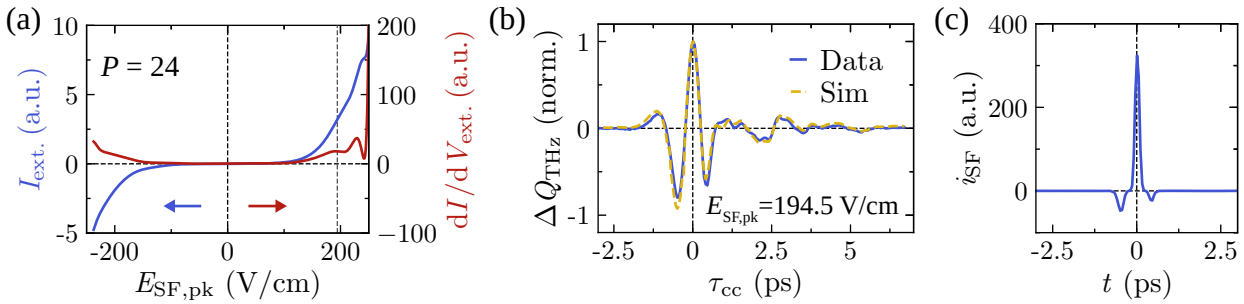

Figure 3.9 Successful waveform validation. (a) Extracted $I(V)$ using the THz-CC measurement shown in (b), blue curve. (b) Measured THz-CC waveform (blue curve) and the corresponding simulated waveform (yellow curve) obtained using the extracted $I(V)$. (c) Simulated current pulse generated in the STM junction by the strong-field pulse.

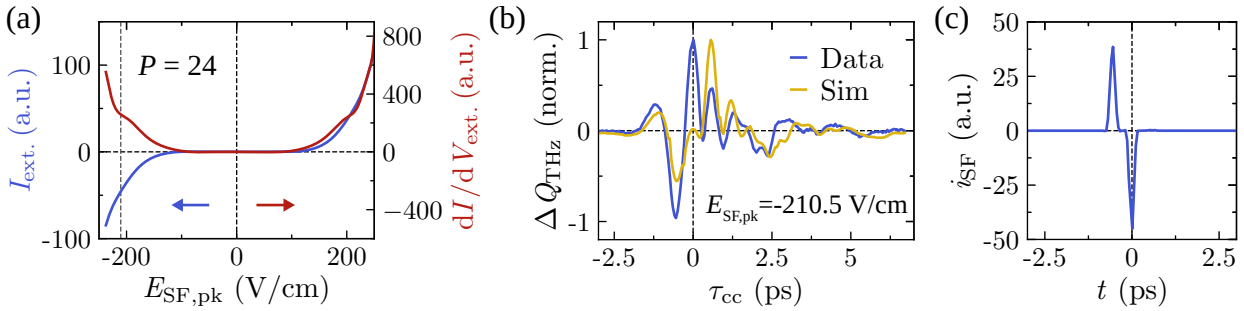

Figure 3.10 Unsuccessful waveform validation. (a) Extracted $I(V)$ using the THz-CC measurement shown in (b), blue curve. (b) Comparison between the measured THz-CC waveform (blue curve) and the simulated waveform (yellow curve) showing a clear mismatch. This mismatch indicates that the measured THz-CC waveform does not represent the genuine terahertz waveform in the tunnel junction. (c) Simulated current pulse generated in the STM junction.

inversion algorithm yields accurate $I-V$ and $\mathrm{d}I/\mathrm{d}V$ curves. (ii) The simulated current pulse based on these extracted curves and the measured THz-CC waveform (for the corresponding strong-field strength) should be sub-cycle and unipolar if the voltage pulse shape is accurate. (iii) The terahertz waveform predicted by a simulated THz-CC measurement using this current pulse should match the measured THz-CC waveform. If this test fails, the waveform validation is considered unsuccessful. The corresponding code is publicly available [1].

The two field strengths in Fig. 3.9 and Fig. 3.10 are chosen to portray the contrast between a successful and an unsuccessful validation. The results of simulating the THz-CC measurement and the time-dependent current induced by the strong-field pulse in the junction are shown in subfigure (b) and (c) of Fig. 3.9 and Fig. 3.10. In each case, the input waveform shape was scaled to the peak field strength used in the experiment, as indicated by the dashed lines in the respective subfigures (a). For the positive polarity pulse in Fig. 3.9, the simulation yields a dominantly unipolar current pulse and shows excellent agreement between the measured and simulated THz-CC waveforms. This confirms that the corresponding waveform was accurately sampled and can be considered

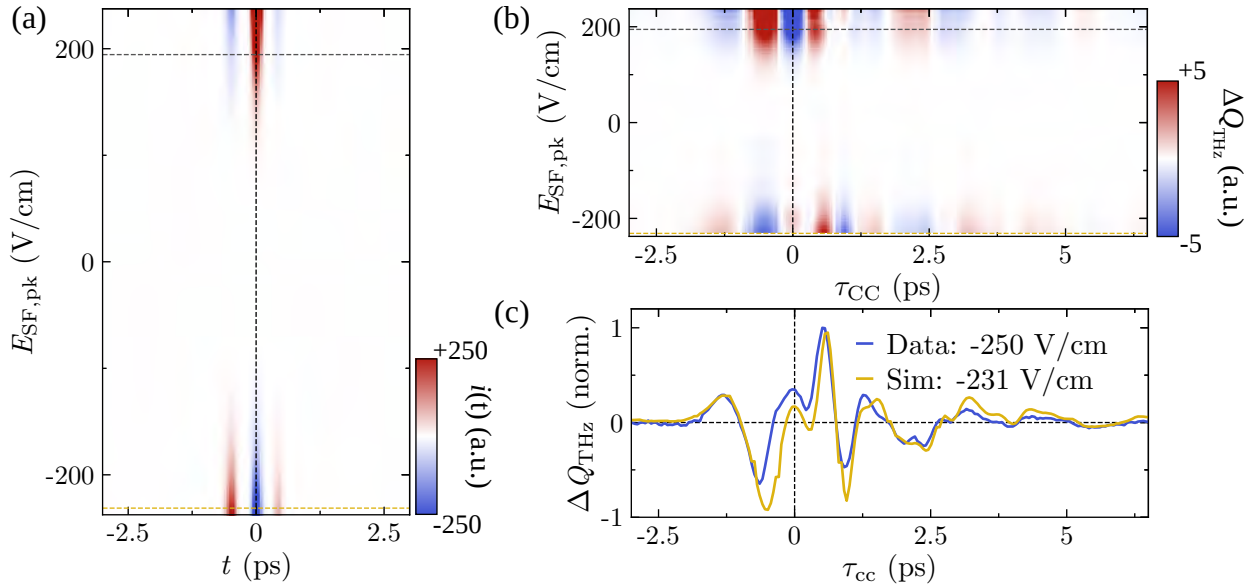

Figure 3.11 Using a validated waveform to predict artifacts in THz-CC measurements. (a) Map of current pulses generated by the validated waveform in Fig. 3.9, applied to the corresponding extracted $I - V$ curve over the full range of terahertz field strengths. (b) Simulated THz-CC measurements across the same range of terahertz field strengths using the validated waveform and corresponding extracted $I - V$ curve. (c) Comparison between an experimental waveform that exhibits measurement artifacts (blue curve) acquired at $E_{THz} = -250$ V/cm (from Fig. 3.5(a)) and a simulated THz-CC waveform at $E_{THz} = -231$ V/cm that is obtained using the validated waveform (yellow curve).

validated. In contrast, the negative polarity pulse in Fig. 3.10 produces a bipolar current pulse and exhibits poor agreement between the measured and simulated THz-CC waveforms. Consistent with the earlier qualitative analysis, the strong-field pulse with dominantly negative polarity drives current on both sides of the $I - V$ curve, and is therefore not suitable for accurate waveform reconstruction. Consequently, the extracted $I - V$ curve, dI/dV curve, and time-dependent current in Fig. 3.10 are also inaccurate, since the inversion algorithm critically depends on an accurate input waveform.

3.4.3 Simulating THz-CC measurement artifacts

A further demonstration of a successful waveform validation is that the extracted $I - V$ curve and validated waveform can be used to predict distortions in THz-CC measurements at other field strengths. Figure 3.11(a) shows the time-dependent current induced by the validated strong-field waveform (Fig. 3.9(b)) across the full range of field strengths. In the field strength region where the waveform was validated (near the top dashed horizontal line in Fig. 3.11(a)), the current pulse is clearly dominated by a single positive peak. In contrast, for the same field strength and opposite polarity, the positive current peak near $t = -500$ fs and the negative current peak near $t = 0$ ps are comparable in magnitude, indicating a bipolar current response.

Using the same validated waveform and extracted $I - V$ curve,the THz-CC measurement can be simulated across a wide range of field strengths (Fig. 3.11(b)), which can be compared to the experimental data shown in Fig. 3.5(a). One prominent artifact observed in the simulation at large negative field strengths is a secondary positive peak at a delay of approximately +0.5 ps, which is also seen in the experimental data (see Fig. 3.11(c) for comparison).

3.5 Alternative methods to enforce unipolar current pulses

3.5.1 Bias voltage control

In some cases, it is not possible to tune the parameters to induce a unipolar current pulse because the LDOS of the sample leads to current contributions from both sides of the $I - V$ curve regardless of the terahertz field polarity or amplitude. For metallic samples such as Au(111) [2], this limitation can be overcome by applying a static bias voltage to offset the terahertz pulse quiescent point along the voltage axis of the $I - V$ curve (Fig. 3.12(a)). This approach is valid provided that the applied d.c. voltage only changes the relative Fermi level between the tip and sample and does not introduce additional effects such as tip-induced band bending. If this is the case, the instantaneous total voltage in the junction can be written as $V(t) = V_{\mathrm{THz}}(t) + V_{\mathrm{d.c.}}$. Shifting the terahertz pulse along the voltage axis can, in some samples, enable current rectification from specific features in the LDOS, such as defect states [15].

Here, as a demonstration using Au(111), a d.c. voltage is applied to shift the quiescent point into a regime where the strong-field pulse induces a unipolar current response (Fig. 3.12(a)). This enables accurate waveform measurements even for negative field polarity, whereas previous sections show that THz-CC measurements on Au(111) at negative polarity without an applied d.c. voltage typically contain artifacts (Fig. 3.10 and Fig. 3.11). Figure 3.12(b) shows a series of THz-STS curves with different $V_{\mathrm{d.c.}}$. The curve labeled 'Ref' has $V_{\mathrm{d.c.}} = 0.1$ V and is the same as the curve in Fig. 3.5(b). Applying a large positive d.c. voltage leads to an increased positive Q_{THz} for both terahertz pulse polarities. Similarly, if the applied d.c. voltage is made increasingly negative, Q_{THz} eventually becomes negative for both terahertz polarities. The negative (positive) value of Q_{THz} at positive (negative) $E_{\mathrm{SF,pk}}$ can be understood as a consequence of the terahertz pulse being shifted sufficiently far towards the negative (positive) onset of the $I - V$ curve that the smaller amplitude half-cycles with polarity opposite to the main peak contribute more strongly to rectification than the main peak.

To further highlight the effect of applying a static bias voltage, terahertz pulse autocorrelations (see setup in Fig. 2.13(c)) can serve as a diagnostic tool to coarsely indicate whether multi-cycle or bipolar current pulses are present. A typical terahertz pulse autocorrelation at a d.c. bias of 0 V over Au(111) is shown in Fig. 3.12(c) for both field polarities (light red and light blue). At positive $E_{\mathrm{SF,pk}}$, the rectified charge remains positive over the full range of measurement. At negative $E_{\mathrm{SF,pk}}$,

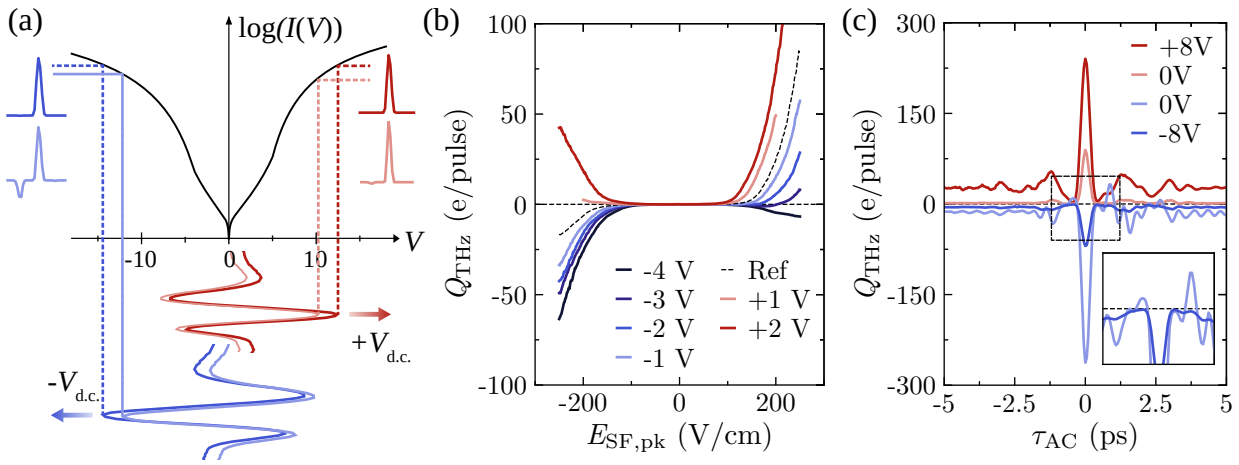

Figure 3.12 Using the static bias voltage to enforce a unipolar current pulse. (a) Schematic illustrating how a static bias voltage, $V_{\mathrm{d.c.}}$, shifts the quiescent point of the tunnel junction, enabling a terahertz voltage pulse to generate unipolar or bipolar current pulses. The $I-V$ curve is a simulated example based on the Simmons model (not including image charge). (b) THz-STS measurements acquired at $I_{\mathrm{d.c.}} = 100\,\mathrm{pA}$ and at various static bias voltages (see legend; $V_{\mathrm{d.c.}} = 0.1\,\mathrm{V}$ for the reference). (c) Terahertz pulse autocorrelations at $E_{\mathrm{SF,pk}} = +273$ V/cm ($V_{\mathrm{SF,pk}} = +13$ V) (red lines) and $E_{\mathrm{SF,pk}} = -273$ V/cm ($V_{\mathrm{SF,pk}} = -13$ V) (solid blue line) with $V_{\mathrm{d.c.}} = 0$ V, $z = z_0$ (dark red, dark blue) and $V_{\mathrm{d.c.}} = \pm 8$ V, $z = z_0 + 9\,\text{Å}$. The inset is a zoom into the central region of the autocorrelations (dashed black rectangle). The THz-AC measurements were performed at constant height with the feedback disengaged at $V_0 = 20$ mV, $I_0 = 200$pA with a different tip compared to the other measurements in this section.

the rectified charge crosses the line $Q_{\mathrm{THz}} = 0$ e/pulse several times (inset of Fig. 3.12(c)), indicating that a small adjustment of the terahertz pulse phase is enough to completely change the sign of Q_{THz}. This behavior suggests that the strong-field current pulse is bipolar and multi-cycle. However, when a large d.c. bias voltage is applied, the THz-AC measurements for both field polarities no longer cross the line $Q_{\mathrm{THz}} = 0$ e/pulse. While these measurements are not sufficient on their own to determine a suitable bias voltage, they can serve as a cross-check for the situations illustrated in Fig. 3.12(a).

THz-CC measurements are performed using a static bias voltage offset (Fig. 3.13(a)) and compared to the validated reference waveform from Section 3.4.2 (Fig. 3.13(a)). In this approach, $E_{\mathrm{SF,pk}} > 0$ is combined with positive d.c. voltages and $E_{\mathrm{SF,pk}} < 0$ with negative d.c. voltages (Fig. 3.12(a)). To establish a baseline independent of the STM junction, the EOS measurements in Fig. 2.14(b) and (c) are considered, which demonstrate that the two terahertz waveforms of opposite polarity are nearly identical inverted replicas of each other. Therefore, despite the terahertz pulses of opposite polarity following slightly different optical paths, their waveform shapes within the STM junction are expected to be very similar. Consequently, any major differences between the waveforms sampled with a d.c. voltage present and the validated reference waveform are attributed

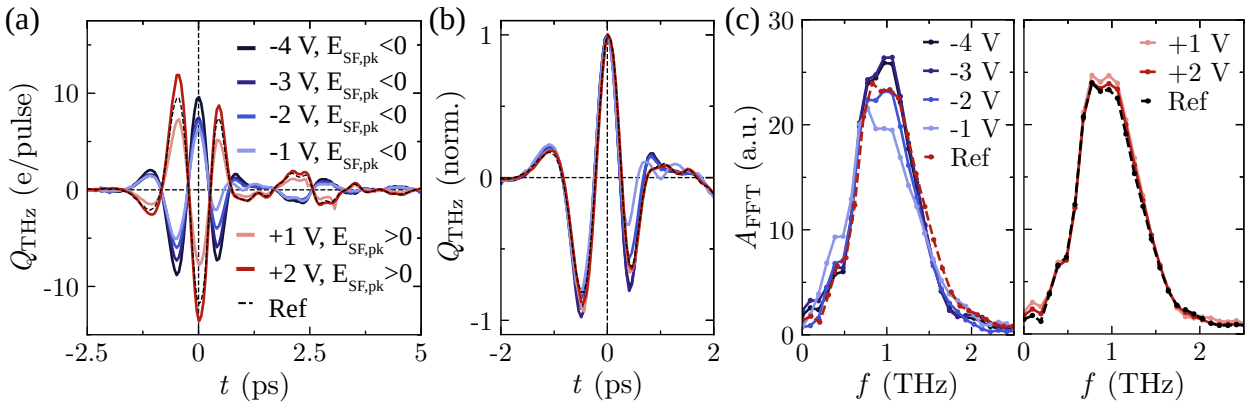

Figure 3.13 THz-CC measurements with a static bias voltage. (a) THz-CC waveforms with an applied static bias acquired at $E_{\mathrm{SF,pk}} = -237.5\,\mathrm{V/cm}$ (blue curves), $E_{\mathrm{SF,pk}} = 187.5\,\mathrm{V/cm}$ (light red curve), $E_{\mathrm{SF,pk}} = 200\,\mathrm{V/cm}$ (dark red curve) and $E_{\mathrm{SF,pk}} = 194.5\,\mathrm{V/cm}$ for the validated reference waveform (black dashed curve). (b) Normalized THz-CC waveforms from (a). (c) Corresponding amplitude spectra of the waveforms in (b) acquired via FFT using a Hamming window. Left: Amplitude spectra for waveforms at negative bias voltages compared to the amplitude spectrum of the validated reference waveform (red curve). Right: Amplitude spectra for waveforms at positive bias voltages compared to the reference (black curve).

to inaccurate waveform sampling.

Normalizing all of the waveforms (Fig. 3.13(b)) reveals that the measurement performed at $V_{\mathrm{d.c.}} = -1\,\mathrm{V}$ deviates from the reference waveform. For a clearer comparison,the FFT amplitudes are calculated and the measurements for $E_{\mathrm{SF,pk}} < 0$, $V_{\mathrm{d.c.}} < 0$ (Fig. 3.13(c), left) and for $E_{\mathrm{SF,pk}} > 0$, $V_{\mathrm{d.c.}} > 0$ (Fig. 3.13(c), right) are separately compared to the reference ($E_{\mathrm{SF,pk}} > 0$, $V_{\mathrm{d.c.}} = 0.1$ V). While the positive-bias amplitude spectra closely reproduce the reference, clear deviations are observed for negative d.c. voltages. The strong differences for $V_{\mathrm{d.c.}} = -1\,\mathrm{V}$ are attributed to competing rectification contributions from the positive and negative onsets of the $I - V$ curve, resulting in waveform sampling with a bipolar current pulse. At $V_{\mathrm{d.c.}} = -3\,\mathrm{V}$ and $V_{\mathrm{d.c.}} = -4\,\mathrm{V}$ the overall waveform shape resembles the validated reference waveform; however, the negative half-cycles are enhanced and the spectral amplitude around 1 THz is increased. This behavior is consistent with the quiescent point of the junction being driven sufficiently far toward the negative onset such that multiple half-cycles of the terahertz pulse contribute appreciably to a multi-cycle current pulse. Meanwhile, $V_{\mathrm{d.c.}} = -2\,\mathrm{V}$ represents an intermediate regime in which the main peak of the strong-field pulse samples the negative onset while also avoiding additional current contributions that would distort the waveform. The remaining minor differences between this measurement and the validated waveform are attributed to the two field polarities exhibiting slightly different optical alignment while propagating to the STM tip.

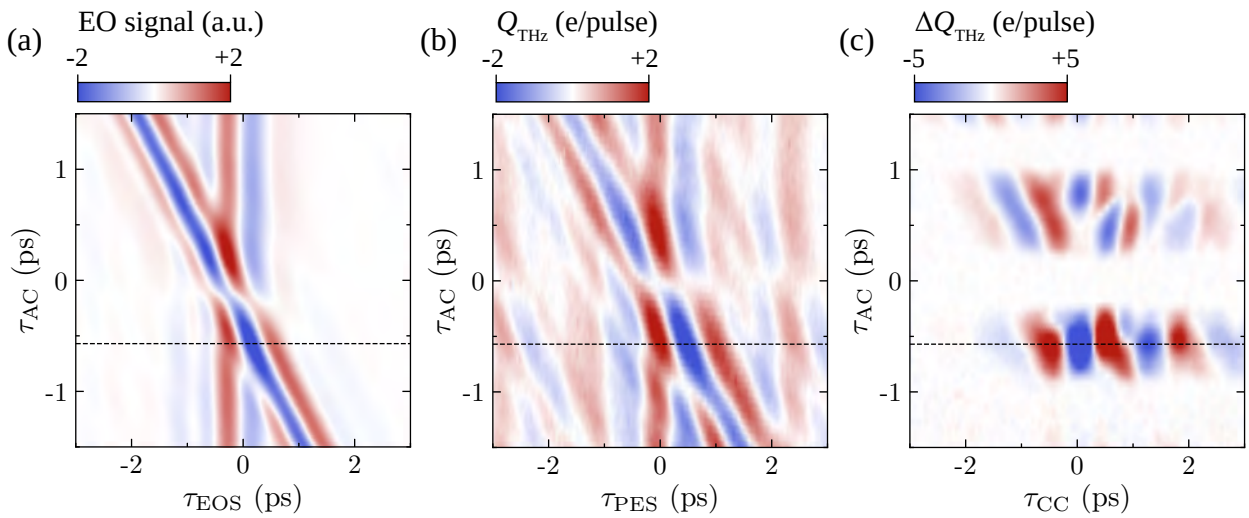

Figure 3.14 EOS, PES and THz-CC of free-space tailored terahertz pulses. The terahertz pulses are tailored in free-space by employing the cross-correlation scheme in Fig. 2.13(d). The delay τ_{AC} between the pulses of opposite polarity is varied along the vertical axis of (a) to (c). In (a) the pulse train measured with EOS in free-space before the STM junction. In (b) the terahertz near-field waveforms are measured by PES at full terahertz electric field strength, $V_{d.c.} = +6\,V$ and $I_{d.c.} = +200\,pA$ with the tip retracted about 300 nm from the Au(111) surface. The optical pump pulse had a 515 nm center wavelength, $\sim$ 230 fs pulse duration, 10 nJ pulse energy, $\sim 50\,\mu J/cm^2$ fluence and a linear polarization along the tip axis (p-polarized). (c) Differential rectified charge map, $\Delta Q_{THz}(\tau_{CC})$ measured at full terahertz electric field strength.

3.5.2 Free-space waveform shaping

Due to the inherent bipolar nature of electromagnetic transients incident onto the tip, a coherent field-driven process such as THz-STM benefits from precision control of the terahertz pulse phase and field asymmetry. In THz-CC measurements, waveform asymmetry, i.e., a cosine-like waveform shape, is advantageous, as it is more likely to induce unipolar current pulses and thereby simplifies data analysis. If alignment to the tip cannot achieve the desired pulse shape, (for example, due to fixed alignment by *in situ* optics, as is the case in some THz-STM systems) the pulses can instead be shaped in free space using a setup such as that shown in Fig. 2.13(d).

Figure 3.14(a) shows the pulse train resulting from the pulse shaping setup as a function of the delay τ_{AC} between the two pulses of opposite field polarity. Adjusting the waveform shaping delay, τ_{AC}, modifies the symmetry and peak amplitude of the terahertz near-field waveform, while minor differences in field strength between the two constructing pulses lead to an asymmetry between $\tau_{AC} > 0$ and $\tau_{AC} < 0$. In Fig. 3.14(b) this measurement is repeated at the STM tip with PES, i.e. by retracting the tip several hundred nanometers from the sample and illuminating the apex with a train of 515 nm laser pulses. Differences between Fig. 3.14(a) and Fig. 3.14(b) are due to the coupling into the scanhead and the transfer function of the tip. In Fig. 3.14(c), THz-CC is employed to capture the differential rectified charge in tunneling conditions directly over the Au(111) surface

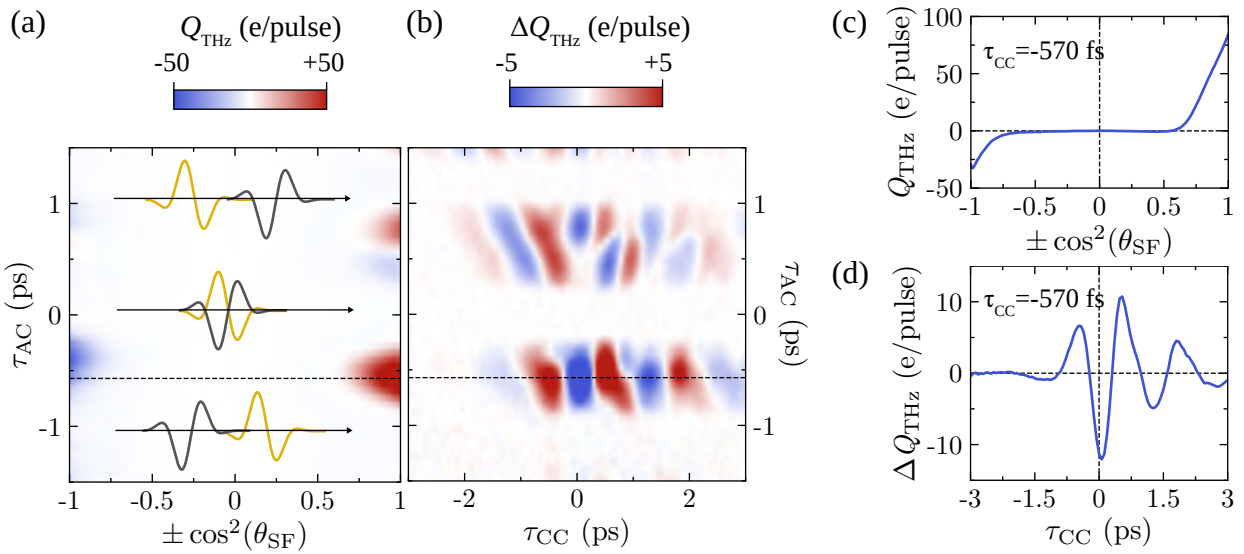

Figure 3.15 Tailoring the THz-STM junction via free-space waveform shaping. (a) Rectified charge map, $Q_{\mathrm{THz}}(\theta_{\mathrm{SF}}, \tau_{\mathrm{AC}})$ with illustrations of the ordering of the pulses during free-space pulse shaping. Measurements were performed in constant-current mode with $V_{\mathrm{d.c.}} = 3\,\mathrm{mV}$, $I_{\mathrm{d.c.}} = 200\,\mathrm{pA}$. (b) Differential rectified charge map, $Q_{\mathrm{THz}}(\theta_{\mathrm{SF}}, \tau_{\mathrm{AC}})$, measured at full terahertz electric field strength. (c) and (d) show horizontal linecuts at $\tau_{\mathrm{AC}} = -570\,\mathrm{fs}$ for the measurements in (a) and (b) (dashed lines).

as a function of τ_{AC}. It is immediately clear that the pulse shape defined by τ_{AC} plays a significant role for this type of measurement.

To explain the differential rectified charge map from Fig. 3.14(c) in more detail and explore the local parameter space further, Figure 3.15(b) shows it side-by-side with a 2D map of Q_{THz} as a function of waveform shaping delay and terahertz field strength attenuation via the WGP angle, θ_{SF} (Fig. 3.15(a)). The Q_{THz} map illustrates how the terahertz pulses interact with the junction. Similarly to applying a static bias voltage, the pulse shape can determine the shape of the THz-STS measurement. A strong contrast with opposite sign for opposite pulse polarity indicates regions of maximum waveform asymmetry.

Naively, one might consider Fig. 3.15(b) as a map of all possible terahertz near-field voltage transients in the range $-1.25\,\mathrm{ps} \geq \tau_{\mathrm{AC}} \leq +1.25\,\mathrm{ps}$; however, testing the validity of each waveform (horizontal cross-section) requires one to perform the validation described in the previous sections for every choice of τ_{AC}, and not all τ_{AC} yield a unipolar, sub-cycle current pulse for the same field strength. Furthermore, the map contains wide ranges of τ_{AC} where ΔQ_{THz} is well below the noise floor. This is because the strong-field voltage amplitude is significantly reduced due to deconstructive interference between opposite polarity terahertz fields.

$\tau_{\mathrm{AC}} = -570\,\mathrm{fs}$ is identified to have desirable characteristics for this STM tip and Au(111) sample configuration, such as a bipolar Q_{THz} for opposing polarities of $E_{\mathrm{SF,pk}}$ and a substantially larger

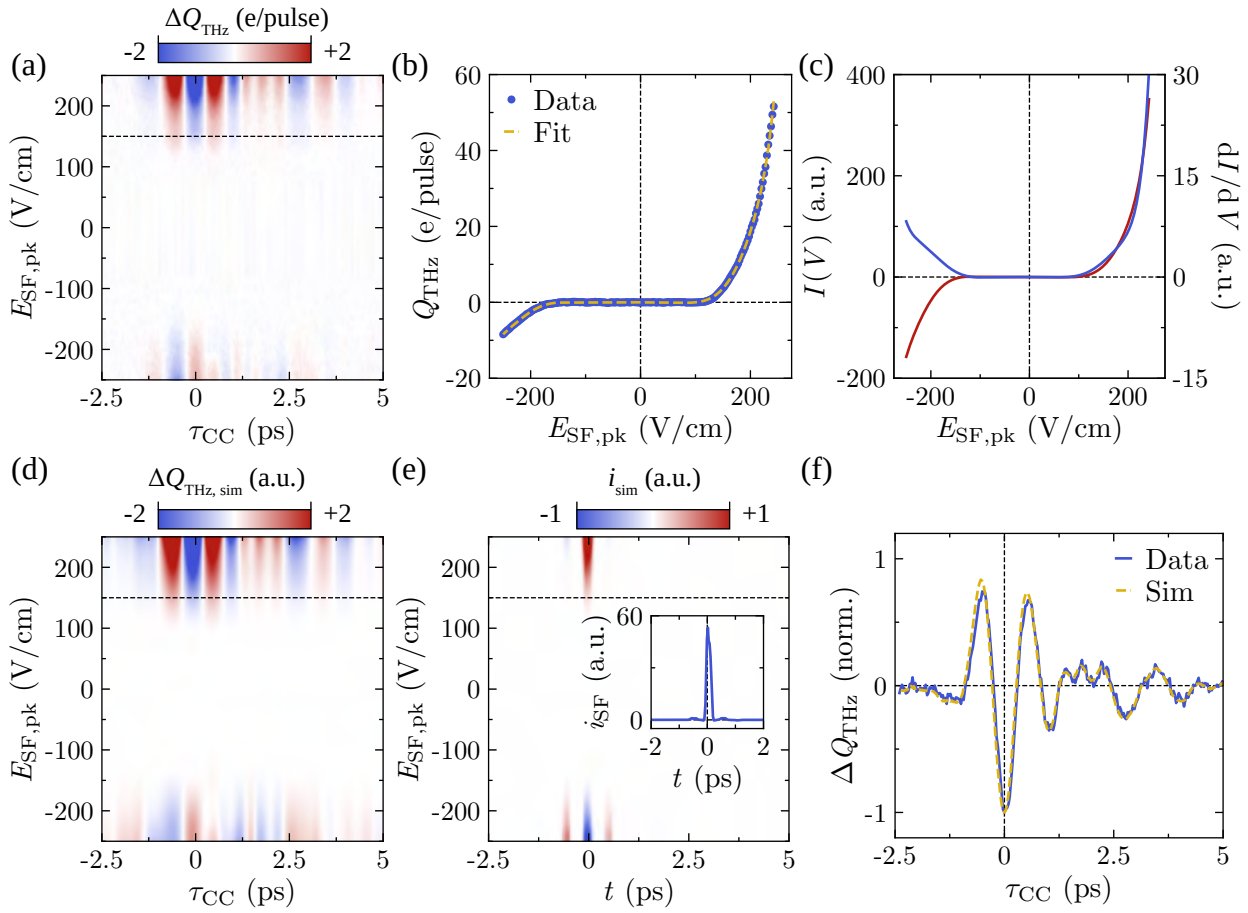

Figure 3.16 Validation of tailored terhertz-nearfields. (a) Differential rectified charge map, $\Delta Q_{\mathrm{THz}}(\tau_{\mathrm{CC}}, E_{\mathrm{SF,pk}})$ acquired in constant current mode with $V_{\mathrm{d.c.}} = 10\,\mathrm{mV}$ and $I_{\mathrm{d.c.}} = 100\,\mathrm{pA}$. (b) Measured THz-STS curve (blue) with polynomial fit of highest order $P = 11$. The measurement was performed in constant height with the tip height set by $V_{\mathrm{d.c.}} = 10\,\mathrm{mV}$ and $I_{\mathrm{d.c.}} = 100\,\mathrm{pA}$ and no bias voltage applied. (c) Extracted $I(V)$ and $\mathrm{d}I/\mathrm{d}V$ curves. (d) Simulated THz-CC measurements using the waveform at $E_{\mathrm{SF,pk}} = 150\,\mathrm{V/cm}$, indicated by the dashed line in (a), and the extracted $I(V)$ curve in (c). (e) Simulated current pulses using the waveform at $E_{\mathrm{SF,pk}} = 150\,\mathrm{V/cm}$. The inset shows the current pulse for $E_{\mathrm{SF,pk}} = 150\,\mathrm{V/cm}$. (f) Validated waveform measurement and simulation at $E_{\mathrm{SF,pk}} = 150\,\mathrm{V/cm}$ (indicated by dashed lines in (a) and (d)).

rectified charge compared to other waveform delays (Fig. 3.15(c)). This delay, $\tau_{\mathrm{AC}} = -570\,\mathrm{fs}$, also produces a THz-CC measurement with a cosine-like shape (Fig. 3.15(d)).

The quantitative waveform validation procedure described in Section 3.4.2 can now be applied to the selected pulse shape with $\tau_{\mathrm{AC}} = -570\,\mathrm{fs}$ (Fig. 3.16) and compared to the untailored pulse (Fig. 3.17) of the same tip-sample combination. For Fig. 3.16 and Fig. 3.17, subfigures (a) and (b) show the corresponding THz-CC and THz-STS measurements. The free-space tailored THz-STS curve in Fig. 3.16(b) clearly exhibits a higher degree of bipolarity compared to the unshaped measurements in Fig. 3.17(b). While the validation can be carried out for both cases, yielding extracted $I(V)$ and $\mathrm{d}I/\mathrm{d}V$ curves in (c), simulated THz-CC measurements in (d) and simulated

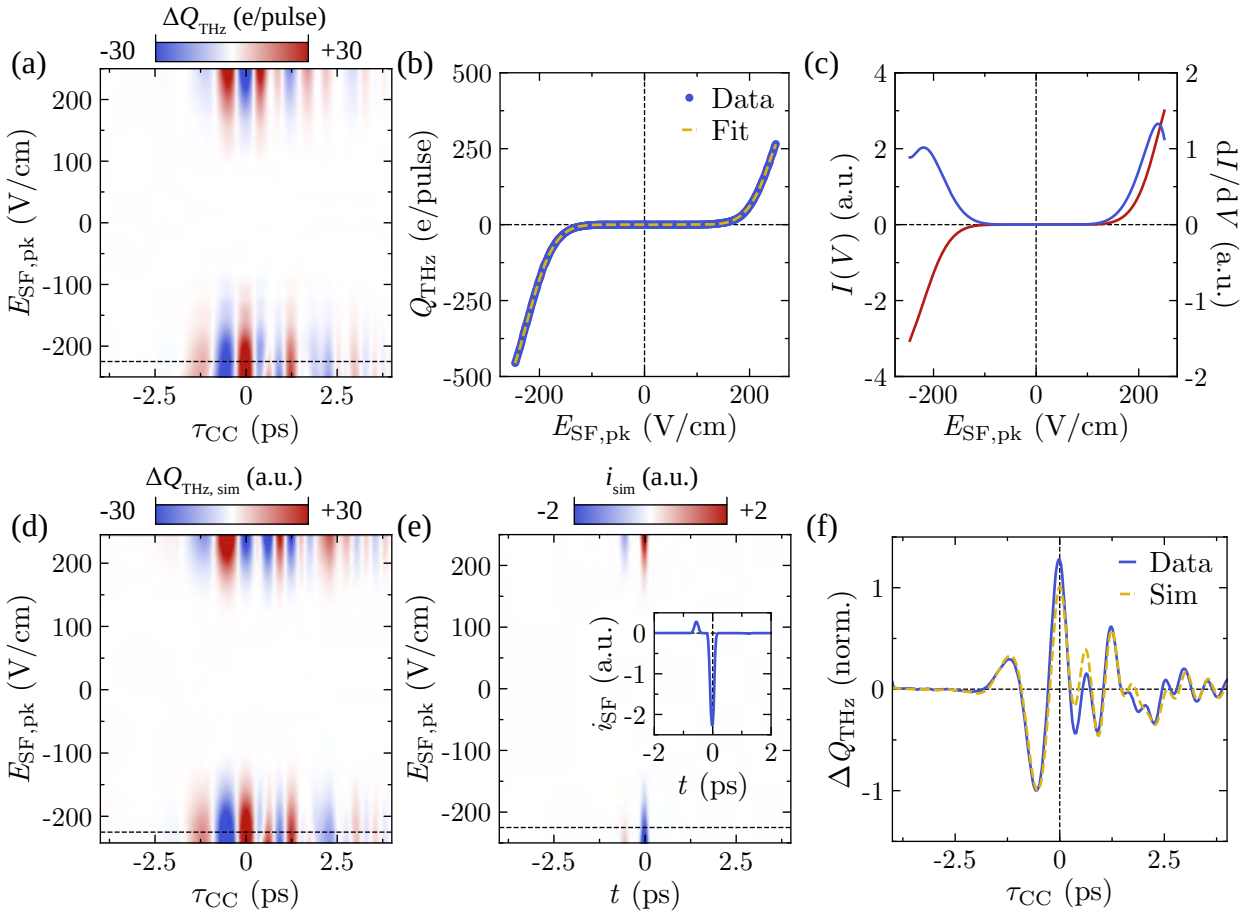

Figure 3.17 Validation of untailored terhertz-nearfields. (a) Differential rectified charge map, $\Delta Q_{\mathrm{THz}}(\tau_{\mathrm{CC}}, E_{\mathrm{SF,pk}})$ acquired in constant current mode with $V_{\mathrm{d.c.}} = 10\,\mathrm{mV}$ and $I_{\mathrm{d.c.}} = 100\,\mathrm{pA}$. (b) Measured THz-STS curve (blue) with polynomial fit of highest order $P = 14$. The measurement was performed in constant height with the tip height set by $V_{\mathrm{d.c.}} = 10\,\mathrm{mV}$ and $I_{\mathrm{d.c.}} = 100\,\mathrm{pA}$ and no bias voltage applied. (c) Extracted $I(V)$ and $\mathrm{d}I/\mathrm{d}V$ curves. (d) Simulated THz-CC measurements using the waveform at $E_{\mathrm{SF,pk}} = -225\,\mathrm{V/cm}$, indicated by the dashed line in (a), and the extracted $I(V)$ curve in (c). (e) Simulated current pulses using the waveform at $E_{\mathrm{SF,pk}} = -225\,\mathrm{V/cm}$. The inset shows the current pulse for $E_{\mathrm{SF,pk}} = -225\,\mathrm{V/cm}$. (f) Validated waveform measurement and simulation at $E_{\mathrm{SF,pk}} = -225\,\mathrm{V/cm}$ (indicated by dashed lines in (a) and (d)).

currents in (e), the agreement between measured and simulated waveforms in subfigure (f), as well as the current pulse shown in the inset of subfigure (e) is superior for the tailored pulse (Fig. 3.16) compared to the unshaped case (Fig. 3.17).

3.6 Atomic-scale THz-TDS

The first application of THz-TDS on the atomic-scale using the technique described in preceding sections was demonstrated on a localized defect on a silicon-doped GaAs(110) surface by Jelic *et al.* [2]. The results are briefly summarized here as a proof of principle. A detailed discussion of the investigated defect on the GaAs(110) surface, including its identification as a so-called DX center, is provided in Ref. [2].

In THz-TDS, a reference and a sample electric field waveform are compared to extract the sample dielectric function [3, 54]. THz-TDS has been implemented in s-SNOM, where gold is typically used as a reference substrate due to its flat spectral response at terahertz frequencies. The same approach is adopted here for atomic-scale THz-TDS in a THz-STM junction.

Figure 3.18 shows measurements performed on a Au(111) surface to establish a reference waveform for THz-TDS. THz-CC waveforms (Fig. 3.18(a)) were acquired both before and after the dataset recorded on the GaAs(110) sample, without changing the terahertz alignment on the tip or the tip itself. Only minor differences are observed in the time-domain (Fig. 3.18(b)) and spectral amplitude (Fig. 3.18(c)), and both waveforms satisfy the waveform validation criteria. An average of the measurements acquired before and after the GaAs(110) dataset is therefore used as the reference for performing THz-TDS on GaAs(110).

Figure 3.19(a) shows the surface of the silicon-doped GaAs(110) sample recorded in topography mode. Atomic rows and several distinct defect types are visible. A THz-STM image of the dark

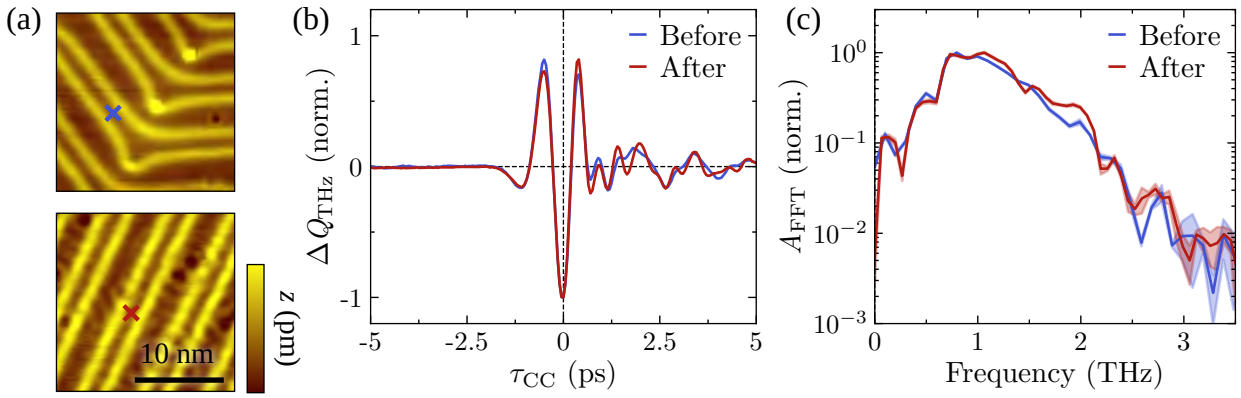

Figure 3.18 Waveform on Au(111) as a reference for THz-TDS. (a) STM topography images of Au(111) before (top; $V_{\mathrm{d.c.}} = 1\,\mathrm{V}$, $I_{\mathrm{d.c.}} = 100\,\mathrm{pA}$, height range 25 pm) and after (bottom; $V_{\mathrm{d.c.}} = 0.1\,\mathrm{V}$, $I_{\mathrm{d.c.}} = 100\,\mathrm{pA}$, height range 25 pm) atomic-scale THz-TDS on GaAs(110). (b) and (c) THz-CC waveforms (b) and spectra (c) acquired on Au(111) before (blue cross in (a), 2 averages) and after (red cross in (a), 5 averages) atomic-scale THz-TDS on GaAs(110).

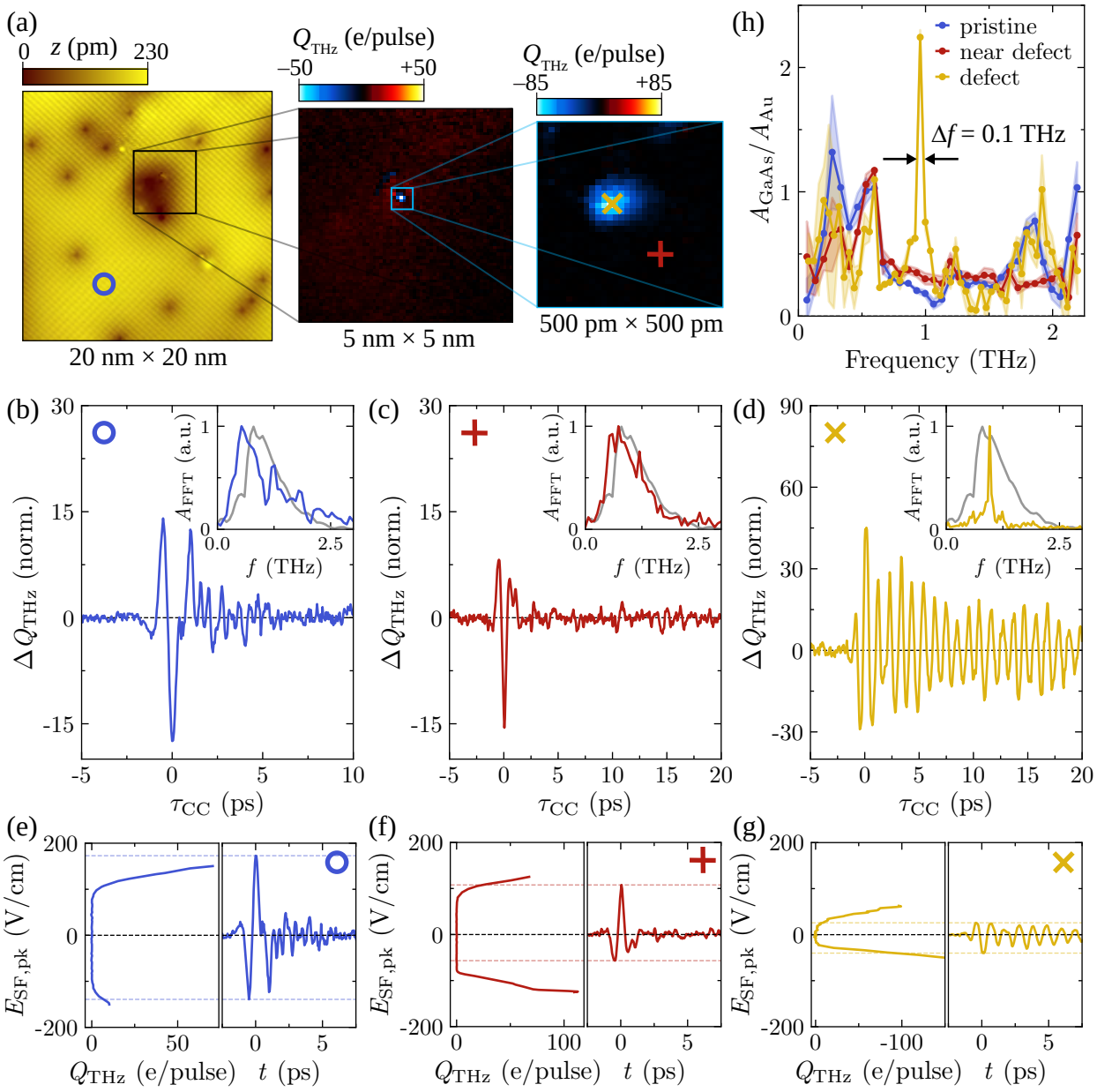

Figure 3.19 Atomic-scale THz-TDS on GaAs(110). (a) Left: STM topography image of a silicon-doped GaAs(110) surface ($V_{d.c.}$ = 1.2 V, $I_{d.c.}$ = 30 pA). Center: THz-STM image ($V_{d.c.}$ = 1.2 V, $I_{d.c.}$ = 100 pA, $E_{SF,pk}$ = 75 V/cm). Right: THz-STM image ($V_{d.c.}$ = 1.2 V, $I_{d.c.}$ = 100 pA, $E_{SF,pk}$ = 40 V/cm). (b)-(d) THz-CC waveforms with the tip located at the corresponding positions in (a) and acquired at $E_{WF,pk}$ = −8 V/cm. Blue circle in (b), $E_{SF,pk}$ = 170 V/cm; Red plus in (c), $E_{SF,pk}$ = 110 V/cm; yellow cross in (d), $E_{SF,pk}$ = 40 V/cm. The insets show the corresponding spectral amplitude (A_{GaAs}) with the gold reference (A_{Au}) in gray. (e)-(g) $Q_{THz} - E_{SF,pk}$ curves (left) and THz-CC waveforms from (b) to (d) (right) for the tip positions in (a), acquired at $V_{d.c.}$ = 1.2 V and $I_{d.c.}$ = 100 pA. The y-axis in (g) is shown in reverse due to an inverted phase over the resonator defect. (h) Spectral amplitude (A_{GaAs}) of each THz-CC waveform in (b)-(d) divided by the spectral amplitude measured over gold (A_{Au}).

region in the center reveals a feature with high contrast in the rectified charge Q_{THz} scans (center and right of Fig. 3.19(a)), localized to $\sim 0.01\,\mathrm{nm}^2 = 1\,\mathrm{Å}^2$, corresponding to atomic-scale dimensions (GaAs(110) surface unit-cell dimensions 565 pm × 400 pm). THz-CC waveform measurements were performed on the pristine surface (Figures 3.19(b)), in the vicinity of the high-contrast feature (Figures 3.19(c)) and directly on the feature itself (Figures 3.19(d)). In semiconductors with a well-defined band gap, such as GaAs, the waveform polarity and field strength can be tuned to generate current on only one side of the $I - V$ characteristic, thereby inducing a unipolar current pulse. This is illustrated for the three measurement locations in Figures 3.19(e) to (g).

To perform THz-TDS, the amplitude spectra for the THz-CC waveforms are compared to the Au(111) reference spectrum (insets in Figs. 3.19(b) to (d)). Dividing the GaAs(110) amplitude spectra by that of Au(111) yields the results in Fig. 3.19(h). All GaAs(110) waveforms exhibit contrast relative to Au(111) at around 0.5 THz. Most prominently, the defect itself exhibits a pronounced resonance at about 1 THz with a narrow full width at half maximum of $\Delta f \approx 0.1$ THz. By comparison to calculations, this spectral signature at 1 THz is key to identifying the defect as a likely DX center, which is known to contribute to reduced charge carrier mobility of GaAs at increased silicon doping levels [55–58]. In conventional STM imaging, without access to the dielectric contrast information provided by THz-TDS, a DX center is indistinguishable from other defects. These results therefore highlight the importance of atomic-scale THz-TDS for accessing physical properties that are otherwise inaccessible.

3.7 Discussion and conclusions

Atomic-scale THz-TDS is a promising tool for exploring the local terahertz polarizability in a light-coupled STM system. To capture accurate near-field waveforms, and therefore spectroscopy, for arbitrary tunnel junctions, a thorough understanding of the measurement parameters and their interactions is indispensable. This chapter has presented qualitative and quantitative methods to optimize and validate cross-correlation waveform measurements for THz-TDS in a THz-STM junction.

Although the THz-CC measurement technique has already been implemented in multiple experimental systems [2, 15, 22, 23, 25, 33, 35], further theory is required to connect the measurements to the local physical properties of the sample. For comparison, in conventional, far-field THz-TDS, the Fresnel coefficients allow the complex dielectric function to be extracted directly from waveform measurements [3]. Meanwhile, in s-SNOM implementations of THz-TDS, the point-dipole model and related models provide a connection between the scattered terahertz electric field and the local dielectric function under the tip [34]. In contrast, the length scales involved in THz-STM, and particularly the extreme confinement of the terahertz fields at the tip apex [2], necessitate a new approach. An important consideration will be how these localized terahertz fields interact with

phonons away from the Γ-point of the Brillouin zone [25] and surface polaritons [34].

Further experimental and theoretical work is needed to clarify how the phase information obtained from the FFT of the measured waveforms compares to the phase information extracted in conventional THz-TDS. A key distinction for atomic-scale THz-CC measurements is that the extracted phase is inherently self-referenced. Since the strong- and weak-field pulses are replicas of the same terahertz waveform, any phase shift imposed by the sample affects both pulses equally. Hence, only frequency-dependent phase shifts relative to the main peak of the pulse are resolved in a cross-correlation trace, rather than the absolute phase shift measured in a conventional THz-TDS experiment.

While open questions remain regarding the interpretation of atomic-scale THz-TDS, the measurements presented here establish a comprehensive understanding of how various experimental parameters influence the terahertz near-field waveform measured with THz-CC. In addition to quantitative atomic-scale THz-TDS, the robust framework enables the separation of intrinsic ultrafast material dynamics from measurement artifacts, which will provide a key test of terahertz-pump / terahertz-probe experiments in complex systems.

As THz-CC waveform measurements should be essential for many future THz-STM studies, it is important to identify known situations in which waveform validation may require considerations not included in this work: (i) The oscillating terahertz near-field may coherently drive a dipole in the junction that leads to a coherent modulation of the junction gap width along with the local field [14]. In such a scenario, validation of THz-CC measurements should account for modulation of the dI/dV curve, which is not included in the present work. (ii) In complex materials, the enhanced terahertz fields at the THz-STM tip apex can drive a phase transition to a metastable state that can be read out as a difference in the d.c. current between the ground and metastable states when the latter is long lived [10, 25]. Differential signals of this type do not satisfy the assumption of lightwave-driven tunneling in the present work. Atomic-scale THz-TDS in samples featuring such phase transitions should instead be performed in the regime of lightwave-driven tunneling, as in reference [25] (see Chapter 5). Alternatively, terahertz autocorrelation measurements have been successfully employed for spectral analysis of molecular systems featuring analogous changes to the d.c. current under terahertz pulse excitation [18].

Finally, as an outlook, the framework for near-field waveform measurements provides a springboard to implement yet more sophisticated spectroscopic techniques in THz-STM junctions. In the far-field, coherent detection of terahertz fields, along with advances in source technology, has spurred the development of terahertz magneto-spectroscopy, multi-dimensional nonlinear terahertz spectroscopy, and optical-pump / terahertz-probe spectroscopy with sub-cycle temporal resolution. Each of these possibilities may now be explored on the atomic scale, with the potential to inspire new areas of research.

BIBLIOGRAPHY

[1] Adams, S. THz_sts_algorithm. Available at https://github.com/NanoTHzCoding/THz_STS_Algorithm/blob/main/thzsts.py.

[2] Jelic, V. *et al.* Atomic-scale terahertz time-domain spectroscopy. *Nature Photonics* **18**, 898–904 (2024).

[3] Koch, M., Mittleman, D. M., Ornik, J. & Castro-Camus, E. Terahertz time-domain spectroscopy. *Nature Reviews Methods Primers* **3**, 48 (2023).

[4] Dressel, M. & Grüner, G. *Electrodynamics of Solids: Optical Properties of Electrons in Matter* (Cambridge University Press, Cambridge, 2002). Available at https://www.cambridge.org/core/books/electrodynamics-of-solids/DFDDF1640793690DAFD338BFDD1A18BF.

[5] Neu, J. & Schmuttenmaer, C. A. Tutorial: An introduction to terahertz time domain spectroscopy (THz-TDS). *Journal of Applied Physics* **124**, 231101 (2018).

[6] Jepsen, P. U. Phase Retrieval in Terahertz Time-Domain Measurements: a "how to" Tutorial. *Journal of Infrared, Millimeter and Terahertz Waves* **40**, 395–411 (2019).

[7] Cocker, T. L. *et al.* An ultrafast terahertz scanning tunnelling microscope. *Nature Photonics* **7**, 620–625 (2013).

[8] Yoshida, S. *et al.* Subcycle Transient Scanning Tunneling Spectroscopy with Visualization of Enhanced Terahertz Near Field. *ACS Photonics* **6**, 1356–1364 (2019).

[9] Yoshida, S. *et al.* Terahertz Scanning Tunneling Microscopy for Visualizing Ultrafast Electron Motion in Nanoscale Potential Variations. *ACS Photonics* **8**, 315–323 (2021).

[10] López, L. E. P. *et al.* Atomic-scale ultrafast dynamics of local charge order in a THz-induced metastable state of 1T-TaS_2 (2025). Available at http://arxiv.org/abs/2505.20541. Issue: arXiv:2505.20541 arXiv:2505.20541 [cond-mat].

[11] Cocker, T. L., Peller, D., Yu, P., Repp, J. & Huber, R. Tracking the ultrafast motion of a single molecule by femtosecond orbital imaging. *Nature* **539**, 263–267 (2016).

[12] Peller, D. *et al.* Sub-cycle atomic-scale forces coherently control a single-molecule switch. *Nature* **585**, 58–62 (2020).

[13] Sheng, S. *et al.* Launching Coherent Acoustic Phonon Wave Packets with Local Femtosecond Coulomb Forces. *Physical Review Letters* **129**, 043001 (2022).

[14] Roelcke, C. *et al.* Ultrafast atomic-scale scanning tunnelling spectroscopy of a single vacancy

in a monolayer crystal. *Nature Photonics* **18**, 595–602 (2024).

[15] Allerbeck, J. *et al.* Ultrafast Coulomb blockade in an atomic-scale quantum dot. *Nature Communications* **16**, 10806 (2025).

[16] Wang, L., Xia, Y. & Ho, W. Atomic-scale quantum sensing based on the ultrafast coherence of an H_2 molecule in an STM cavity. *Science* **376**, 401–405 (2022).

[17] Wang, L., Bai, D., Xia, Y. & Ho, W. Electrical Manipulation of Quantum Coherence in a Two-Level Molecular System. *Physical Review Letters* **130**, 096201 (2023).

[18] Xia, Y., Wang, L. & Ho, W. Mechanisms Underlying a Quantum Superposition Microscope Based on THz-Driven Coherent Oscillations in a Two-Level Molecular Sensor. *Physical Review Letters* **132**, 076903 (2024).

[19] Sheng, S. *et al.* Terahertz spectroscopy of collective charge density wave dynamics at the atomic scale. *Nature Physics* **20**, 1603–1608 (2024).

[20] Rai, V. N. *et al.* Influence of atomic-scale defects on coherent phonon excitations by THz near fields in an STM. *Science Advances* **11**, eadz6549 (2025).

[21] Jelic, V. *et al.* Ultrafast terahertz control of extreme tunnel currents through single atoms on a silicon surface. *Nature Physics* **13**, 591–598 (2017).

[22] Sheng, S. *et al.* Control of Surface Plasmon Propagation and Terahertz Near-Field Waveforms in a Scanning Tunneling Microscope. *Nano Letters* **24**, 15291–15299 (2024).

[23] Bobzien, L. *et al.* Ultrafast state-selective tunneling in two-dimensional semiconductors with a phase- and amplitude-controlled THz-scanning tunneling microscope. *APL Materials* **12**, 051110 (2024).

[24] Kimura, K. *et al.* Ultrafast on-demand exciton formation in a single-molecule junction by tailored terahertz pulses. *Science* **387**, 1077–1082 (2025).

[25] Jelic, V. *et al.* Terahertz field control of surface topology probed with subatomic resolution. *Nature Photonics* **19**, 1048–1055 (2025).

[26] Passoni, M., Donati, F., Li Bassi, A., Casari, C. S. & Bottani, C. E. Recovery of local density of states using scanning tunneling spectroscopy. *Physical Review B* **79**, 045404 (2009).

[27] Koslowski, B., Pfeifer, H. & Ziemann, P. Deconvolution of the electronic density of states of tip and sample from scanning tunneling spectroscopy data: Proof of principle. *Physical Review B* **80**, 165419 (2009).

[28] Ammerman, S. E. *et al.* Lightwave-driven scanning tunnelling spectroscopy of atomically

precise graphene nanoribbons. *Nature Communications* **12**, 6794 (2021).

[29] Ammerman, S. E., Wei, Y., Everett, N., Jelic, V. & Cocker, T. L. Algorithm for subcycle terahertz scanning tunneling spectroscopy. *Physical Review B* **105**, 115427 (2022).

[30] Müller, M., Martín Sabanés, N., Kampfrath, T. & Wolf, M. Phase-Resolved Detection of Ultrabroadband THz Pulses inside a Scanning Tunneling Microscope Junction. *ACS Photonics* **7**, 2046–2055 (2020).

[31] Peller, D. *et al.* Quantitative sampling of atomic-scale electromagnetic waveforms. *Nature Photonics* **15**, 143–147 (2021).

[32] Allerbeck, J. *et al.* Efficient and Continuous Carrier-Envelope Phase Control for Terahertz Lightwave-Driven Scanning Probe Microscopy. *ACS Photonics* **10**, 3888–3895 (2023).

[33] Li, H. *et al.* Real-Space Sampling of Terahertz Waveforms Under Scanning Tunneling Microscope. *ACS Photonics* **11**, 1428–1437 (2024).

[34] Cocker, T. L., Jelic, V., Hillenbrand, R. & Hegmann, F. A. Nanoscale terahertz scanning probe microscopy. *Nature Photonics* **15**, 558–569 (2021).

[35] Jelic, V. *et al.* A General Approach to THz Near-Field Waveform Sampling in a Lightwave-Driven Scanning Tunneling Microscope Junction. In *2023 48th International Conference on Infrared, Millimeter, and Terahertz Waves (IRMMW-THz)*, 1–2 (2023). Available at `https://ieeexplore.ieee.org/abstract/document/10299095`.

[36] Martín Sabanés, N. *et al.* Femtosecond Thermal and Nonthermal Hot Electron Tunneling Inside a Photoexcited Tunnel Junction. *ACS Nano* **16**, 14479–14489 (2022).

[37] Wimmer, L. *et al.* Terahertz control of nanotip photoemission. *Nature Physics* **10**, 432–436 (2014).

[38] Herink, G., Wimmer, L. & Ropers, C. Field emission at terahertz frequencies: AC-tunneling and ultrafast carrier dynamics. *New Journal of Physics* **16**, 123005 (2014).

[39] Luo, Y. *et al.* Nanoscale terahertz STM imaging of a metal surface. *Physical Review B* **102**, 205417 (2020).

[40] Abdo, M. *et al.* Variable Repetition Rate THz Source for Ultrafast Scanning Tunneling Microscopy. *ACS Photonics* **8**, 702–708 (2021).

[41] Zhang, H. *et al.* The development of a low-temperature terahertz scanning tunneling microscope based on a cryogen-free scheme. *Review of Scientific Instruments* **95**, 093703 (2024).

[42] Azazoglu, H., Kapitza, P., Mittendorff, M., Möller, R. & Gruber, M. Variable-temperature

lightwave-driven scanning tunneling microscope with a compact, turn-key terahertz source. *Review of Scientific Instruments* **95**, 023703 (2024).

[43] Tachizaki, T., Kanemitsu, Y. & Hirori, H. Time resolution of terahertz scanning tunneling microscopy measurements inside a superconducting magnet using a hollow waveguide. *Review of Scientific Instruments* **96**, 043004 (2025).

[44] Azazoglu, H., Möller, R. & Gruber, M. Thermal expansion in photo-assisted tunneling: Visible light *versus* free-space terahertz pulses. *Surface Science* **743**, 122465 (2024).

[45] Baumberg, J. J. Picocavities: a Primer. *Nano Letters* **22**, 5859–5865 (2022).

[46] Benz, F. *et al.* Single-molecule optomechanics in "picocavities". *Science* **354**, 726–729 (2016).

[47] Chen, X. *et al.* Modern Scattering-Type Scanning Near-Field Optical Microscopy for Advanced Material Research. *Advanced Materials* **31**, 1804774 (2019).

[48] Hillenbrand, R., Abate, Y., Liu, M., Chen, X. & Basov, D. N. Visible-to-THz near-field nanoscopy. *Nature Reviews Materials* **10**, 285–310 (2025).

[49] Siday, T. *et al.* All-optical subcycle microscopy on atomic length scales. *Nature* **629**, 329–334 (2024).

[50] Kaltenecker, K. J., Kelleher, E. J. R., Zhou, B. & Jepsen, P. U. Attenuation of THz Beams: A "How to" Tutorial. *Journal of Infrared, Millimeter, and Terahertz Waves* **40**, 878–904 (2019).

[51] Li, T., Quan, B., Fang, G. & Wang, T. Flexible THz Carrier-Envelope Phase Shifter Based on Metamaterials. *Advanced Optical Materials* **10**, 2200541 (2022).

[52] Yoshioka, K. *et al.* Tailoring Single-Cycle Near Field in a Tunnel Junction with Carrier-Envelope Phase-Controlled Terahertz Electric Fields. *Nano Letters* **18**, 5198–5204 (2018).

[53] Pedregosa, F. *et al.* Scikit-learn: Machine Learning in Python. *J. Mach. Learn. Res.* **12**, 2825–2830 (2011).

[54] Jepsen, P., Cooke, D. & Koch, M. Terahertz spectroscopy and imaging – Modern techniques and applications. *Laser & Photonics Reviews* **5**, 124–166 (2011).

[55] Northrup, J. E. & Zhang, S. B. Dopant and defect energetics: Si in GaAs. *Physical Review B* **47**, 6791–6794 (1993).

[56] Domke, C., Ebert, P., Heinrich, M. & Urban, K. Microscopic identification of the compensation mechanisms in Si-doped GaAs. *Physical Review B* **54**, 10288–10291 (1996).

[57] Ma, J. & Wei, S.-H. Electron-limiting defect complex in hyperdoped GaAs: The D D X center. *Physical Review B* **87**, 115210 (2013).

[58] Kundu, A. *et al.* Effect of local chemistry and structure on thermal transport in doped GaAs. *Physical Review Materials* **3**, 094602 (2019).

CHAPTER 4

ATOMIC-SCALE PHONON SPECTROSCOPY OF 2D HETEROSTRUCTURES

The design of modern electronic devices is guided as much by the intrinsic properties of materials as by the response of materials when interfacing with one another. *"[T]he interface is the device."* is a quote from Herbert Kroemer's Nobel lecture in 2000 emphasizing the important role of the interface in a heterostructure [1]. Recently, mono- to few-layer 2D materials have attracted significant attention to meet the demand for nano-scale electronics [2]. Structural defects in these materials have been shown to play a critical role in electrical and optical properties [3], including the phonon environment [4, 5].

Individual defects in transition metal dichalcogenides (TMDs) have been studied in equilibrium with a focus on their orbital [6] and spin [7] properties. Lattice dynamics have been observed on the nanoscale with near-field microscopy [8] and coherent phonon spectroscopy [9]. THz-STM studies have revealed ultrafast charge-state manipulation of individual defects [10], the dynamics of defect energy levels associated with an acoustic drum mode [11] and the influence of local lattice structure on coherent phonon dynamics [12].

This chapter extends these results by demonstrating the first phonon spectroscopy of a 2D heterostructure sample using atomic-scale THz-TDS (see Chapter 3 and Refs. [13, 14]). Building on the application of atomic-scale THz-TDS to defects in the bulk semiconductor GaAs(110) in the previous chapter [14], this chapter discusses the effect of defects and in-plane heterostructure interfaces between $SnSe_2$ and WSe_2 on the dielectric function. The THz-TDS contrast between pristine $SnSe_2$ and WSe_2 reveals a flexural phonon mode at ~ 2 THz in $SnSe_2$, which is dominated by out-of-plane motion of the Sn atoms. Such flexural modes have been widely studied in graphene and other 2D materials as they play an important role in thermal and mechanical performance [15]. Defects in the lattice of such materials act as scatterers and typically influence the phonons and therefore properties like thermal conductivity [16].

In the study presented here, this effect is demonstrated directly on the atomic scale via phonon spectroscopy on a Sn-site substitutional defect as well as at different locations approaching an in-plane interface of the heterostructure. The measurements reveal local damping of the flexural phonon mode, directly linked to the spatial proximity to such lattice disorders. Further, THz-STM imaging at low tip heights [17] reveals the atomic lattice in the vicinity of defects and interfaces, which is often overshadowed by a high LDOS in conventional STM imaging, facilitating its atomic-scale characterization.

The heterostructure samples used for this study were fabricated by the the group of P. Zhang at Michigan State University [18]. The VSe_2 and VTe_2 samples presented in the outlook were provided by the group of W.-W. Pai (Taiwan National University). All density functional theory (DFT)

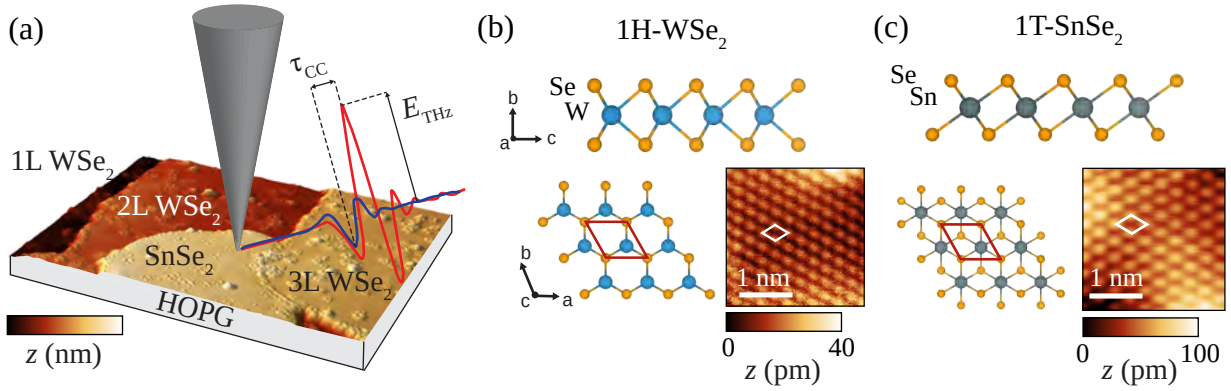

Figure 4.1 Characterization of a TMD heterostructure sample. (a) Schematic of the STM tip above a 3D representation of the $WSe_2/SnSe_2$ heterostructure surface. The topography (constant current, $V_{\mathrm{d.c.}} = 1.3\,\mathrm{V}$, $I_{\mathrm{d.c.}} = 10\,\mathrm{pA}$) shows the area where the majority of the following measurements were performed. The red (blue) pulse incident on the tip-sample junction indicates the strong (weak) field pulse for THz-CC waveform sampling. (b) Lattice structure of the 1H phase of WSe_2 shown from the side (top) and from the top (bottom left). The atomically-resolved topography scan at the bottom right was measured at $V_{\mathrm{d.c.}} = -1\,\mathrm{V}$, $I_{\mathrm{d.c.}} = 10\,\mathrm{pA}$. (c) Structures and topography ($V_{\mathrm{d.c.}} = 1.3\,\mathrm{V}$, $I_{\mathrm{d.c.}} = 11\,\mathrm{pA}$) for the 1T-$SnSe_2$ surface. The unit cells are shown in red in the top view schematic and in white in the topography scans.

calculations were performed by the group of J. L. Mendoza-Cortes (Michigan State University).

4.1 Characterization of the $WSe_2/SnSe_2$ lateral heterostructure sample

The lateral heterostructure sample used for this study was grown by molecular beam epitaxy (MBE), where single to few atomic layers are grown by exposing a heated substrate to a beam of atoms from a heated source, such that they assemble on the substrate with high thickness precision. Here, highly oriented pyrolytic graphite (HOPG) is used as a substrate. The growth procedure was performed in two steps: (1) Few-layer growth of WSe_2 and (2) sub-monolayer growth of $SnSe_2$. After growth, the sample was transported from the MBE growth system to the THz-STM system while maintaining UHV pressure with a UHV transfer suitcase. A representative area of the sample is shown in Fig. 4.1(a). $SnSe_2$ typically grows from the edges of the third- or forth-layer WSe_2 islands, forming an in-plane interface. Both surfaces can thus be studied using the THz-STM methods introduced in previous chapters, including atomic-scale THz-TDS. Both WSe_2 and $SnSe_2$ are layered materials, and each layer consists of metal atoms sandwiched between Se atoms (Fig. 4.1(b) and Fig. 4.1(c), top).

As mentioned in the Introduction, 2D materials exist in various polytypes or structural phases determined by the combination of chalcogen and transition metal [19]. The lowest energy coordination for WSe_2 is trigonal prismatic in the 1H-phase (Fig. 4.1(b)). In contrast, $SnSe_2$ is octrahedrally coordinated by Se, which corresponds the 1T phase (Fig. 4.1(c)). The in-plane lattice parameter of WSe_2 (DFT of bulk WSe_2: $\vec{a} = \vec{b} = 3.23\,\text{Å}$) is smaller than $SnSe_2$ (DFT of bulk

$SnSe_2$: $\vec{a} = \vec{b} = 3.78$ Å). This can be seen in the atomically resolved STM images of the surface in Fig. 4.1(b) and Fig. 4.1(c). Since tungsten is a transition metal, its 5d orbitals participate strongly in W–Se bonding via d–p hybridization with the Se 4p states [20, 21]. This more directional covalent bonding increases the effective local force constants, leading to a stiffer lattice in WSe_2 compared to $SnSe_2$, where Sn–Se bonding is more polar and dominated by Sn 5s/5p–Se 4p interactions [22].

For a basic characterization of the sample, conventional STM measurements are performed over a larger-scale area of the sample (Fig. 4.2(a)). $SnSe_2$ can be distinguished from WSe_2 by its growth behavior. It typically grows on the side of three- or four-layer WSe_2 and exhibits more rounded edge shapes compared to WSe_2. Further, at positive d.c. bias voltages of 1-2 V, the atomic corrugations is clearly visible on $SnSe_2$. Several defect types are found on both the WSe_2 and $SnSe_2$ surfaces, which have different appearances at positive versus negative bias voltages (Fig. 4.2(b)). A line cut across multiple WSe_2 layers reveals a layer height of approximately 0.5 to 0.6 nm (Fig. 4.2(c)). DFT calculations of bulk WSe_2 reveal a metal-to-metal distance of around 0.65 nm, in good agreement with the experiment considering substrate and vacuum interface effects. Both layer-dependent dI–dV curves (Fig. 4.2(d)) and the calculated density of states (DOS) (Fig. 4.2(e)) display the semiconducting character of WSe_2 and confirm the assignments of the layer thickness (for example through the valence band shape of 1L WSe_2). It is important to note that the upper edge of the valence band is aligned to the Fermi level ϵ_F in the DFT calculations by convention. Figure 4.2(e) compares the evolution of the band gap with the number of layers. The trend agrees well between data and theory. The smaller measured band gap is attributed to the influence of the HOPG substrate, which is not considered in the calculation.

In the following, the focus is on 3L WSe_2 islands and $SnSe_2$ islands on the same level (1L $SnSe_2$ on 2L WSe_2 on HOPG). Comparison of dI/dV curves on adjacent surfaces reveals a much smaller band gap for $SnSe_2$ compared to WSe_2 (Fig. 4.3(a)). This is also clearly visible in THz-STS measurements (Fig. 4.3(b), top). The narrow band gap and steep conduction band onset of $SnSe_2$ lead to positive rectified charge for positive as well as negative polarity field strengths. Using THz-CC waveforms measured in the same location, the dI/dV characteristic probed by the terahertz pulses can be extracted (Fig. 4.3(b), bottom). The relative band gap difference observed for steady-state dI/dV measurements of $SnSe_2$ versus WSe_2 is reproduced, including the asymmetry of the $SnSe_2$ band gap with respect to the Fermi level. The calculation of the electronic DOS in Fig. 4.3(c) for 3L WSe_2 and 1L $SnSe_2$ on 1L WSe_2 support the experimental findings (aside from the band gap magnitude due to substrate effects).

4.2 Pristine-surface phonon contrast revealed by atomic-scale THz-TDS

The THz-CC waveform measurements on the WSe_2 and $SnSe_2$ surfaces used for the dI-dV extraction in Fig. 4.3(b) are shown in Fig. 4.4(a). The respective FFT amplitudes reveal a clear

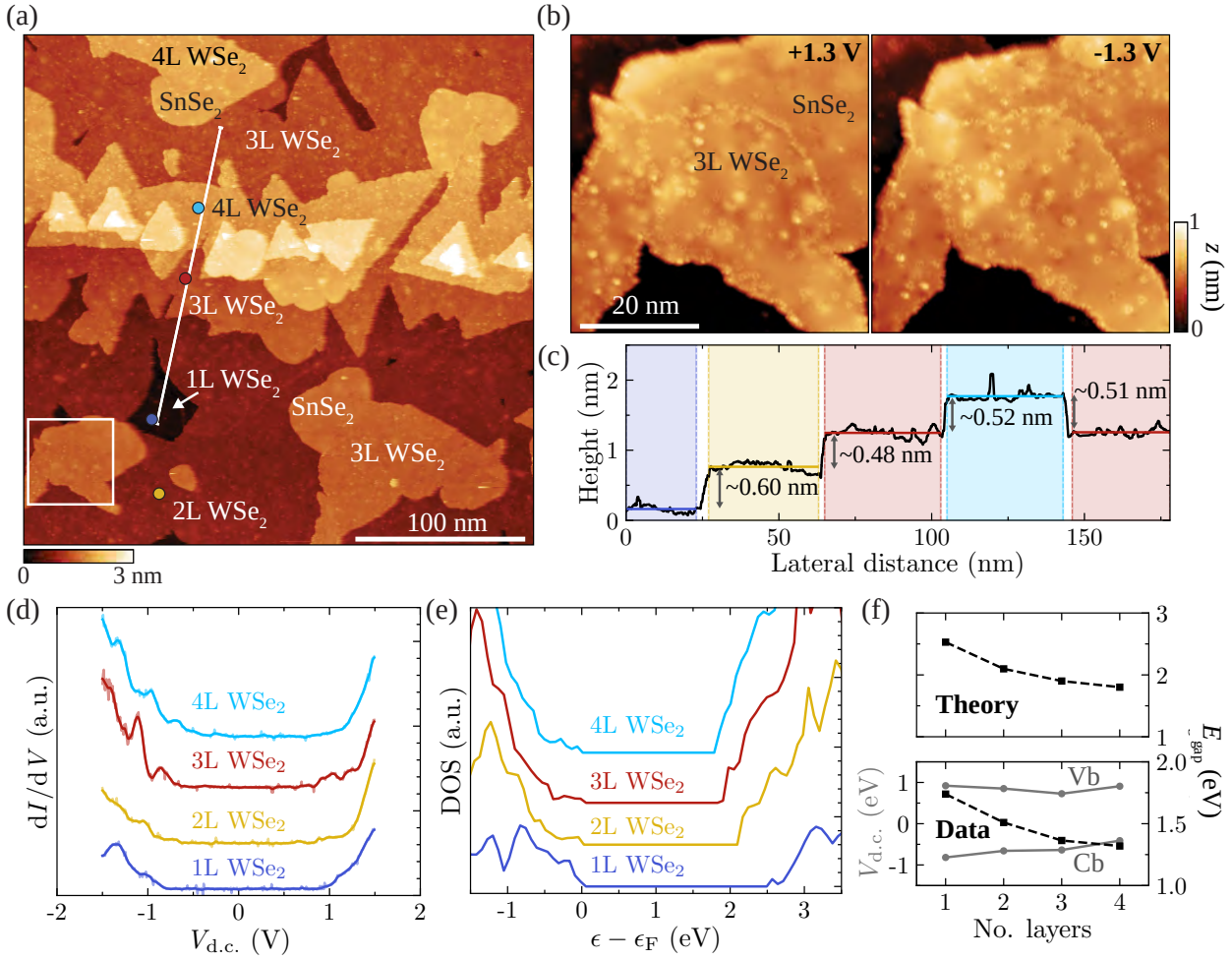

Figure 4.2 Characterization of the sample layers. (a) Large-scale topography scan ($V_{\mathrm{d.c.}} = 1.3$ V, $I_{\mathrm{d.c.}} = 15$ pA) showing the layered structure of the $WSe_2/SnSe_2$ heterostructure sample. (b) Zoom-in on a region on the third layer above the HOPG surface, where in-plane interfaces between WSe_2 and $SnSe_2$ are typically found. Multiple defect types are visible on both surfaces and appear different for positive (left) and negative (right) bias voltages. The scans were performed in constant current mode with $I_{\mathrm{d.c.}} = 10$ pA. (c) Cross section along the white line in (a) showing the approximate layer step height from 1L to 4L WSe_2. (d) dI–dV measurements in the locations marked with circles of the respective colors in (a). The curves are offset vertically for clarity and the measurement parameters before disengaging the feedback loop were $V_{\mathrm{d.c.}} = 1.5$ V, $I_{\mathrm{d.c.}} = 100$ pA. The modulation amplitude was $V_{\mathrm{mod}} = 15$ mV. The data are shown averaged over four measurements. The raw data is shown in the background. A Gaussian filter ($\sigma = 2$) was applied to yield the solid line. (e) DFT-calculated DOS for mono-layer to four-layer WSe_2, offset vertically for clarity. Due to the nature of the calculation, all curves are aligned such that the valence band starts at the Fermi level ϵ_{F}. (f) Top: Band gap as a function of the number of WSe_2 layers from the DFT calculations in (e). Bottom: Experimental valence band (VB, top gray), conduction band (CB, bottom gray) and band gap (black) as a function of layer number from the data in (d).

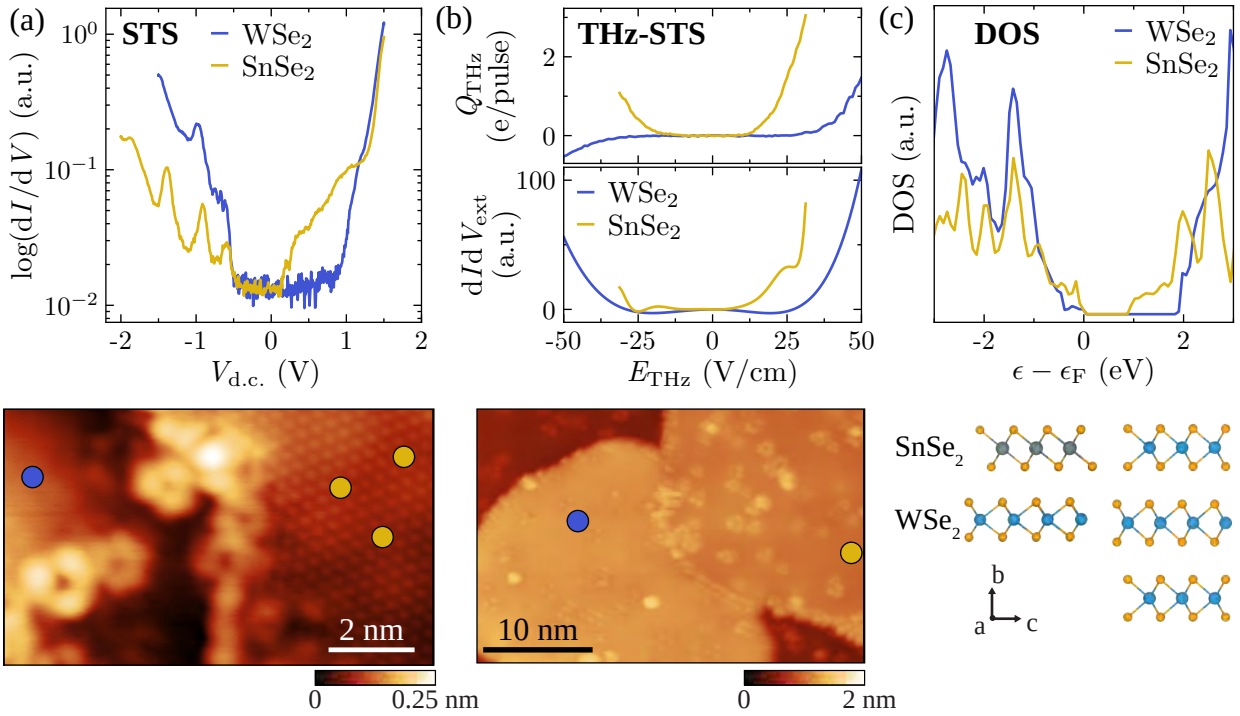

Figure 4.3 Electronic structure via dI–dV measurements. (a) Top: Conventional dI-dV measurements on the WSe_2 surface (blue) and $SnSe_2$ surface (yellow). The STM parameters were set to $V_{d.c.} = 1.5\,V$, $I_{d.c.} = 100\,pA$ with a modulation amplitude of $V_{mod} = 15\,mV$ for all measurements before disengaging the feedback loop. The data are shown averaged over ten measurements for WSe_2 and averaged over three locations (see bottom) with 10 averages each. Bottom: Topography scan ($V_{d.c.} = 1.3\,V$, $I_{d.c.} = 10\,pA$) highlighting the measurement locations. (b) Top graph: THz-STS measurements performed in the locations shown in the bottom topography. For both measurements the feedback loop was disengaged at $V_{d.c.} = 1.3\,V$, $I_{d.c.} = 10\,pA$. Following that, the tip was approached by 5 Å. The average of 5 measurements is shown. Center graph: dI/dV curves extracted from the THz-STS curves using the inversion approach (see Ref. [23] and Chapter 3). Bottom scan: $V_{d.c.} = 1.3\,V$, $I_{d.c.} = 10\,pA$. (c) Top: DFT-calculated DOS for a monolayer $SnSe_2$ on monolayer WSe_2 heterostructure (optimized structure, see bottom left) and for triple layer WSe_2 (bottom right).

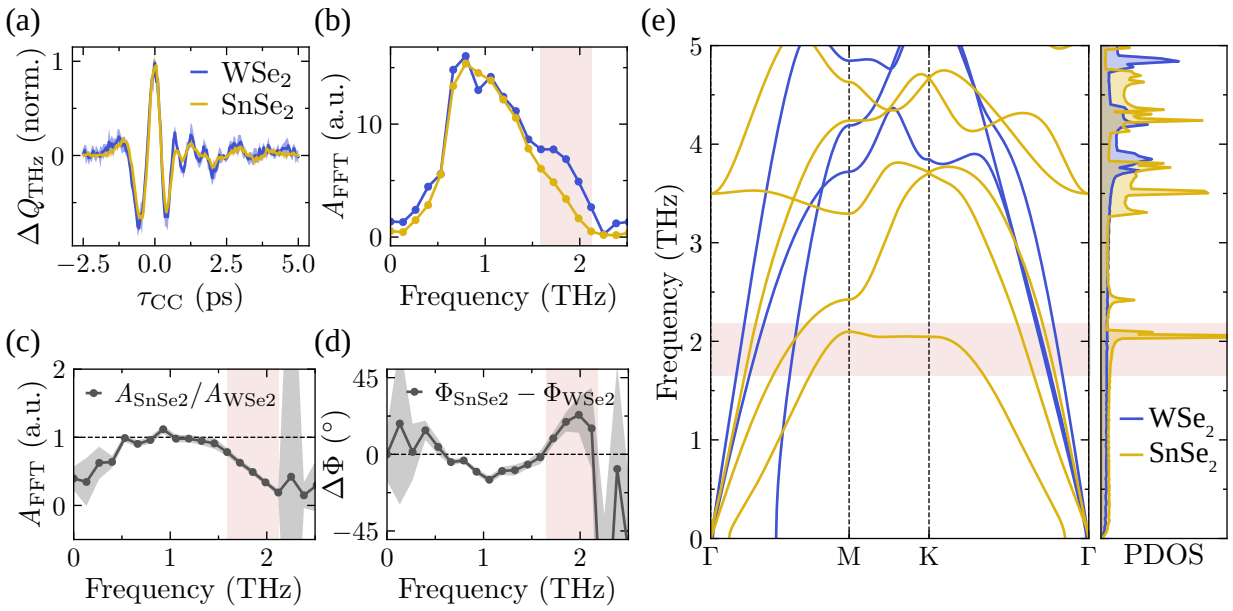

Figure 4.4 THz-TDS of WSe_2 versus $SnSe_2$. (a) Validated near-field waveforms measured with THz-CC in the locations shown in Fig. 4.3(b) (bottom). For both measurements the feedback loop was disengaged at $V_{\mathrm{d.c.}} = 1.3\,\mathrm{V}$, $I_{\mathrm{d.c.}} = 10\,\mathrm{pA}$. Following that, the tip was approached by 5 Å. The average of 5 measurements with the standard deviation in slightly lighter color is shown. The peak field strength was set to $E_{\mathrm{THz,pk}} = 28.1\,\mathrm{V/cm}$ on WSe_2 and to $E_{\mathrm{THz,pk}} = 47.9\,\mathrm{V/cm}$ on $SnSe_2$. (b) Average of the amplitudes after Fourier transforming each of the five waveform measurements individually. (c) Divided amplitudes calculated by dividing the complex FFTs of the waveforms in (a). The error is calculated via bootstrap sampling over the individual measurements. (d) Subtracted phases (angle calculated from the division of the complex Fourier transforms). Error calculated as in (c) but for the relative deviation of the angle. (e) Phonon band structure on the left and phonon density of states along the high symmetry path (integration along the x-axis) on the right for monolayer $SnSe_2$ (8×8 supercell) and WSe_2 (5×5 supercell) structures. The negative frequencies near the Γ point are numerical errors and calculations with larger supercells to avoid this are underway. The red-shaded area in (b), (c), (d) and (e) highlights the main differences between WSe_2 and $SnSe_2$.

spectral difference around 1.8-2.2 THz, where the amplitude of $SnSe_2$ is attenuated relative to WSe_2 (Fig. 4.4(b)). THz-TDS, i.e., dividing the complex Fourier transforms of the waveforms and calculating the amplitude and phase, directly reveals the differences in the local sample response in the terahertz range (Fig. 4.4(c) and (d)). The error (shaded area) is calculated by bootstrap sampling five individual measurements per surface location. The difference in the amplitude spectra manifests as an attenuation in amplitude for $SnSe_2$ referenced to WSe_2 starting at $\sim$ 1.8 THz and continuing to increase to about 2.2 THz, where it drops again and reaches the edge of the measurement bandwidth. This is also evident as a feature in the phase difference in Fig. 4.4(d). The behavior consistently persists in the same frequency range for both amplitude and phase and demonstrates the benefit of time-domain measurements. To explain the contrast between the surfaces, the phonon band structures and phonon density of states of both materials (calculations shown for monolayers, in agreement with the literature [24]) are considered (Fig. 4.4(e)). In accordance with the earlier mention of a stiffer WSe_2 lattice, the phonon bands for WSe_2 lie higher in energy, outside of the measurement bandwidth. The lowest lying acoustic out-of-plane (ZA) phonon branch of $SnSe_2$, on the other hand, is flat at $\sim$ 2 THz and prominently shows up in the phonon density of states (PDOS) calculated by integration over the high symmetry paths.

An acoustic phonon corresponds to a collective lattice vibration whose long-wavelength limit is a uniform translation of the crystal. Consequently, its frequency vanishes at the Brillouin-zone center, $\omega(\vec{k} \rightarrow 0) = 0$, as required by translational invariance. The out-of-plane ZA phonon mode is also referred to as the flexural phonon mode [25]. For a finite wavevector, $\vec{k}$, the displacement pattern varies from unit cell to unit cell and the atoms in their respective unit cells move out-of-phase with each other. Therefore, the acoustic branches disperse to finite frequencies. In $SnSe_2$, the out-of-plane acoustic (ZA) branch reaches a nearly flat dispersion near the zone edge (M–K) around $\sim$ 2 THz, which produces a significant contribution to the PDOS in this frequency range. Unlike far-field optical probes that primarily couple to $\vec{k} \approx 0$ excitations, the THz-STM junction is highly localized in real space and can therefore contain substantial in-plane momenta [26, 27]. Local disorder and the broken translational symmetry at the tunnel junction can also contribute to relaxing the momentum selection rules. Combined, these effects enable sensitivity to finite-momentum phonons that contribute to the local complex response. Finally, coupling to the HOPG substrate and the asymmetry introduced by the vacuum/sample interface can further influence the experiment compared to the calculated phonon spectrum, but the presence of the feature near $\sim$ 2 THz remains consistent with the contrast observed in the measurement. Calculations for the $SnSe_2$ monolayer show that the atomic motion in the $\sim$ 2 THz flat phonon band between the M and K points is dominated by out-of-plane motion of the Sn atoms with the motion between adjacent unit cells out of phase. The Se atoms contribute with a weaker motion, which is purely in-plane at the K point and mostly in-plane with a small out-of-plane component at the M point.

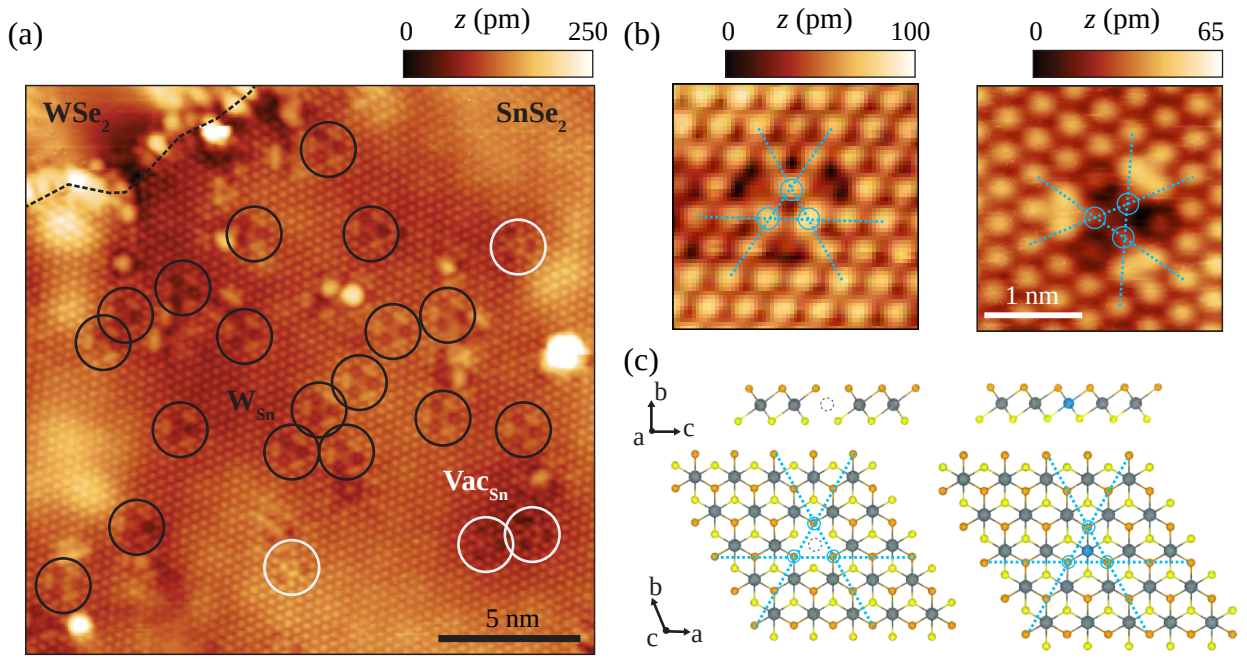

Figure 4.5 Defects on $SnSe_2$ monolayer islands. (a) Atomically-resolved area on a $SnSe_2$ island with a typical number of defects. The most common types are identified as Sn vacancies, Vac_{Sn} (white circles), and W substitutional atoms in Sn sites, W_{Sn} (black circles). The topography scan was recorded at $V_{d.c.} = 1.3\,V$ and $I_{d.c.} = 21\,pA$. (b) Zoom-in topography scans of the Vac_{Sn} (left; $V_{d.c.} = 1\,V$, $I_{d.c.} = 50\,pA$) and W_{Sn} (right; $V_{d.c.} = 1.3\,V$, $I_{d.c.} = 20\,pA$) defects with blue line and circled Se atoms to emphasize the threefold symmetry. (c) Lattice structures of the defects above in (b) shown as a side view (top) and top view (bottom) with blue lines and circles demonstrating the symmetry as in (b). Top Se atoms (orange), bottom Se atoms (yellow), Sn atoms (gray) and W atoms (blue).

4.3 Atomic defect-induced modification of the $SnSe_2$ phonon response

The $SnSe_2$ surface shows a variety of atomic-scale defect types (Fig. 4.5(a)) scattered all over the islands. In defect-free areas, such as the bottom right in Fig. 4.5(a), a Moiré pattern due to the lattice mismatch with the underlying WSe_2 layer is faintly visible. The two most common defect types are circled in white and black and will be identified in the following. Typically, TMD samples predominantly show chalcogen vacancies or substitutions and metal vacancies [3, 28–32]. Figures 4.5(b) and (c) show close-up topography scans of both types with lines along the Se atom symmetry axes and circles around the three Se atoms closest to the defect center. The threefold symmetry, as well as the center of the defects being situated at a Sn atom location, i.e., enclosed by three Se atoms, indicates that the metal site is the epicenter. A straightforward guess is therefore that one of the defect types is a Sn vacancy, Vac_{Sn} (Fig. 4.5(c), left), while the other type is a different atom in the Sn site, in other words, a substitutional defect (Fig. 4.5(c), right). The latter is mostly reported after intentional doping to tune the electronic and magnetic properties of TMDs [31, 33]. In the case here, the most likely candidate for the substitutional atom is tungsten

due to the heterostructure growth procedure. When WSe_2 is grown in the first step of the process, clusters of W atoms can form on the HOPG substrate and around the edges of the WSe_2 islands. The incorporation of such isolated W atoms into the $SnSe_2$ lattice during the second growth step represents a plausible origin of the observed W_{Sn} substitutional defects.

STM imaging at positive and negative bias voltages (i.e., above and below the Fermi level) of both defect types (Fig. 4.6(a)) reveals strong differences with distinct charge density signatures. However, it is hard to tell the lattice structure around the defect. THz-STM can operate at much lower tip heights compared to conventional STM [17, 26]. It can thus reveal the underlying lattice (Fig. 4.6(b)). For the defect at the top of Fig. 4.6(b), all top Se atoms are clearly visible and barely distorted. For the defect at the bottom of Fig. 4.6(b), the Se atoms are also visible but the three innermost atoms appear darker. Comparison to calculated charge densities reveals the defects as a Vac_{Sn} (Fig. 4.6(a), top right) and as a W atom in a Sn site, W_{Sn} (Fig. 4.6(a), bottom left). The first consideration is the lateral extent of the defect state. Figure 4.6(c) shows isosurfaces for both defects. The LDOS for the vacancy is more closely concentrated around the defect center compared to the LDOS for the W substitution. Further, good agreement is achieved with the calculated conductance and valence band charge density maps in Fig. 4.6(d) and (e).

To exclude Se vacancies, because of their abundance in other TMD defect studies (e.g., Ref. [28]), a variety of configurations were calculated but none showed agreement with the experiment (Fig. 4.7). Because of the 1T phase coordination of $SnSe_2$, Se defects typically do not show the threefold symmetry observed in the experiment (Fig. 4.7(a)-(e)). The triple vacancy in Fig. 4.7(f) is three-fold symmetric but can be excluded due to the visibility of the Se atoms in the THz-STM and some of the topography scans. Further, it seems unlikely that the most common defect type stems from a three-atom defect. Therefore, the defects in Fig. 4.5 and Fig. 4.6 are identified as W_{Sn} for the most common vacancy and Vac_{Sn} as the second most common.

The topography scans in Fig. 4.6(a) demonstrate that the defects influence the local electronic environment. Now, attention is turned to the most prominent defect, W_{Sn}, to investigate how it modifies the phonon response compared to pristine $SnSe_2$. THz-CC measurements were performed on the defect and compared to a nearby location on the pristine surface (Fig. 4.8(a)). The amplitude spectrum of the W_{Sn} defect compared to the pristine $SnSe_2$ surface (both referenced to pristine WSe_2 from Fig. 4.8(b)) reveals that there is a contrast in the region of the ZA phonon mode between the two locations. The spectral amplitude on the defect is less attenuated compared to the pristine $SnSe_2$ surface but still shows a contrast compared to WSe_2. This indicates that the substitutional defect weakens the mode but does not completely annihilate it. To understand the physical origin, the phonon band structure of $SnSe_2$ is plotted with gray and orange indicating the dominance of the Sn versus Se atoms along the phonon bands (Fig. 4.8(c)). The flat band, responsible for the contrast in THz-TDS, is dominated by the Sn atoms. That means that if an Sn atom is replaced by

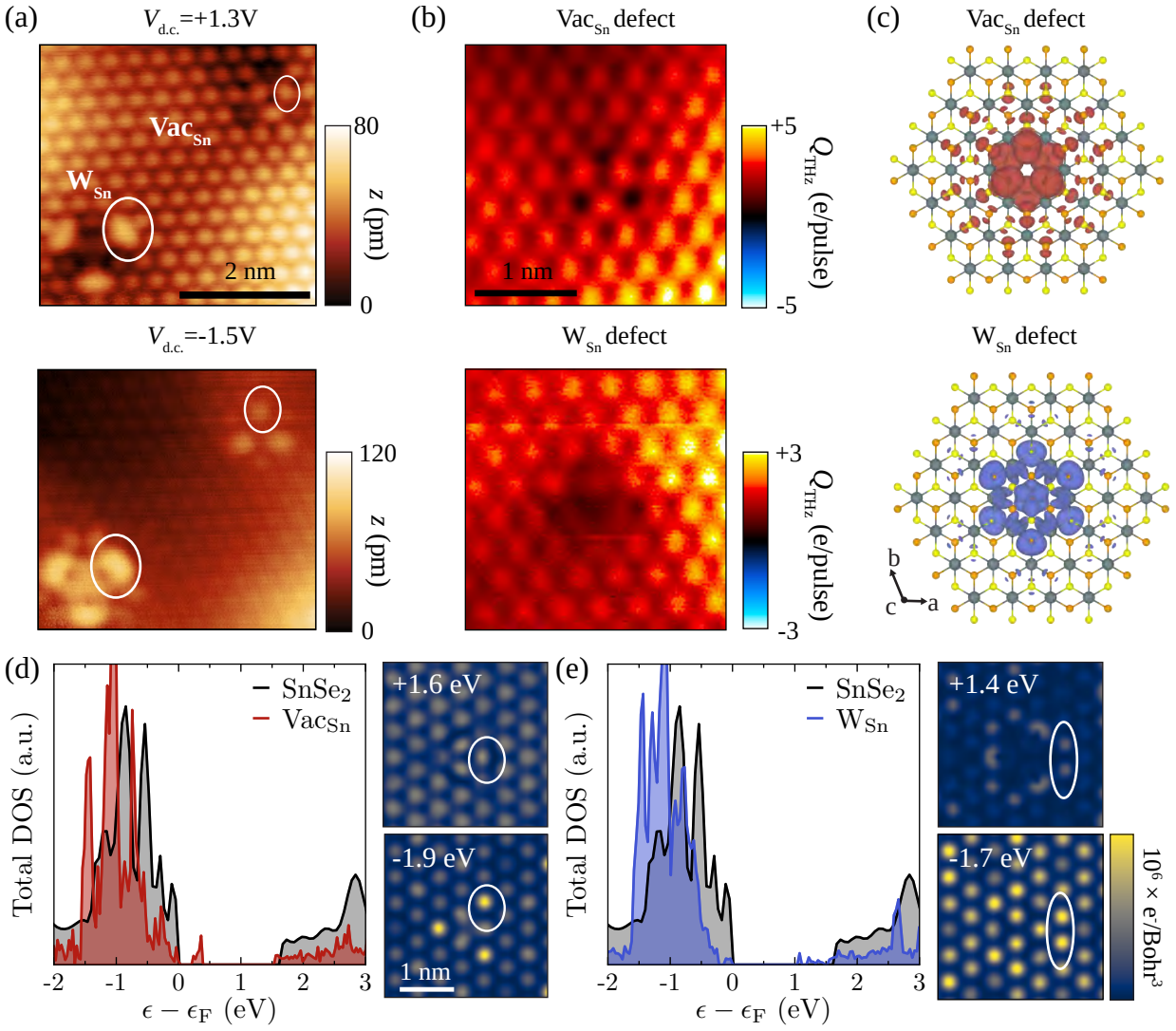

Figure 4.6 Spatial distribution of the charge density around Sn-site defects. (a) Topography images of an area with the two most common defects, W_{Sn} (bottom left of each scan) and Vac_{Sn} (top right of each scan) for positive bias on the top ($V_{d.c.}$ = 1.3 V, $I_{d.c.}$ = 10 pA) and negative bias on the bottom ($V_{d.c.}$ = −1.5 V, $I_{d.c.}$ = 10 pA). (b) THz STM imaging at low tip height of the defects in (a). Measurement parameters: Tip height set by $V_{d.c.}$ = 1 V, $I_{d.c.}$ = 10 pA, $E_{THz,pk}$ = 21.9 V/cm, tip approached by 3.75 Å (Vac_{Sn}) and 3.25 Å (W_{Sn}). (c) Isosurfaces of the charge density around both defects, i.e. a 3D surface of all points with the same electron-density value to visualize the spatial distribution and localization of the defect-induced electronic states. W_{Sn} (corresponding mostly to the highest valence band); Vac_{Sn} (corresponding mostly to the lowest conduction band). (d) Left: Calculated DOS for monolayer $SnSe_2$ and an Sn vacancy in a monolayer. Spatial distribution of the calculated charge density at energies above (top) and below (bottom) the Fermi level. The white ellipses indicate features that compare to the data in (a). The color map scaling is [0,1]×10^6 e/Bohr^3 for the top plot and [0,1]×10^6 e/Bohr^3 at the bottom. (e) Same as (d) but for the substitutional W atom in a Sn monolayer. The color map scaling is [0,4]×10^6 e/Bohr^3 for the top plot and [0,8]×10^6 e/Bohr^3 at the bottom.

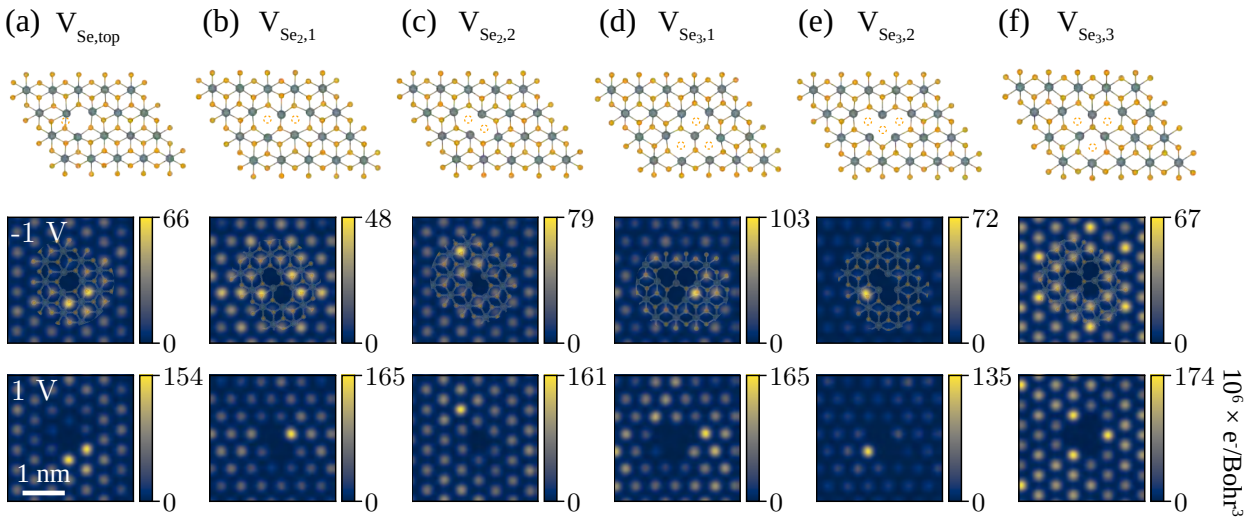

Figure 4.7 Excluding Se vacancy defects. Top: Structures with several Se vacancy configurations ranging from a single missing Se atom (a) to double vacancies ((b) and (c)) to triple vacancies ((d), (e) and (f)). Below, the DFT calculated charge density images (integrated from the Fermi level to the voltage indicated in the top left), comparable to STM images, are shown for the negative (top) and (positive) sides of the Fermi level. The top charge density plots are overlaid with the structures to identify the contributing atoms.

a W atom, the phonon mode is influenced on a local scale. Figure 4.8(d) illustrates this behavior in a sketch, where the atomic motion of the mode is simplified to a one-dimensional chain. For a lattice with alternating Se and Sn atoms connected by springs with spring constant, k_{Sn-Se}, the introduction of a W atom would come with a more rigid spring constant, k_{W-Se}, consistent with the mainly covalent bonding in WSe_2. For the acoustic mode near the Γ point, this does not matter, as the whole chain moves in-phase and out-of-plane (up and down). However, away from the Γ point in the region of the flat band, M–K, the atoms still move in the out-of-plane direction, but the atoms in adjacent unit cells are out-of-phase with each other and move in an alternating pattern, as indicated by the arrows at the bottom of Fig. 4.8(d). Now, the more stiff W-Se bonds come into play and locally dampen the up-and-down motion.

4.4 Distance-dependent damping of the $SnSe_2$ phonon signature near the interface

In addition to zero-dimensional point defects, the heterostructure sample offers 1D defects, in other words in-plane interfaces, at which the local phonon environment can be explored. Figure 4.9 shows the interface between $SnSe_2$ and WSe_2 at different bias voltages. The states along the interface appear disordered and defects appear close to the interface on both sides. Especially for negative bias, the interface-associated states extend far away from the interface and merge with the states of a nearby W_{Sn} defect in the $SnSe_2$ lattice. To investigate the phonon environment, THz-CC measurements were performed with varying proximity to the interface. Their spectral amplitudes

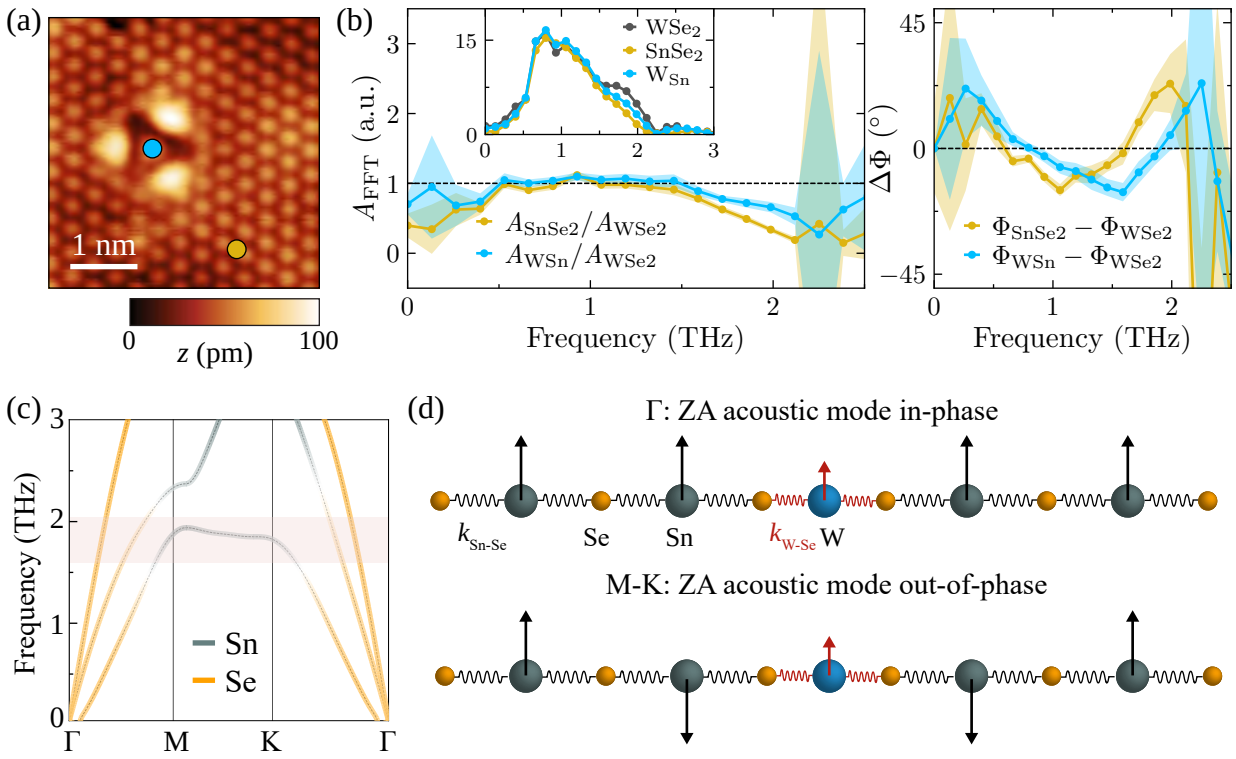

Figure 4.8 Phonon suppression by W_{Sn} defect on $SnSe_2$. (a) Topography scan of an isolated W_{Sn} defect on the $SnSe_2$ surface ($V_{d.c.}$ = 1.3 V, $I_{d.c.}$ = 10 pA). (b) Results of atomic-scale THz-TDS performed on pristine $SnSe_2$ compared to a W_{Sn} defect as indicated in (a) both referenced to the same location on the pristine WSe_2 surface (see Fig. 4.4), which lacks the 2 THz mode. Left inset: Amplitude spectra of THz-CC waveform measurements (set of five measurements, constant height with 5 Å approach, initial tip height set by $V_{d.c.}$ = 1.3 V, $I_{d.c.}$ = 10 pA, terahertz field strength $SnSe_2$: 28.1 V/cm, W_{Sn} defect: 37.5 V/cm) in the locations marked in (a) as well as on WSe_2 (Fig. 4.4(b)). Left main graph: divided amplitude spectra of the W_{Sn} defect referenced to the WSe_2 surface (blue curve). THz-TDS of the pristine $SnSe_2$ surface, is shown in yellow for comparison referenced to the same pristine WSe_2 location. On the W_{Sn} defect, the 2 THz mode is suppressed compared to the pristine $SnSe_2$ surface. Right panel: Subtracted phase spectra showing a consistent feature. (c) Phonon band structure of the acoustic modes in pristine $SnSe_2$. The colors indicate which atom species dominates (gray: Sn, orange: Se). The lowest band corresponds to the out-of-plane (ZA) acoustic flexural mode. (d) Simplified schematic of the atom movement in the ZA branch. Top: Toward the Γ-point $\omega(q \rightarrow \Gamma) = 0$; all atoms move in-phase out-of-plane. Bottom: Away from the Γ-point toward the edge of the Brillouin zone, the movement remains out-of-plane but the atoms of different unit cells move out-of-phase with each other. The spring constant for k_{W-Se} (red springs) is more rigid than k_{Sn-Se} (black springs) leading to a suppression of the Sn-dominated phonon mode at the defect site.

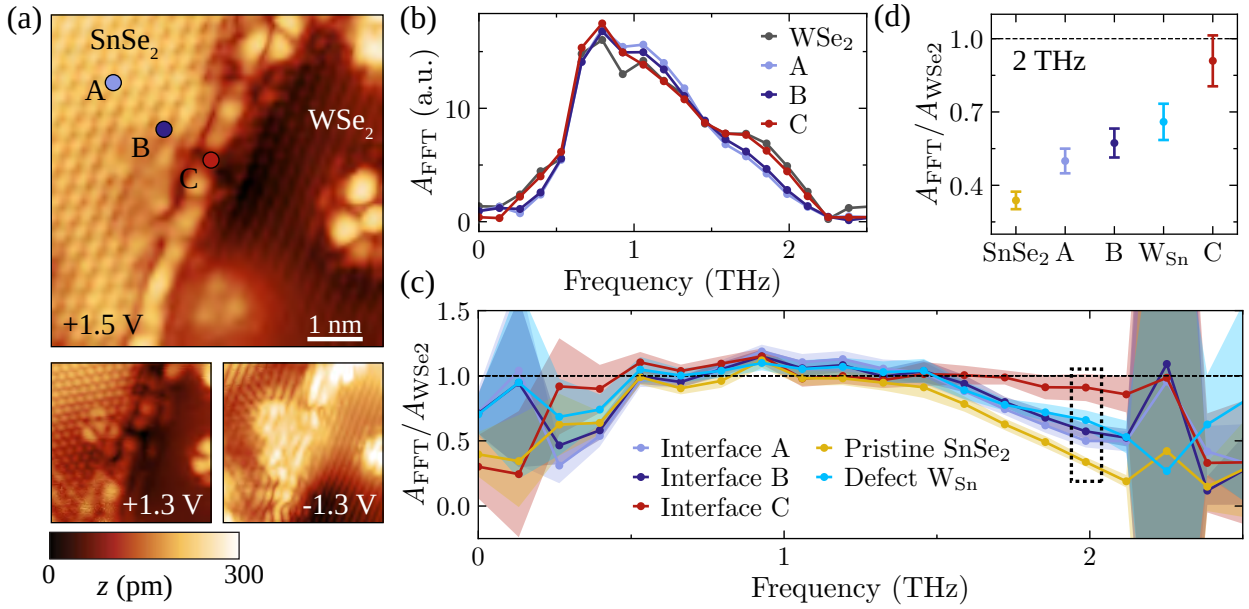

Figure 4.9 Phonon suppression at the in-plane interface. (a) Topography scans of an in-plane interface with $SnSe_2$ on the left and WSe_2 on the right. Measurement parameters: $I_{d.c.} = 50\,pA$, $V_{d.c.} = 1.5\,V$ (top), $I_{d.c.} = 10\,pA$, $V_{d.c.} = 1.3\,V$ (bottom left), $I_{d.c.} = 50\,pA$, $V_{d.c.} = -1.3\,V$ (bottom right). (b) Amplitude spectra retrieved via FFT using a Hamming window from THz-CC waveforms recorded in the locations A, B and C indicated in (a) and on pristine WSe_2 (which is used as a reference for THz-TDS). The spectra are shown as averages of three measurements (five for WSe_2) and were recorded in constant height mode with the tip approached by 5 Å from $I_{d.c.} = 10\,pA$, $V_{d.c.} = 1.3\,V$. The field strength for A, B and C was 34.4 V/cm and 28.1 V/cm for the WSe_2 reference. (c) Amplitudes of locations A, B and C divided by the WSe_2 reference shown for comparison with the divided amplitudes from Fig. 4.8(b). (d) Divided amplitudes at 2 THz (black dashed box in (c)) ordered by magnitude for the different locations on the sample.

along with that of the pristine WSe_2 surface reference are shown in Fig. 4.9(b). Similar to the W_{Sn} defect in Fig. 4.8, the amplitude in the frequency region of the flexural phonon mode grows larger with increasing proximity to the interface compared to the WSe_2 reference. The relative attenuation of the phonon mode with regard to different features on the $SnSe_2$ surface can be extracted from the divided spectra using pristine WSe_2 as a reference, which lacks phonon density of states in this frequency range (Fig. 4.9(c)). The divided amplitudes at 2 THz are ordered by magnitude in Fig. 4.9(c). This results in an increased attenuation of the pristine $SnSe_2$ phonon mode from small attenuation at location A (farthest away from interface), then location B near the interface, followed by the measurement directly on the W_{Sn} defect (from Fig. 4.8) and finally the interface (location C) that attenuates the phonon modes within error margins of the WSe_2 surface, which does not exhibit the mode and therefore accounts for full attenuation.

Imaging at ultra-low tip heights using THz-STM, as already demonstrated for the defects in Fig. 4.6(b), is also a promising tool for the investigation of the in-plane interface. The section

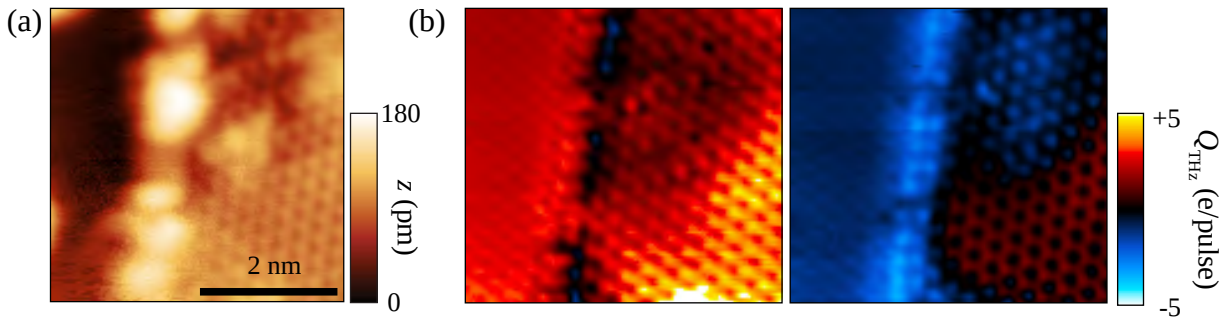

Figure 4.10 THz-STM imaging of the in-plane interface with low tip heights. (a) Topography scan of an in-plane interface region with WSe_2 on the left and $SnSe_2$ on the right ($I_{d.c.}$ = 10 pA, $V_{d.c.}$ = 1.3 V). (b) THz-STM imaging of the same area with positive (negative) field polarity on the left (right). The tip was approached by 4 Å from $I_{d.c.}$ = 10 pA, $V_{d.c.}$ = 1.3 V and the terahertz field strength was set to $E_{THz,pk}$ = 21.9 V/cm.

of interface (WSe_2 left, $SnSe_2$ right) in Fig. 4.10(a), imaged with conventional STM topography, appears disordered. Imaging with THz-STM, however, reveals the atomic lattice connectivity at the interface. The disordered region observed in the top right corner on the $SnSe_2$ lattice in Fig. 4.10(a), can be investigated more closely with THz-STM imaging. In fact, it seems as if the top Se atoms are present but distorted from the regular lattice periodicity. Further, this region of the $SnSe_2$ lattice shows negative rectified charge when imaged with negative terahertz field strength opposed to the typical positive signal for both field strength polarities (see THz-STS in Fig. 4.3(b)). Likely, this irregular lattice region is due to the growth process where the $SnSe_2$ grew off the side of the WSe_2. An explanation for the lattice distortion could be atoms intercalated between the top $SnSe_2$ layer and the WSe_2 underneath.

4.5 Discussion and conclusions

In GaAs(110), the defect exhibited a resonance different from the surface, whereas for the TMD heterostructure the defect and in-plane interface suppress a surface resonance. Phonon-defect scattering is often treated within macroscopic transport models, where the scattering rate is described as a function of defect density [4]. However, atomic-scale phonon spectroscopy can reveal which defects or interfaces have the most pronounced effect on the phonons in a material and can, for example, inform the growth procedure to prefer metal- or chalcogen-rich evaporation to tune the phonon properties of a heterostructure device in the future. Flexural phonon modes, such as the one studied in this chapter play a dominant role in thermal transport properties of 2D materials, e.g., in graphene [34], which are highly relevant when using such materials to design devices. Developing a better microscopic understanding of phonon-defect and phonon-interface scattering is desirable as these processes can become particularly important at low temperatures and in heterostructure samples.

While the calculated phonon and electronic band structures agree well with the experimental

results, the mechanism with which the terahertz pulses couple to the lattice vibration remains to be explained in more detail on a theoretical level. The flexural acoustic mode studied here represents an out-of-plane atomic motion, aligned with the direction of the terahertz field at the STM tip. The mode observed at the GaAs(110) defect in the previous chapter appeared as a peak in the referenced spectrum (i.e., it increased the spectral amplitude relative to the pristine surface). The same behavior is observed for optical phonon modes on WTe_2 discussed in the next Chapter. In the case of $SnSe_2$ referenced to WSe_2 the acoustic phonon mode appears as a dip in the amplitude spectrum. This difference may reflect distinct coupling mechanisms. While the response in GaAs(110) and WTe_2 may be dominated by resonant enhancement of the local polarization (e.g., the GaAs(110) defect acting as a locally resonant dipole), the flexural acoustic mode in $SnSe_2$ may instead primarily modify the local junction response through damping and absorption, which results in a suppression of the referenced amplitude.

In conclusion, in the $SnSe_2/WSe_2$ heterostructure, W atoms at Sn sites and at in-plane interfaces locally suppress a phonon mode. These results demonstrate that atomic-scale THz-TDS is a powerful tool for developing a microscopic understanding of the dielectric and phonon environment of a material and how these are influenced by local disorder. Ultimately, this opens a path toward microscopic phonon engineering in layered materials.

4.6 Outlook: From local disorder to collective order in 2D materials

So far, the focus of atomic-scale THz-TDS measurements has been on atomic-scale defects and how they either carry features in the complex dielectric function (Chapter 3) [14] or how they influence the dielectric environment locally on a surface exhibiting a phonon mode (this Chapter). As a next step, samples with a collective order are considered. Of particular interest are monolayer 2D materials with a charge density order. Charge density wave (CDW) materials in bulk form, namely TaS_2 and $NbSe_2$, have already shown interesting results with THz-STM [35, 36]. Mono- to few-layer samples with confinement of the CDW order both vertically by the substrate and vacuum and laterally by the edges of islands is relevant for nanoscale device design, where these confinement effects play a major role.

Figure 4.11 and Fig. 4.12 show preliminary data demonstrating the potential of such samples, in this case VSe_2 and VTe_2. Both materials were grown by molecular beam epitaxy, capped with multiple chalcogen (Se and Te) layers. The surface was decapped *in situ* by evaporating the protecting layers through heating. Figure 4.11(a) shows monolayer VSe_2 islands on HOPG with small bi-layer islands at the bottom center of the scan. The zoom in on the VSe_2 surface in Fig. 4.11(b) shows the CDW on the VSe_2 surface, while Fig. 4.11(c) demonstrates a clean HOPG substrate. Imaging the VSe_2 surface with different terahertz field strengths and both polarities reveals a pattern associated with the CDW (Fig. 4.11(d)), but with a different shape than observed

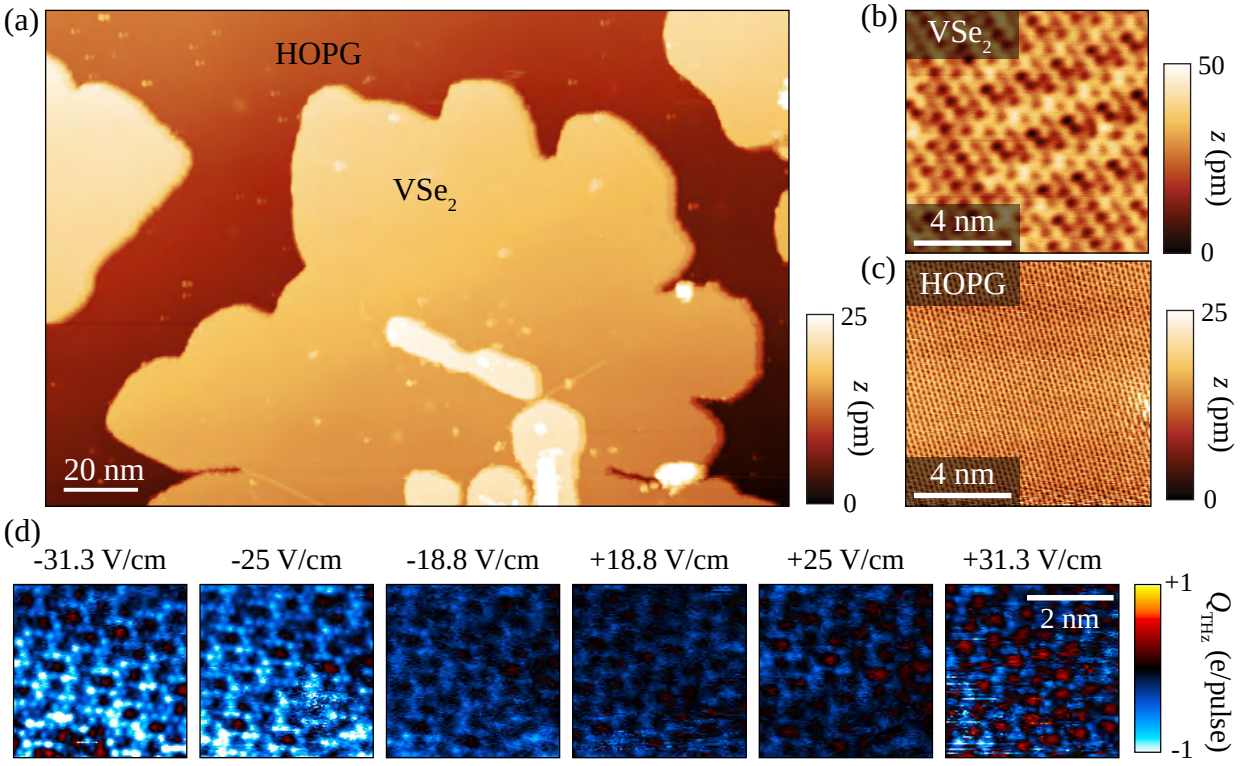

Figure 4.11 Monolayer VSe_2 islands on HOPG. (a) Large-scale topography scan of several VSe_2 islands ($I_{d.c.}$ = 8 pA, $V_{d.c.}$ = 1.5 V). (b) Close-up topography image of an area on VSe_2 ($I_{d.c.}$ = 10 pA, $V_{d.c.}$ = −1.0 V). (c) Close-up of the HOPG substrate ($I_{d.c.}$ = 100 pA, $V_{d.c.}$ = −0.5 V). (d) A series of THz-STM images at different field strengths indicated at the top. Imaging was performed in constant height with the tip approached by 3.5 Å from $I_{d.c.}$ = 100 pA, $V_{d.c.}$ = 1.0 V.

in the conventional STM topography. These are promising preliminary results as the sensitivity of THz-STM imaging to the CDW pattern opens up multiple possibilities for future measurements, such as terahertz- or optical-pump-driven dynamics.

If Se is replaced by Te in the lattice, the material continues to exhibit a CDW order, but on top of that, its appearance strongly depends on the d.c. bias voltage. Figure 4.12 shows STM topography images of this effect on a monolayer VTe_2 sample. Besides the shape of the CDW changing with bias, the topography scans, taken across a domain boundary clearly show the influence of line and point defects on the CDW pattern. This promises a versatile playground for THz-STM, combining the defect-related methods and results from this and the previous thesis chapter with collective order.

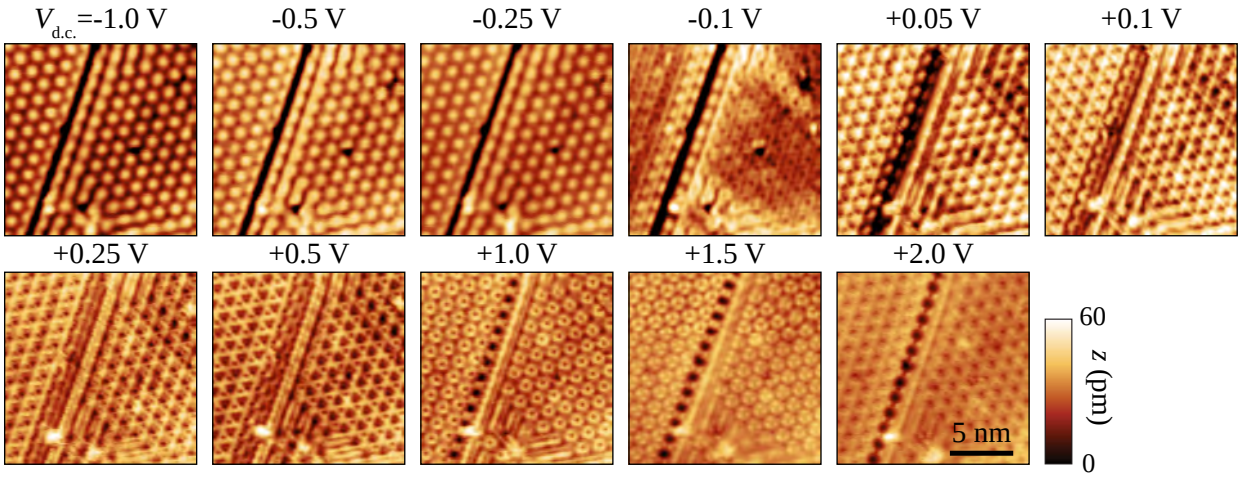

Figure 4.12 Bias-dependent charge density wave in VTe_2. Topography images on a monolayer VTe_2 island showing the charge density wave pattern around a domain boundary. The measurements were performed at the d.c. bias voltages indicated above and at $I_{d.c.}$ = 50 pA.

BIBLIOGRAPHY

[1] The Nobel Prize in Physics 2000. Available at https://www.nobelprize.org/prizes/physics/2000/kroemer/lecture/.

[2] Liu, A. *et al.* The Roadmap of 2D Materials and Devices Toward Chips. *Nano-Micro Letters* **16**, 119 (2024).

[3] Hong, J. *et al.* Exploring atomic defects in molybdenum disulphide monolayers. *Nature Communications* **6**, 6293 (2015).

[4] Hase, M. & Kitajima, M. Interaction of coherent phonons with defects and elementary excitations. *Journal of Physics: Condensed Matter* **22**, 073201 (2010).

[5] Radic, A., Liu, B., Rao, A. & Lambrick, S. Defect-modified acoustic phonons in a single layer of MoS_2 (2026). Available at http://arxiv.org/abs/2503.14464. ArXiv:2503.14464 [cond-mat].

[6] Schuler, B. *et al.* Large Spin-Orbit Splitting of Deep In-Gap Defect States of Engineered Sulfur Vacancies in Monolayer WS_2. *Physical Review Letters* **123**, 076801 (2019).

[7] Cochrane, K. A. *et al.* Spin-dependent vibronic response of a carbon radical ion in two-dimensional WS_2. *Nature Communications* **12**, 7287 (2021).

[8] Plankl, M. *et al.* Subcycle contact-free nanoscopy of ultrafast interlayer transport in atomically thin heterostructures. *Nature Photonics* **15**, 594–600 (2021).

[9] Liu, S. *et al.* Nanoscale coherent phonon spectroscopy. *Science Advances* **8**, eabq5682 (2022).

[10] Allerbeck, J. *et al.* Ultrafast Coulomb blockade in an atomic-scale quantum dot. *Nature Communications* **16**, 10806 (2025).

[11] Roelcke, C. *et al.* Ultrafast atomic-scale scanning tunnelling spectroscopy of a single vacancy in a monolayer crystal. *Nature Photonics* **18**, 595–602 (2024).

[12] Rai, V. N. *et al.* Influence of atomic-scale defects on coherent phonon excitations by THz near fields in an STM. *Science Advances* **11**, eadz6549 (2025).

[13] Jelic, V. *et al.* A General Approach to THz Near-Field Waveform Sampling in a Lightwave-Driven Scanning Tunneling Microscope Junction. In *2023 48th International Conference on Infrared, Millimeter, and Terahertz Waves (IRMMW-THz)*, 1–2 (2023). Available at https://ieeexplore.ieee.org/abstract/document/10299095.

[14] Jelic, V. *et al.* Atomic-scale terahertz time-domain spectroscopy. *Nature Photonics* **18**, 898–904 (2024).

[15] Jiang, J.-W., Wang, B.-S., Wang, J.-S. & Park, H. S. A review on the flexural mode of graphene: lattice dynamics, thermal conduction, thermal expansion, elasticity and nanomechanical resonance. *Journal of Physics: Condensed Matter* **27**, 083001 (2015).

[16] Callaway, J. & von Baeyer, H. C. Effect of Point Imperfections on Lattice Thermal Conductivity. *Physical Review* **120**, 1149–1154 (1960).

[17] Ammerman, S. E. *et al.* Lightwave-driven scanning tunnelling spectroscopy of atomically precise graphene nanoribbons. *Nature Communications* **12**, 6794 (2021).

[18] Dong, X. *et al.* Growth and Electronic Properties of $SnSe_2$ Films on Reconstructed, (111)-Oriented SrTiO3 Substrates. *The Journal of Physical Chemistry C* **127**, 16732–16739 (2023).

[19] Manzeli, S., Ovchinnikov, D., Pasquier, D., Yazyev, O. V. & Kis, A. 2D transition metal dichalcogenides. *Nature Reviews Materials* **2**, 17033 (2017).

[20] Chhowalla, M. *et al.* The chemistry of two-dimensional layered transition metal dichalcogenide nanosheets. *Nature Chemistry* **5**, 263–275 (2013).

[21] Lu, T. *et al.* Synthesizability of transition-metal dichalcogenides: a systematic first-principles evaluation. *Materials Futures* **2**, 015001 (2023).

[22] Kaliyan, G., Sivasamy, R. & Espinoza-González, R. Electronic structure, optical and thermodynamic studies on 2D $SnSe_2$ nanosheet: A first-principles investigation. *Superlattices and Microstructures* **133**, 106182 (2019).

[23] Ammerman, S. E., Wei, Y., Everett, N., Jelic, V. & Cocker, T. L. Algorithm for subcycle terahertz scanning tunneling spectroscopy. *Physical Review B* **105**, 115427 (2022).

[24] Cai, Q., Wei, B., Sun, Q., Said, A. H. & Li, C. Monolayer-like lattice dynamics in bulk WSe_2. *Materials Today Physics* **28**, 100856 (2022).

[25] Zhao, W. L. Z., Tikhonov, K. S. & Finkel'stein, A. M. Flexural phonons in supported graphene: from pinning to localization. *Scientific Reports* **8**, 16256 (2018).

[26] Cocker, T. L., Jelic, V., Hillenbrand, R. & Hegmann, F. A. Nanoscale terahertz scanning probe microscopy. *Nature Photonics* **15**, 558–569 (2021).

[27] Jelic, V. *et al.* Terahertz field control of surface topology probed with subatomic resolution. *Nature Photonics* **19**, 1048–1055 (2025).

[28] Barja, S. *et al.* Identifying substitutional oxygen as a prolific point defect in monolayer transition metal dichalcogenides. *Nature Communications* **10**, 3382 (2019).

[29] Chen, H.-Y. *et al.* Atomically Resolved Defect-Engineering Scattering Potential in 2D Semi-

conductors. *ACS Nano* (2024).

[30] Yue, C. *et al.* Identification and Manipulation of Atomic Defects in Monolayer SnSe. *ACS Nano* **18**, 25478–25488 (2024).

[31] Schuler, B. *et al.* How Substitutional Point Defects in Two-Dimensional WS_2 Induce Charge Localization, Spin–Orbit Splitting, and Strain. *ACS Nano* **13**, 10520–10534 (2019).

[32] Mitterreiter, E. *et al.* The role of chalcogen vacancies for atomic defect emission in MoS_2. *Nature Communications* **12**, 3822 (2021).

[33] Andriotis, A. N. & Menon, M. Tunable magnetic properties of transition metal doped MoS_2. *Physical Review B* **90**, 125304 (2014).

[34] Lindsay, L., Broido, D. A. & Mingo, N. Flexural phonons and thermal transport in graphene. *Physical Review B* **82**, 115427 (2010).

[35] Sheng, S. *et al.* Terahertz spectroscopy of collective charge density wave dynamics at the atomic scale. *Nature Physics* **20**, 1603–1608 (2024).

[36] López, L. E. P. *et al.* Atomic-scale ultrafast dynamics of local charge order in a THz-induced metastable state of 1T-TaS_2 (2025). Available at http://arxiv.org/abs/2505.20541. Issue: arXiv:2505.20541 arXiv:2505.20541 [cond-mat].

CHAPTER 5

TERAHERTZ FIELD CONTROL OF SURFACE TOPOLOGY PROBED WITH SUBATOMIC RESOLUTION

Light-induced phase transitions offer a method to dynamically modulate topological states in bulk complex materials. Yet, next-generation devices demand nanoscale architectures with contact resistances near the quantum limit and precise control over local electronic properties. The layered material WTe_2 has gained attention as a likely Weyl semimetal, with topologically protected linear electronic band crossings hosting massless chiral fermions. The results presented in this chapter demonstrate a local phase transition facilitated by light-induced shear motion of a single atomic layer at the surface of bulk WTe_2, thereby opening the door to nanoscale device concepts. Ultrafast terahertz fields enhanced at the apex of an atomically sharp tip couple to the key interlayer shear mode of WTe_2 via a ferroelectric dipole at the interface, inducing a structural phase transition at the surface to a metastable state. Subatomically resolved differential imaging, combined with hybrid-level density functional theory, reveals a shift of 7 ± 3 picometers in the top atomic plane. Tunneling spectroscopy links electronic changes across the phase transition with the electron and hole pockets in the band structure, suggesting a reversible, light-induced annihilation of the topologically-protected Fermi arc surface states in the top atomic layer.

This chapter closely follows Ref. [1].

5.1 Introduction

With technology reaching the limits of conventional design and fabrication, next-generation device concepts based on nanoscale architectures, terahertz clock rates, and complex material systems are becoming increasingly important. For example, light-induced phase transitions in complex materials promise a route to ultrafast switching of versatile electronic and photonic devices [2–7]. Materials with switchable, topologically non-trivial phases are especially intriguing because of their symmetry-protected states, which offer unique electronic properties.

Theoretical calculations [8–23] and experimental studies with STM [16–18], angle-resolved photoemission spectroscopy (ARPES) [9–13, 24, 25], and transport measurements [14] suggest that the non-centrosymmetric T_d phase of bulk WTe_2 is a type-II Weyl semimetal at low temperature. Weyl semimetals are characterized by the presence of 3D linear electronic band crossings, which split into pairs of so-called Weyl points (WPs) with opposite chirality due to the absence of inversion symmetry. The WPs are non-degenerate in momentum space and connected by topologically protected open-energy-contour surface states [26] (Fig. 5.1(a)). These states exist exclusively in the surface band structure and are called Fermi arc surface states. Weyl semimetals can be classified into type-I, where the WPs are located at the Fermi level and appear as points in the Fermi surface (Fig. 5.1(b), left), and type-II, where the Weyl cones are tilted, such that the WPs appear as the

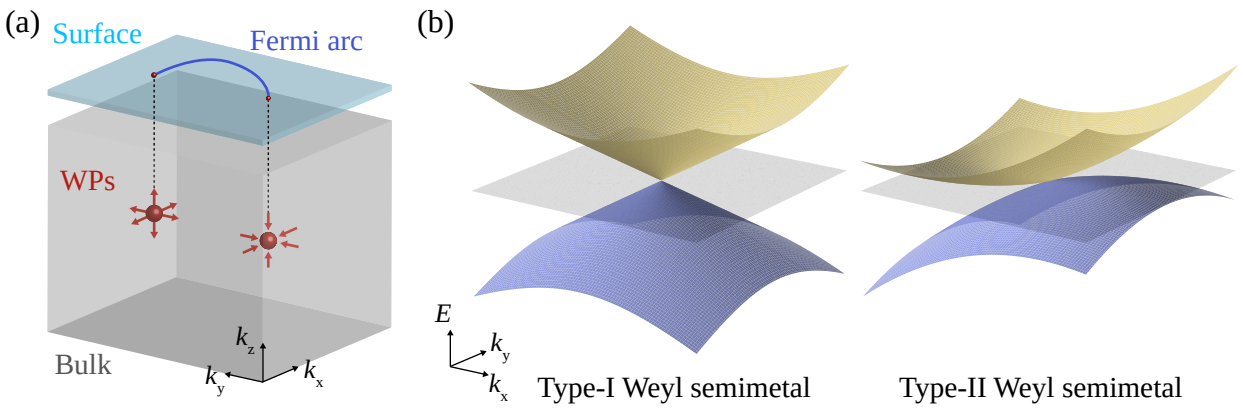

Figure 5.1 Type-II Weyl semimetals. (a) Weyl points (WPs) are monopoles of opposite chirality in the bulk momentum space. Projected onto the surface, they are connect by a Fermi arc surface state. (b) Left: Type-I Weyl semimetal with a point-like Fermi surface constituting the Weyl point. Right: Type-II Weyl semimetal, where the Weyl point is the touching point between an electron and a hole pocket.

contact point of an electron and a hole pocket (Fig. 5.1(b), right) [8].

In addition to these topological properties, ultrafast excitation at visible [27, 28], near-infrared [19–21, 28–30], mid-infrared [19] and terahertz [19] frequencies has been shown to drive an interlayer shear mode in WTe_2. When this shear displacement reaches a critical amplitude, it induces a structural phase transition that restores inversion symmetry, which leads to an annihilation of the Weyl points and, hence, a topological electronic phase transition from a Weyl semimetal to a trivial semimetal [19].

In contrast to its bulk form, monolayer WTe_2 is a quantum spin Hall insulator in its low-temperature ground state [31]. Moreover, the stacking of few-layer WTe_2 leads to spontaneous out-of-plane electric polarization [32–35]. The orientation of this ferroelectric dipole can be switched through a sliding motion of the top atomic layer, which can be induced by a vertical field on the scale of 0.1–0.2 V/nm when applied uniformly normal to the sample surface [32, 35]. A similar shift of the top atomic layer of bulk WTe_2 has been activated by static doping with adsorbed potassium atoms [36].

The results presented in the following show that terahertz fields enhanced at the atomically sharp STM tip apex and polarized normal to a bulk WTe_2 surface couple to its ferroelectric dipole. When these terahertz near-fields exceed 1 V/nm, they induce a localized structural phase transition of the topmost atomic layer, driving it from the low-temperature T_d phase to a metastable state characterized by both shear translation and intralayer distortion. As a result, the electronic structure at the vacuum interface undergoes a phase transition, where the top layer can no longer host Fermi arc surface states. Since the region of phase transition is localized, this effectively constitutes a light-induced heterostructure. Density functional theory (DFT) calculations using hybrid exchange-

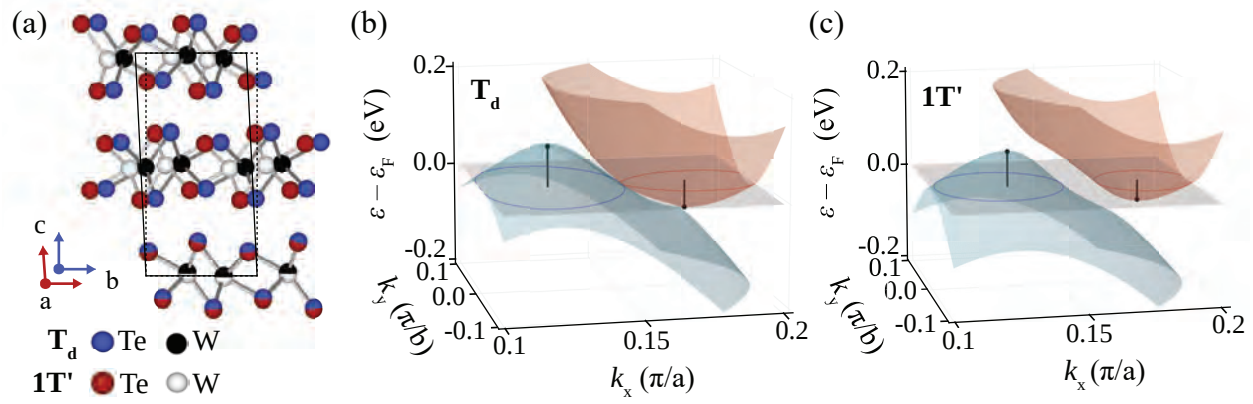

Figure 5.2 Structural and electronic phases of WTe_2. (a) Unit cells for the orthorhombic T_d phase (blue and black spheres) and monoclinic 1T' phase (red and white spheres). The solid black line highlights the ≈4° tilt of the unit cell for 1T' with respect to T_d (dashed black line). (b),(c) Three-dimensional visualization of the band structure for the optimized bulk T_d phase in (b) and 1T' phase in (c) along the $k_x - k_y$ plane, near the band crossing.

correlation functionals are integral to this analysis, providing a comprehensive understanding of the ground and metastable states observed in experiments along with insight into the stability of the Weyl points.

5.2 Shear motion induced by tip-enhanced terahertz-fields

A single layer of WTe_2 is comprised of tungsten atoms sandwiched between tellurium atoms (Fig. 5.2(a)). In a bulk crystal, these layers are stacked through van der Waals bonding. Intermetallic bonding between the tungsten atoms leads to zigzag chains in the $\vec{a}$-axis of the unit cell, which distorts the otherwise hexagonal structure and results in a corrugated surface [16–18, 23, 37]. The T_d phase (blue and black atoms in Fig. 5.2(a)), which is the low temperature ground state of WTe_2, has an orthorhombic unit cell with broken inversion symmetry. In 2015, T_d-WTe_2 was proposed as a candidate type-II Weyl semimetal [8]. In contrast, 1T'-WTe_2 – the lattice structure at high temperature [38] or high pressure [39] – is monoclinic and inversion symmetric (red and white atoms in Fig. 5.2(a)), which prohibits Weyl points in the band structure. Figure 5.2(b) and (c) show the 3D electronic band structure (calculated by DFT, see methods section in Ref. [1] for computational details) in the region of momentum space where the Weyl point band crossings in the T_d phase (Fig. 5.2(b)) are lifted for the 1T' phase (Fig. 5.2(c)) of WTe_2. The transition from T_d-WTe_2 to 1T'-WTe_2 is associated with a shift of the individual layers, resulting in a change of the angle between the unit cell vectors $\vec{b}$ and $\vec{c}$ from 90° to ≈94°.

All experiments presented in the following were conducted using the experimental setup described in Chapter 2.5. The WTe_2 samples are commercially sourced (2Dsemiconductors USA) single crystals, grown using the float zone technique to prevent halide contamination, with a confirmed purity of 99.9999% (6N). Before loading them into the STM chamber, the WTe_2 crystals

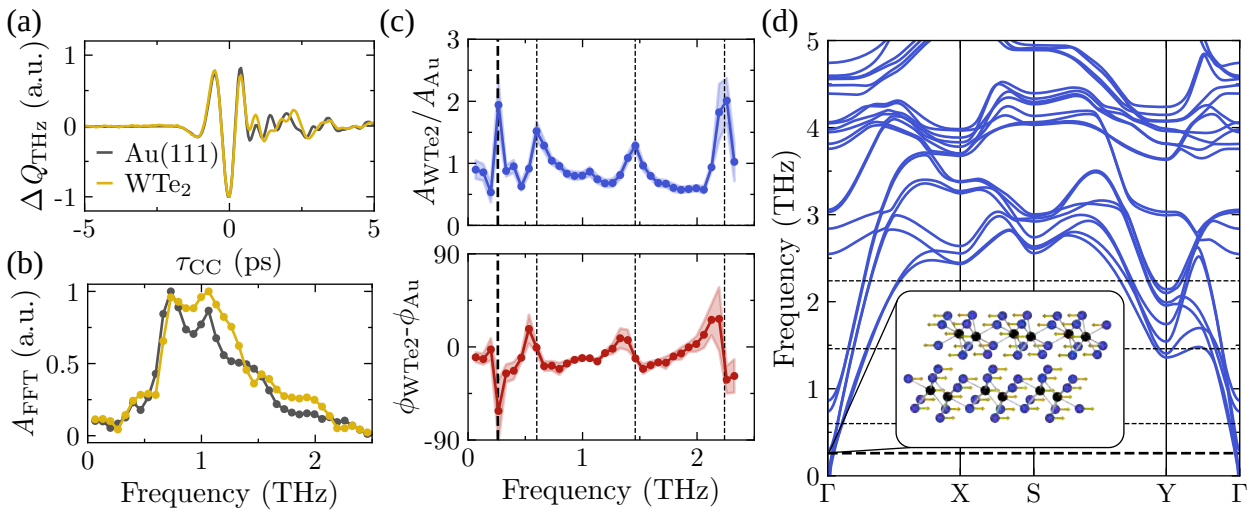

Figure 5.3 Atomic-scale THz-TDS of WTe_2. (a) THz-CC waveforms acquired on a WTe_2 surface (yellow curve) and Au(111) surface (gray curve). Parameters during waveform acquisition on WTe_2: $V_{d.c.}$ = 1 V, $I_{d.c.}$ = 100 pA, $E_{THz,pk}$ = 190 V/cm, $E_{WF,pk}$ = 7 V/cm, and on Au(111): $V_{d.c.}$ = 10 mV, $I_{d.c.}$ = 100 pA, $E_{THz,pk}$ = 150 V/cm, $E_{WF,pk}$ = 7 V/cm. The data are shown as mean values of five individual scans. (b) Amplitude spectra of the waveforms shown in (a). (c) THz-TDS of the tunnel junction shows resonances at 0.26 THz, 0.60 THz, 1.46 THz and 2.24 THz (dashed black lines) in both the spectral amplitude (top, blue) and phase (bottom, red). The THz-TDS shown here utilizes the waveforms in (a). The data is shown as mean values ± standard deviation of five individual scans. (d) Phonon dispersion of T_d-WTe_2 calculated using DFT with the hybrid PBE0 functional of a two-layer slab along the Γ−X−S−Y−Γ path. Inset: Schematic of the shear mode associated with a phase transition in WTe_2, occurring at a frequency of 0.26 THz (arrow lengths are exaggerated for clarity).

were affixed to a metallic sample holder plate using conductive epoxy resin. To cleave the sample *in situ*, a ceramic rod was attached to the WTe_2(001) surface with epoxy and cleaved under ultrahigh-vacuum (UHV) inside the STM chamber at 77 K, revealing an atomically clean surface with a low density of defects and step-edges. A terrace was not directly observed in the STM scan area except for a single instance.

The STM bias voltage, $V_{d.c.}$, determines the difference between the Fermi levels of the tip and sample and thereby defines the energy range of electronic states contributing to the tunnel current, I_{STM}, from the WTe_2 sample. The ultrafast terahertz pulses coupled to the STM tip experience a field enhancement of $>10^5$ at its apex [40–44]. As a result, terahertz pulses with peak fields of 20 V/cm in free space generate transient fields of approximately 1 V/nm across the tip–sample junction, driving a tunnel current I_{STM} measured via lock-in detection (see Chapter 2.5.2.2). In this chapter, I_X and I_Y represent the in-phase and out-of-phase components of the terahertz lock-in signal.

Atomic-scale THz-TDS (see Chapter 3 for details) is performed to determine the dielectric

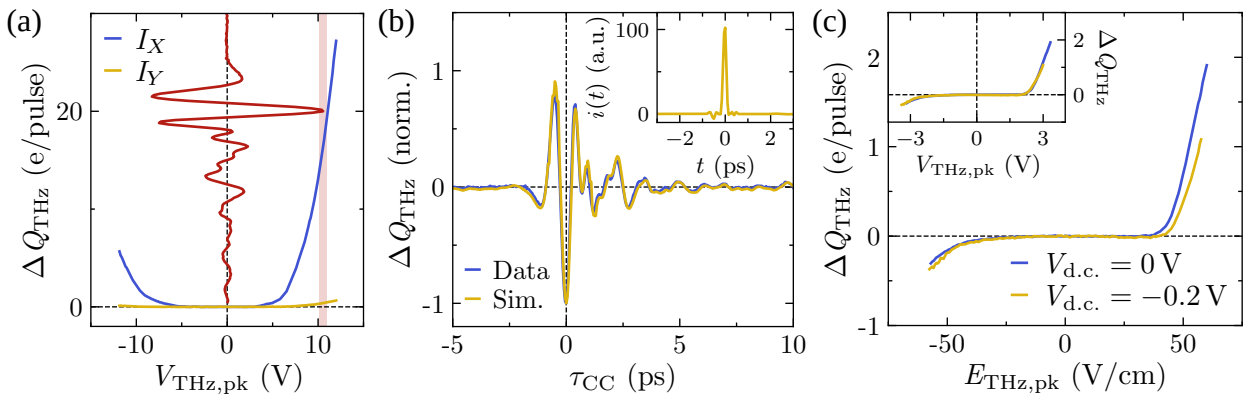

Figure 5.4 WTe_2 near-field waveform validation and voltage calibration. (a) $I_{\mathrm{THz}} - V_{\mathrm{THz,pk}}$ curve with both in-phase (I_{X}, blue curve) and out-of-phase (I_{Y}, yellow curve) components of the terahertz-induced tunnel current (I_{THz}). The strong terahertz pulse (red curve) indicates where waveform sampling takes place along the $I_{\mathrm{THz}} - V_{\mathrm{THz,pk}}$ curve. The red shading shows the range of the weak terahertz pulse, with a peak field strength of $E_{\mathrm{THz,pk}} = 7\,\mathrm{V/cm}$ ($V_{\mathrm{THz,pk}} = 0.4\,\mathrm{V}$). (b) Measured (blue curve) and simulated (yellow curve) THz-CC waveforms confirming that the waveform input to the simulation (blue curve) is an accurate representation of the terahertz voltage transient at the STM tip apex. Inset: Simulated current pulse generated by the terahertz voltage waveform applied to the $I - V$ characteristic that was extracted from the $I_{\mathrm{THz}} - V_{\mathrm{THz,pk}}$ curve in (a) using a polynomial model with $N = 11$. The presence of a single unipolar current pulse validates the waveform measured on WTe_2 via THz-CC (blue curve in (b)). The validation of the waveform on Au(111) that was used for this study is shown in Chapter 3. (c) Voltage calibration performed for the terahertz waveform on WTe_2. A pair of $I_{\mathrm{X}} - E_{\mathrm{THz,pk}}$ curves acquired at $V_{\mathrm{d.c.}} = 0\,\mathrm{V}$ (blue line) and $V_{\mathrm{d.c.}} = -0.2\,\mathrm{V}$ (yellow line) are used to calibrate the peak terahertz voltage by translating the yellow line along the x-axis by 3.6 V/cm (inset), equivalent to 0.20 V, which results in a calibration constant of $\alpha = (1\,\mathrm{V})/(18\,\mathrm{V/cm})$. The measurements were performed on WTe_2 at constant tip height after a 200 pm tip retraction from an initial tip–sample separation set by $V_{\mathrm{d.c.}} = 10\,\mathrm{mV}$, $I_{\mathrm{d.c.}} = 100\,\mathrm{pA}$.

response of the tip-sample junction at terahertz frequencies. For atomic-scale THz-TDS each terahertz pulse is divided into a strong-field pulse and a weak-field replica. The strong-field pulse creates a unipolar current pulse in the junction through lightwave-driven tunneling. By scanning the temporal delay between the weak-field pulse and the strong-field pulse, a terahertz near-field waveform is recorded for the weak pulse through the time dependence of I_{X}.

Prior to the measurements on WTe_2, a single crystal Au(111) sample (cleaned by repeated cycles of argon ion bombardment and annealing to 850 K) was used to acquire a reference waveform for atomic-scale THz-TDS (Fig. 5.3(a), gray) and to prepare the tip apex for all measurements on WTe_2. After exchanging samples from Au(111) to WTe_2, while preserving the alignment of the terahertz-pulse-train on the tip apex, the near-field waveform was recorded on the WTe_2 surface (Fig. 5.3(a), yellow). The waveform was successfully validated following the procedure described in Chapter 3 (good agreement between measured and simulated waveform and a strong-field induced unipolar

current pulse). The validation measurements and results are shown in Fig. 5.4(a) and (b). Terahertz field to STM voltage calibrations (following the procedure described in Chapter 2.5.3.3) yields a calibration factor of $\alpha = (1\,\mathrm{V})/(18\,\mathrm{V/cm})$ for measurements performed on the WTe_2 surface (Fig. 5.4(c)) and $\alpha = (1\,\mathrm{V})/(15\,\mathrm{V/cm})$ for measurements on Au(111).

The amplitude spectra, obtained from FFT of the oscillating near-field waveforms in the tunnel junction, of both reference and sample waveform are displayed in Fig. 5.3(b). The blue spectrum at the top of Fig. 5.3(c) shows the spectral amplitude for the WTe_2 sample obtained from division by the reference spectrum measured on Au(111) to remove the spectral response of antenna coupling to the tip. The red spectrum in Fig. 5.3(c) shows the corresponding phase difference between reference and sample.

The peaks at 0.26 THz, 0.60 THz, and 2.24 THz in the experimental spectra agree with past literature [19, 21, 27–30, 45, 46] and the phonon band structure at the Γ point calculated for this study (Fig. 5.3(d)). Meanwhile, the peak at 1.46 THz may be spectrally bright due to the broad range of momentum vectors in the evanescent terahertz near-field at the tip apex [43], which can excite phonons away from the Γ point. The atomic motion for the 0.26 THz mode is illustrated in the inset of Fig. 5.3(d). This mode is associated with the phase transition from T_d to 1T' [19–21, 27–30, 46]. Despite its primarily in-plane motion (and hence in-plane dipole), the 0.26 THz shear mode is driven by the vertically oriented terahertz near-fields, which couple to the out-of-plane ferroelectric dipole at the surface [32–35]. While field-driven hole doping has been proposed as one mechanism for initiating this shear motion [19], other studies [19–21, 27–30, 46] have attributed its non-resonant excitation to impulsive stimulated Raman scattering [20, 29] or displacive excitation of coherent phonons [27, 28, 30]. However, no clear signatures of these mechanisms, such as the surge in tunnel current that would be expected with field-induced carrier doping, were observed in the measurements presented in this chapter. The absence of doping signatures, the presence of a strongly enhanced out-of-plane terahertz near-field, and the close agreement between the measured terahertz spectral resonances and DFT-predicted shear mode frequencies all support coupling via an out-of-plane ferroelectric dipole as the dominant mechanism driving the interlayer shear mode in the experiments presented here.

5.3 Real-space differential imaging

Surprisingly, increasing the peak terahertz field in the STM junction (left-to-right in Fig. 5.5(a)) modifies the WTe_2 surface charge density observed in STM topography maps. This change is reversible, with the topography returning to its original state when the terahertz field is reduced. The top tellurium atoms of WTe_2 are the main contributors to the surface charge density [37]. Along the $\vec{b}$-axis, both the upper and lower tellurium atoms of the corrugated surface are visible at low terahertz fields, whereas only the topmost atoms contribute substantially to the image at high

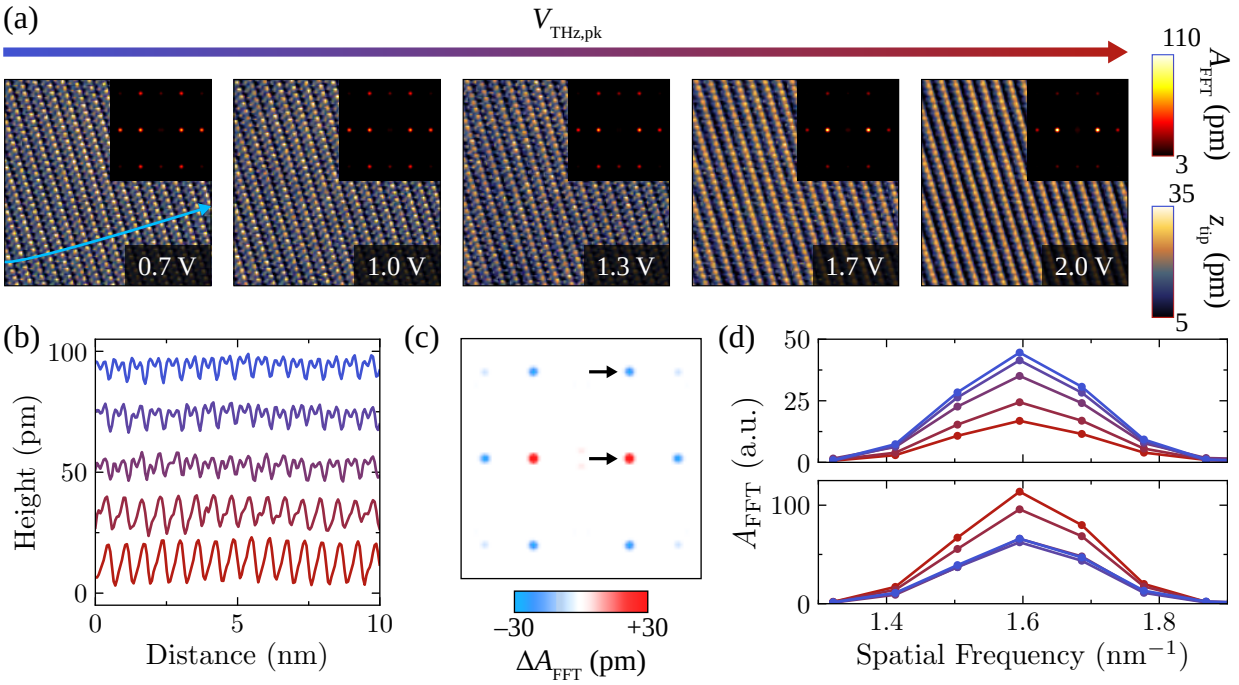

Figure 5.5 STM topography under terahertz pulse illumination. (a) STM topography acquired at $V_{\mathrm{d.c.}} = 10\,\mathrm{mV}$ and $I_{\mathrm{d.c.}} = 100\,\mathrm{pA}$ with $V_{\mathrm{THz,pk}}$ at 0.7 V (left), 1.0 V (middle left), 1.3 V (middle), 1.7 V (middle right) and 2.0 V (right). Chopper frequency 477 Hz; image size 10 nm × 10 nm. Insets: Symmetrized 2D Fourier transforms ($8\,\mathrm{nm}^{-1} \times 8\,\mathrm{nm}^{-1}$) of the topography images. (b) Cross-sections of the respective topography scans in (a) along the light blue arrow. The cross-sections are vertically offset for clarity. (c) Difference image between the right-most and left-most 2D Fourier transforms in (a). (d) Horizontal cross-sections of the Fourier peaks denoted by black arrows in (c), where the top graph corresponds to the top arrow and the bottom graph to the bottom arrow.

fields. The evolution of the surface periodicity is further emphasized in the cross-sections along the $\vec{b}$-axis in Fig. 5.5(b). Fig. 5.5(c) is a difference image of the Fourier amplitudes between the highest and lowest terahertz field strength (insets in Fig. 5.5(a)). Fig. 5.5(d) shows the peaks, indicated by arrows in Fig. 5.5(c), as a function of spatial frequency and field strength.

Such a strong influence of terahertz fields on topography has not been previously observed, suggesting a long-lived excitation of the sample to a metastable state, rather than an ultrafast tunnel current induced by the terahertz pulses [40, 42–44, 47]. Notably, within the experimental geometry employed here, the metastable state could not be produced using static electric fields from the STM tip alone. It could only be accessed using a terahertz electromagnetic drive, which can apply higher electric fields than STM due to the closer tip-sample proximity during THz-STM operation [48]. The STM topography modifications are observed under terahertz near-fields of $E_{\mathrm{THz,pk}} \approx 1\,\mathrm{V/nm}$, which are concentrated at the tip apex and decay radially outward. These terahertz fields are comparable to the static electric fields necessary for ferroelectric switching of

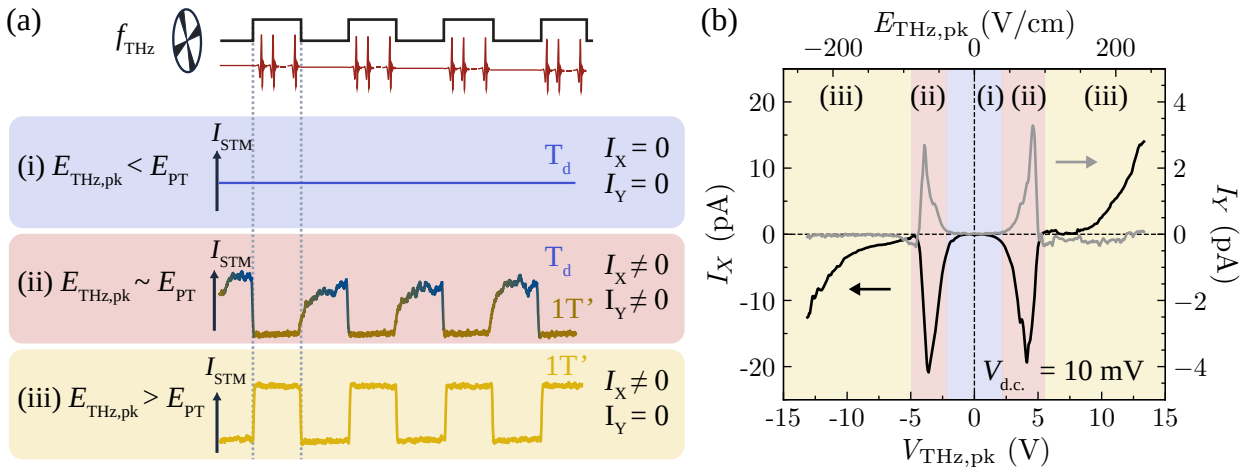

Figure 5.6 Terahertz field interaction regimes on WTe_2. (a) Schematic showing the different interaction regimes of WTe_2 within a THz-STM tunnel junction while an optical chopper modulates the incident terahertz-pulse-train (top). Experimental oscilloscope traces at $f_{THz} = 45$ Hz are shown for interaction regimes (ii),(iii) and a schematic constant line for regime (i) where no terahertz-induced signal is detected. (b) I_{THz}-$V_{THz,pk}$ curve on the WTe_2 surface acquired at $V_{d.c.} = -10$ mV and $z = z_0$ with the tip height, z_0, set by $V_0 = 10$ mV, $I_0 = 100$ pA. The solid black line shows the in-phase component (I_X), while the solid gray line shows the out-of-phase component (I_Y).

few-layer WTe_2 [33, 35] and the mid-infrared far-fields used to drive the phase transition in a bulk sample [19].

To measure the terahertz-induced phase transition in the THz-STM setup, the terahertz pulse train is modulated at a frequency f_{THz} (Fig. 5.6(a), top). Three regimes can be identified from the temporal response of the tunnel current I_{STM} (measured with an oscilloscope rather than a lock-in amplifier in Fig. 5.6(a)):

Regime i – Low terahertz field strength: For low field strengths, the terahertz pulse train does not affect the topography image or the tunnel current (schematically indicated by the constant line in Fig. 5.6(a)), and hence neither I_X nor I_Y is detected.

Regime iii – High terahertz field strength: For high field strengths, the terahertz pulse train induces a square-wave modulation of the tunnel current, producing a signal in I_X only ($I_Y = 0$), which corresponds to lightwave-driven tunneling [40, 42–44, 47–59].

Regime ii – Intermediate terahertz field strength: For intermediate field strengths, although the tunnel current is modulated at f_{THz}, it only responds rapidly when the terahertz pulse-train is unblocked. When the terahertz pulses are blocked by the chopper, the tunnel current recovers exponentially on a timescale comparable to the chopping period. This tunnel current behavior results from the terahertz-field-induced phase transition of T_d-WTe_2 to a metastable state, followed by a gradual return to the T_d phase. Since the metastable state is long-lived, the sample does not decay to the T_d ground state between individual terahertz pulses (spaced by 1 μs). Rather, the

ground state is recovered during the time that the chopper blade blocks the terahertz pulse train. The pronounced impact of the terahertz field on the topography observed in regime ii is unprecedented in THz-STM, as the peak field is present in the tunnel junction for only a fraction of a picosecond every microsecond, resulting in minimal modulation of the total current (and hence topography).

The signal measured using lock-in detection at higher modulation frequency in Fig. 5.6(b), referenced to a chopper in the terahertz beamline, consists of both an in-phase (I_X) and out-of-phase (I_Y) component due to the millisecond-scale recovery of the terahertz-induced phase transition toward the ground state. In THz-STS, sharp peaks emerge in both I_X and I_Y for terahertz near-fields of $\approx 1\,\mathrm{V/nm}$. However, the peaks and the out-of-phase signal are only observed in the presence of a small STM bias voltage, which can be just a few mV, and therefore applies a field two to three orders of magnitude lower than the terahertz pulse across the 1 nm tunnel gap. The d.c. bias is critical because the terahertz field drives the phase transition while the d.c. bias acts as read-out, with the detected signal corresponding to the difference in current between the T_d phase and the metastable phase for a given tip position and $V_{d.c.}$. Only I_Y is exclusively associated with the difference measurement between the two phases because I_X additionally includes contributions from lightwave-driven tunneling, where the terahertz field acts as a quasi-static bias in the strong-field limit, as observed in previous THz-STM studies [40, 42–44, 47, 48].

The measurements for atomic-scale THz-TDS and the terahertz voltage calibration (Fig. 5.4) were performed within regime iii at field strengths that are larger than what is needed to drive the interlayer shear mode ($\sim 1\,\mathrm{V/nm}$) to ensure a lightwave-driven tunneling signal.

In THz-STM of WTe_2 the field enhancement is critical, as driving the phase transition requires terahertz pulses with peak amplitudes that are on the order of $10\,\mathrm{MV/cm}$ ($1\,\mathrm{V/nm}$), while the terahertz field strength incident on the tip is only $10\,\mathrm{V/cm}$. The precise $E_{THz,pk}$ required for regime ii is determined by both the microscopic tip geometry and the tip-sample distance, as both factors contribute to the overall field enhancement. When operating in regime ii, it is ensured that the sample has mostly recovered back to the T_d phase of WTe_2 from the terahertz-field-induced metastable state during the one millisecond window that the terahertz pulse train is fully blocked by the optical chopper operating at $f_{THz} = 477$ Hz (the modulation frequency used for all measurements unless indicated otherwise).

This recovery is verified by comparing the phase transition behavior at a reduced chopping frequency (Fig. 5.7(a)), ensuring consistent modulation of the field-driven phase transition throughout experiments. Fig. 5.7(a) shows how increasing the field strength from regime i into regime ii changes the signal from a square wave (quasi-instantaneously following the chopper modulation) to a clear decay associated with the decay of the excited state. Fig. 5.7(b) and (c) additionally illustrate the behavior at full chopping speed and the impact of the terahertz field strength and d.c. voltage on the lock-in output signal.

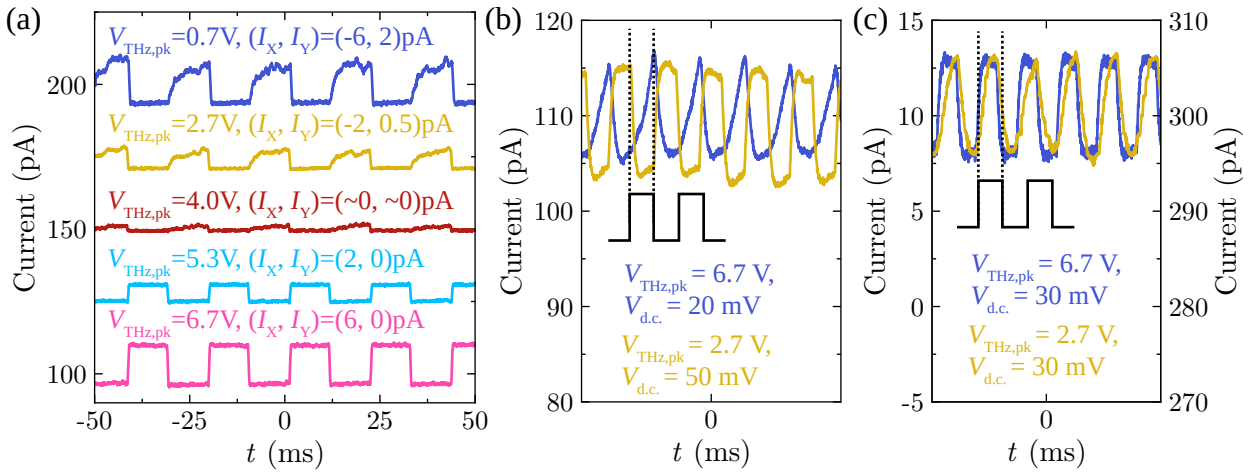

Figure 5.7 Oscilloscope traces of the total tunnel current. (a) A set of time traces acquired at $f_{\mathrm{THz}} = 45\,\mathrm{Hz}$, $V_{\mathrm{d.c.}} = 30\,\mathrm{mV}$ and $I_{\mathrm{d.c.}} = 100\,\mathrm{pA}$. The traces are vertically offset for clarity. The annotations state the terahertz-induced voltage and the average lock-in signal for both output channels. (b) A pair of time traces acquired at $V_{\mathrm{d.c.}} = 20\,\mathrm{mV}$, $I_{\mathrm{d.c.}} = 110\,\mathrm{pA}$, $V_{\mathrm{THz,pk}} = 6.7\,\mathrm{V}$ (blue curve) and $V_{\mathrm{d.c.}} = 50\,\mathrm{mV}$, $I_{\mathrm{d.c.}} = 110\,\mathrm{pA}$, $V_{\mathrm{THz,pk}} = 2.7\,\mathrm{V}$ (yellow curve), and a square-wave modulation of the terahertz-pulse-train at $f_{\mathrm{THz}} = 477\,\mathrm{Hz}$ (black curve). Yellow curve $(I_{\mathrm{X}}, I_{\mathrm{Y}}) = (+5\,\mathrm{pA}, 0\,\mathrm{pA})$; blue curve $(I_{\mathrm{X}}, I_{\mathrm{Y}}) = (-2\,\mathrm{pA}, +2\,\mathrm{pA})$. (c) A pair of time traces acquired at $V_{\mathrm{d.c.}} = 30\,\mathrm{mV}$, $I_{\mathrm{d.c.}} = 10\,\mathrm{pA}$, $V_{\mathrm{THz,pk}} = 6.7\,\mathrm{V}$ (blue curve) and $V_{\mathrm{d.c.}} = 30\,\mathrm{mV}$, $I_{\mathrm{d.c.}} = 300\,\mathrm{pA}$, $V_{\mathrm{THz,pk}} = 2.7\,\mathrm{V}$ (yellow curve), and a square-wave modulation of the terahertz-pulse-train at $f_{\mathrm{THz}} = 477\,\mathrm{Hz}$ (black curve). Yellow curve $(I_{\mathrm{X}}, I_{\mathrm{Y}}) = (+2\,\mathrm{pA}, -1.5\,\mathrm{pA})$; blue curve $(I_{\mathrm{X}}, I_{\mathrm{Y}}) = (+2\,\mathrm{pA}, 0\,\mathrm{pA})$.

Figure 5.8(a) shows how $V_{\mathrm{d.c.}}$ affects atomically resolved I_{X} and I_{Y} images of a top-surface tellurium vacancy [37]. For finite bias voltages of $V_{\mathrm{d.c.}} = \pm 5.5\,\mathrm{mV}$, the I_{Y} images exhibit similar spatial features and signal strengths but opposite polarity, whereas the I_{Y} signal is negligible for $V_{\mathrm{d.c.}} = 0\,\mathrm{V}$. Meanwhile, a purely lightwave-driven image is obtained in the I_{X} channel for $V_{\mathrm{d.c.}} = 0\,\mathrm{V}$, but for $V_{\mathrm{d.c.}} \neq 0$, I_{X} contains both lightwave-driven and phase-difference contributions.

The opposite polarity of the I_{X} and I_{Y} signals arises naturally from the standard lock-in detection scheme when the measured signal is approximately 90° out of phase with the reference (see Chapter 2.5.2.2). In the experimental setup, I_{X} corresponds to the in-phase component, which is typically dominated by lightwave-driven tunneling (the terahertz pulse acts as a quasi-static bias in the strong-field limit). In contrast, I_{Y} captures the out-of-phase component, which primarily reflects the d.c. tunnel current modulated by oscillations between the terahertz-field-induced metastable state and the ground state. At a modulation frequency of several hundred Hertz, the excitation of the metastable state in WTe_2 (probed by the d.c. tunnel current) exhibits a significant phase offset relative to the lightwave-driven tunneling response (as seen in the behavior of the total current in Fig. 5.6), such that one channel typically registers a positive amplitude while the other registers a negative one. As the modulation frequency is lowered (providing the surface

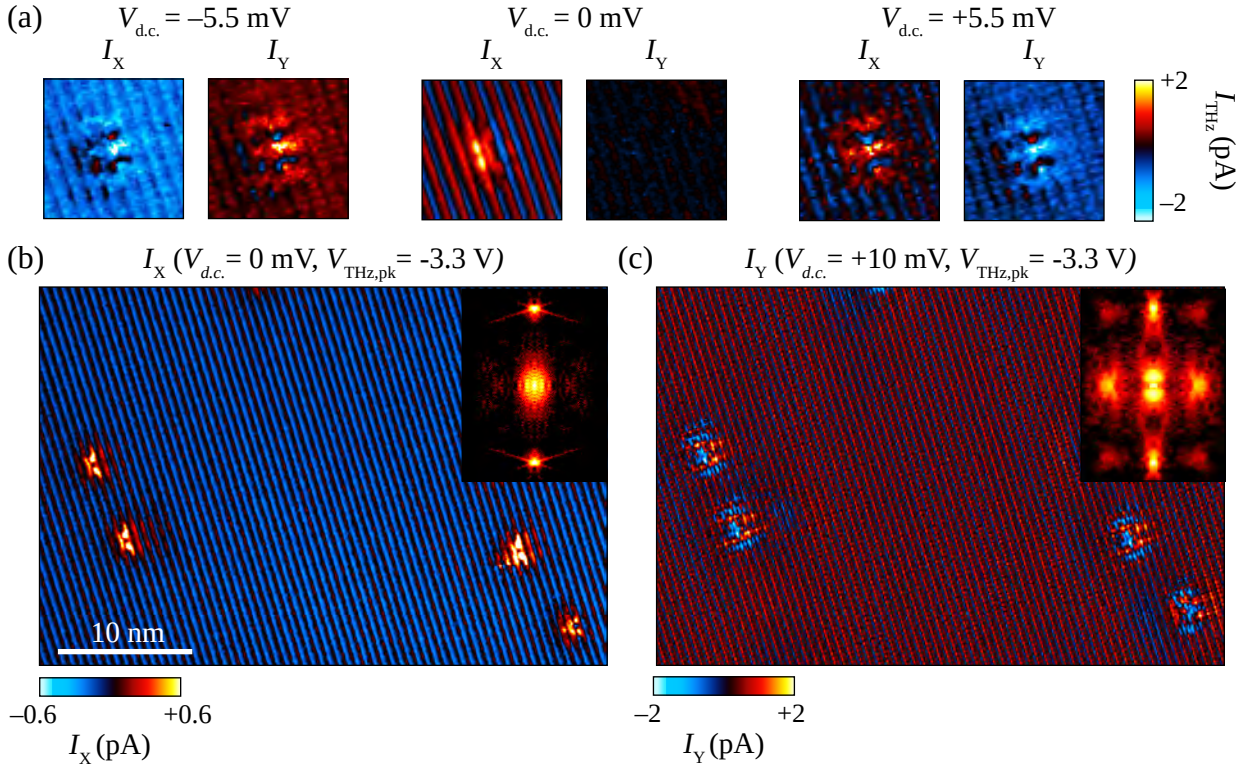

Figure 5.8 Differential atomic imaging of a terahertz-driven phase transition. (a) THz-STM images of a 5 nm × 5 nm area showing both $I_X(x, y)$ and $I_Y(x, y)$ for a WTe_2 surface defect acquired at $V_{d.c.} = -5.5$ mV (left), $V_{d.c.} = 0$ V (middle) and $V_{d.c.} = 5.5$ mV (right). The left and right image pairs were acquired at $I_{d.c.} = 100$ pA and $V_{THz,pk} = -3.3$ V, while the middle image pair was acquired at $V_{THz,pk} = -2.8$ V and the tip was approached 150 pm to enhance lightwave-driven tunneling ($z = z_0 - 150$ pm). (b) Conventional THz-STM rectified current map, $I_X(x, y)$, of a 42 nm × 28 nm area acquired at constant height with $V_{d.c.} = 0$ V, $V_{THz,pk} = -1.7$ V and $z = z_0 - 50$ pm. The tip height z_0 was set by $V_{d.c.} = 10$ mV, $I_{d.c.} = 100$ pA. (c) Out-of-phase THz-STM image, $I_Y(x, y)$, of the same area acquired at $V_{d.c.} = 10$ mV, $V_{THz,pk} = -2.2$ V and $I_{d.c.} = 100$ pA. A 100 pm full-width-half-maximum 2D Gaussian was convolved with the images for noise reduction. Insets in (b) and (c): Symmetrized 2D Fourier transforms with dimensions 3 nm^{-1} × 4 nm^{-1}.

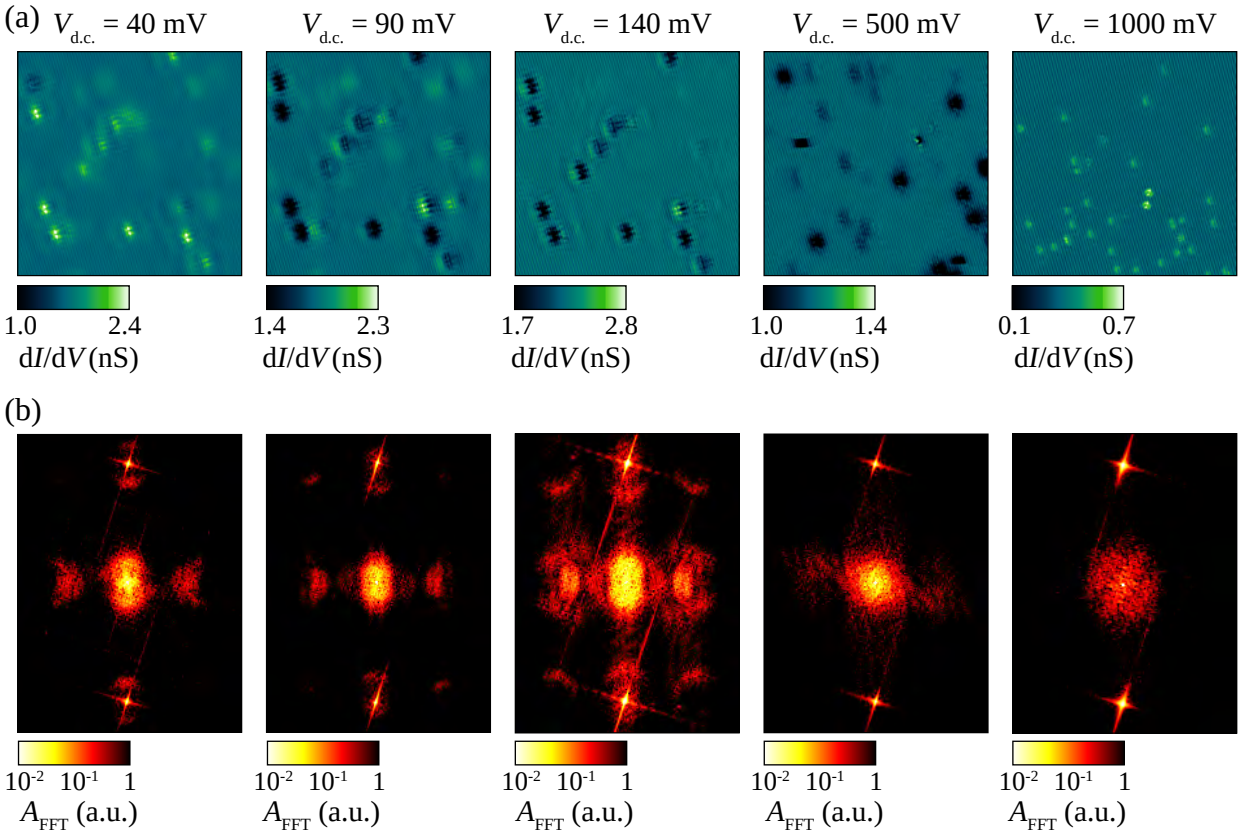

Figure 5.9 Atomic-scale conductance mapping of WTe_2. (a) Spatially-resolved conductance (dI/dV) maps of a WTe_2 surface acquired at a constant-current of $I_{d.c.}$ = 100 pA and $V_{d.c.}$ set to 40 mV (left), 90 mV (middle left), 140 mV (middle), 500 mV (middle right) and 1000 mV (right). Image size 50 nm × 50 nm; $V_{a.c.}$ = 5 mV (left, middle left, middle) and $V_{a.c.}$ = 10 mV (middle right, right). (b) Fourier-transform STM (FT-STM) image for each respective conductance map positioned above in (a). Image size 3 nm^{-1} × 4 nm^{-1}.

with sufficient time to relax between cycles), the signal induced by the metastable state becomes increasingly in-phase with the lock-in reference, reducing its projection onto I_Y and consequently lowering the signal-to-noise ratio of this channel. Also, since the d.c. bias polarity determines the direction of the d.c. tunnel current that probes the surface LDOS under terahertz pulse illumination, reversing its polarity naturally leads to a sign reversal of the phase-difference contribution to I_X and I_Y (Fig. 5.8(a)).

Comparing images acquired over a larger area with multiple surface defects reveals a clear distinction between the two measurement modes. Lightwave-driven tunneling (Fig. 5.8(b)) reflects the LDOS up to the terahertz peak voltage, while the d.c. readout via I_Y (Fig. 5.8(c)) probes the LDOS difference between the two phases up to $V_{d.c.}$. The insets show 2D-FFTs of the corresponding THz-STM scans. The features just to the left and right of the central peak can be associated with quasiparticle standing waves in the surface state, as observed by differential conductance imaging

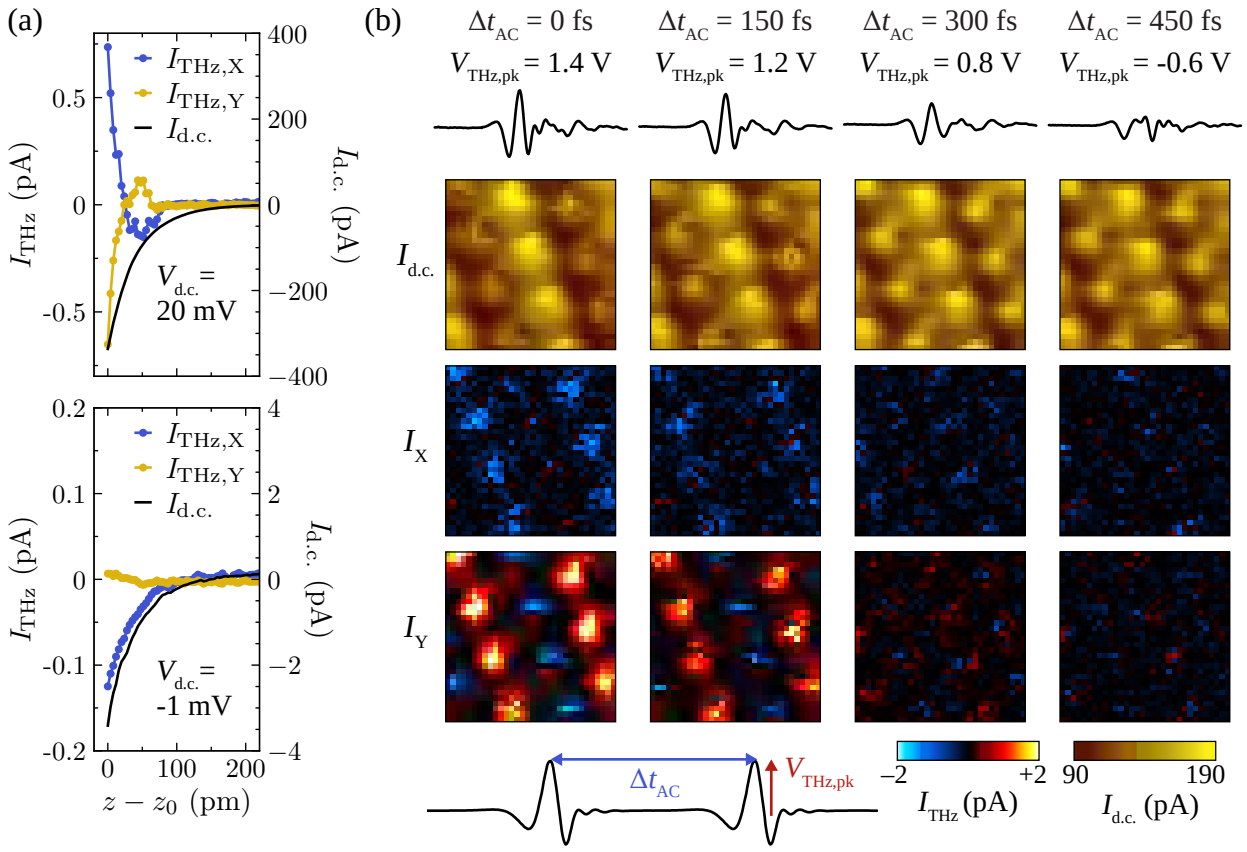

Figure 5.10 Nonlinearity of the transition. (a) Tip retraction scan acquired at $V_{\mathrm{THz,pk}}$ = 1.2 V and $V_{\mathrm{d.c.}}$ = 20 mV (top) and $V_{\mathrm{d.c.}}$ = −1 mV (bottom). The initial tip height, z_0, set by $V_{\mathrm{d.c.}}$ = − 20 mV and $I_{\mathrm{d.c.}}$ = − 300 pA. (b) A set of constant-height spatio-temporal terahertz pulse autocorrelation images with the total tunnel current ($I_{\mathrm{d.c.}}$, top row), along with the in-phase (I_{X}, middle row) and out-of-phase (I_{Y}, bottom row) terahertz-pulse-induced tunnel current for different Δt_{AC}, indicated at the top with the corresponding terahertz pulse temporal profile for each time delay. Scan parameters: $V_{\mathrm{d.c.}}$ = 10 mV; $z = z_0$; $V_{\mathrm{THz,pk}}$ = 1.4 V; image size 1 nm × 1 nm; feedback loop disengaged at V_0 = 10 mV and I_0 = 100 pA. Bottom left: Schematic showing two terahertz pulses, each with an electric field amplitude of $V_{\mathrm{THz,pk}}$, separated by a time delay Δt_{AC}.

(Fig. 5.9), and may indicate electron scattering involving Fermi arc surface states [16–18, 23]. These features are present in Fig. 5.8(c) because the tunneling electrons have energies determined by $V_{\mathrm{d.c.}}$, which lies within the energy range of the surface states in WTe_2, including topologically-protected Fermi arc surface states [16–18, 23]. However, in Fig. 5.8(b), most of the lightwave-driven electrons have energies well beyond the surface states near the Fermi level, resulting in faint arc-like features. It is important to note that Figs. 5.8(b) and (c) differ from quasiparticle interference imaging [16, 18, 23, 60] in that they are energy-integrated representations of the corresponding voltage window.

The nonlinearity of the transition from regime ii to regime i is further highlighted using two complementary approaches: a tip retraction scan that gradually reduces the local terahertz field

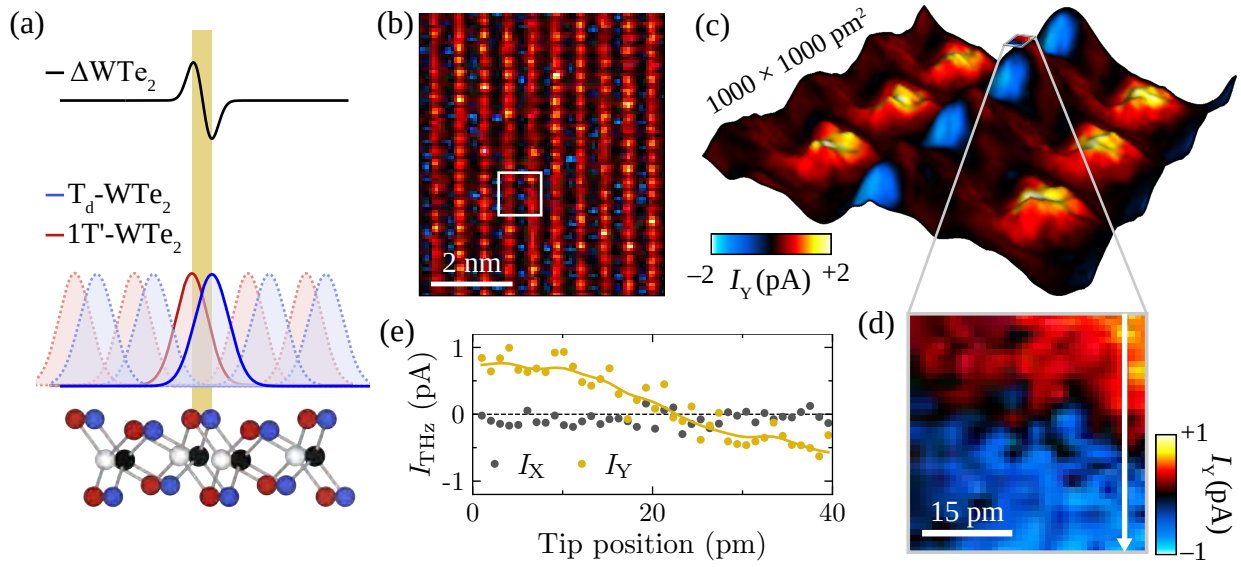

Figure 5.11 Picometer-scale microscopy of the terahertz-driven transition. (a) Schematic showing how picometer-scale differences in the local electronic properties between T_d (blue line) and 1T' (red line) phases in WTe_2 lead to subatomic resolution microscopy via I_Y (black line). (b) Out-of-phase THz-STM image, $I_Y(x, y)$, acquired at $V_{d.c.} = 10$ mV, $I_{d.c.} = 100$ pA and $V_{THz,pk} = -1.7$ V. Scan size 6 nm × 8 nm. (c) Perspective view of $I_Y(x, y)$ overlaid onto a 3D texture generated by the simultaneously acquired $I_{d.c.}(x, y)$, where $I_{d.c.}$ spans 100 pA to 220 pA. The white box in (b) shows where (c) was acquired. The constant-height THz-STM image in (c) was acquired at $V_{d.c.} = 10$ mV, $V_{THz,pk} = -1.4$ V and tip height of $z = z_0 - 30$ pm with z_0 set by $V_{d.c.} = 10$ mV and $I_{d.c.} = 100$ pA; Gaussian smoothing filter full-width-half-maximum 15 pm. (d) Picometer-scale image in the location indicated in (c). Constant-height THz-STM image, $I_Y(x, y)$, acquired at $V_{d.c.} = 10$ mV, $V_{THz,pk} = -1.4$ V and tip height of $z = z_0 - 35$ pm with z_0 set by $V_{d.c.} = 10$ mV and $I_{d.c.} = 100$ pA; Gaussian smoothing filter full-width-half-maximum 2 pm. (e) Vertical cross-section of I_X (gray circles) and I_Y (yellow circles and yellow line for filtered data) indicated by the white arrow in (d).

with and without a d.c. bias voltage present (Fig. 5.10(a)), and a THz-STM autocorrelation imaging dataset in which the local terahertz field is lowered via destructive interference between two identical terahertz pulses (Fig. 5.10(b)). In both cases, I_X and I_Y are abruptly quenched by a small reduction in the terahertz near-field amplitude. The sign inversion observed for I_X and I_Y in Fig. 5.10(a), top, likely arises from changes in the relative magnitudes of the surface LDOS associated with the metastable and ground states, which switch in dominance as the tip retracts. By comparison, in regime iii, the excitation is strong enough that the ground state is not recovered when the pulse train is blocked and the sample remains in the metastable state.

5.4 Picometer-scale microscopy

Since the phase transition is structural in nature [19, 21, 27–30, 45, 46], I_Y is a measure of not only the difference in LDOS between the two phases, but also the spatial shift of the top atomic plane. This differential measurement mode, illustrated in Fig. 5.11(a), allows us to

capture details of the phase transition in real space with resolution beyond what is possible with conventional atomically resolved STM [61]. Subatomic spatial resolution has been achieved with atomic force microscopy [62–64], enabled by the 40 pm decay of the interaction potential [63]. Although the tunnel current decays over a longer distance, differential STM images assembled by subtracting the normalized current at moderate tip height from that at lower tip height have also captured picometer-scale features [63]. Critically, the approach to subatomic resolution imaging presented here is intrinsically differential: measuring a changing surface rather than relying on post-processing. By employing lock-in detection, the signal-to-noise ratio of picometer-scale imaging with tunneling microscopy is drastically improved. Direct differential imaging of the two phases also greatly mitigates effects due to sample drift, which would otherwise obscure subatomic detail in a post-subtraction of the images. The experimental images were acquired with the system in thermal equilibrium, with a lateral drift rate of approximately 1 picometer per minute.

Subatomic spatial resolution of the phase transition is demonstrated via $I_Y(x,\ y)$ in Fig. 5.11(b)–(d). Figure 5.11(c) shows an area encompassing six of the lower tellurium atoms (strong positive signal), while Figs. 5.11(d) focuses on the subatomic image contrast near the upper tellurium atoms, identified by overlaying the differential signal with a 3D representation of the simultaneously recorded $I_{\mathrm{d.c.}}(x,\ y)$) signal in Fig. 5.11(c). The cross-sections in Fig. 5.11(e) emphasize the subatomic spatial resolution of I_Y, revealing features with dimensions that are approximately one-tenth of the interatomic spacing.

Next, the spatial distribution of I_Y (Fig. 5.11(c) and Fig. 5.12(b)) is compared with the calculated charge density maps for T_d-WTe_2 and 1T'-WTe_2. Figure 5.12(a) and (c) show separate charge density maps for each of the phases, with each image representing the spatial distribution of the charge density integrated from 0 to 10 meV (relative to the Fermi level), following the Tersoff-Hamann approximation [61]. Before subtracting the images, a relative shift along the $\vec{b}$-axis is introduced, which is the direction of shear motion expected during the phase transition. The magnitude of this shift is used as a fit parameter when subtracting the charge densities for each phase, $\rho_{T_d} - \rho_{1T'}$, arriving at a differential charge density map between the two phases (Fig. 5.12(d) and (e)). A shift of the top atomic plane by 7 ± 3 pm captures the key features observed in the experimental data (Fig. 5.12(d)).

Due to the different symmetries of the two phases of WTe_2, the layers shift in pairs across the phase transition, resulting in an approximately commensurate periodic lattice every 12 layers due to the ≈4° mismatch between the unit cells of T_d and 1T' (Fig. 5.13(a)). Figure 5.13(b) shows four layers of the lattice structures for T_d-WTe_2 and 1T'-WTe_2, with the bottom layer aligned for comparison. Calculations find that the relative lateral shift between unpaired layers is 100 pm (e.g., between the second and third layers in Fig. 5.13(b)), whereas it is only a few picometers for paired layers (between the first and second layers, and between the third and fourth layers in Fig. 5.13(b)).

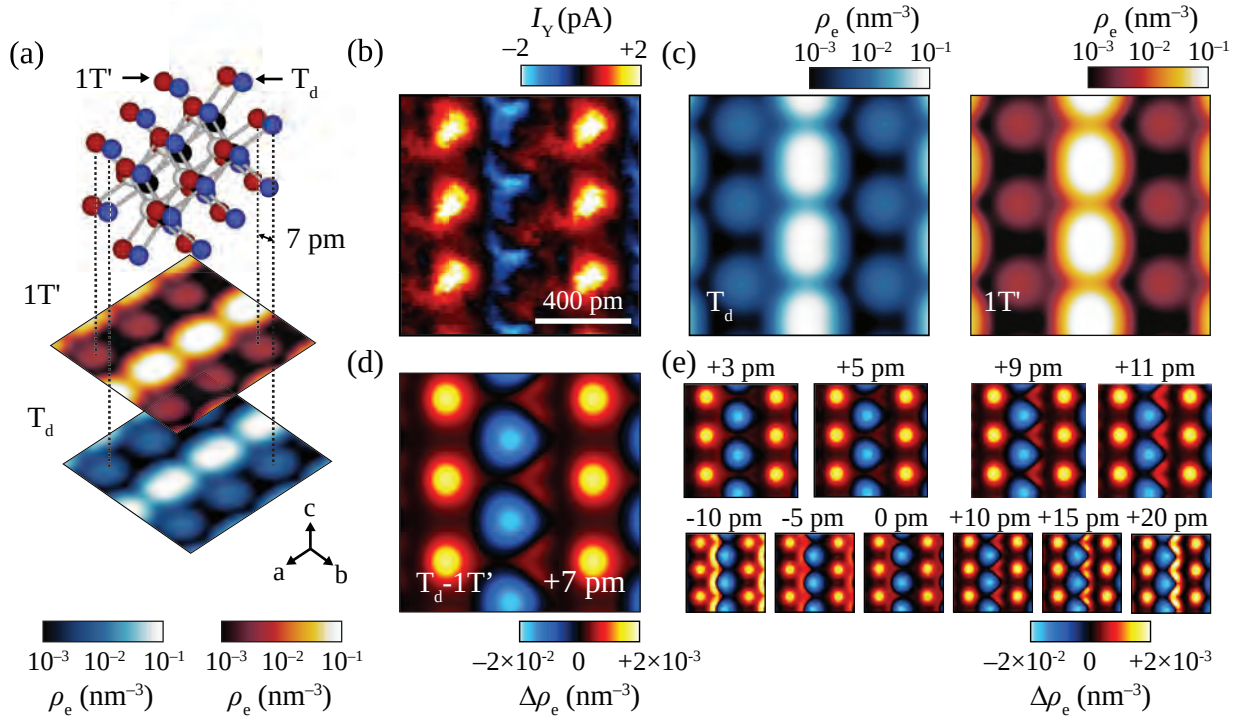

Figure 5.12 Extracting the picometer-scale shift of the WTe_2 surface. (a) Simulated charge densities for T_d (bottom) and 1T' (middle) with a schematic (top) showing the atomic positions for each phase (the atomic lattice separation of 7 pm is amplified for visual clarity). (b) Experimental constant-height THz-STM image $I_Y(x, y)$ from Fig 5.11(c). (c) Surface charge density integrated from 0 to 10 meV above the Fermi level calculated using hybrid-DFT for the T_d (left) and 1T' (right) phases of WTe_2. (d),(e) Difference images between the simulated charge densities of T_d and 1T' for a 1000 pm × 1000 pm square area ($\rho_{T_d} - \rho_{1T'}$). Subtracted charge densities ($\rho_{T_d} - \rho_{1T'}$) from (c) are shown with the horizontal offset indicated above each image. A shift of 7 pm in (d) agrees best with the data in (b). A tolerance of ±3 pm is estimated based on the reasonable agreement of the charge density differences for an offset of 4 pm to 10 pm (see upper row in (e)). The bottom row in (e) shows larger shifts in both directions and the subtraction without an offset (0 pm), demonstrating that the shift is confined to 7 ± 3 pm to match the measurement in (b).

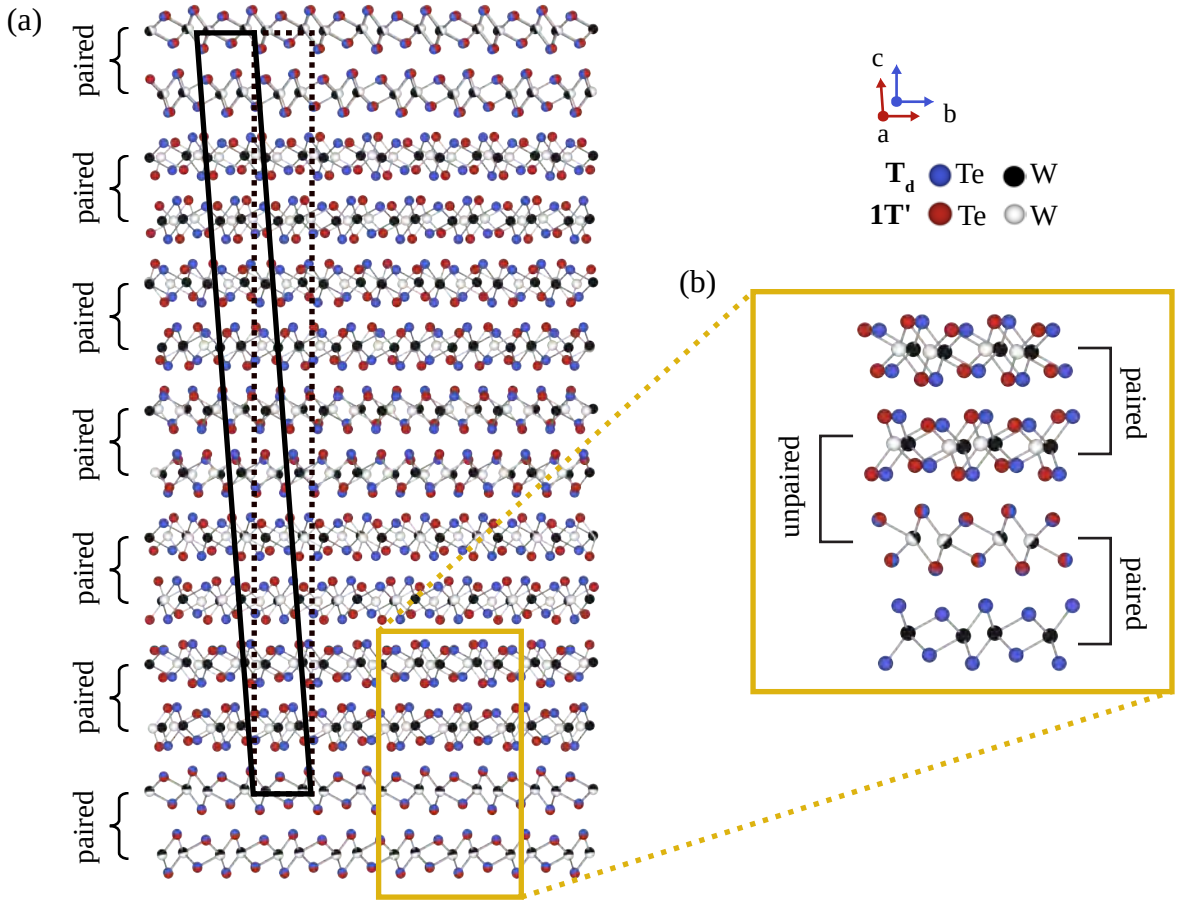

Figure 5.13 Relative shift of the atoms between WTe_2 layers. (a) The T_d and 1T' lattice alignment is approximately commensurate every 12 layers. The solid black parallelogram highlights the 4° tilt of the supercell for 1T' with respect to T_d (dashed black rectangle). (b) Four layers of the orthorhombic T_d phase (blue and black spheres) and monoclinic 1T' phase (red and white spheres). When the lattices of both phases are overlaid, the layers can be grouped with regard to their relative shift between the phases along the $\vec{b}$-axis, as illustrated. The atoms in the bottom layer of both phases are aligned to the same positions within 0.3 pm (only the T_d phase atoms are visible).

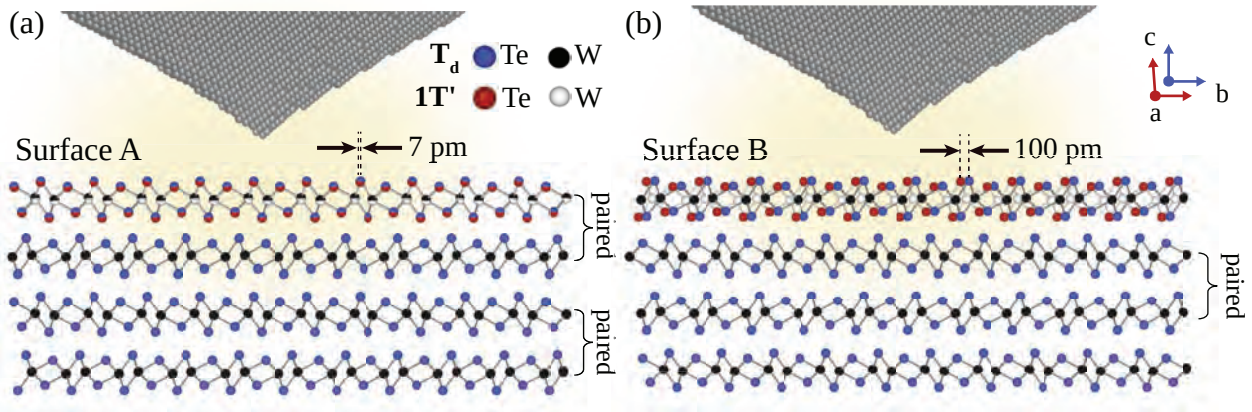

Figure 5.14 Shift of the top atomic layer in WTe_2. Side views are shown along the $\vec{a}$-axis of T_d-WTe_2 (blue and black spheres) and 1T'-WTe_2 (red and white spheres). (a) On Surface A, the top layer shifts by approximately 7 pm relative to the adjacent paired layer beneath it. (b) On Surface B, the top layer shifts by approximately 100 pm relative to the adjacent unpaired layer beneath it.

The close correspondence between the extracted shift of the top atomic layer (Figs. 5.12) and the calculated shifts between paired layers (Fig. 5.13) suggests that the surface (1) is paired with the layer directly below it, which remains stationary, and (2) translates in-plane by only 7 ± 3 pm relative to this underlying layer. Both the interlayer shear motion and the intralayer distortion of the surface layer to the 1T'-WTe_2 configuration, are necessary to reproduce the experimental data, as subtracting shifted charge densities for the T_d phase alone is insufficient.

The terahertz-pulse-induced phase transition in WTe_2 is strongly influenced by the broken inversion symmetry of the T_d phase, resulting in two distinct surface terminations [9, 11, 12, 18, 24, 36], labeled 'Surface A' and 'Surface B'. The strong terahertz field that drives the phase transition is concentrated at the surface layer, rapidly decaying inside the sample and radially away from the tip [41]. In the experiments, nearly the entire WTe_2 crystal remains in the T_d phase, except for a nanoscale area near the tip apex where terahertz pulses induce a metastable state on Surface A, shifting the surface layer by 7 ± 3 pm into a structure resembling 1T'-WTe_2. In T_d-WTe_2, Surface A is structurally paired with its adjacent subsurface layer, exhibiting a relative lateral shift of only a few picometers between corresponding lattice sites in the T_d versus 1T' phases (Fig. 5.14(a)). The extracted experimental shift for the surface layer relative to the tip apex (7 ± 3 pm) confirms that the second layer remains stationary; otherwise, the surface layer would shift approximately 100 pm, which was not observed in the experiments presented here. In contrast, for Surface B the interfacial layer is unpaired, which means that driving the surface layer of T_d-WTe_2 into a metastable phase resembling 1T'-WTe_2 requires a 100 pm shift relative to the subsurface layer (Fig. 5.14(b)).

During the THz-STM measurements, the terahertz-pulse-induced phase transition is not consistently observed across all regions of the sample, often requiring multiple attempts to find an area that exhibits the effect. This inconsistency may result from either the need for a particular

structural strain or occasionally landing on Surface B, where attempts to locally drive a 100-pm lateral shift between adjacent layers are strongly suppressed by the surrounding atomic lattice, which remains structurally unperturbed due to insufficient local terahertz field strength. Notably, a large interplanar shift has been realized in few-layer WTe_2 by applying static fields on the order of volts per nanometer through large-contact-area electrodes, triggering a polarity switch in the out-of-plane ferroelectric dipole [32–35].

5.5 Electronic character of the metastable state

Figures 5.2(a) (T_d phase) and 5.2(b) (1T' phase) show the 3D bulk band structures in the (k_x–k_y) plane near the Weyl points (covering only half of the first Brillouin zone due to symmetry). Figure 5.15(a) shows the bulk bands along the Γ–k_x direction (Γ–X for T_d and Γ–Z for 1T'). In the 1T'-WTe_2 phase, centrosymmetry enforces band degeneracy, whereas in the T_d-WTe_2 phase, centrosymmetry breaking lifts this degeneracy, resulting in band crossings (Weyl points) where the valence and conduction bands touch. Projecting the bulk bands along the surface normal in the k_z direction reveals the range of energies and (k_x, k_y) values that host bulk electronic states, as shown in Fig. 5.15(c) and (d). The electronic surface bands, including Fermi arc states, occupy the regions of energy and in-plane momentum between the bulk projections [8]. Thus, a phase transition from T_d-WTe_2 to 1T'-WTe_2, which restores the bulk band degeneracy, allows surface states to emerge in regions of energy-momentum space that were previously inaccessible. Simultaneously, Fermi arc surface states connecting Weyl points in T_d-WTe_2 disappear upon annihilation of the Weyl points across the phase transition.

The prominent quasiparticle standing waves observed around surface defects in Fig. 5.8(c) – which even change sign between adjacent maxima and minima – illustrate that I_Y is dominated by the differences between the surface states of the ground and metastable phases. Experimentally tuning $V_{d.c.}$ therefore explores the electronic differences at the surface (as measured by I_Y) for energies near the Fermi level (Fig. 5.15(b)). A differential signal between the two phases is only observed for biases between ±30 mV and find that I_Y is maximized at energies coinciding with the extrema of the non-degenerate bulk bands, which appear only in T_d-WTe_2 (compare with Fig. 5.15(a)). Since the bulk bands of each phase define the allowed energies and momenta of the corresponding surface states, this is the energy range where surface bands exhibit the greatest variation between phases and also where Fermi arc surface states reside. The differential current between phases is therefore consistent with a topological phase transition of the top atomic layers, where the electronic structure of the surface shifts from that of T_d-WTe_2 to one consistent with the surface of 1T'-WTe_2, while the WTe_2 bulk remains in the T_d phase. Since topologically protected Fermi arc surface states necessarily arise from Weyl points in the bulk, these states are expected to shift below the surface in the experiments, relocating to the new interface of T_d-WTe_2 underneath

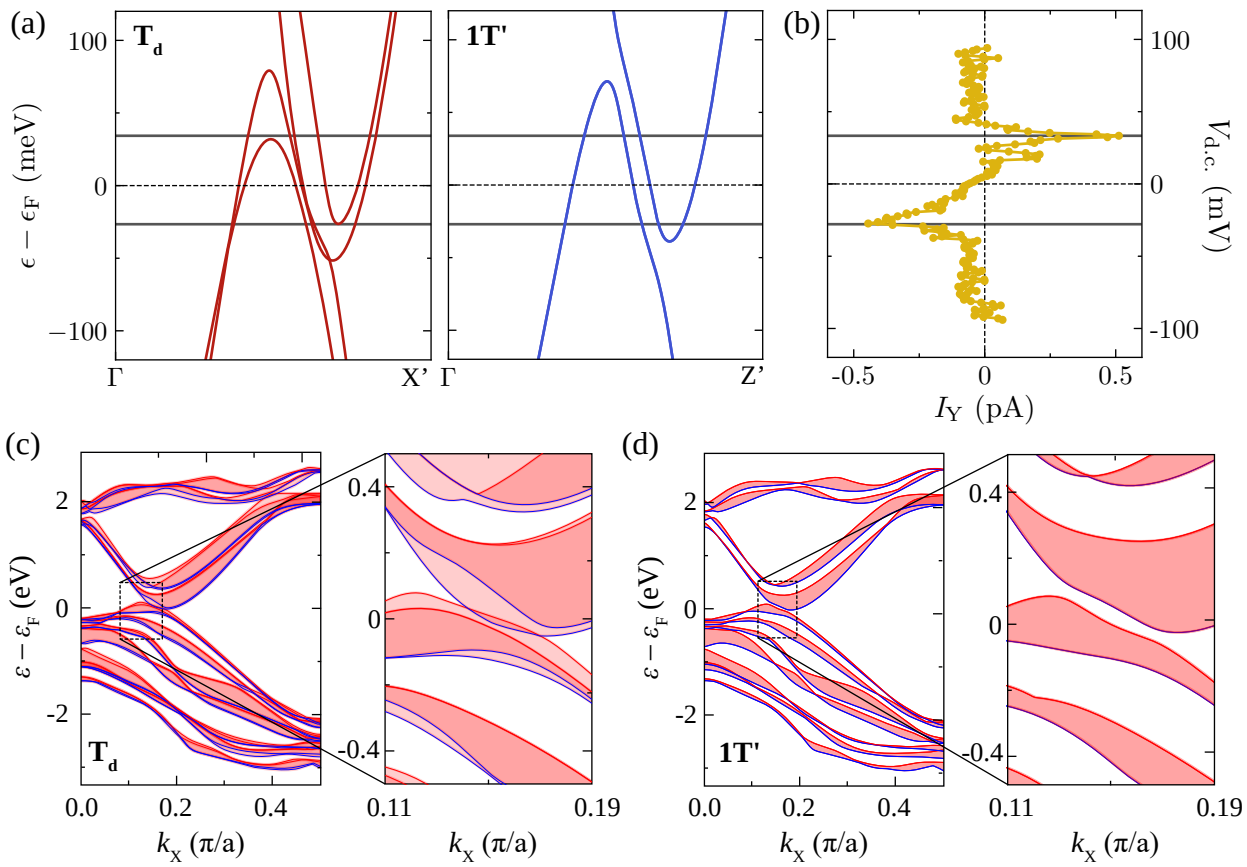

Figure 5.15 Identifying a topological symmetry switch in WTe_2. (a) Band structure along the high symmetry direction, $\Gamma - X'$, for the T_d phase and the equivalent path, $\Gamma - Z'$, for the 1T' phase. (b) Out-of-phase component of the measured tunnel current (I_Y) as a function of $V_{d.c.}$, covering the range where topologically protected Fermi arc surface states reside in bulk T_d-WTe_2. The terahertz peak voltage is set to $E_{THz,pk}$ = 72 V/cm, ensuring that the field strength underneath the tip apex and in the surrounding area induces a phase transition from T_d-WTe_2 to the metastable state resembling 1T'-WTe_2. The feedback loop was opened at $V_{d.c.}$ = 10 mV and $I_{d.c.}$ = 100 pA. The dark gray horizontal lines in (a) and (b) mark the energy positions of the vertices (local extrema) of the non-degenerate valence and conduction bands that are present only in the T_d phase. The two pairs of Weyl points occur at (ϵ, k_x, k_y) = (−12.6, ± 0.1516, 0) and (ϵ, k_x, k_y) = (−51.1, ± 0.1707, 0) with ϵ, k_x and k_y in units of meV, π/a and π/b, respectively. (c),(d) Calculations using hybrid-level DFT of T_d-WTe_2 (c) and 1T'-WTe_2 (d) bulk states shown along the k_x direction (Γ–X for T_d and Γ–Z for 1T') and projected along the surface normal, i.e., the k_z direction (Γ–Z for T_d and Γ–B for 1T'). Projections are shown as transparent red shaded regions. The minima and maxima for each band projection are shown as blue and red lines, respectively. The magnification highlights where band crossings occur in the T_d phase.

the shifted layer.

5.6 Discussion and conclusions

The ability to locally switch surface topology presents an exciting opportunity for actively controlling electronic transport in quantum materials at the atomic scale. Hybrid-level DFT calculations reveal that the Weyl points in WTe_2 are highly sensitive to subtle changes in the interlayer coupling (see Ref. [44] for details), with strain along the $\vec{c}$-axis causing their creation or annihilation, consistent with previous studies [8, 9, 11, 13, 19, 36, 65, 66]. This sensitivity opens avenues for the design of device architectures that can selectively quench topologically protected transport channels, thereby enabling dynamic lightwave control over quantum states. The success of such an approach relies on the spatial confinement and strength of the terahertz near-field at the tip apex, which acts as a localized trigger for inducing phase transitions and governs the lateral extent of the metastable state.

The experiments presented in this chapter indicate that the terahertz field strength, surface termination, and local strain distribution are all critical factors influencing the observed phenomena. Although quantifying the lateral extent of the tip-induced phase transition in cleaved bulk samples is challenging with THz-STM, it may be more easily addressed in few-layer WTe_2 islands. The topological nature of WTe_2 is fragile, with narrowly separated Weyl points in momentum space that can be annihilated by external perturbations such as electric fields [19], strain [1, 19, 66], adsorbates [36], or temperature [9, 11, 15]. The mere existence of Weyl points in WTe_2 has been the subject of ongoing debate, as numerous theoretical studies have yielded conflicting results.

This uncertainty arises in part from the need to account for nonlocal interactions and strong spin–orbit coupling, both of which pose challenges for conventional DFT approaches. In response, increasingly sophisticated computational methods incorporating a portion of exact exchange have been developed to better capture the electronic structure and topological properties [67, 68]. Furthermore, it is noted that while the experimental measurement in Fig. 5.15(b) is consistent with a topological phase transition between a Weyl semimetal and a trivial semimetal, this observation alone is not sufficient to conclusively confirm the existence of Weyl nodes. Instead, the topological nature of the WTe_2 sample is inferred from theoretical calculations and linked to experiment through the comparisons shown in Figs. 5.12(b),(d) and Figs. 5.15(a),(b).

In addition to driving spatially localized phase transitions, THz-STM provides the capability to experimentally resolve dynamically modulated surface states in real space with picometer-scale resolution. Further yet, the prospect of quasiparticle interference imaging with THz-STM promises complementary momentum-space measurements that can help identify the evolution of electronic properties within topological materials. Moreover, lightwave-driven STM uniquely facilitates ultrafast time-domain exploration of quantum material surface dynamics at the atomic

scale. These capabilities establish the groundwork for systems where emergent topological phases can be accessed and controlled [2–7], ultimately enabling novel device architectures that exploit metastable phase transitions to precisely control electron transport and spin currents.

BIBLIOGRAPHY

[1] Jelic, V. *et al.* Terahertz field control of surface topology probed with subatomic resolution. *Nature Photonics* **19**, 1048–1055 (2025).

[2] Basov, D. N., Averitt, R. D. & Hsieh, D. Towards properties on demand in quantum materials. *Nature Materials* **16**, 1077–1088 (2017).

[3] de la Torre, A. *et al.* Colloquium: Nonthermal pathways to ultrafast control in quantum materials. *Reviews of Modern Physics* **93**, 041002 (2021).

[4] Ma, Q., Grushin, A. G. & Burch, K. S. Topology and geometry under the nonlinear electromagnetic spotlight. *Nature Materials* **20**, 1601–1614 (2021).

[5] Bao, C., Tang, P., Sun, D. & Zhou, S. Light-induced emergent phenomena in 2D materials and topological materials. *Nature Reviews Physics* **4**, 33–48 (2022).

[6] Karni, O., Esin, I. & Dani, K. M. Through the Lens of a Momentum Microscope: Viewing Light-Induced Quantum Phenomena in 2D Materials. *Advanced Materials* **35**, 2204120 (2023).

[7] Zhai, E. *et al.* The rise of semi-metal electronics. *Nature Reviews Electrical Engineering* **1**, 497–515 (2024).

[8] Soluyanov, A. A. *et al.* Type-II Weyl semimetals. *Nature* **527**, 495–498 (2015).

[9] Wang, C. *et al.* Observation of Fermi arc and its connection with bulk states in the candidate type-II Weyl semimetal WTe_2. *Physical Review B* **94**, 241119 (2016).

[10] Feng, B. *et al.* Spin texture in type-II Weyl semimetal WTe_2. *Physical Review B* **94**, 195134 (2016).

[11] Bruno, F. Y. *et al.* Observation of large topologically trivial Fermi arcs in the candidate type-II Weyl semimetal WTe_2. *Physical Review B* **94**, 121112 (2016).

[12] Sánchez-Barriga, J. *et al.* Surface Fermi arc connectivity in the type-II Weyl semimetal candidate WTe_2. *Physical Review B* **94**, 161401 (2016).

[13] Di Sante, D. *et al.* Three-Dimensional Electronic Structure of the Type-II Weyl Semimetal WTe_2. *Physical Review Letters* **119**, 026403 (2017).

[14] Li, P. *et al.* Evidence for topological type-II Weyl semimetal WTe_2. *Nature Communications* **8**, 2150 (2017).

[15] Zhang, Q. *et al.* Lifshitz Transitions Induced by Temperature and Surface Doping in Type-II

Weyl Semimetal Candidate Td-WTe_2. *physica status solidi (RRL) – Rapid Research Letters* **11**, 1700209 (2017).

[16] Lin, C.-L. *et al.* Visualizing Type-II Weyl Points in Tungsten Ditelluride by Quasiparticle Interference. *ACS Nano* **11**, 11459–11465 (2017).

[17] Zhang, W. *et al.* Quasiparticle interference of surface states in the type-II Weyl semimetal WTe_2. *Physical Review B* **96**, 165125 (2017).

[18] Yuan, Y. *et al.* Quasiparticle interference of Fermi arc states in the type-II Weyl semimetal candidate WTe_2. *Physical Review B* **97**, 165435 (2018).

[19] Sie, E. J. *et al.* An ultrafast symmetry switch in a Weyl semimetal. *Nature* **565**, 61–66 (2019).

[20] Hein, P. *et al.* Mode-resolved reciprocal space mapping of electron-phonon interaction in the Weyl semimetal candidate Td-WTe_2. *Nature Communications* **11**, 2613 (2020).

[21] Guan, M.-X., Wang, E., You, P.-W., Sun, J.-T. & Meng, S. Manipulating Weyl quasiparticles by orbital-selective photoexcitation in WTe_2. *Nature Communications* **12**, 1885 (2021).

[22] Das, P. K. *et al.* Electronic properties of candidate type-II Weyl semimetal WTe_2. A review perspective. *Electronic Structure* **1**, 014003 (2019).

[23] Kwon, H. *et al.* Quasiparticle interference and impurity resonances on WTe_2. *Nano Research* **13**, 2534–2540 (2020).

[24] Wu, Y. *et al.* Observation of Fermi arcs in the type-II Weyl semimetal candidate WTe_2. *Physical Review B* **94**, 121113 (2016).

[25] Caputo, M. *et al.* Dynamics of out-of-equilibrium electron and hole pockets in the type-II Weyl semimetal candidate WTe_2. *Physical Review B* **97**, 115115 (2018).

[26] Yan, B. & Felser, C. Topological Materials: Weyl Semimetals. *Annual Review of Condensed Matter Physics* **8**, 337–354 (2017).

[27] Ji, S., Grånäs, O. & Weissenrieder, J. Manipulation of Stacking Order in Td-WTe_2 by Ultrafast Optical Excitation. *ACS Nano* **15**, 8826–8835 (2021).

[28] Qi, Y. *et al.* Traversing Double-Well Potential Energy Surfaces: Photoinduced Concurrent Intralayer and Interlayer Structural Transitions in XTe_2 (X = Mo, W). *ACS Nano* **16**, 11124–11135 (2022).

[29] Drueke, E., Yang, J. & Zhao, L. Observation of strong and anisotropic nonlinear optical effects through polarization-resolved optical spectroscopy in the type-II Weyl semimetal Td-WTe_2. *Physical Review B* **104**, 064304 (2021).

[30] Soranzio, D. *et al.* Strong modulation of carrier effective mass in WTe_2 via coherent lattice manipulation. *npj 2D Materials and Applications* **6**, 71 (2022).

[31] Tang, S. *et al.* Quantum spin Hall state in monolayer 1T'-WTe_2. *Nature Physics* **13**, 683–687 (2017).

[32] Fei, Z. *et al.* Ferroelectric switching of a two-dimensional metal. *Nature* **560**, 336–339 (2018).

[33] Yang, Q., Wu, M. & Li, J. Origin of Two-Dimensional Vertical Ferroelectricity in WTe_2 Bilayer and Multilayer. *The Journal of Physical Chemistry Letters* **9**, 7160–7164 (2018).

[34] Ni, Z. *et al.* Mechanically Tunable Spontaneous Vertical Charge Redistribution in Few-Layer WTe_2. *The Journal of Physical Chemistry C* **124**, 2008–2012 (2020).

[35] Xiao, J. *et al.* Berry curvature memory through electrically driven stacking transitions. *Nature Physics* **16**, 1028–1034 (2020).

[36] Rossi, A. *et al.* Two phase transitions driven by surface electron doping in WTe_2. *Physical Review B* **102**, 121110 (2020).

[37] Chen, W.-H. *et al.* Noncentrosymmetric characteristics of defects on WTe_2. *Physical Review B* **106**, 075428 (2022).

[38] Tao, Y., Schneeloch, J. A., Aczel, A. A. & Louca, D. Td to 1T' structural phase transition in the WTe_2 Weyl semimetal. *Physical Review B* **102**, 060103 (2020).

[39] Zhou, Y. *et al.* Pressure-induced Td to 1T' structural phase transition in WTe_2. *AIP Advances* **6**, 075008 (2016).

[40] Jelic, V. *et al.* Ultrafast terahertz control of extreme tunnel currents through single atoms on a silicon surface. *Nature Physics* **13**, 591–598 (2017).

[41] Peller, D. *et al.* Quantitative sampling of atomic-scale electromagnetic waveforms. *Nature Photonics* **15**, 143–147 (2021).

[42] Cocker, T. L., Peller, D., Yu, P., Repp, J. & Huber, R. Tracking the ultrafast motion of a single molecule by femtosecond orbital imaging. *Nature* **539**, 263–267 (2016).

[43] Cocker, T. L., Jelic, V., Hillenbrand, R. & Hegmann, F. A. Nanoscale terahertz scanning probe microscopy. *Nature Photonics* **15**, 558–569 (2021).

[44] Jelic, V. *et al.* Atomic-scale terahertz time-domain spectroscopy. *Nature Photonics* **18**, 898–904 (2024).

[45] Hein, P. *et al.* A combined laser-based angle-resolved photoemission spectroscopy and two-

photon photoemission spectroscopy study of Td–WTe_2. *Journal of Physics: Condensed Matter* **32**, 345503 (2020).

[46] He, B. *et al.* Coherent optical phonon oscillation and possible electronic softening in WTe_2 crystals. *Scientific Reports* **6**, 30487 (2016).

[47] Cocker, T. L. *et al.* An ultrafast terahertz scanning tunnelling microscope. *Nature Photonics* **7**, 620–625 (2013).

[48] Ammerman, S. E. *et al.* Lightwave-driven scanning tunnelling spectroscopy of atomically precise graphene nanoribbons. *Nature Communications* **12**, 6794 (2021).

[49] Yoshioka, K. *et al.* Real-space coherent manipulation of electrons in a single tunnel junction by single-cycle terahertz electric fields. *Nature Photonics* **10**, 762–765 (2016).

[50] Müller, M., Martín Sabanés, N., Kampfrath, T. & Wolf, M. Phase-Resolved Detection of Ultrabroadband THz Pulses inside a Scanning Tunneling Microscope Junction. *ACS Photonics* **7**, 2046–2055 (2020).

[51] Garg, M. & Kern, K. Attosecond coherent manipulation of electrons in tunneling microscopy. *Science* **367**, 411–415 (2020).

[52] Yoshida, S. *et al.* Terahertz Scanning Tunneling Microscopy for Visualizing Ultrafast Electron Motion in Nanoscale Potential Variations. *ACS Photonics* **8**, 315–323 (2021).

[53] Ammerman, S. E., Wei, Y., Everett, N., Jelic, V. & Cocker, T. L. Algorithm for subcycle terahertz scanning tunneling spectroscopy. *Physical Review B* **105**, 115427 (2022).

[54] Wang, L., Xia, Y. & Ho, W. Atomic-scale quantum sensing based on the ultrafast coherence of an H_2 molecule in an STM cavity. *Science* **376**, 401–405 (2022).

[55] Li, H. *et al.* Real-Space Sampling of Terahertz Waveforms Under Scanning Tunneling Microscope. *ACS Photonics* **11**, 1428–1437 (2024).

[56] Siday, T. *et al.* All-optical subcycle microscopy on atomic length scales. *Nature* **629**, 329–334 (2024).

[57] Roelcke, C. *et al.* Ultrafast atomic-scale scanning tunnelling spectroscopy of a single vacancy in a monolayer crystal. *Nature Photonics* **18**, 595–602 (2024).

[58] Bobzien, L. *et al.* Ultrafast state-selective tunneling in two-dimensional semiconductors with a phase- and amplitude-controlled THz-scanning tunneling microscope. *APL Materials* **12**, 051110 (2024).

[59] Sheng, S. *et al.* Terahertz spectroscopy of collective charge density wave dynamics at the

atomic scale. *Nature Physics* **20**, 1603–1608 (2024).

[60] Zhussupbekov, K. *et al.* Imaging and identification of point defects in $PtTe_2$. *npj 2D Materials and Applications* **5**, 14 (2021).

[61] Chen, C. J. *Introduction to Scanning Tunneling Microscopy Third Edition*. Monographs on the Physics and Chemistry of Materials (Oxford University Press, Oxford, New York, 2021), third edition, new to this edition:, third edition, new to this edition: edn.

[62] Giessibl, F. J., Hembacher, S., Bielefeldt, H. & Mannhart, J. Subatomic Features on the Silicon (111)-(7×7) Surface Observed by Atomic Force Microscopy. *Science* **289**, 422–425 (2000).

[63] Welker, J. & Giessibl, F. J. Revealing the Angular Symmetry of Chemical Bonds by Atomic Force Microscopy. *Science* **336**, 444–449 (2012).

[64] Emmrich, M. *et al.* Subatomic resolution force microscopy reveals internal structure and adsorption sites of small iron clusters. *Science* **348**, 308–311 (2015).

[65] Chang, T.-R. *et al.* Prediction of an arc-tunable Weyl Fermion metallic state in $Mo_xW_{1-x}Te_2$. *Nature Communications* **7**, 10639 (2016).

[66] Kim, H.-J., Kang, S.-H., Hamada, I. & Son, Y.-W. Origins of the structural phase transitions in $MoTe_2$ and WTe_2. *Physical Review B* **95**, 180101 (2017).

[67] Erba, A. *et al.* CRYSTAL23: A Program for Computational Solid State Physics and Chemistry. *Journal of Chemical Theory and Computation* **19**, 6891–6932 (2023).

[68] Bodo, F., Desmarais, J. K. & Erba, A. Spin current density functional theory of Weyl semimetals. *Physical Review B* **105**, 125108 (2022).

CHAPTER 6

CONCLUSIONS AND OUTLOOK

The demand for technological advancement and fundamental scientific research converges in the field of layered materials, since they are both promising for next-generation devices and a platform for exploring rich physical phenomena. By using a local, ultrafast probe, this thesis investigates layered materials to address fundamental questions about their atomic-scale, low-energy properties. In the following, the main results are summarized and placed in perspective, before near-term and longer-term scientific opportunities are outlined.

6.1 Conclusions

Overall, the results presented in this thesis demonstrate atomic-scale probing and control of low-energy excitations in layered materials while advancing the experimental technique of THz-STM.

The main advances of this thesis are as follows:

- Developing a self-consistent measurement and data-analysis concept for retrieving the terahertz near field via the tunneling current with atomic-scale precision (Chapter 3).
- Demonstrating local phonon spectroscopy associated with atomic-scale surface features on 2D material surfaces (Chapter 4).
- Using tip-enhanced terahertz pulses to drive and read out a structural topological phase transition and spatially resolving it with sub-picometer resolution (Chapter 5).

Taken together, these results advance THz-STM as a tool for ultrafast, atomically resolved measurements of local electrodynamics and for terahertz field-driven control of low-energy properties. Additionally, they deepen the understanding of electric field coupling to the crystal lattice and the role of atomic-scale disorder in 2D material systems. The remainder of this section discusses each of the three main chapters by summarizing their central outcomes, the state of the capabilities established in this work, and the open questions and opportunities they motivate.

Chapter 3 (Control and validation of terahertz near-fields for atomic-scale time-domain spectroscopy): The goal of this chapter was to develop a robust measurement parameterization and data-analysis/validation framework that enables THz-TDS in an STM tunnel junction with atomic-scale spatial resolution. The central idea is a self-consistent, data-driven validation procedure in which acquisition parameters are iteratively adjusted until the terahertz electric field waveform is accurately retrieved via the terahertz-driven tunneling current. This technique is broadly applicable to STM-compatible samples and is straightforward to implement in existing THz-STM setups, requiring little to no additional hardware.

The framework is benchmarked on Au(111), serving as the standard reference sample, across multiple STM tips and free-space waveform shapes. Within this approach, suitable field-strength and polarity regimes can be identified quantitatively, and the d.c. bias voltage can be used as an additional degree of freedom to access a wider range of operating conditions and to validate the waveform qualitatively. As a first demonstration of atomic-scale THz-TDS contrast, a defect on GaAs(110) exhibits a strong resonance at $\sim 1\,\mathrm{THz}$. Comparison to calculations allows it to be identified as the technologically relevant DX center, which had not previously been spatially resolved.

Overall, atomic-scale THz-TDS with the associated data analysis and validation framework adds a measurement capability to THz-STM that previously only existed at the hundreds of nanometer scale. In practice, while the technique is generally applicable to all conducting materials, the shape of the current-voltage characteristic can make it challenging to tune the acquisition parameters such that the strong-field pulse induces a clean unipolar current pulse in certain cases. In addition, the waveform retrieval requires sufficient signal-to-noise ratio of the terahertz-induced tunneling current when chopping the weak-field pulse train. Open questions remain regarding (i) a fully microscopic interpretation of the extracted complex dielectric response and (ii) how changes in the local $I - V$ curve under photoexcitation or field-driven modification by an additional pump pulse impact the terahertz readout. These points directly motivate the outlook directions on atomic-scale THz-TDS discussed in the next section.

Chapter 4 (Atomic-scale phonon spectroscopy of 2D heterostructures): The goal of this chapter was to investigate how atomic-scale features such as defects and in-plane interfaces modify the local low-energy phonon environment. This was addressed by applying atomic-scale THz-TDS on a $WSe_2/SnSe_2$ heterostructure sample. Waveforms were acquired on the pristine surfaces where WSe_2 served as a reference due to its low featureless phonon density of states within the measurement bandwidth. In addition, measurements were performed on a defect in $SnSe_2$, identified as a W substitution on a Sn site, and at several locations on $SnSe_2$ approaching an in-plane interface with WSe_2.

A spectral contrast at $\sim 2\,\mathrm{THz}$ is observed as an amplitude dip in THz-TDS between the pristine $SnSe_2$ and WSe_2 surfaces. This is in agreement with DFT calculations of the phonon dispersions of both materials, where $SnSe_2$ exhibits a flat acoustic phonon band (large phonon density of states) in this frequency range, whereas WSe_2 does not show any significant phonon density of states in the experimental bandwidth. Using WSe_2 as a reference, different locations on $SnSe_2$ are explored, with the overall observation that approaching an in-plane interface as well as measuring at the location of a substitutional defect locally suppresses the $\sim 2\,\mathrm{THz}$ feature. The $2\,\mathrm{THz}$ phonon mode is a flexural mode where the Sn atoms perform an out-of-plane movement. Away from the center of the Brillouin zone, this movement is out-of-phase for adjacent unit cells. The suppression of the mode

is explained by increased local lattice stiffness when W replaces Sn and near the interface, which modifies the local force constants and influences the lattice motion. As an additional outcome, THz-STM imaging at low tip height can be used to image the lattice connection of the two materials at the interface with atomic resolution, which can be less apparent in conventional STM imaging when a high electronic density of states dominates the contrast.

These results establish atomic-scale THz-TDS as a tool for probing the local phonon environment in the vicinity of atomic-scale features. In principle, this technique is compatible with a wide range of STM-compatible samples; however, due to the bandwidth of the terahertz pulses, the sample must be chosen such that the relevant phonon modes lie in this range. A broader bandwidth terahertz pulse could allow a larger frequency range to be studied in the future. Nevertheless, a wide range of materials exhibit low-energy phonons within the present bandwidth, and additionally, low-energy collective phenomena (e.g., charge-density waves) are expected to show strong local modulation near defects and interfaces. As shown in the preliminary data at the end of this chapter, experiments with samples exhibiting CDWs are already underway.

Chapter 5 (Terahertz field control of surface topology with subatomic resolution): The goal of this chapter was to investigate the terahertz pulse-induced topological phase transition, associated with a shear-mode, in layered material WTe_2 on a local scale. The transition is driven by the terahertz pulses enhanced at the STM tip apex and the spatial and electronic differences between phases are read out via the out-of-phase component of the terahertz tunneling current. Measurements of topography under terahertz illumination, the total current recorded during terahertz field modulation, and bias-dependent THz-STM images of the in-phase and out-of-phase tunneling current support a terahertz-field-driven change of the surface electronic structure and movement of the surface layer. The experiments were performed on bulk WTe_2 with free-space terahertz field strengths of $100\,\mathrm{V/cm}$, which corresponds to junction fields on the order of $1-10\,\mathrm{V/nm}$ due to tip enhancement.

The first key result is that terahertz fields enhanced at an STM tip can drive the shear mode associated with the phase transition, as demonstrated by atomic-scale THz-TDS measurements on the WTe_2 surface. Changes in topography, together with a delayed response on microsecond timescales, indicate a transition from the ground state into a metastable state followed by relaxation when the terahertz pulse train is blocked. The electronic and spatial contrast between the phases is resolved via the out-of-phase component with sub-picometer scale resolution. In combination with theory, this is consistent with the transition being confined to the top atomic layer. The contrast is present within the bias window corresponding to the band-structure region in which the type-II Weyl points are predicted and where electronic changes are expected across the phase transition. Together, these results demonstrate that THz-STM can both locally drive and probe a phase transition in a layered material. This work provides the first demonstration of a light-induced

heterostructure formed by locally switching the phase relative to the surrounding material.

More broadly, this project advances THz-STM as a platform that can induce metastable states with ultrafast terahertz pulses while directly measuring the differences between ground state and metastable configurations, even when the relaxation occurs on timescales far slower than the terahertz period. Since many materials, particularly layered materials, exhibit metastable states that can be induced by terahertz frequency pulses, this technique is not limited to bulk WTe_2. The range of relaxation dynamics that can be accessed with this approach is set by the field-modulation protocol (e.g., optical chopper rate, typically milli- to microseconds). A consistent bias-dependent out-of-phase signal requires sufficient contrast in the electronic band structure between the phases. Resolving spatial differences between the phases further relies on a shift of the surface charge density during the transition. Finally, there is an ongoing discussion in the literature regarding whether WTe_2 in its ground state robustly hosts type-II Weyl points. The measurements presented in this thesis do not provide a definitive determination of the Weyl nature of WTe_2, but instead reveal a terahertz-driven modification in the relevant energy range. An important question is the lateral extend of the phase transition around the tip apex. A potential strategy to quantify this is discussed in the outlook. Further, the details of the mechanism by which the terahertz field drives the phase transition is not fully understood. The measurements indicate that the peak field strength is a key parameter, but it is unclear whether the response depends on resonant (frequency-dependent) driving or primarily on the electric field. The latter would be consistent with ferroelectric bilayer switching, which was achieved by using static electric fields. [1]

A common thread across all main thesis chapters is the ability of THz-STM to use ultrafast terahertz pulses to generate a tunnel current across the tip-sample-junction that carries information about the electronic and optical properties of the sample localized to the atomic scale. In this thesis, this progresses from adding atomic-scale THz-TDS as a new technique to the THz-STM tool box, to extracting contrast of the dielectric environment related to atomic-scale features on a TMD heterostructure sample, and finally to driving and reading out a phase transition with sub-picometer spatial resolution. Together, these results show that THz-STM is uniquely well suited to study material properties and their response to electric fields. Several open questions and practical constraints are highlighted in the chapter-specific discussions above. The following section builds on these by outlining immediate next steps, as well as longer-term scientific opportunities in 2D materials and beyond.

6.2 Outlook

This outlook section is organized into two parts. First, near-term directions are discussed that are direct extensions of the results of this thesis. Second, longer-term goals and opportunities are presented that have the potential to further develop the capabilities of the THz-STM technique.

Near-term developments:

- *Time-resolved atomic-scale THz-TDS.* s-SNOM at terahertz frequencies has recently progressed from THz-TDS to time-resolved terahertz spectroscopy, revealing the ultrafast dynamics of the dielectric function on the 10–100 nm scale [2–6]. Therefore, a natural next step for atomic-scale THz-TDS is to add time resolution. In practice, this requires incorporating a pump pulse into the measurement scheme and implementing a pump-probe protocol in which the recorded terahertz near-field waveform constitutes the probe. The waveform validation framework presented in this thesis provides a basis to disentangle pump-induced dynamics of the complex dielectric response from pump-induced changes to the tunnel junction and its electronic states. The THz-STM setup presented in Chapter 2.5 has the capabilities to perform time-resolved terahertz spectroscopy and the implementation of such measurements is already underway.

- *Determining the lateral extent of the terahertz-driven phase transition.* The measurements on bulk WTe_2 raise the question of the lateral extent of the driven phase transition around the STM tip and how it may be influenced by disorder, such as defects, domain boundaries and strain. The bulk material experiments established a phase-contrast readout scheme based on the out-of-phase component of the terahertz tunneling current. To address the lateral extent question, a promising near-term approach is to apply the same procedure to mono- to few-layer WTe_2 samples with well-defined step edges and/or isolated islands. By mapping the phase transition contrast along or as a function of distance away from symmetry-breaking features, a characteristic interaction length scale (or field-driven radius around the tip) may be extracted.

- *Ultrafast quasi-particle interference (QPI) mapping.* In conventional STM, QPI is employed to extract the surface electronic band structure from real-space STM images. The momentum-space is mapped by Fourier transform of bias-dependent $\mathrm{d}I/\mathrm{d}V$ images with interference patterns that arise from quasiparticle scattering at surface defects or step edges. The large-area images of WTe_2 presented in this thesis (Fig. 5.8) demonstrate that THz-STM can achieve the signal-to-noise ratio required for recording QPI-scale maps and that it can resolve dynamically modulated surface states in real space with picometer-scale resolution. It is important to note that differential imaging of the phase transition is a special case in which quasiparticle scattering reveals the electronic differences between two phases. By contrast, in lightwave-driven tunneling, the THz-STM scan contains information over the full whole voltage range sampled by the pulse for the current state of the material. A near-term proof-of-principle, building on the WTe_2 measurements, is therefore to demonstrate QPI-like contrast using terahertz-induced signals under steady-state conditions, ideally using a sample that

has demonstrated unique signatures in conventional QPI. Such measurements can be used to benchmark how the terahertz-driven tunneling current (which effectively samples a finite range of the nonlinear I–V characteristic) relates to the energy-selective $\mathrm{d}I/\mathrm{d}V$ maps typically used. Building on such a demonstration, an eventual pump–probe implementation would enable ultrafast QPI, i.e., QPI maps as a function of pump–probe delay and terahertz field strength. This requires exceptional system stability, since it entails acquiring large-area images with a range of parameter configurations (field strength, delay, and/or bias voltage) at constant experimental conditions.

Long-term goals and opportunities:

- *Microscopic theoretical description of atomic-scale THz-TDS.* A thorough theoretical analysis tailored to the THz-STM junction geometry will be critical for interpreting future atomic-scale contrast in terahertz near-field spectroscopy. An atomic tunnel junction differs fundamentally from the electrodynamic models commonly used for scattering-type near-field probes [7–9]. A quantitative interpretation of experimental findings requires theory that connects strong-field lightwave-driven tunneling [10–14] to the local material response and an atomic-scale description of the electromagnetic environment of a material surface including non-equilibrium effects and the role of disorder.

- *Extending the frequency range of atomic-scale THz-TDS.* The THz-CC approach for waveform sampling introduced in this thesis is not restricted to terahertz excitation and should therefore be extendable to lightwave-driven tunneling processes at higher frequencies [15–19], provided the experiments operate in the strong-field regime [20]. Pulses of different frequencies may be combined, such as using a strong-field multi-terahertz pulse to sample a weak-field terahertz pulse. Extending the bandwidth (e.g., toward multi-terahertz or mid-infrared pulses) would grant access to a wider range of elementary excitations and could enable atomic-scale spectroscopy across a larger frequency window.

- *Investigating collective phenomena in 2D materials.* Atomic-scale THz-TDS in combination with the sensitivity to phase transitions provides a strong motivation to further pursue the study of collective behavior in 2D materials, such as charge-density-waves (as shown in the preliminary measurements included at the end of Chapter 4). Recent publications highlight the relevance of collective excitations in 2D materials using THz-STM [21, 22]. Many of these exhibit intrinsically low-energy modes (often in the terahertz range) and can host metastable states, making them ideally suitable for terahertz-field-driven control. A long-term research direction is therefore to combine atomic-scale terahertz spectroscopy with controlled strong-field terahertz excitation to study how collective order parameters evolve in

such samples, especially near defects, domain walls, and interfaces, and to explore whether terahertz fields can reproducibly access metastable states in a local environment.

The various future directions described above emphasize that the outcomes of this thesis not only advance the current state of THz-STM, but also provide a starting point for a broader class of experiments. Near-term goals include adding time resolution to atomic-scale THz-TDS, establishing ultrafast QPI, and leveraging custom sample design to isolate specific effects. Longer-term opportunities include expanding the frequency bandwidth, deepening the understanding of the underlying microscopic light-matter interaction, and targeting collective excitations in 2D materials - all while pushing the experiment's spatiotemporal resolution to new limits.

BIBLIOGRAPHY

[1] Fei, Z. *et al.* Ferroelectric switching of a two-dimensional metal. *Nature* **560**, 336–339 (2018).

[2] Eisele, M. *et al.* Ultrafast multi-terahertz nano-spectroscopy with sub-cycle temporal resolution. *Nature Photonics* **8**, 841–845 (2014).

[3] Yao, Z. *et al.* Photo-induced terahertz near-field dynamics of graphene/InAs heterostructures. *Optics Express* **27**, 13611–13623 (2019).

[4] Pizzuto, A., Mittleman, D. M. & Klarskov, P. Laser THz emission nanoscopy and THz nanoscopy. *Optics Express* **28**, 18778–18789 (2020).

[5] Plankl, M. *et al.* Subcycle contact-free nanoscopy of ultrafast interlayer transport in atomically thin heterostructures. *Nature Photonics* **15**, 594–600 (2021).

[6] Siday, T. *et al.* Ultrafast Nanoscopy of High-Density Exciton Phases in WSe_2. *Nano Letters* **22**, 2561–2568 (2022).

[7] Cocker, T. L., Jelic, V., Hillenbrand, R. & Hegmann, F. A. Nanoscale terahertz scanning probe microscopy. *Nature Photonics* **15**, 558–569 (2021).

[8] Keilmann, F. & Hillenbrand, R. Near-field microscopy by elastic light scattering from a tip. *Philosophical Transactions of the Royal Society A: Mathematical, Physical and Engineering Sciences* **362**, 787–805 (2004).

[9] Chen, X. *et al.* Modern Scattering-Type Scanning Near-Field Optical Microscopy for Advanced Material Research. *Advanced Materials* **31**, 1804774 (2019).

[10] Kwok, Y., Chen, G. & Mukamel, S. STM Imaging of Electron Migration in Real Space and Time: A Simulation Study. *Nano Letters* **19**, 7006–7012 (2019).

[11] Shi, T., Cirac, J. I. & Demler, E. Ultrafast molecular dynamics in terahertz-STM experiments: Theoretical analysis using the Anderson-Holstein model. *Physical Review Research* **2**, 033379 (2020).

[12] Frankerl, M. & Donarini, A. Spin-orbit interaction induces charge beatings in a lightwave-STM – single molecule junction. *Physical Review B* **103**, 085420 (2021).

[13] Hu, Z., Kwok, Y., Chen, G. & Mukamel, S. Carrier-Envelope-Phase Modulated Currents in Scanning Tunneling Microscopy. *Nano Letters* **21**, 6569–6575 (2021).

[14] Banerjee, S. & Zhang, P. Scaling of Time-Dependent Tunneling Current in Terahertz Scanning Tunneling Microscopes. *Physical Review Applied* **18**, 024011 (2022).

[15] Müller, M., Martín Sabanés, N., Kampfrath, T. & Wolf, M. Phase-Resolved Detection of Ultrabroadband THz Pulses inside a Scanning Tunneling Microscope Junction. *ACS Photonics* **7**, 2046–2055 (2020).

[16] Rybka, T. *et al.* Sub-cycle optical phase control of nanotunnelling in the single-electron regime. *Nature Photonics* **10**, 667–670 (2016).

[17] Garg, M. & Kern, K. Attosecond coherent manipulation of electrons in tunneling microscopy. *Science* **367**, 411–415 (2020).

[18] Lloyd-Hughes, J. *et al.* The 2021 ultrafast spectroscopic probes of condensed matter roadmap. *Journal of Physics: Condensed Matter* **33**, 353001 (2021).

[19] Arashida, Y. *et al.* Subcycle Mid-Infrared Electric-Field-Driven Scanning Tunneling Microscopy with a Time Resolution Higher Than 30 fs. *ACS Photonics* **9**, 3156–3164 (2022).

[20] Park, S. B. *et al.* Direct sampling of a light wave in air. *Optica* **5**, 402–408 (2018).

[21] Sheng, S. *et al.* Terahertz spectroscopy of collective charge density wave dynamics at the atomic scale. *Nature Physics* **20**, 1603–1608 (2024).

[22] López, L. E. P. *et al.* Atomic-scale ultrafast dynamics of local charge order in a THz-induced metastable state of 1T-TaS_2 (2025). Available at http://arxiv.org/abs/2505.20541. Issue: arXiv:2505.20541 arXiv:2505.20541 [cond-mat].